Study of Phenomenologies During Templated Solid-State Dewetting of Thin Single Crystal Films

by

Gye Hyun Kim

B.S., Materials Science and Engineering, University of California at Berkeley, 2010

M.S., Materials Science and Engineering, Massachusetts Institute of Technology, 2012

Submitted to the Department of Materials Science and Engineering

in partial fulfillment of the requirements for the degree of

Doctor of Philosophy in Materials Science and Engineering

at the

MASSACHUSETTS INSTITUTE OF TECHNOLOGY

February 2016

Signature of Author …….
Department of Materials Science and Engineering
January 13, 2016

Certified by …….
Carl V. Thompson

Stavros Salapatas Professor of Materials Science and Engineering
Thesis Advisor

Accepted by ……
Donald R. Sadoway

John F. Elliott Professor of Materials Chemistry
Chair, Departmental Committee on Graduate Students

Study of Phenomenologies During Templated Solid-State Dewetting of Thin Single Crystal Films

by

Gye Hyun Kim

Submitted to the Department of Materials Science and Engineering on January 13 2016,
in partial fulfillment of the requirements of the degree of Doctor of Philosophy in
Materials Science and Engineering

Abstract

Generally, thin films are away from equilibrium in the as-deposited state and will agglomerate, or dewet, to form islands given sufficient atomic mobility. This dewetting process can occur in the solid state, well below the films' melting temperature. Dewetting initiates from film-substrate-vapor three-phase boundaries, which can form naturally via natural hole formation in the continuous film or be intentionally made via pre-patterning of the film. These boundaries, or film edges, then retract via capillarity-driven mass transport. As the edges retract, many phenomena occur, making the dewetting morphology complex. Dewetting of thin films has traditionally been considered undesirable in the microelectronics industry, but more recent studies utilized dewetting in many applications, including sensors, solar cells, fuel cells, and catalysts for nanowire and nanotube growth.

Solid-state dewetting of single crystal films leads to a very regular morphology, due to anisotropy in surface energy and surface self-diffusivity. When such films are templated by pre-patterning, regular dewetting patterns, much smaller than the original templates, can be made. Thus, templated dewetting can be a potential method for generating complex nanostructures with sub-lithographic length scales. However, controlling such dewetting patterns necessitates in-depth quantitative understanding of anisotropic solid-state dewetting.

The research described in this thesis focused on detailed analysis of individual dewetting phenomenologies, using single crystal Ni films as a model system. The rate of capillarity-driven edge retraction was found to depend strongly on the in-plane orientation of the edge and the ambient condition. It was determined that the surface structure of the top facet under different ambient conditions are closely linked to the differences in the edge retraction rates. As the edge retracts, a thickening rim forms due to mass accumulation at the edge. Also, a valley can form ahead of the rim under certain conditions, and this valley can pinch off the rim, resulting in wire-like structures. This pinch-off phenomenon was also found to be strongly dependent on the in-plane orientation of the retracting edge. It was determined that pinch-off occurs more easily when the additional surface energy cost associated with initiation of valley formation is smaller. The retracting rim itself can also become unstable and can form finger-like structures similar to the cellular structures that often form during solidification. It was found that mass is rejected from the finger tip, so that the rim at the tip maintains a constant height and the fingered front moves at a constant rate. A steady-state model for the motion of a fingered front was developed and found to be in agreement with experiments. This model accounts for the lateral rejection of mass to form wire-like structures between the fingers, and shows that the finger spacing is determined by the velocity of the finger tips relative to the diffusivity governing mass rejection. Both pinch-off and the fingering instability result in wire-like structures, and these structures can undergo a Rayleigh-like instability in later stages, in which they break up into smaller particles.

The characteristic spacing of the dewetted particles was also found to be strongly dependent on the in-plane crystallographic orientation of the wire-like structures. It was further found that for a fixed cross-sectional area, the total surface energy of the wire-like structure determines the particle spacing. Lastly, it was found that while natural holes that form in single crystal films initially have polygonal shapes, as their growth slows, corners often begin to retract faster than the straight edges, in a way similar to the fingers on a fingered front. A computational model was developed for such a corner instability, and the balance between the thinning of the corner tip due to tip lengthening and the thickening of the tip due to mass accumulation during retraction was found to determine the condition under which the corner retracts at a constant rate.

Thesis Advisor: Carl V. Thompson
Title: Stavros Salapatas Professor of Materials Science and Engineering

Acknowledgement

When I graduated from college five years ago, I was proud that I graduated with highest honors and that I won the departmental citation award conferred to the only one person in the department. To be honest, I had not realized that there still was a lot of room inside myself for growth. Then I started my next stage of life at MIT as graduate student, with much pride probably extending towards the realm of hubris. It took about one additional month until I realized that I still needed to learn, when I bombed the first midterm exam in both Thermodynamics and Quantum Mechanics. That first semester was filled with stress and awe to every impossibly difficult exam problem I faced. But I also realized during that time that all the smart people at MIT that I felt were way ahead of me were a great resource I can learn from, and without these colleagues would I not have been able to get out of the mire.

So was true in my thesis research. ***Carl***, my thesis advisor, was a great teacher from whom I could clearly see what I needed to learn more. I was able to get done and learn a lot during my graduate study only because his huge passion for dewetting and his insight have always made me feel supported whenever I encountered difficult problems. My thesis committee members, ***Professors Carter and Ross***, have also offered many fruitful comments for my thesis research since the qualifying exam till the very last thesis defense. I have also benefited from a number of collaborators in many parts of my thesis research. ***Rae*** has offered a number of modeling insights I could not see myself alone. Many of my publications got much more convincing stories thanks to the seamless collaboration with her. ***Soli*** and ***Nagy*** have also offered many great insights for my research and their passion for dewetting has also motivated me a lot. ***Wen*** and ***Professor Yildiz*** have also provided tremendous help with surface structure measurements and analyses. More recently, ***Yoon Ah*** has also joined us and her results also gave me further insight. There are many other collaborators I simply cannot name all. Additionally, I would also like to acknowledge the past and current Thompson Group members. Specifically, ***Jongpil*** has been a great mentor, from whom I could very quickly pick up the skills needed for my research. ***Hang*** has also provided huge help with the vacuum system I had much difficulty with. ***Swee-Ching*** also was very helpful when I had to tackle difficult sample-making with FIB. I would also like to acknowledge many staff members, including ***Rich, Kurt, Gary, and Mark*** for being very useful resources when I was faced with equipment- or process-wise difficulties. I would like to sincerely thank all for the huge support for the last 5 years.

Life at MIT oftentimes got quite stressful. It was only with countless social interactions over countless counts of chicken and beer with my friends that I was able to refresh myself and get back on track. I specifically thank my New England 88 friends: ***Donghun, Han Kyul, Hyung Won, Dongkwan, Sucheol, Kyel, Sangjun, Sung Kwan, Ingon, Jongwoo, Hyunkwang, Taeyeon, Junghyun, Anna, Grace, Siwon, Kyungyong***, and many others. My old Berkeley friends have also been always supportive: ***Professor Glaeser, Hong-Chan, Dongwoo, Kyung Jun, Sharon, Brian***, and many others. I also thank my KGMSE friends: ***Jinhyuk, Mansoo, Jiyoun, Sangtae, Sehoon***, and many others.

Along with research, this last 5 years has been a very important period of my life. This was the time when I had a chance to truly ponder on and decide what I would like to do, and the time when I was given many opportunities to explore the potential choices I can make. Doing so was not always easy and pleasant; sometimes I got disappointed in myself that I made no effort to find my true interest when I was younger. There also was a painful wait regarding my immigration that took much longer than expected. To enhance my business acumen I also

studied for CFA exams during every weekend for the last 2 years. However, I am gifted that I wasn't standing alone among all of these personal difficulties and challenges. Even though it meant pretty much the longest distance relationship possible in the planet, ***Jiwon*** has supported my decision to study at MIT from the beginning. And she has continued doing so for 5.5 freakin' years. I have always been thankful to her for making me feel that I am a person worthy of waiting for this much time from halfway across the globe. Honestly, I don't have a very loving personality that expresses emotions much and this is one of the things I always feel sorry for, but this time I really have to say this: I love you, and thank you, ***Jiwon***. The same goes to my family. Thank you and love you, my mother, ***Sug Kyeong***, my father, ***Young Han***, and my brother, ***Gi Hyun***, for always supporting my decision and for never forgetting about me all the way across the Pacific.

Preface

This thesis work is a compilation of the research work completed or in progress during the graduate program at Massachusetts Institute of Technology for the degree of Doctor of Philosophy in Materials Science and Engineering. I hereby state that much of the material included in this thesis has been or will be published in peer-reviewed journals and my Master's Degree thesis. The following is the list of publications, accurate as of January 13 2016, that contain part of the material in this thesis, sometimes verbatim. Proper citations are also added in the appropriate sections.

1. **Gye Hyun Kim**, W. Ma, B. Yildiz, and C.V. Thompson, "Effect of Annealing Ambient on Anisotropic Retraction of Edges During Solid-State Dewetting of Thin Single Crystal Films," (in process).
2. **Gye Hyun Kim**, S. Jahangir, N. Valanoor, and C.V. Thompson, "The Steady-State Finger Period During Solid-State Dewetting of Single Crystal Films," *Acta Materialia* (submitted).
3. R.V. Zucker*****, **Gye Hyun Kim*,** J. Ye, W.C. Carter, and C.V. Thompson, "The Reaction Kinetics of Edges and Corners of Holes in Agglomerating Single Crystal Thin Films," *Journal of Applied Physics* (submitted).
4. **Gye Hyun Kim** and C.V. Thompson, "Effect of Surface Energy Anisotropy on Rayleigh-Like Solid-State Dewetting and Nanowire Stability," *Acta Materialia* **84** (2015).
5. R.V. Zucker, **Gye Hyun Kim**, W.C. Carter, and C.V. Thompson, "A Model for Solid-State Dewetting of a Fully-Faceted Thin Film," *Comptes Rendus Physique* **14** 7 (2013).
6. **Gye Hyun Kim**, R.V. Zucker, J. Ye, W.C. Carter, and C.V. Thompson, "Quantitative Analysis of Anisotropic Edge Retraction by Solid-State Dewetting of Thin Single Crystal Films," *Journal of Applied Physics* **113**, 043512 (2013).
7. **Gye Hyun Kim**, "Quantitative Analysis of Anisotropic Edge Retraction During Solid-State Dewetting of Thin Single Crystal Films," Master's Thesis, MIT, Cambridge (2012).

*****Equal contribution

Table of Contents

List of Tables

List of Figures

Figure 1-13. Formation of one, two or three wires by pinch-off, after Dornel et al.

Figure 1-14. Number of wires formed by pinch-off versus an angular function of equilibrium contact angle, simulated with an isotropic surface energy. The straight lines show the boundaries of the 1-, 2-, and 3-wire formations.

Figure 1-15. Deepening of valleys and pinch-off of edges in a natural hole in Ni(110) film. The flow rate of reducing gas (5% H_2 + 95% N_2) was 2310sccm. (a)-(c) Top-down AFM images. (d)-(f) AFM height profiles. Annealing times are indicated in the images.

Figure 1-16. Dewetting of gold films on fused silica by propagation of natural holes. (a) An optical micrograph of growing holes. Dark region is the gold and bright region is the exposed silica substrate. (b) An SEM image showing uneven accumulation of gold near the retracting edges. Bright region is the gold and dark region is the exposed silica substrate.

Figure 1-17. Stroboscopic image of the growth of a dewetting hole showing the propagation of fingers in a SOI structure, after Cheynis et al.

Figure 1-18. KMC simulation showing propagation of fingers. The dark blue region indicates the exposed substrate and other colors indicate the regions of different film thicknesses.

Figure 1-19. AFM images of growing natural holes in Ni(100) before and after the development of corner instability.

Figure 1-20. Schematic diagram of the diffusion field around a natural hole, after Ye and Thompson.

Figure 1-21. Development of the Rayleigh-like instability in copper nanowires after annealing at the temperatures indicated in each micrograph.

Figure 1-22. AFM images of growing natural holes in Ni(100) and Ni(110) films at two different reducing gas flow rates. The annealing time is indicated in the images. (a)-(b) Ni(100), 2310sccm of 5% H_2+95% N_2. (c)-(d) Ni(100), 12sccm. (e)-(f) Ni(110), 2310sccm. (g)-(h) Ni(110), 12sccm.

Figure 1-23. (a) The reference film edge profile is shown for various times after the annealing begins. The aspect ratio is 1:1, and the units of both the vertical and horizontal scale are micrometers. (b) The influence of the absolute value of reference surface energy on the film edge retraction distance vs. time. Each curve is labeled with the surface energy in J/m^2. The relative magnitudes of the surface energies of individual facets were kept the same. (c) The diffusivity on each set of symmetrically-related facets was changed to show its effects on the retraction distance vs. time. All plots are reproduced from Zucker et al.

Figure 1-24. Formation of ordered arrays of Au particles by pre-patterning of oxidized Si substrates. Under the appropriate pit spacing, size and film thickness, all of the deposited gold diffuses into the pits to form ordered arrays. Scale bar indicates 500μm.

Figure 1-25. Formation of ordered Au islands by pre-patterning the gold film. Unlike continuous films (**a**), patterned films can generate ordered arrays of islands in polycrystalline films (**b-d**), controlled by the aspect ratios of the initial pattern. Scale bars indicate 5μm.

Figure 1-26. Dewetting of square patches patterned in a Ni(110) film. Dewetting morphology is clearly dependent on the initial orientation and the size of the patches. The gray dashed lines indicate the initial shapes of the patches. Scale bars indicate 10μm.

Figure 2-1. The Balzers ultrahigh vacuum e-beam evaporation system.

Figure 2-2. Schematic illustration of HRXRD scan settings. Each parameter was carefully adjusted to maximize signal from the epitaxial film.

Figure 2-3. **(a)** 2θ-ω scan of Ni(100) film. **(b)** 2θ-ω scan of Ni(110) film. **(c)** (111) in-plane peak of MgO(100). **(d)** (111) in-plane peak of MgO(110). **(e)** (111) in-plane peak of Ni(100) deposited on MgO(100). **(f)** (111) in-plane peak of Ni(110) deposited on MgO(110).

Figure 2-4. **(a)** 2θ-ω scan of Ni(111) film. **(b)** (2206) in-plane peak of sapphire ($1\bar{1}20$). **(c)** (113) in-plane peak of Ni(111) deposited on sapphire ($1\bar{1}20$).

Figure 2-5. The tube furnace used for thermal annealing with an oxygen measurement tube installed. The probe is installed on a rail carefully aligned with the tube furnace so that the probe can be inserted smoothly in the tube.

Figure 2-6. The Perkin-Elmer e-beam evaporation system. A RHEED system is also installed inside the main chamber. The system operates with a rotary pump and a cryopump.

Figure 3-1. (a) and (c) Retraction distance versus annealing time with 5% H_2 + 95% N_2 flowing at a rate of 2310sccm. (b) and (d) Retraction distance versus annealing time with 5% H_2 + 95% N_2 flowing at a rate of 95sccm. The out-of-plane orientation of the Ni film and the in-plane retraction directions are indicated in each figure. The inset images are AFM images of the natural holes under each experimental condition. Corresponding in-plane directions are indicated with the images.

Figure 3-2. (a) and (c) Retraction distance versus annealing time with 5% H_2 + 95% N_2 flowing at a rate of 95sccm. (b) and (d) Retraction distance versus annealing time with 2% H_2 + 98% Ar flowing at a rate of 390sccm. Under these flow rates, the same partial pressure of oxygen was measured. The out-of-plane orientation of the Ni film and the in-plane retraction directions are indicated in each figure.

Figure 3-3. Oxygen partial pressure profiles along the tube furnace under different annealing ambient. A distance of zero indicates the sample surface. Due to the physical constraints of the oxygen probe, the closest distance away from the sample surface the probe could measure was 1.5cm.

Figure 3-4. LEED patterns for Ni(110) and Ni(100) surfaces collected in vacuum or under low pressures of H_2 or O_2. Specific ambient conditions are indicated in Table 3-1. The patterns in the first row ((a)-(c)) are for (110) surfaces and those in the second row ((d)-(f)) are for (100) surfaces. White circles are drawn as visual aids to indicate the diffraction spots. White dashed lines indicate the unit cells of surface structures. Some diffraction spots are not visible because the electron source blocks the screen.

Figure 3-5. Surface structures of (a)-(c) Ni(110) and (d)-(f) Ni(100) under different annealing conditions. The darker spheres are the atoms on the top layer and the lighter spheres are the atoms underneath the top layer. Details of the annealing conditions are provided in Table 3-1.

Figure 3-6. An illustration of ledges propagating in different directions for Ni(100) surfaces with different terrace/facet reconstructions. The single darkest sphere indicates an atom diffusing from the uppermost terrace to the adjacent terrace. The second darkest layer of spheres is the uppermost layer of atoms, and the lightest spheres form the layer underneath that layer, as well as the surface atoms of the adjacent terrace. Orange arrows indicate the shortest paths for diffusion of atoms over the ledges.

Figure 3-7. (a) and (c) Cross-sectional SEM images of retracting rims of kinetically stable edges for Ni(100) films annealed under reducing gas (5% H_2 + 95% N_2) flowing at 2310sccm. (b) and (d) Cross-sectional SEM images of retracting rims of kinetically stable edges for Ni(100) films annealed under reducing gas (5% H_2 + 95% N_2) flowing at 95sccm. The images were obtained after a 50-hour anneal. The macroscopic retraction direction of the kinetically stable edge and the direction normal to the cross-sectional plane (and parallel to the length of the edge) are also indicated in the individual figures.

Figure 4-1. Schematic diagram of the experimental pattern. A row of long patches ranging 2-30μm in width (1μm increment) and 500μm in length is patterned in the [001] and [$1\bar{1}0$] directions in Ni(110) films.

Figure 4-2. AFM images of retracting rims after a 10-hour anneal at 890°C under 2310sccm of reducing gas. All rims retract from the left to the right. (a) Rim retracting in the [$1\bar{1}0$] in Ni(110). (b) Rim retracting in the [001] in Ni(110).

Figure 4-3. Retraction and pinch-off of patterned patches of varying widths in Ni(110) after a 28-hour anneal at 890°C under 2310sccm of reducing gas. Scale bars indicate 10μm. The crystallographic orientation of edge retraction is indicated in the figure.

Figure 4-4. (a)-(b) Edge retraction distance over time in Ni(110) patches annealed at 890°C under 2310sccm of reducing gas. (c)-(d) Minimum Ni(110) film thickness at the valleys after annealing at 890°C under 2310sccm of reducing gas. The retraction orientations are provided in the plots. Measurements were made with the patches of 30μm in initial width and 500μm in initial length.

Figure 4-5. (a)-(d) Schematic representation of a 2-wire formation via pinch-off. Two deepening valleys ahead of the retracting rims merge before pinch-off. (e)-(h) Schematic representation of a 3-wire formation via pinch-off. Two deepening valleys separately pinch off the retracting rims.

Figure 4-6. Schematic diagram of valley deepening and pinch-off.

Figure 4-7. A schematic diagram of a simplified retracting rim and microfaceted valley formation for the purpose of modeling.

Figure 4-8. Cross-sectional SEM images of equilibrated Ni particles in Ni(110), annealed at 890°C under 95sccm of reducing gas.

Figure 4-9. Surface energies of the equilibrium facets relative to the top facet surface energy in Ni(110). As defined in Figure 4-8, facet angle refers to the angle between the top facet and the facet of interest.

Figure 4-10. Critical pinch-off width vs. additional surface energy cost associated with microfaceted valley formation, in the kinetically stable patches in Ni(110) films. The additional surface energy cost is normalized by the valley depth and the top facet surface energy. The retraction orientation of the kinetically stable edges and the individual flow rates of the reducing gas are indicated in the figure.

Figure 5-1. Fingering instability in a photolithographically patterned single-crystal Ni(110) film. Dashed lines in the large image indicate the initial shape of the pattern. It can be seen that the steady-state finger period is different from the wavelength of the initial edge instability (See inset). The Ni islands in the inset image are artifacts of the initial edge instability. The pattern was heated at 900°C under a vacuum level of low 10^{-6} torr.

Figure 5-2. Schematic illustration of a fingering instability. Key terminologies used in the model are also defined.

Figure 5-3. (a) Relationship between the finger period λ and the tip retraction rate v. v was normalized by the surface diffusivity along the side D_m to remove temperature effects. (b) Relationship between the finger period λ and the thermal energy (kT). (c) Relationship between the finger period λ and the initial film thickness h. All experimental data are reproduced from Cheynis et al.

Figure 6-1. (a) A top-down AFM image of a natural hole after 12 hours of annealing. (b) A top-down AFM image of a natural hole after 24 hours of annealing. (c) A three-dimensional view of a natural hole after the corners became unstable. (d) A cross-sectional AFM profile of the edge and the tip at the corner of a natural hole after a 12-hour anneal. (e) A cross-sectional AFM profile of the edge and the tip at the corner of a natural hole after a 24-hour anneal. (f) The cross-sectional rim area at the edge and the tip of a natural hole at different retraction distances (distance is measured from the center of the hole). The dashed line is a linear fit for the first three data points for the edge, and is intended as a visual guide. The annealing time for each data point is indicated in the figure. Samples were annealed at 890°C under a reducing gas (5% H_2 + 95% N_2) flow of 2310sccm.

Figure 6-2. Experimental results for dewetting of holes that were lithographically pre-patterned in Ni(100) films. (a) Schematic illustration showing the relative sizes of the initial hole patterns. (b) SEM images of patterned holes after a 16-hour anneal show the corner instability. The initial hole sizes, defined as the length of the edge of the patterned square holes, are written below each hole. The images are scaled to have the same magnification. The spacing between the dashed black lines is the reported "transition" size. (c) The normalized rim cross-sectional areas at the center of the edges for different patterned hole sizes after a 16-hour anneal. The rim area is normalized by the retraction distance multiplied by the film thickness. (d) The retraction distances at the tip and the edge for different patterned hole sizes after a 16-hour anneal. An initial hole size of 0 indicates a natural hole. The samples were annealed at 890°C under a reducing gas (5% H_2 + 95% N_2) flow of 2310sccm.

Figure 6-3. The assumed geometry of the corner of a hole. All distances are normalized to the film thickness *H*. The rim has height r_{tip} at the tip of the corner and height r_{edge} along the straight edge of the hole. The rim height gradually increases from r_{tip} to r_{edge} over a distance *L*. The anisotropy of the film material holds the apparent angle of the corner, α, and the radius of curvature of the triple line at the tip, b_{tip}, at constant values.

Figure 6-4. Schematic of the corner geometry. Definitions of the arc length coordinates s_{para} and s_{perp}. The origin is at the midpoint of the triple line at the corner tip, and the points used to calculate $\frac{\partial^2 \kappa}{\partial s_{para}^2}$ and $\frac{\partial^2 \kappa}{\partial s_{perp}^2}$ are marked.

Figure 6-5. A detailed schematic of the tip geometry is shown. Part (a) shows the film at time *t*. Part (b) shows the film at time *t+dt*. The initial rim height, $r_{tip}(t)$, is known, and b_{tip} is constant. The new rim height, $r_{tip}(t+dt)$, is found by volume conservation: the volume in the rim at time *t* plus the volume swept up in the time *dt* must equal the volume in the rim at time *t+dt*. The volume swept up during retraction is that contained in the region of radial thickness *w*, shown in (a). Part (c) also shows the film at time *t+dt*. The dark-shaded portions of the rim are now part of the transition region, and are no longer part of the corner tip. This is because b_{tip} is fixed by the anisotropy of the film material, preventing the arc length of the tip region from increasing with time.

Figure 6-6. A contour plot of the rate of rim height change at the tip is shown. Warm colors indicate that the rim is thickening with time for a given r_{tip} and b_{tip}; cool colors indicate that the rim thins with time. The heavy black line is the steady-state rim height at the tip, r^*_{tip}.

Figure 6-7. Experimental and model results for the rim height and retraction distance as a function of time. The red data and curves are for the edge of the hole, and the blue data and curves are for the tip. The model was run with experimentally obtained values for b_{tip} and *L*. The model overestimates the height of the rim at the edge, and therefore underestimates the retraction distance at the edge. However, the model correctly reproduces the retraction distance vs. time scaling, which goes as time to the 2/5 power.

Figure 7-1. Schematic illustration of the formation of a wire-like structure from a film patterned into a strip, and the subsequent development of a Rayleigh-like decomposition of the wire into an array of particles.

Figure 7-2. (a) Schematic diagram of patterned strips. (b)-(c) Development of a Rayleigh-like instability in Ni(110) strips with an initial width of 2.44μm and thickness of 130nm annealed at 890^0C under 2310sccm of reducing gas for 130 hours.

Figure 7-3. Particle spacing or perturbation wavelength as a function of the in-plane crystallographic direction of the axis of strips patterned from Ni(111) films on (a) sapphire($1\bar{1}20$) and (b) MgO(111), and annealed at 890^0C under 2310sccm of reducing gas for 300 hr. Initial strip widths are indicated in the plots. The strip thickness was 130nm in all cases. The angles are referenced to the $[\bar{2}11]$ orientation.

Figure 7-4. Particle spacing or perturbation wavelength as a function of the in-plane crystallographic direction of the axis of strips patterned from (a)-(b) Ni(100) and (c)-(d) Ni(110) films on MgO, after annealing at 890^0C under 2310sccm of reducing gas for 300 hr. Initial strip

widths are indicated in the plots. The strip thickness was 130nm in all cases. The angles are relative to the [010] in-plane orientation for (100) films (in (a) and (b)) and the $[1\bar{1}0]$ in-plane orientation for (110) films (in (c) and (d)).

Figure 7-5. Particle spacing or perturbation wavelength as a function of the in-plane crystallographic direction of the axis of strips patterned from (a)-(b) Ni(100) and (c)-(d) Ni(110) films on MgO, after annealing at 890^0C under 95sccm of reducing gas for 300 hr. Initial strip widths are indicated in the plots. The strip thickness was 130nm in all cases. The angles are relative to the [010] in-plane orientation for (100) films (in (a) and (b)) and the $[1\bar{1}0]$ in-plane orientation for (110) films (in (c) and (d)).

Figure 7-6. (a)-(b) Cross-sectional SEM images of equilibrated Ni particles on (a) sapphire$(1\bar{1}20)$ and (b) MgO(111). (c)-(d) Top-down views of Ni islands on (c) sapphire$(1\bar{1}20)$ and (d) MgO(111). The particles were annealed at 890^0C under 2310sccm of reducing gas.

Figure 7-7. Cross-sectional and top-down SEM images of the equilibrated particles formed from (a)-(c) Ni(100) and (d)-(f) Ni(110) strips on MgO. Inset images show top views of the particles. Dashed lines indicate locations of cross sections. Arrows in the inset images indicate the orientation of the wire axis. The particles were annealed at 890^0C under 2310sccm of reducing gas.

Figure 7-8. Cross-sectional SEM images of wires bound by facets with surface normals perpendicular to the wire axis of (a)-(b) Ni(100) and (c)-(d) Ni(110) wires on MgO. The same set of facets and shapes are observed for the equilibrated particle cross-sections. The particles were annealed at 890^0C under 2310sccm of reducing gas.

Figure 7-9. Cross-sectional SEM images of retracting rims on both sides of patterned square patches in the $[0\bar{1}1]$ orientation in Ni(111) on MgO and sapphire. Due to the hexagonal symmetry of Ni(111), the rims at the opposite edges of the same patch do not have the same set of facets. The patches were annealed at 890^0C for 10 hours under 2310sccm of reducing gas.

Figure 7-10. (a) Edge retraction distance of patterned square patches in Ni(111) on MgO and sapphire after 7 hours of annealing at 890^0C under 2310sccm of reducing gas. (b) Edge retraction distance of patterned square patches of Ni(111) on MgO and sapphire in the $[0\bar{1}1]$ orientation.

Figure 7-11. Development of a Rayleigh-like instability in strips patterned from (110) Ni films on MgO. (a)-(c) show strips with initial width-to-thickness ratios greater than 1 (w = 3.2μm and h = 130nm). (d)-(f) show strips with initial width-to-thickness ratios equal to 1 (w = 130nm and h = 130nm). Strips were annealed at 890^0C for the indicated times. Dashed lines indicate initial strip shapes. Note that the wide strip developed edge facets as its edges retracted, but that the period of these facets was much smaller than the final particle spacing. The narrow strips did not form edge facets before decomposing into particles.

Figure 7-12. Comparison of perturbation wavelengths measured at the wire end and the body of the wire formed from (a) 0.809μm-wide strips in Ni(100) under 2310sccm of reducing gas, (b) 0.850μm-wide strips in Ni(110) under 2310sccm of reducing gas.

Figure 7-13. Linear relationship between particle spacing or perturbation wavelength and the effective radii of wires from (a) Ni(100) and (b) Ni(110) films on MgO annealed under

2310sccm of reducing gas. Angles in the legend indicate orientations of the axes of the wires and indices in brackets indicate the directions normal to the edges of the strips, as defined in Figure 7-1. For (a), 0 degrees corresponds to a wire with an edge normal in the [010] orientation; for (b), 0 degrees corresponds to a wire with edge normal $[00\bar{1}]$. *A* indicates the proportionality constant from a linear fit.

Figure 7-14. Linear relationship between particle spacing or perturbation wavelength and the effective radii of wires from (a) Ni(100) and (b) Ni(110) films on MgO annealed under 95sccm of reducing gas. Angles in the legend indicate orientations of the axes of the wires and indices in brackets indicate the directions normal to the edges of the strips, as defined in Figure 7-1. For (a), 0 degrees corresponds to a wire with an edge normal in the [010] orientation; for (b), 0 degrees corresponds to a wire with edge normal $[00\bar{1}]$. *A* indicates the proportionality constant from a linear fit.

Figure 7-15. Break-up of Ni(110) wires in a Kinetic Monte Carlo simulation. *N* indicates the number of iteration steps.

Figure 7-16. Cross-sections and top-down views of equilibrated Ni particles formed from (a)-(c) Ni(100) and (d)-(f) Ni(110) films in Kinetic Monte Carlo simulations. Dashed lines indicate monolayers.

Figure 7-17. Particle spacing or perturbation wavelength from Kinetic Monte Carlo simulations for (a) (100) and (b) (110) FCC strips. The angles are relative to the [010] in-plane orientation for (100) films (in (a)) and the $[1\bar{1}0]$ in-plane orientation for (110) films (in (b)).

Figure 7-18. Particle spacing as a function of normalized effective radii from the Kinetic Monte Carlo simulations. "n x n" indicates strips with an aspect ratio of 1 and "wide" indicates strips with widths larger than their thickness. The indexes in square brackets are the in-plane directions normal to the edge of the strip and the angles are relative to the [010] in-plane orientation for (100) films ((a) and (c)) and the $[1\bar{1}0]$ in-plane orientation for (110) films ((b) and (d)).

Figure 7-19. Comparison of perturbation wavelengths measured at the wire end and the body of the wire for (a) 6ML-wide, 3ML-thick, 100ML-long wires of Ni(100) in the KMC simulation, (b) 6ML-wide, 3ML-thick, 100ML-long wires of Ni(110) in the KMC simulation.

Figure 7-20. Relationship between the normalized particle spacing or perturbation wavelength as a function of the normalized surface energy of the wire perimeter, $\gamma_{f,0}$, as defined in the text. Data are shown only for wires bound by equilibrium facets with surface normals perpendicular to the wire axis.

Figure 8-1. Dewetting of cross patches with pre-patterned internal circular holes patterned from a Ni(110) film. (a)-(c) are SEM images of dewetted patterns with an initial edge length of 10.8μm. (d)-(i) are SEM images of dewetted patterns with an initial edge length of 18.4μm. The initial size of internal holes was bigger in the patches shown in (d) through (f) than in the patches shown in (g) through (i), as indicated by gray dashed lines. The gray dashed lines indicate the initial shapes of the patches. The annealing time was 1020 minutes and the thickness of the film was 120nm. Scale bars indicate 10μm.

Figure 8-2. Propagation of pre-patterned holes on Ni(110) by dewetting. The square holes initially are 5μm in length and the initial spacing between the hole edges is 10μm. Bright regions in the micrographs are Ni. The angles of clockwise rotation are 0, 15, and 45 degrees, respectively, and the annealing times are 0, 1, 4, 9, and 12 hours, respectively. Scale bars, 10μm.

Figure 8-3. Fabrication of micro-scale graphene patterns by tape delamination of pre-patterned Ni, following interfacial graphene layer (IGL) growth. The schematic in (a) shows the tape delamination of Ni leaving the patterned IGL on SiO_2. (b) SEM shows the delaminated Ni patterns on tape while the interfacial graphene on SiO_2 is confirmed by (c) 2-D Raman map.

Figure A1-1. Schematic diagram of the diffusion field around a natural hole, after Ye and Thompson.

Figure A1-2. Schematic illustration of the pattern used to template the corner instability.

Figure A1-3. SEM images of the patterned corners in Ni(100) oriented along (a)-(e) 0 degrees from [010] and (f)-(j) 45 degrees from [010].

Figure A1-4. SEM images of the patterned corners in Ni(110) oriented along (a)-(e) 0 degrees from $[1\bar{1}0]$ and (f)-(j) 45 degrees from $[1\bar{1}0]$.

Figure A1-5. Retraction distance measurements for the corners patterned with different corner angles in different corner orientations in Ni(100) after a 12-hour anneal.

Figure A1-6. Retraction distance measurements for the corners patterned with different corner angles in different corner orientations in Ni(110) after a 12-hour anneal.

Figure A2-1. A schematic illustration of the initial pattern used for the experiments. Straight edges were patterned in different in-plane orientations in single crystal Ni(110) films.

Figure A2-2. SEM micrograph of the Ni patches after a 3-hour anneal at 900°C. Fingering instability was observed, and the fingers propagated along the $[1\bar{1}3]$ orientations.

Figure A2-3. Relationship between steady-state finger spacing and annealing temperature.

Figure A2-4. (a) SEM micrograph of the as patterned straight edge. (b) SEM micrograph of the straight edge after 6.5 hours of annealing under a reducing gas (5% H_2 and 95% N_2) flowing at 95sccm. (c) SEM micrograph of the as patterned rough edge, whose roughness was caused by poor adhesion of the photoresist. (d) SEM micrograph of the rough edge after 6.5 hours of annealing under a reducing gas (5% H_2 and 95% N_2) flowing at 95sccm.

Figure A2-5. Degree of fingering instability versus RMS roughness of the as patterned edge. Different samples were annealed under different annealing conditions, but no ambient dependence was observed. Rather, above a certain RMS roughness value, fingering instability began to be observed. 2% H_2 + 98% Ar was flown at a rate of 390sccm and 5% H_2 + 95% N_2 was flown at a rate of 95sccm. These are the flow rates where the same oxygen partial pressure was measured. The base pressure for the vacuum annealing was $1x10^{-6}$torr. The annealing temperature was 900°C in all cases.

Figure A2-6. SEM micrograph of the as patterned edge with intentionally made perturbations. The smallest wavelength (a) was not resolved due to lithographic limits and isotropic etching.

Figure A2-7. SEM micrograph of the patterned edges after a 240-min anneal at 800°C in vacuum.

Figure A2-8. SEM micrograph of the patterned edges after a 180-min anneal at 900°C in vacuum.

Figure A2-9. Steady-state finger wavelength measurement for patterns with different intended perturbation wavelengths at different annealing temperatures in vacuum. The intended wavelengths are: Pattern 1 = 1.79μm; Pattern 2 = 2.68μm; Pattern 3 = 3.58μm; Pattern 4 = 4.47μm; Pattern 5 = 5.36μm; Pattern 6 = 7.15μm. Note that no measurements exist for Patterns 1 and 2 as no fingering was observed.

Figure A3-1. Propagation of pre-patterned holes on Ni(100) by dewetting. The square holes initially are 5μm in length and the initial spacing between the hole edges is 10μm. Bright regions in the micrographs are Ni. The angles of clockwise rotation are 0, 35, and 45 degrees, respectively, and the annealing times are 0, 1, 4, 9, and 12 hours, respectively. Scale bars, 10μm.

Figure A3-2. Propagation of pre-patterned holes on Ni(100) by dewetting. The square holes initially are 15μm in length and the initial spacing between the hole edges is 10μm. Bright regions in the micrographs are Ni. The angles of clockwise rotation are 0, 35, and 45 degrees, respectively, and the annealing times are 0, 1, 4, 9, and 12 hours, respectively. Scale bars, 10μm.

Figure A3-3. Propagation of pre-patterned holes on Ni(110) by dewetting. The square holes initially are 5μm in length and the initial spacing between the hole edges is 10μm. Bright regions in the micrographs are Ni. The angles of clockwise rotation are 0, 15, and 45 degrees, respectively, and the annealing times are 0, 1, 4, 9, and 12 hours, respectively. Scale bars, 10μm.

Figure A3-4. Propagation of pre-patterned holes on Ni(110) by dewetting. The square holes initially are 15μm in length and the initial spacing between the hole edges is 10μm. Bright regions in the micrographs are Ni. The angles of clockwise rotation are 0, 15, and 45 degrees, respectively, and the annealing times are 0, 1, 4, 9, and 12 hours, respectively. Scale bars, 10μm.

Figure A3-5. Propagation of pre-patterned holes on Ni(110) by dewetting. The square holes initially are 5μm in length and the initial spacing between the hole edges is 15μm. Bright regions in the micrographs are Ni. The angles of clockwise rotation are 0, 30, and 45 degrees, respectively, and the annealing times are 0, 1, 4, 9, and 12 hours, respectively. Scale bars, 10μm.

Figure A3-6. Propagation of pre-patterned holes on Ni(110) by dewetting. The square holes initially are 15μm in length and the initial spacing between the hole edges is 15μm. Bright regions in the micrographs are Ni. The angles of clockwise rotation are by a 15 degree interval, and the annealing times are 0, 4, 9, and 12 hours, respectively. Scale bars, 10μm.

Figure A3-7. Propagation of pre-patterned holes on Ni(100) by dewetting. The rectangular holes initially are 5x10μm in size and the initial spacing between the hole edges is 10μm. Bright regions in the micrographs are Ni. The angles of clockwise rotation are 0 and 35 degrees, respectively, and the annealing times are 0, 1, 4, 9, and 12 hours, respectively. Scale bars, 10μm.

Figure A3-8. Propagation of pre-patterned holes on Ni(110) by dewetting. The rectangular holes initially are 5x10μm in size and the initial spacing between the hole edges is 10μm. Bright regions in the micrographs are Ni. The angles of clockwise rotation are 0, 35, and 90 degrees, respectively, and the annealing times are 0, 1, 4, 9, and 12 hours, respectively. Scale bars, 10μm.

Figure A3-9. Propagation of pre-patterned holes on Ni(110) by dewetting. The rectangular holes initially are 5x20μm in size and the initial spacing between the hole edges is 15μm. Bright regions in the micrographs are Ni. The angles of clockwise rotation are 0, 35, and 90 degrees, respectively, and the annealing times are 0, 1, 4, 9, and 12 hours, respectively. Scale bars, 10μm.

Chapter 1. Introduction

1.1. Phenomenologies of Dewetting in Thin Films [1]

Generally, thin solid films are far from equilibrium in the as-deposited state and therefore are unstable or metastable at most. Thus, when such films are heated to a sufficiently high temperature and sufficient atomic mobility is allowed, the film lowers its total energy by agglomerating or dewetting to form islands. This dewetting phenomenon can be observed well below the films' melting temperature in the solid state. Therefore, this has been one of the major problems in the microelectronics industry [2, 3]. On the other hand, recent research demonstrates that dewetting can also be used to make arrays of particles for various applications, including sensors [4], catalysts for carbon nanotube growth [5], and those for semiconductor nanowires [6].

When a thin film is deposited on a substrate, three different interfaces exist: the film-vapor, the substrate-vapor, and the film-substrate interfaces. As the system moves toward equilibrium, the agglomerating film evolves into a morphology that minimizes the total energy of the system, and this is expressed in terms of these interfacial energies in Young's equation [7], assuming isotropic energies:

$$\gamma_{sv} = \gamma_{fs} + \gamma_{fv} \cos\theta \qquad (1\text{-}1)$$

where γ_{sv} indicates the substrate-vapor interfacial energy, γ_{fs} the film-substrate interfacial energy, and γ_{fv} the film-vapor interfacial energy. In films with isotropic surface and interfacial energies, this determines the equilibrium contact angle at the three-phase boundary of the film, the substrate, and the vapor. In this case, the equilibrium shape is a spherical cap, as shown in Figure 1-1. When the equilibrium contact angle θ is zero, the film covers or wets the entire substrate surface and can still remain thermodynamically stable. If the system has a nonzero contact angle, there is a thermodynamic driving force for the film to dewet.

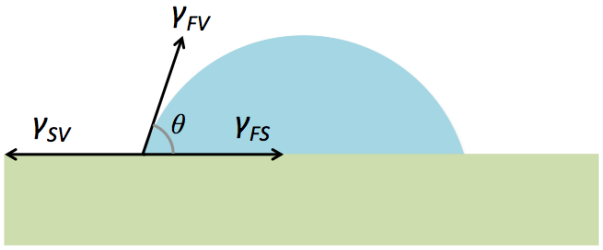

Figure 1-1. Schematic diagram of the equilibrium shape of an island on a substrate with isotropic surface and interfacial energies.

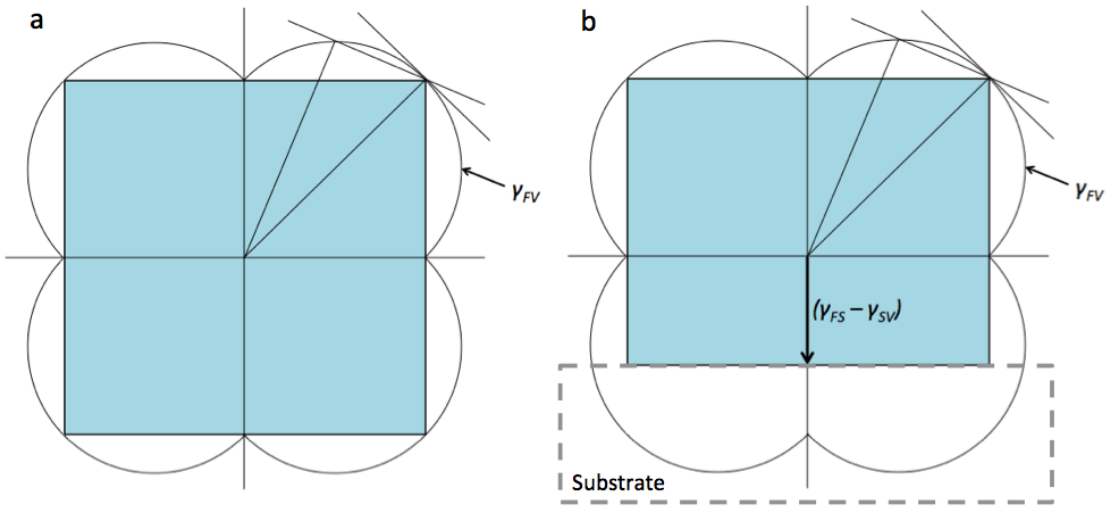

Figure 1-2. (a) The Wulff-Herring construction and (b) the Winterbottom construction.

For materials with anisotropic surface and interfacial energies, the equilibrium shape can be calculated by using the Wulff-Herring [8, 9] and the Winterbottom [10] constructions. As illustrated in Figure 1-2(a), the equilibrium Wulff shape of a free-standing material can be determined by obtaining the envelope of lines (in 2-dimensional structures) or planes (in 3-dimensional structures), drawn, at the anisotropic film-vapor interfacial energy curve, normal to the line originating from the center of the interfacial energy curve in all orientations. In thin-film structures, there is a substrate-film interface and the energy at the interface has to be adjusted.

The Winterbottom construction can be used to accommodate the changes, as illustrated in Figure 1-2(b). The film-vapor interfacial energy in the orientation normal to the film-substrate interface is replaced by the vector having the same orientation but its magnitude is decreased by the adhesion energy of the film-substrate interface.

For initiation of dewetting, a portion of the substrate needs to be exposed and a three-phase boundary of the film, the substrate, and the vapor should exist. Therefore, dewetting initiates either at pre-existing holes or patterned edges of the film, or after formation of natural holes. Pre-patterning of the film is one way to introduce three-phase boundaries. Pre-existing holes or defects large enough to expose the substrate-vapor interface are also places where dewetting can initiate. Even in films without any pre-existing holes or patterned edges, however, dewetting can occur at elevated temperatures. In this case, dewetting is followed by the formation of natural holes that expose the substrate-vapor interface and the three-phase boundary. For an infinite defect-free planar surface with isotropic surface energies without any stress effects, Mullins [11] showed that the surface is stable against all perturbations where a linear stability analysis is applicable. This also is the case in a film on a substrate with a nonzero contact angle, if the amplitude of the perturbation is smaller than the film thickness. Generally, however, thin films are not perfectly defect-free, and defects in the films make natural hole formation easier. For instance, Srolovitz and Safran [12] studied the evolution of grain boundary grooves at simplified 2-dimensional grain boundaries via capillarity-induced surface self-diffusion, as schematically illustrated in Figure 1-3.

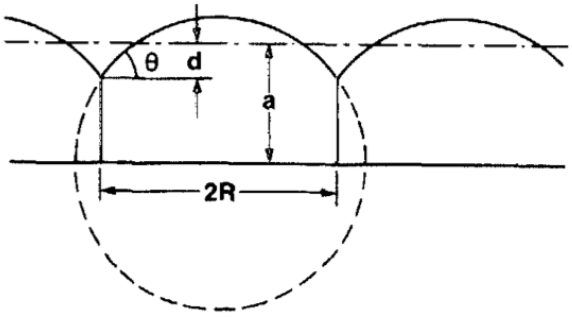

Figure 1-3. Growth of grooves at grain boundaries via capillarity-induced surface self-diffusion, after Srolovitz and Safran [12].

Using a similar construction as in Figure 1-1, it is found that the groove angle θ, at thermodynamic equilibrium, is:

$$\theta = sin^{-1}(\frac{\gamma_{gb}}{2\gamma_{fv}}) , \quad (1\text{-}2)$$

where γ_{gb} refers to the grain boundary energy and γ_{fv} the film-vapor interfacial energy. When equilibrium is attained, grooves of depth d will form, which can be geometrically calculated as [12]:

$$d = R\frac{2-\cos\theta-\cos^3\theta}{3\sin^3\theta} . \quad (1\text{-}3)$$

When this depth exceeds the thickness of the film and reaches the film-substrate interface, natural holes can form and be subject to further growth.

After the substrate-vapor interface is exposed and three-phase boundaries form, dewetting initiates, the three-phase boundaries retract, and the holes grow by capillarity-driven atomic diffusion, which results from the chemical potential gradient that can be obtained from the Gibbs-Thomson equation [7]. For surfaces with isotropic energies:

$$\mu = \mu^0 + \kappa\gamma_{fv}\Omega , \quad (1\text{-}4)$$

where μ^0 is the chemical potential for a zero-curvature surface, κ the local surface curvature, γ_{fv} the film-vapor interfacial energy, and Ω the atomic volume. Surfaces with different local curvatures have different chemical potentials, and therefore material flows from the region of a high μ to the region of a low μ, if there is sufficient atomic mobility.

There are two mechanisms of capillarity-driven mass transport for non-viscous thin films: surface self-diffusion and evaporation-condensation [13]. If atoms move via surface self-diffusion, the atomic flux J_s can be expressed as [7]:

$$J_s = -\left(\frac{D_s\gamma_{fv}}{kT}\right)\nabla_s\kappa , \quad (1\text{-}5)$$

where D_s indicates the surface self-diffusivity, γ_{fv} the film surface energy, kT the thermal energy, and κ the local surface curvature. As can be seen in Equation (1-5), the direction of the atomic flux is parallel to the surface in the surface self-diffusion kinetics. If atoms instead transport by the evaporation-condensation mechanism, the direction of the atomic flux J_v is perpendicular to the surface and is given by [7]:

$$J_v = K(P^0 - P_{eq}(\kappa)) , \tag{1-6}$$

where K is the rate constant, P^0 the vapor pressure of the ambient, and $P_{eq}(\kappa)$ the equilibrium vapor pressure at a region with a local curvature κ. As the vapor pressures of the films are usually small at temperatures that allow solid-state dewetting, it is generally accepted [14, 15] that the dominant mechanism for the solid-state dewetting of thin films is capillarity-driven surface self-diffusion.

1.1.1. Growth of Holes and Retraction of Edges [1]

Polycrystalline films do not have a long-range ordered crystal structure, and thus, at size scales larger than those of individual grains, irregular structures occur via dewetting. Thus, the shape of the natural holes is not uniform, as illustrated in Figure 1-4 [16], and generally assumed to be circular for modeling purposes. Brandon and Bradshaw [16] studied this isotropic-like hole propagation and developed a model describing the rate of edge, or three-phase boundary, retraction by analyzing Equation (1-5), assuming the edge retraction leads to the accumulation of material near the edge and a semicircular rim forms due to the accumulation, as illustrated in Figure 1-5. In their model, the edge retraction distance x scales as:

$$x = K\frac{t^{2/5}}{h^{3/5}} , \tag{1-7}$$

where t is time, h the initial thickness of the film, and K a kinetic constant. The rate of edge retraction decreases with time because the flux of material away from the retracting edges leads

to accumulation and thickening of the rim at the edges. This decrease in local curvature near the retracting edges leads to a decrease in the driving force for mass transport, thereby decreasing the retraction rate.

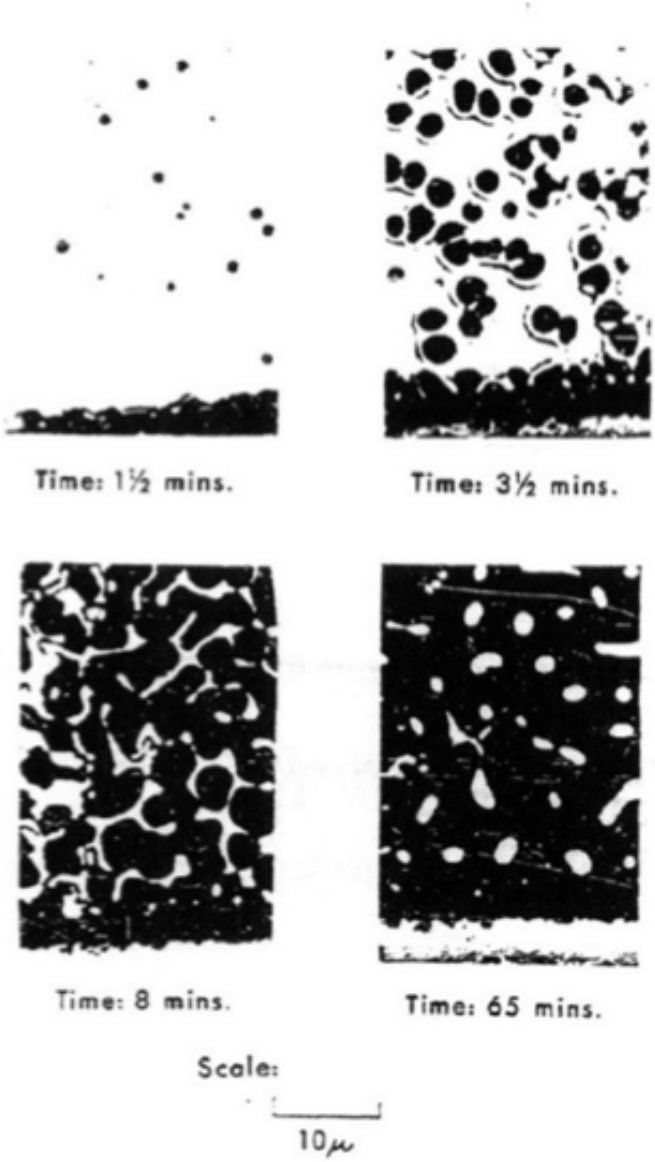

Figure 1-4. Optical micrographs of morphological evolution during solid-state dewetting of 110nm-thick Ag films on mica substrates [16]. Black areas indicate natural holes. The film was annealed at 360 °C in air. Annealing times are provided under the individual micrographs.

Similar models have been developed [15, 17, 18] by solving Equation (1-5) for isotropic γ_{fv} and applying different initial and boundary conditions. Although the details of the models vary, all have a power-law time dependence of the edge retraction rate in common.

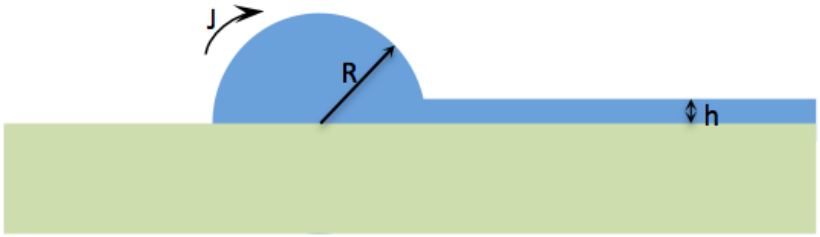

Figure 1-5. Retraction of edges and thickening of rims in the Brandon-Bradshaw model [16]. As the edges retract, capillarity-driven surface self-diffusion leads to material accumulation near the edges and the thickening rims retain the shape of a semicircle of radius *R*.

Although the absence of long range order in polycrystalline films allows easier analysis and modeling of dewetting by assuming isotropic surface energies and surface self-diffusivities, due to inherent defects such as point defects, dislocations, and grain boundaries, it is very difficult to precisely control and predict how the films dewet. Using solid single crystal films, however, crystallographic constraints and anisotropy in surface energy and surface diffusivity provide much better control of the way the films dewet and reproducibility of the dewetted patterns. The dewetting phenomenologies observed in polycrystalline films also occur in single crystal films in a much more regular and controllable way, providing a potential for solid-state dewetting to be used as a method to generate complex structures.

Study of dewetting in single crystal films arose with the studies on silicon-on-insulator (SOI) structures. Nuryadi et al. [19] observed that the growing natural holes in SOI structures dewet into arrays of islands that align to certain crystallographic orientations. Danielson et al. [20] also observed a similar hole propagation behavior. An illustration is provided in Figure 1-6.

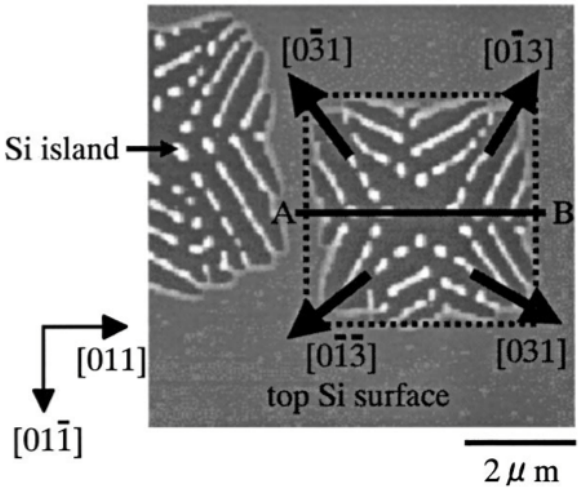

Figure 1-6. AFM image of growing natural holes in SOI(100) structures. Formation of ordered arrays of islands along certain crystallographic orientations is observed, after Nuryadi et al [19].

A regular dewetting morphology has also been observed in other systems. Ye and Thompson [21] studied the propagation of natural holes in thin single crystal Ni films, and observed a regular natural hole morphology, as illustrated in Figure 1-7.

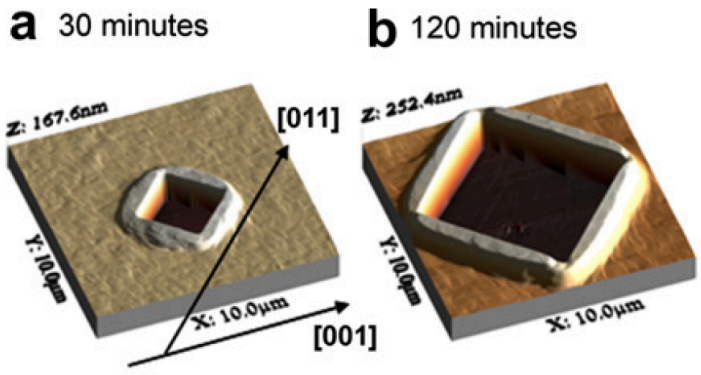

Figure 1-7. AFM images of natural holes in Ni(100) after annealing at 900°C under 2310sccm of reducing gas (5% H_2 + 95% N_2) for **(a)** 30 minutes and **(b)** 120 minutes [22].

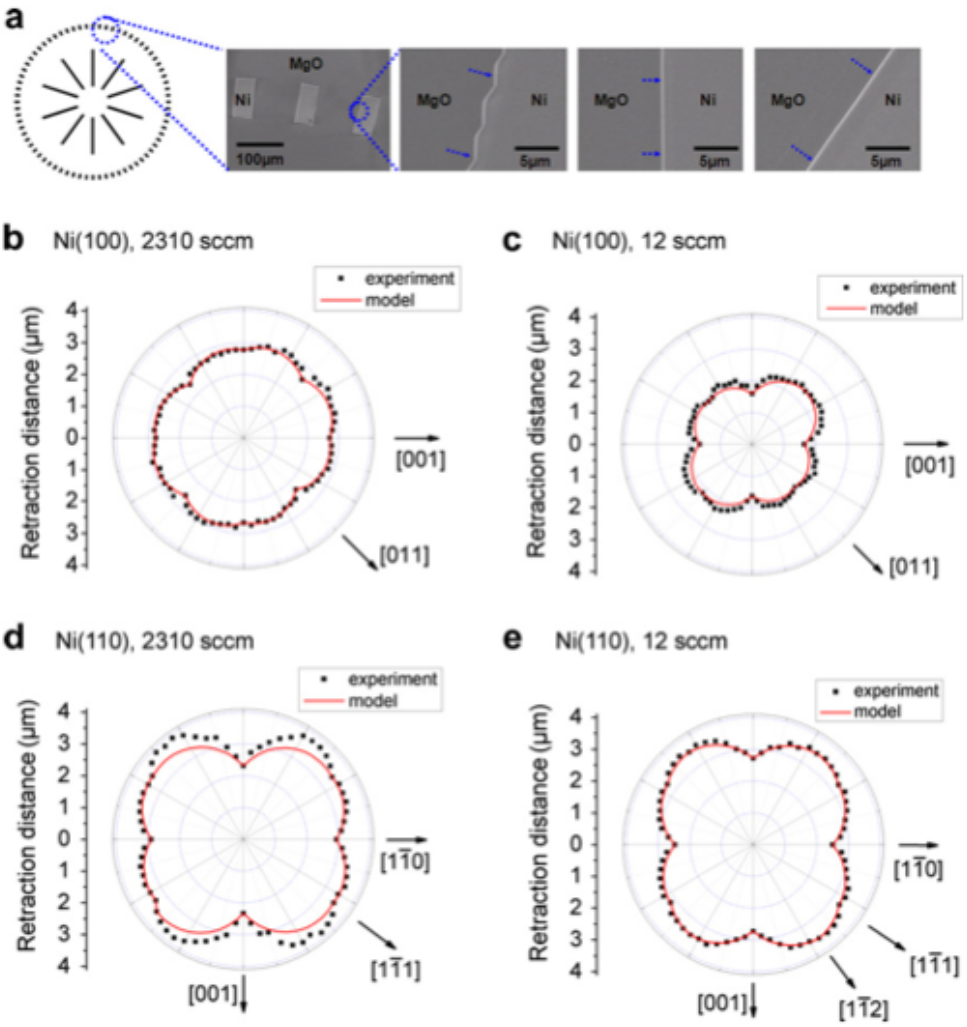

Figure 1-8. Anisotropic edge retraction velocities [22]. (a) Development of kinetically stable facets by a faceting instability. (b)-(e) Kinetic Wulff plots of the edge retraction distances after 318-minute anneals. Film orientations and flow rates of 5% H_2 + 95% N_2 reducing gas are indicated in each plot.

Due to anisotropy in surface and interfacial energies and surface self-diffusivities, the edge retraction rates in single crystal films are anisotropic, resulting in the polygonal shape of natural holes in such films. This anisotropy in the retraction rate is closely related to the kinetic stability of edges in different crystallographic orientations. Ye and Thompson [22] showed that such anisotropic retraction rates can be plotted to generate a kinetic Wulff plot as shown in Figure 1-8. Also, they observed that there exists a set of kinetically stable orientations corresponding to local cusps in the kinetic Wulff plot, and the retraction rates in all other

orientations can be successfully modeled by a geometric combination of the retraction rates of these kinetically stable orientations, noticing that all other edges in non-kinetically stable orientations undergo a faceting instability and develop combinations of kinetically stable edges (Figure 1-8(a)). Kim et al. [23] further studied the retraction behavior of the kinetically stable edges over time and showed that although experimentally determined retraction rates were different for different in-plane crystallographic orientations of the edges and different out-of-plane film orientations, the time scaling of their retraction rates was similar. The retraction distance x_o scaled as $x_o \propto t^n$ with n~0.4. The time scaling of the rim height and width was also found to be similar (n~0.2). This scaling is similar to that found in computational modeling using isotropic surface energies [8], as shown in Figures 1-9 and 1-10.

Although several analytical models have been developed to analyze isotropic dewetting, no simple analytical models thus far have been developed to analyze edge retraction in single crystal films due to difficulty associated with anisotropic surface and interfacial energies and diffusivities. Analysis of solid-state dewetting in single crystal films, therefore, usually requires development of numerical models and such models generally require a large computational load.

Carter et al. [24] studied morphological evolution of structures using a computational method called the method of crystalline formulation. By assuming that the shape of interest is solely composed of facets appearing in the equilibrium Wulff shape and solving the diffusion equation on each facet rather than tracking individual atoms, they could significantly reduce the computational load arising from anisotropic surface energies and diffusivities. Along with being able to successfully describe the dewetting morphologies in many different structures, they could also describe the differences that different capillarity-driven mass transport mechanisms [7], the surface diffusion kinetics and evaporation-condensation kinetics, make during the morphological evolution of structures, as illustrated in Figure 1-11. A similar model has been developed for thin film structures to study solid-state dewetting in thin films with anisotropic surface and interfacial energies and diffusivities [23, 25, 26]. Some results generated from the crystalline formulation method are also illustrated in Figures 1-9 and 1-10.

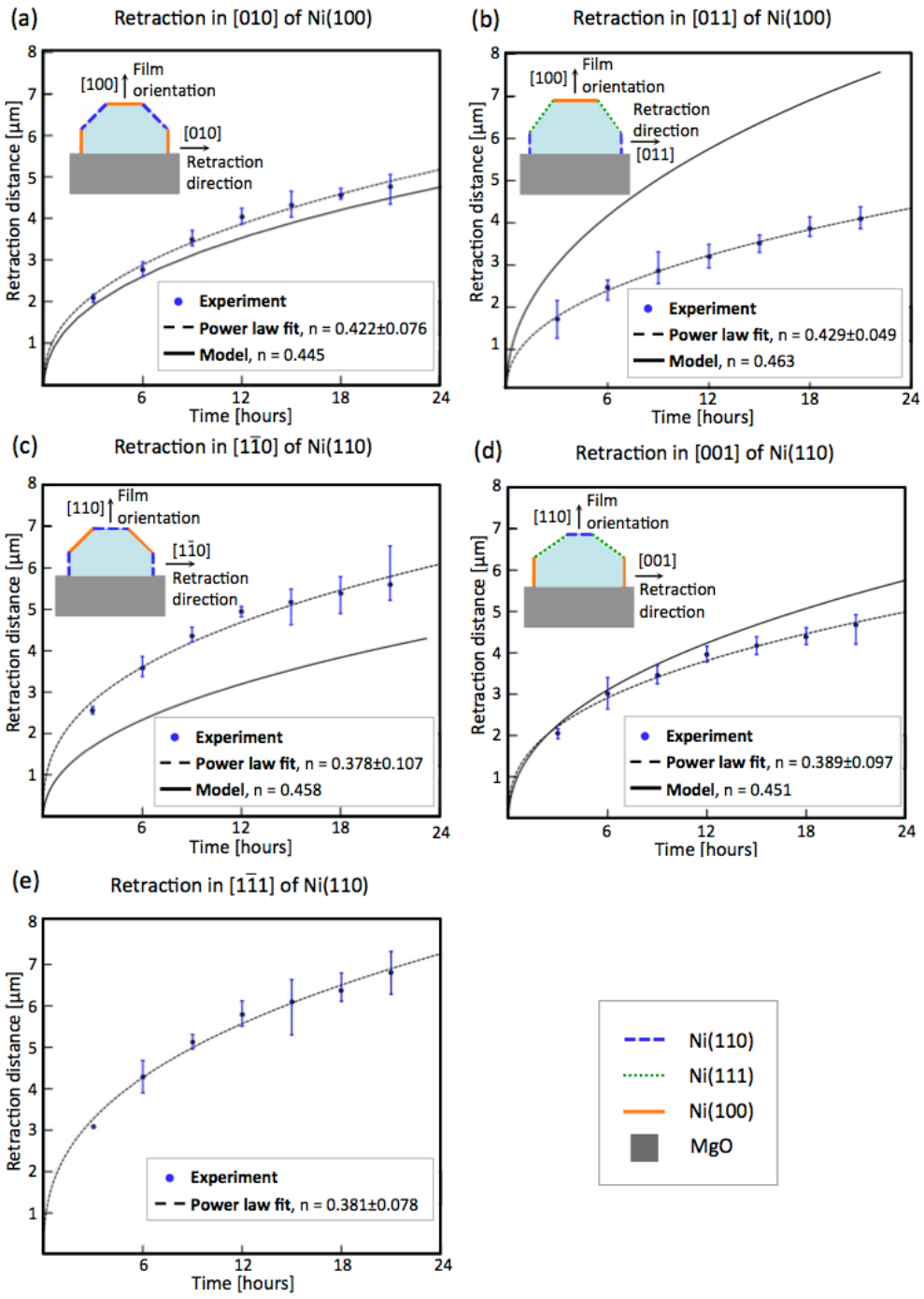

Figure 1-9. Retraction rates of kinetically stable edges for Ni(100) and Ni(110) films [23]. The samples were annealed at 890°C under a 2310 sccm reducing gas (5% H_2 + 95% N_2) flow. The exponents for power law fits are also given. The modeling results were obtained from the crystalline formulation method. Appropriate equilibrium Winterbottom shapes were obtained using *Wulffmaker*, a program for equilibrium shape generation [27].

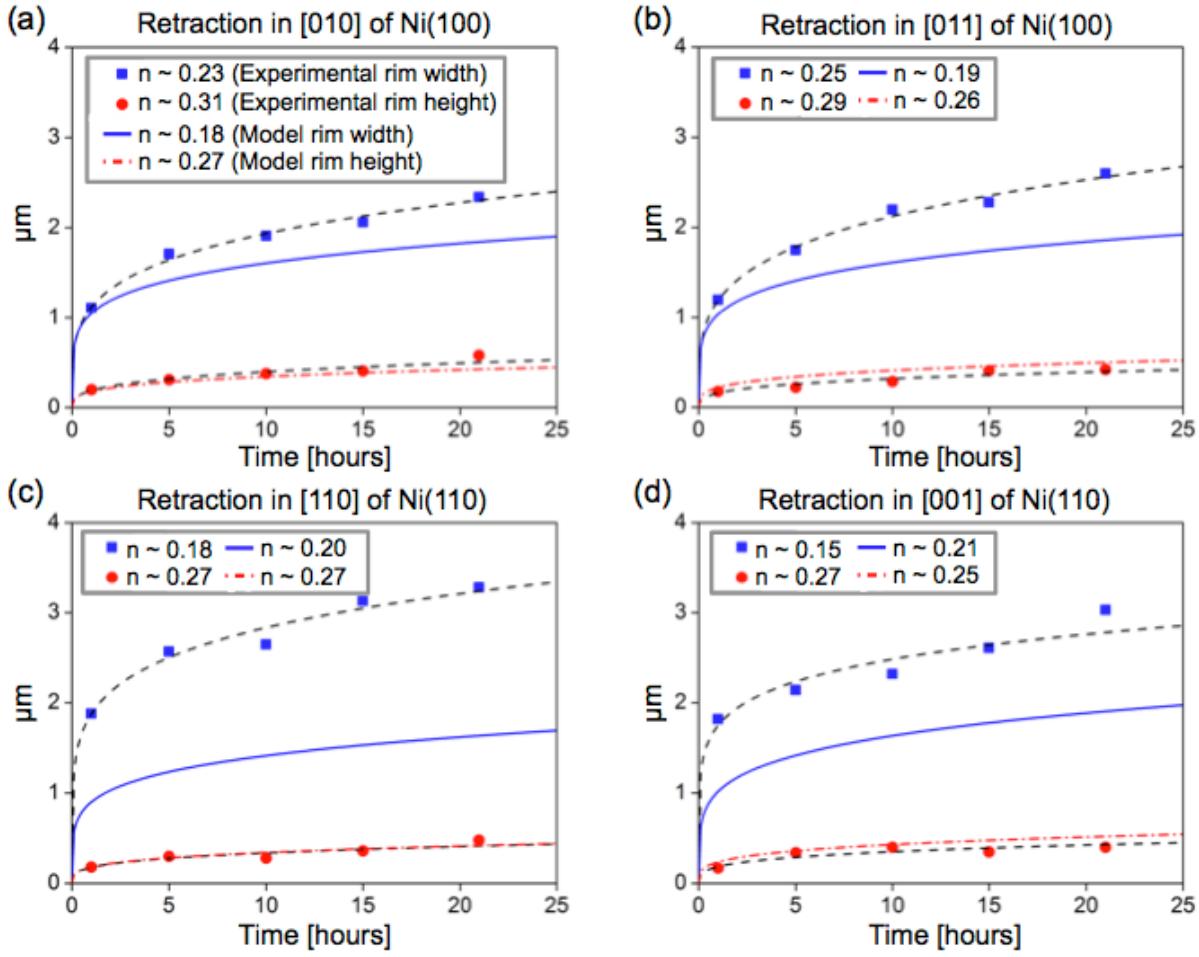

Figure 1-10. Evolution of rim height and width [23]. Rim heights are defined as the distance between the highest point of the retracting rim and the undewetted flat film, and rim widths are defined as the distance between the retracting edge front and the point ahead of the rim where the thickness equals that of the undewetted flat film. The modeling results were obtained from the crystalline formulation method.

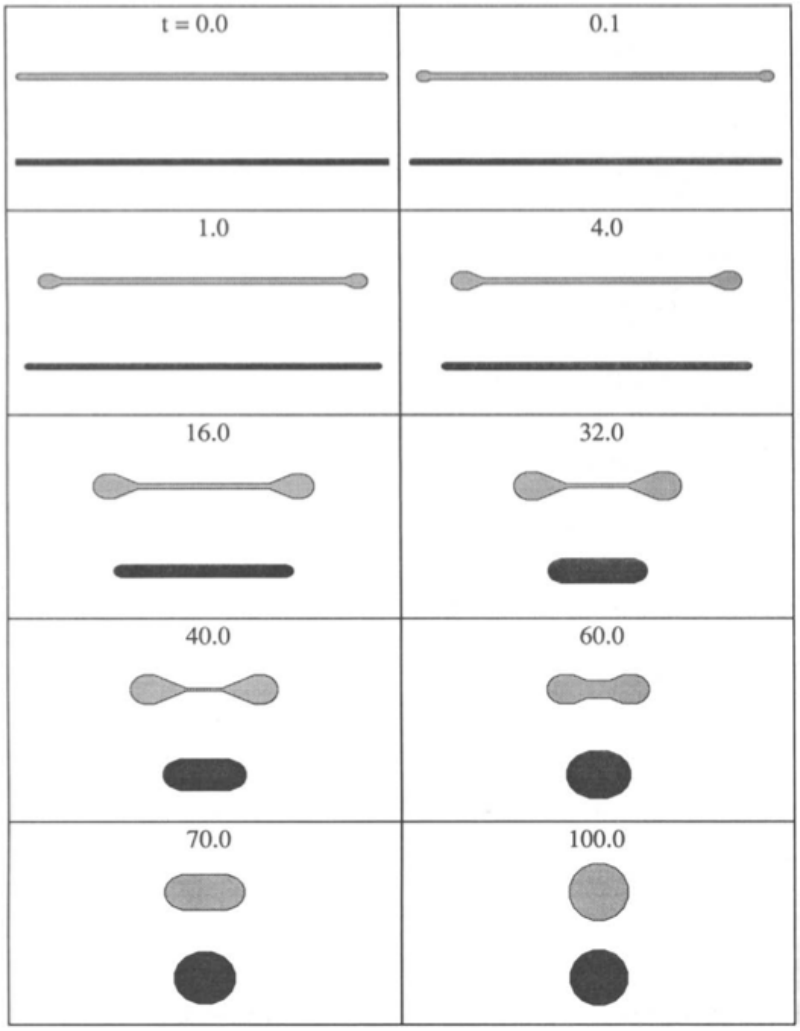

Figure 1-11. Time evolution of an elongated rectangle with a regular 16-gon Wulff shape [24]. The light gray structure evolves according to the surface diffusion kinetics while the dark gray structure evolves by the evaporation-condensation kinetics.

Dornel et al. [18] conducted a numerical analysis of capillarity-driven edge retraction using a conventional anisotropic n-fold symmetric Wulff plot by numerically solving Equation (1-5) assuming the dominant mechanism of mass transport is surface self-diffusion. However, they did not consider anisotropy in surface self-diffusivity, which may also significantly affect the edge retraction rate in single crystal films.

As an alternative, the kinetic Monte Carlo (KMC) method has been used to simulate natural hole propagation and growth by edge retraction in silicon-on-insulator (SOI) structures.

Bussmann et al. [28] and Cheynis et al. [29] simulated the dynamics of dewetting in SOI systems and compared the result to the actual hole propagation morphology in SOI systems, as illustrated in Figure 1-12. However, because KMC simulations generally consider energetic relationships of individual atoms in a system with their adjoining atoms, the computational load of such simulations exponentially increases with increasing system size and thus they are not suitable for analysis of dewetting at a very large scale. The abovementioned work was conducted using a KMC simulation with three atomic monolayers.

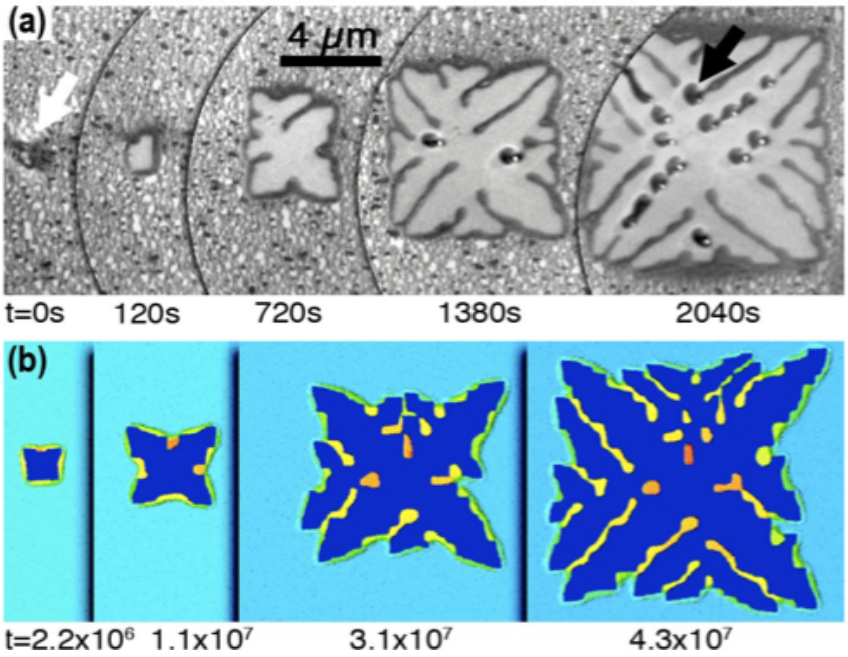

Figure 1-12. **(a)** LEEM images of dewetting of 22nm-thick SOI structures annealed at 870 °C [28]. **(b)** KMC simulation of dewetting with an initial film thickness of 3 layers [28]. Times after which the images were taken are provided under the images.

1.1.2. Pinch-off Phenomenon by Valley Formation

In dewetting simulations for films with isotropic surface energies and diffusivities or with anisotropic surface energies and isotropic diffusivities, it has been observed [15, 17, 18] that in the later stage of edge retraction, valleys form ahead of the retracting edges. When the depth of the valleys becomes large enough to reach the film-substrate interface, the retracting edge is separated from the remainder of the film and the newly developed edge again begins to retract,

leaving a long wire behind. This phenomenon is referred to as mass shedding or pinch-off. If the patch is even wider and the individual valleys reach the interface before they merge, three wires are formed, as illustrated in Figure 1-13.

Dornel et al. [18] simulated the pinch-off behavior and formation of wires in films with isotropic surface energies. As shown in Figure 1-14, pinch-off is favored as the width-to-thickness ratio of the films increases and as the equilibrium contact angle at the vapor-film-substrate three-phase boundary increases.

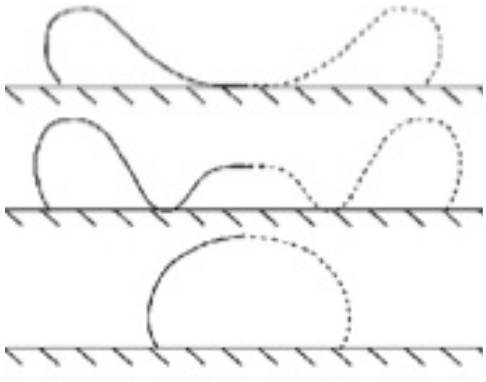

Figure 1-13. Formation of one, two or three wires by pinch-off, after Dornel et al [18].

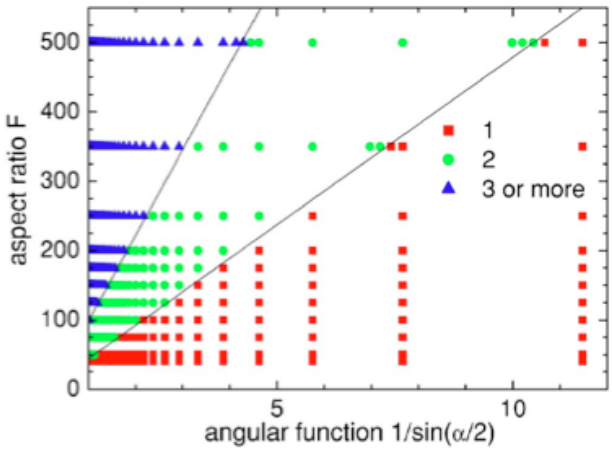

Figure 1-14. Number of wires formed by pinch-off versus an angular function of equilibrium contact angle, simulated with an isotropic surface energy [18]. The straight lines show the boundaries of the 1-, 2-, and 3-wire formations.

To model films of anisotropic surface energies and surface diffusivities, the method of crystalline formulation has been used [13, 23-25], where the structure of interest is assumed to be completely faceted. However, no valley formation has been observed in such models unless faceted valleys are initially introduced.

Pinch-off of films by mass shedding during dewetting is difficult to observe experimentally, because formation of natural holes at randomly distributed defects often expose the substrate-vapor interface before pinch-off occurs. Dewetting in single crystal films markedly decreases such problems, and valley formation ahead of the retracting edge and the pinch-off phenomenon has recently been observed in solid-state dewetting of SOI [18] and single crystal Ni films on single crystal MgO substrates [21], as illustrated in Figure 1-15.

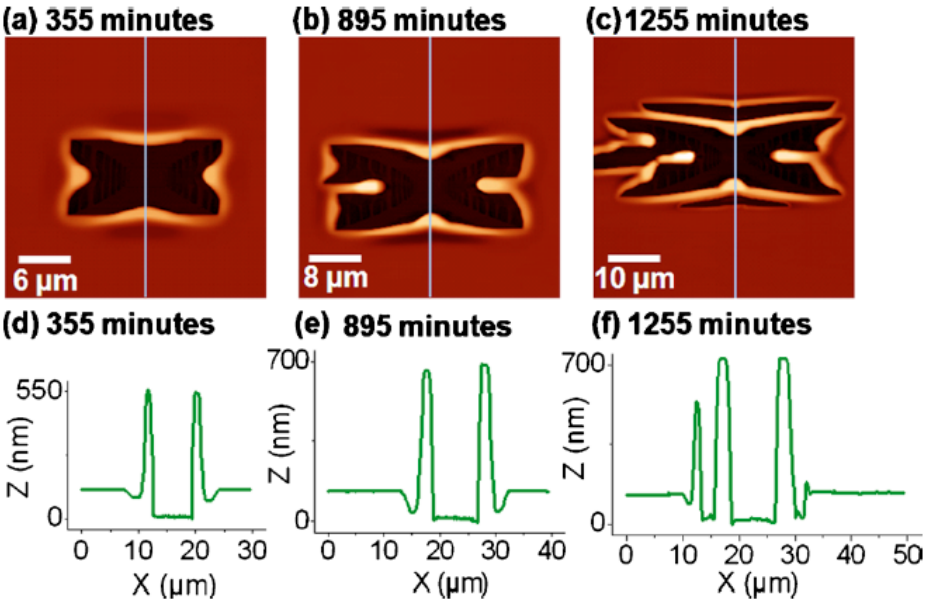

Figure 1-15. Deepening of valleys and pinch-off of edges in a natural hole in Ni(110) film [21]. The flow rate of reducing gas (5% H_2 + 95% N_2) was 2310sccm. (a)-(c) Top-down AFM images. (d)-(f) AFM height profiles. Annealing times are indicated in the images.

1.1.3. Fingering Instability [30]

In the later stages of natural hole propagation and edge retraction, other dewetting instabilities may develop. Jiran and Thompson [14] observed that gold films deposited on fused silica substrates develop an edge instability as natural holes propagate. As illustrated in Figure 1-16, the propagating holes develop fingers analogous to the cellular structure that often form during solidification.

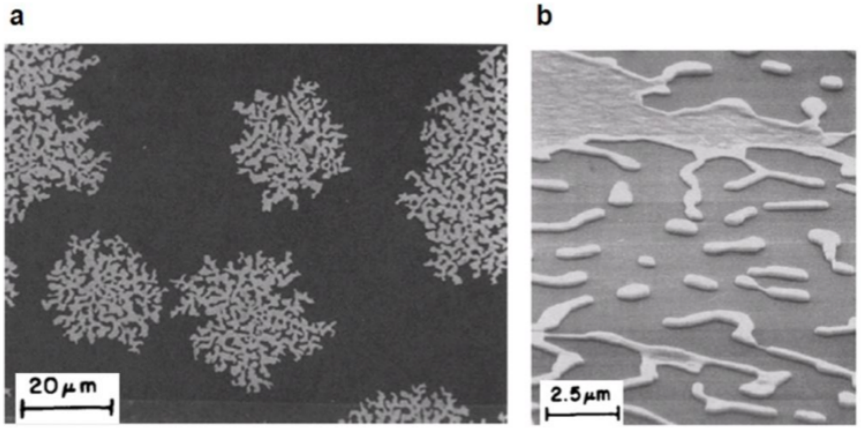

Figure 1-16. Dewetting of gold films on fused silica by propagation of natural holes [14]. (a) An optical micrograph of growing holes. Dark region is the gold and bright region is the exposed silica substrate. (b) An SEM image showing uneven accumulation of gold near the retracting edges. Bright region is the gold and dark region is the exposed silica substrate.

Jiran and Thompson attributed this instability to the uneven accumulation of material near the retracting edges. Because it is not likely to have a perfectly uniform thickness over all retracting edges, some fluctuations in the thickness of the rim lead to nonuniform edge retraction velocities, as they are dependent on the film thickness (See Equation (1-7) for example). As the faster retracting dewetting fronts in the edge move ahead, the material transported from the faster retracting dewetting fronts accumulate at the slower retracting dewetting fronts, further retarding their retraction. Jiran and Thompson further found that the faster retracting dewetting fronts retract at a constant rate. Based on the observation and based on the model of Brandon and

Bradshaw [16], Jiran and Thompson developed a model for the faster retracting dewetting fronts of the edge, in which the retraction rate scales as [14]:

$$\frac{\Delta x}{\Delta t} = \frac{2D_s\gamma_{fv}\Omega^2}{kT\pi h^3} \tag{1-8}$$

where D_s is the surface self-diffusivity of the film, γ_{fv} the surface energy of the film, Ω the atomic volume, kT the thermal energy, and h the initial film thickness. Because no rim thickening occurs, the retraction rate stays constant over time.

After Jiran and Thompson, similar phenomenologies have been observed during dewetting of single crystal Si films in silicon-on-insulator (SOI) structures [20, 28, 29, 31, 32]. Due to crystallographic constraints, more regular finger morphologies are observed in single crystal films, as illustrated in Figure 1-17. The origin of the initial rim instability was also studied and reported [33].

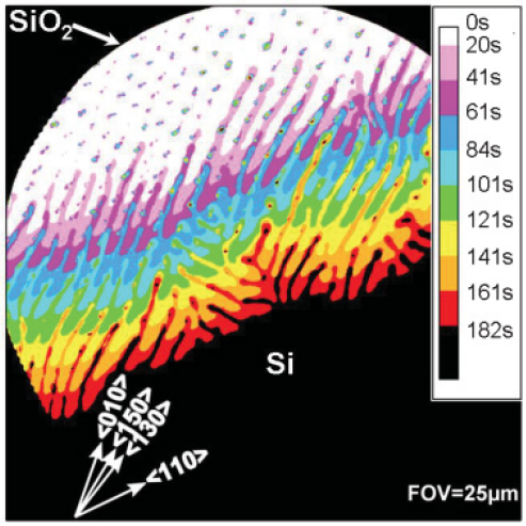

Figure 1-17. Stroboscopic image of the growth of a dewetting hole showing the propagation of fingers in a SOI structure, after Cheynis et al.[29]

Several analyses of the initial fingering instability and characteristics of the finger front have been presented. Kinetic Monte Carlo (KMC) simulations [28, 34] have been developed for

dewetting of thin-film structures and a finger morphology that is similar to the one seen in experiments was observed, as illustrated in Figure 1-18. In the simulations, the velocity of the finger front was observed to evolve toward a constant value, implying a steady state constant shape of the tip corner. A numerical linear stability analysis was also developed and used to establish conditions under which rims are unstable and will develop fingered fronts [34, 35]. This analysis can also be used to estimate the initial period of islands resulting from the fingering instability. Müller and collaborators characterized the geometry of retracting finger fronts in SOI films, and developed a model relating the effective activation energy for front motion to these geometric characteristics [29]. They measured the steady-state finger period under different conditions and reported that the period was dependent on the steady-state tip retraction rate, initial film thickness, and annealing temperature.

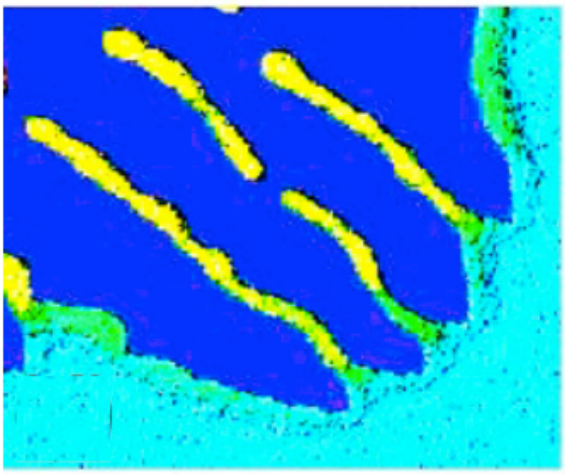

Figure 1-18. KMC simulation showing propagation of fingers [27]. The dark blue region indicates the exposed substrate and other colors indicate the regions of different film thicknesses.

1.1.4. Corner Instability [36]

Thus far, dewetting phenomenologies occurring at the edges of the thin film have been discussed. When natural holes form in single crystal films, however, anisotropy in surface energy and diffusivity make the natural holes faceted, as previously discussed with Figure 1-7. These polygonal holes have morphologies defined by edges with locally minimum retraction rates.

After the initial stages of growth, the corners of the polygonal holes are observed to retract faster than the centers of the straight edges. This is typically referred to as the corner instability, and leads to dendritic or star-shaped holes [19, 21, 22, 28, 37]. An example of a corner instability is provided in Figure 1-19. Kinetic Monte Carlo simulations of dewetting in single-crystal structures also exhibit corner instabilities [28, 38].

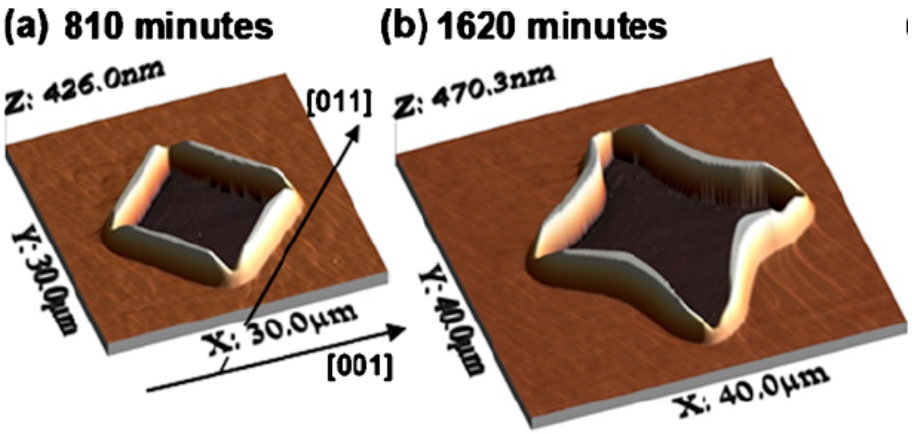

Figure 1-19. AFM images of growing natural holes in Ni(100) before and after the development of corner instability [21].

It has been observed that the retraction rate at corners reaches a constant value, while the retraction rate of the straight edges decreases over time [29]. This occurs because the rim at the tip of the retracting corners reaches a fixed height, while the rims along the straight edges thicken with time in a similar fashion to a retracting infinite, straight edge [29]. The corner instability is fundamentally related to the development of a time-independent shape of the tip of the retracting corner. However, it has not yet been clear why the rim at the tip of the retracting corner reaches a constant value. Chapter 6 of this thesis will discuss this in detail.

Previous work has suggested that the corner instability is associated with mass flow away from the tip of the retracting corner. Ye and Thompson [21] proposed that the corner instability arises due to mass flow away from the tip, onto the flat film. It was suggested that near the corner, there is a two-dimensional diffusion field, while along the edge, there is a one-

dimensional diffusion field as illustrated in Figure 1-20. The two-dimensional field implies transport to a larger area, and therefore enables faster retraction near corners.

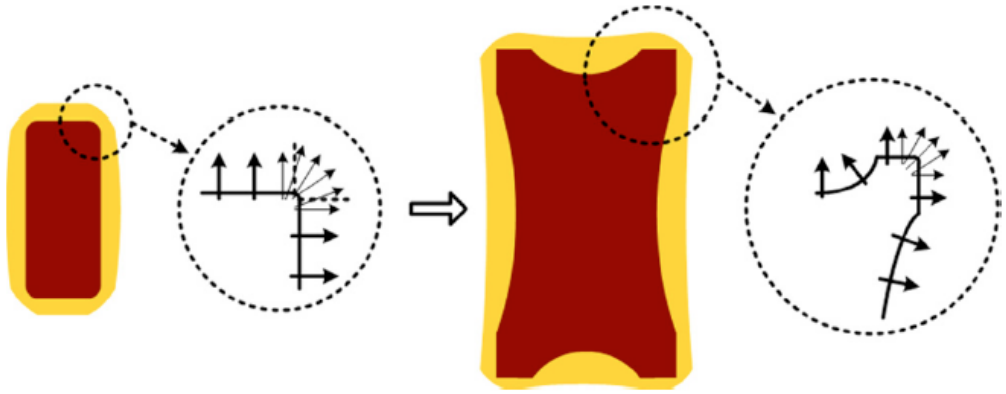

Figure 1-20. Schematic diagram of the diffusion field around a natural hole, after Ye and Thompson [21].

However, the film is not observed to thicken ahead of the retracting rim in experiments [37]. Also, isotropic models of dewetting show no net mass flow onto the flat film [12, 15], and anisotropic models show a small mass flow in the opposite direction, leading to thinning of the bulk film [26]. Rabkin et al.[37] suggested that mass rejected from corners flows along the thickening rim toward the centers of the straight edges, leading to a constant rim size at the corner while the centers of the edges accumulate mass. However, no specific evidence of this mass flow has been presented.

1.1.5. Rayleigh-like Instability [39]

The late stages of dewetting of both continuous and patterned films involve the break-up of wire-like structures into arrays of particles with regular spacings, as illustrated in Figure 1-21. This is also observed in nanowires made using other techniques. Break up of wire-shaped solids with high length-to-diameter ratios has been observed in various free standing nanowires, including Cu [40], Au [41], Co [42], Ni [43], Pt [44], and Si [45], and in various composite structures, including metallic [46-49] and non-metallic [50] wire-like structures in solid matrices and Si-based [45, 51] and metallic [52-55] wire-like patterns made on substrates. In all of these cases, the resulting particles

have a characteristic spacing scaling with the initial cross-sectional area of the wire-like structure, as expected for a Rayleigh-like instability.

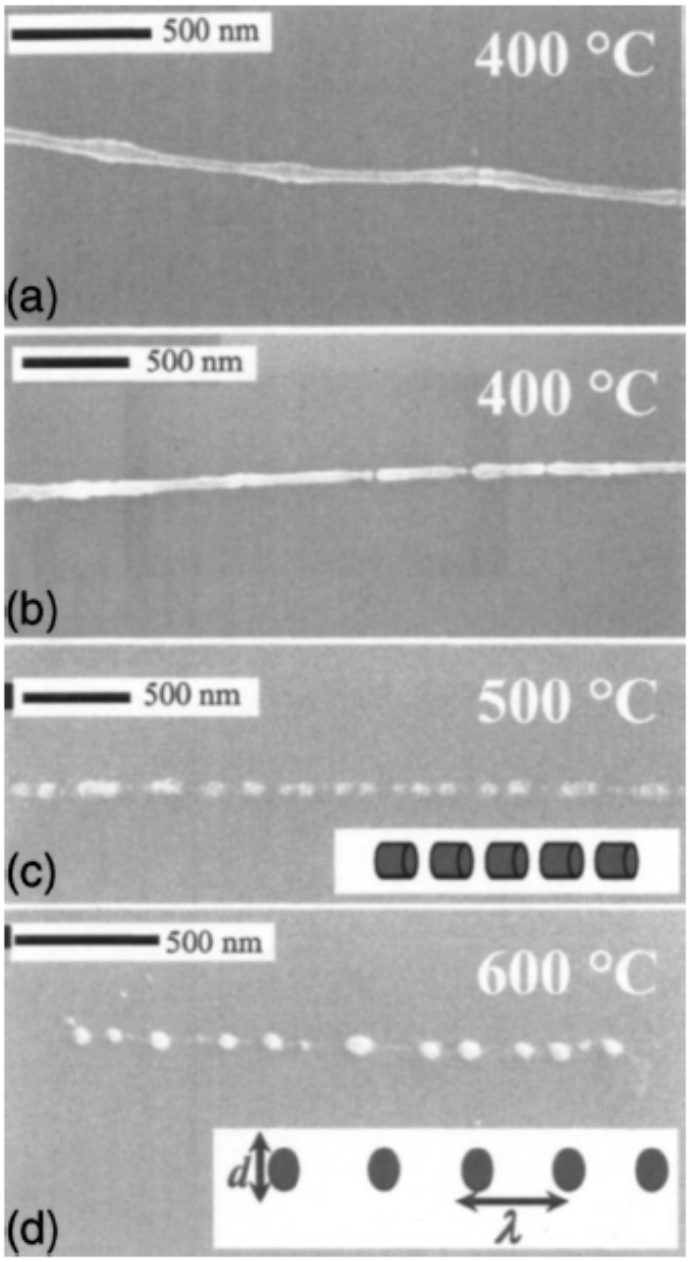

Figure 1-21. Development of the Rayleigh-like instability in copper nanowires after annealing at the temperatures indicated in each micrograph [40].

The inherent energetic instability of liquid cylinders was first discussed by Plateau [56], who observed the breakup of long cylindrical liquid jets into strings of droplets. Lord Rayleigh [57] later showed that infinite cylindrical shapes are inherently energetically unstable when perturbed at sufficiently large wavelengths, and will evolve to form arrays of drops. Later, Nichols and Mullins [58] showed that for solid cylinders with isotropic surface energies evolving through capillarity driven surface diffusion, the minimum wavelength of perturbations that would grow, λ_{crit}, is $2\pi R_o$, and that the most rapidly growing wavelength λ_{max} is equal to $\sqrt{2}\lambda_{crit}$. Isotropic models with various other geometric bounding conditions were subsequently developed, including continuous intergranular phases [59]. McCallum et al [60] treated the case of solid cylinders that partially wetted substrates with contact angles θ. They found that partial wetting increased the stability of wires such that, for $\lambda_{crit} = \alpha R_o$, α is higher for wetting wires (e.g. $\alpha = 8/\sqrt{3}\pi$ for $\theta = \pi/2$) than for cylinders ($\alpha = 2\pi$ for $\theta = \pi$) and that for sufficiently small θ, wires are stable with respect to all perturbations. $\lambda_{max}/\lambda_{crit}$ was found to be approximately $\sqrt{2}$ for all metastable wetting wires (and exactly $\sqrt{2}$ for $\theta = \pi/2$ and π). In all cases, particles that form due to a Rayleigh-like instability are expected to have a characteristic spacing λ_p approximately equal to λ_{max}, so that $\lambda_p \propto R_o$.

In single crystal wires, an anisotropic Rayleigh-like instability is expected due to crystallographic constraints on growth of perturbations. Cahn [61] developed a simple analytic expression for the critical perturbation wavelength of a cylindrical rod with isotropic surface energies about the axis of the cylinder, but surface energy anisotropy for planes rotated with respect to the wire axis. He showed that while the wavelength is still proportional to the initial radius of the cylinder, it also depends on the second derivative of the surface energy, which is a measure of the surface energy anisotropy. This effect can either increase or decrease the range of stability of a wire and significantly affect the spacing of particles when they form. Others have analyzed the effects of more realistic surface energy anisotropies [62-65] but at the cost of significantly increased complexity and reduced generality.

There are limited observations of the effects of surface energy anisotropy on beading of wire-like solids. Karim et al [41] studied both polycrystalline and single crystal Au wires and showed that the single crystal wires had a higher scaling constant than polycrystalline wires with the same diameter, suggesting that the range of metastability was larger for the single crystal wires. Karim et al suggested that this effect was associated with surface energy anisotropy. Barwicz et al [45] subsequently studied free standing wires of single crystal silicon that were patterned in such a way that wire axes lay along three different crystallographic orientations. They found that α was different for different crystallographic orientations, and they also invoked a role for surface energy anisotropy in discussing their results. Enhanced stability has also been noted for Ni wires with specific in-plane orientation formed by solid state dewetting of single crystal films [37, 66]. Glaeser and collaborators [67-69] also observed an anisotropic Rayleigh-like instability for pore channels patterned with axes aligned along different crystallographic orientations relative to that of a single-crystal sapphire matrix. In these studies, channels were patterned with a wide range of crystallographic orientations and it was shown that there were specific orientations for which α had a peaked maximum.

1.2. Effect of Annealing Ambient on Dewetting

Ye and Thompson [22] found that the annealing ambient has a significant effect in the dewetting morphology. They observed that the shape of the natural hole, which is defined by the kinetically stable edges with locally minimum retraction rates, can change under different annealing ambient, as illustrated in Figure 1-22.

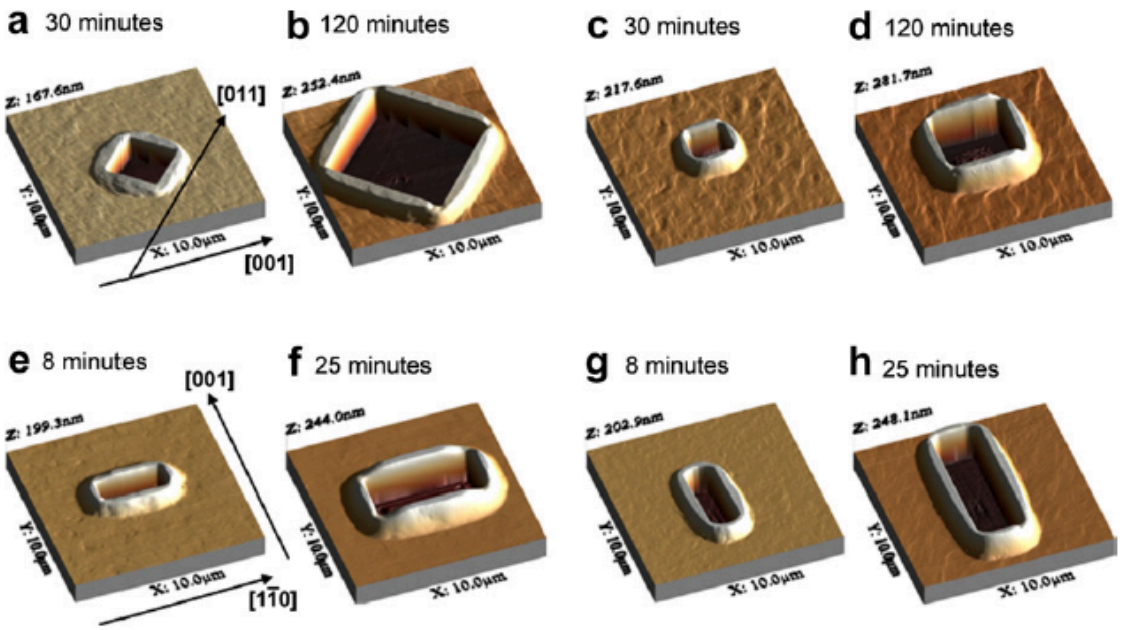

Figure 1-22. AFM images of growing natural holes in Ni(100) and Ni(110) films at two different reducing gas flow rates [22]. The annealing time is indicated in the images. (a)-(b) Ni(100), 2310sccm of 5% H_2+95% N_2. (c)-(d) Ni(100), 12sccm. (e)-(f) Ni(110), 2310sccm. (g)-(h) Ni(110), 12sccm.

Changes in the shape of the natural hole indicate that the relative retraction rates in different crystallographic orientations change under different annealing ambient. Indeed, it can be seen that this is the case, as illustrated in the polar plots of retraction distances in different crystallographic orientations (Figure 1-8).

Zucker et al.[26] used the method of crystalline formulation to simulate the edge retraction of 2-dimensional structures. In their work, they identified that the surface energies and surface self-diffusivities most strongly affect the dewetting kinetics. More specifically, it was found that the surface diffusivity of the top facet most strongly affects the dewetting kinetics. This is illustrated in Figure 1-23 and Table 1-1.

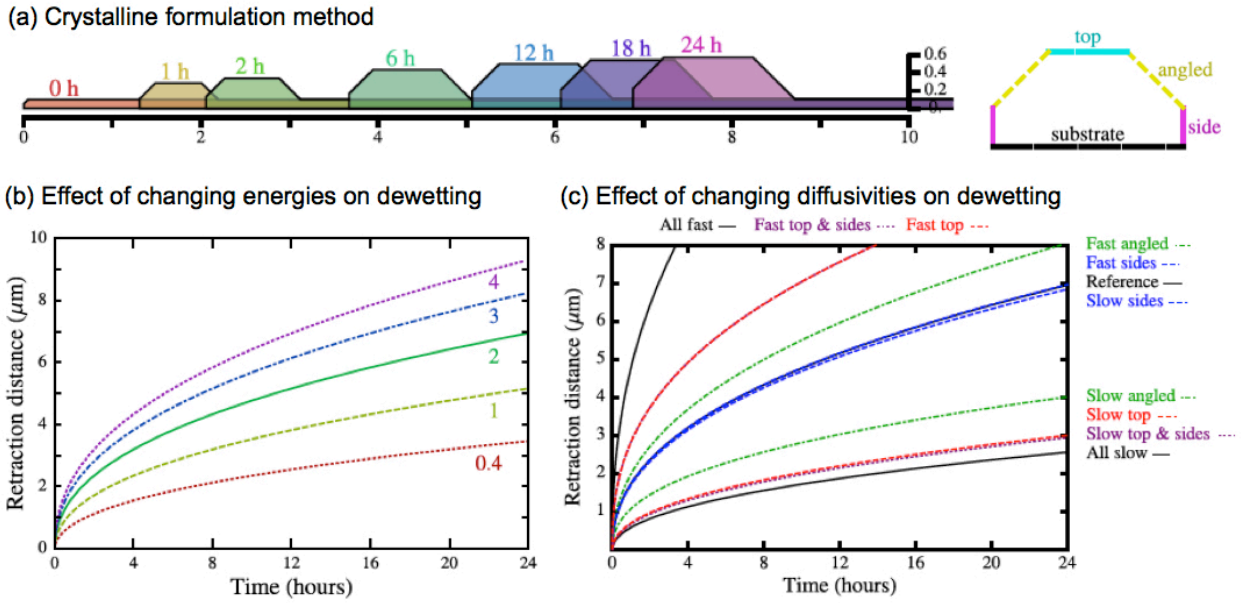

Figure 1-23. (a) The reference film edge profile is shown for various times after the annealing begins. The aspect ratio is 1:1, and the units of both the vertical and horizontal scale are micrometers. (b) The influence of the absolute value of reference surface energy on the film edge retraction distance vs. time. Each curve is labeled with the surface energy in J/m^2. The relative magnitudes of the surface energies of individual facets were kept the same. (c) The diffusivity on each set of symmetrically-related facets was changed to show its effects on the retraction distance vs. time. All plots are reproduced from Zucker et al.[26]

As reducing gas is flown during annealing to prevent oxidation of Ni, the concentration of oxygen and hydrogen can vary depending on the flow rate of the reducing gas. These gas molecules can adsorb to the Ni surface and act as impurities affecting the surface diffusivity and the surface energy. Blakely and Mykura [70] mentioned that depending on the crystal surface the presence of adsorbed impurities can increase or decrease the surface diffusivity. Tung and Graham [71] also observed that different crystal surfaces show different amount of changes in surface diffusivity induced by the adsorbed hydrogen atoms. Chang et al.[72] also reported that reconstructed Ni surfaces induced by adsorbed impurities affect the surface diffusivities. In addition, the surface energies are also known to change by the presence of different impurities on the surface. Meltzman et al.[73] reported that the equilibrium shape and relative surface energies of

the equilibrium facets of Ni change under different annealing ambient. Huang et al.[74] also reported on the effects of hydrogen adsorption on the surface energy anisotropy of Ni.

Therefore, from previous studies, it can be expected that the annealing ambient can significantly affect both the surface energy and the surface diffusivity, and this can significantly affect the dewetting phenomenologies.

Table 1-1. The diffusivity on each facet for each curve shown in Figure 1-23(c) [26].

Curve label	D_{top} / D_0	D_{angled} / D_0	D_{side} / D_0
Reference	1	1	1
All fast	10	10	10
All slow	0.1	0.1	0.1
Fast top	10	1	1
Slow top	0.1	1	1
Fast angled	1	10	1
Slow angled	1	0.1	1
Fast sides	1	1	10
Slow sides	1	1	0.1
Fast top & sides	10	1	10
Slow top & sides	0.1	1	0.1

1.3. Templated Dewetting and Formation of Ordered Structures [1]

As described previously, the absence of long range order in polycrystalline films and the random distribution of many different defects prohibit the formation of any long-range ordered

dewetting morphology in such films. However, dewetting in polycrystalline films has also been used to generate an ordered array of islands by either changing the substrate topography or pre-patterning the films and intentionally directing the atomic flux to desired locations. The study by Giermann and Thompson [75] is an example, in which they pre-patterned oxidized silicon substrates into a matrix of inverted pyramids. Upon deposition and dewetting of thin gold films, they found that under an appropriate pit spacing, pit size, and film thickness that allow the entire gold film to flow into the pits driven by the local curvature gradient, an ordered array of gold particles in the pits is observed, as illustrated in Figure 1-24.

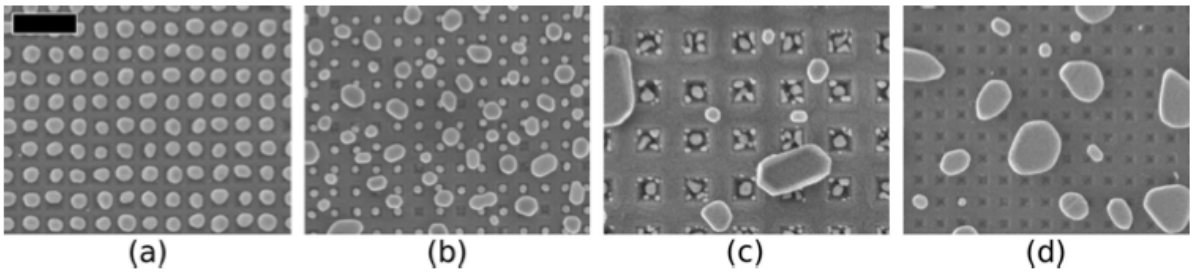

Figure 1-24. Formation of ordered arrays of Au particles by pre-patterning of oxidized Si substrates [75]. Under the appropriate pit spacing, size and film thickness, all of the deposited gold diffuses into the pits to form ordered arrays. Scale bar indicates 500μm.

Pre-patterning of the deposited film before annealing at high temperatures for dewetting is another way to generate ordered structures. Kim et al. [76] showed that polycrystalline Au films can also have an ordered dewetting morphology to some degree when the films are pre-patterned. Although the distribution of islands loses regularity when the initial pattern size becomes too large, they showed that, in patterns of order 10μm, the number and the arrangement of islands formed after dewetting can be controlled by the aspect ratio and the size of the initial pattern, as illustrated in Figure 1-25. However, the degree of order obtainable in templated dewetting in polycrystalline films is limited because randomly distributed defects lead to formation of irregular natural holes that break the regularity imposed by templates.

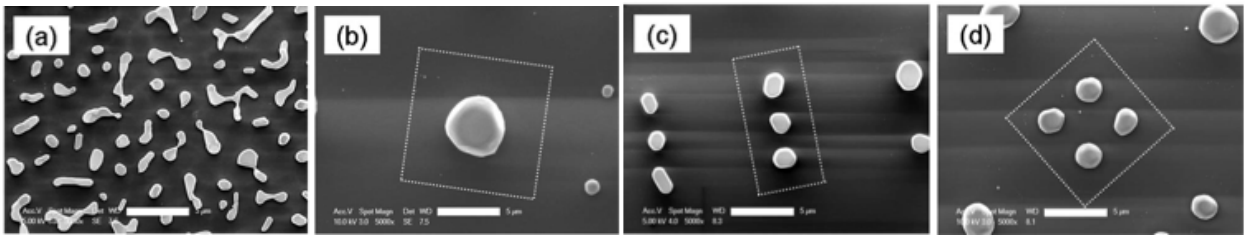

Figure 1-25. Formation of ordered Au islands by pre-patterning the gold film [76]. Unlike continuous films (**a**), patterned films can generate ordered arrays of islands in polycrystalline films (**b-d**), controlled by the aspect ratios of the initial pattern. Scale bars indicate 5μm.

Because of the regular morphology as previously described, dewetting in single crystal films has a potential as a method to generate complex structures. By properly pre-patterning the film, a number of different complex, regular dewetting morphologies, which also are much smaller than the original patterns, can be formed. Ye and Thompson [66] showed that pre-patterned Ni(100) and Ni(110) films can dewet to form complex ordered structures. Because the films have anisotropic surface energies and surface diffusivities, the dewetting morphology also depends on the initial orientation of the patterns. This is illustrated in Figure 1-26.

So far, insufficient data and insufficient models exist to thoroughly understand and predict the dewetting morphology of templated patterns in single crystal films. Thus, in-depth understanding of the phenomenology along with the development of models to describe the process is crucial for solid-state dewetting of single crystal films to be used as an efficient method to generate complex nanostructures.

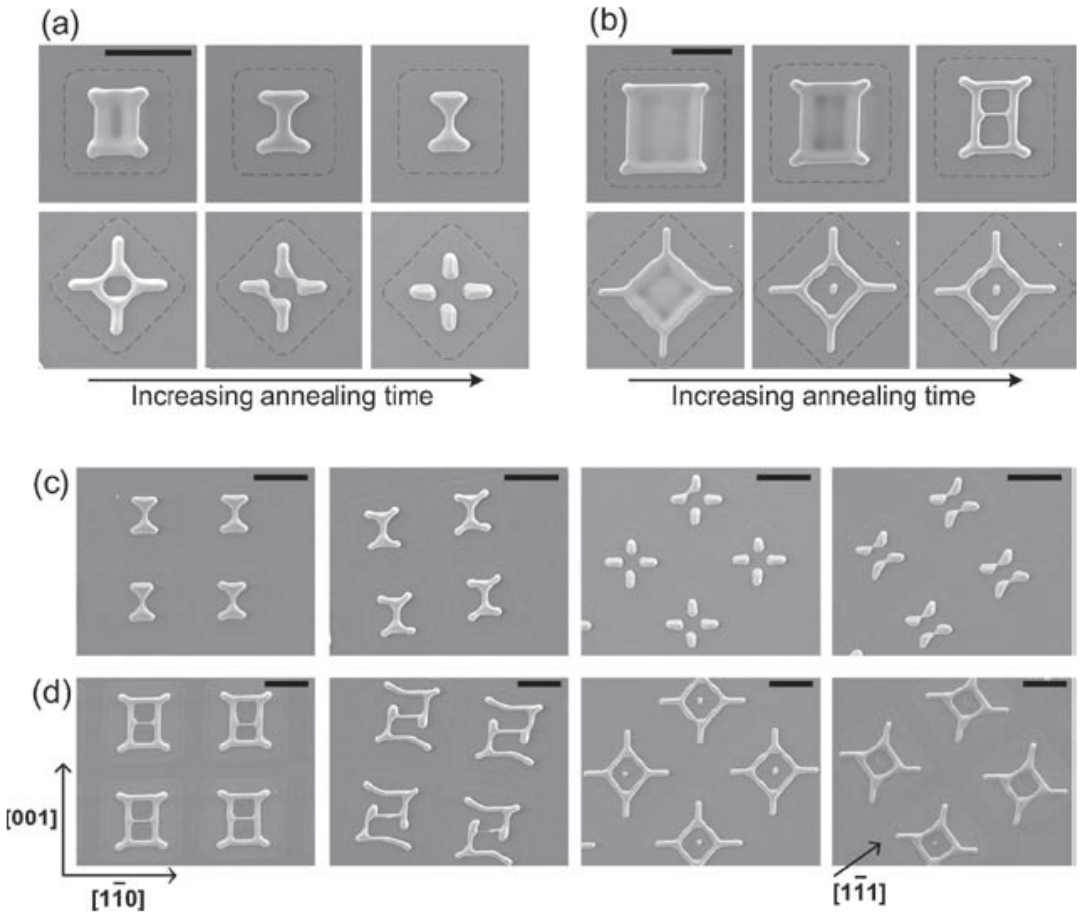

Figure 1-26. Dewetting of square patches patterned in a Ni(110) film [66]. Dewetting morphology is clearly dependent on the initial orientation and the size of the patches. The gray dashed lines indicate the initial shapes of the patches. Scale bars indicate 10μm.

1.4. Scope of Work

Although many dewetting experiments have been conducted thus far to qualitatively study different dewetting phenomenologies, not much effort has been made to quantitatively study the behavior. The goal of this work is to further enhance the quantitative understanding of the mechanisms underlying individual dewetting phenomenologies occurring during the solid-state dewetting of thin single crystal films. These phenomenologies include edge retraction, pinch-off, fingering instability, Rayleigh-like instability, and corner instability. An in-depth understanding of these dewetting phenomenologies and their characteristic length scales will also

be crucial for the templated solid-state dewetting of thin single crystal films to be used as a potential method to generate structures at sub-lithographic length scales.

To achieve this goal, the abovementioned dewetting phenomenologies were experimentally studied and analyzed; furthermore, analytical and computational models were also developed for better understanding of the phenomenon. In addition, a close attention was paid to the effect of annealing ambient and anisotropy in surface energy and surface diffusivity on the dewetting phenomenologies.

Chapter 2. Experimental Methods

2.1. Film Deposition

Because it is known [77-79] that epitaxial Ni of different crystallographic orientations can be grown on MgO, single crystal Ni films deposited on polished single crystal MgO substrates were used as a model system. In some cases, Ni was also deposited on sapphire under the same deposition condition. The films were deposited using a Balzers UMS500 electron-beam deposition system equipped with a turbomolecular pump and a mechanical pump. Because the system does not have a load-lock installed and thus the main chamber is exposed to the atmosphere when samples are loaded, a bake-out process was necessary to have enough desorption of gas molecules from the chamber wall. Before deposition, the chamber was baked at 120 °C and the substrates were heated at 320 °C for 24 hours. The Ni source was briefly heated for evaporation at a chamber temperature of 90 °C and substrate temperature of 270 °C before deposition, while the substrates were blocked from deposition flux, to increase purity of the source. The deposition was initiated at room temperature and at a base pressure of mid-10^{-8} torr and the pressure increased to low-10^{-7} torr during the deposition. The deposition rate was monitored with a quartz crystal deposition sensor.

When an in-situ measurement of the surface structure was necessary for the deposited film, the Perkin-Elmer e-beam evaporation system was used, in which a reflective high energy electron diffraction system is installed. This will be discussed later in this chapter.

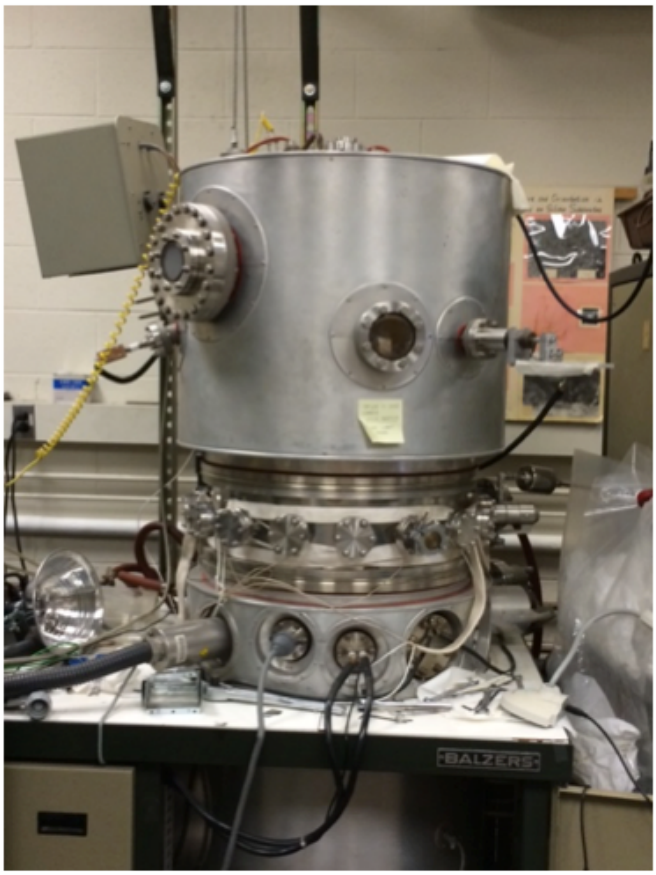

Figure 2-1. The Balzers ultrahigh vacuum e-beam evaporation system.

2.2. X-ray Texture Analysis

Before subjecting the deposited films to dewetting at high temperatures, it was important to determine whether a satisfactory degree of epitaxy is achieved. X-ray texture analysis was used to determine both the out-of-plane and the in-plane orientations of the deposited Ni film. Because epitaxial films are highly textured, it was important to carefully calibrate the x-ray beam alignment with high-resolution angular steps to where the maximum diffraction occurs to correctly detect the diffraction peaks. Therefore, a Bruker HRXRD system in a 2θ-ω scan mode was used to confirm that the deposited film is epitaxial. Because a careful beam alignment is necessary, the actual scan was preceded by a series of detector scans (variation of 2θ), Z scans

(variation of the normal position of sample), rocking curve scans (variation of ω), 2θ-ω scans (variation of both 2θ and ω), and χ scans (variation of tilt angle), to maximize the peak signal of MgO. Different angles in the alignment procedures are illustrated in Figure 2-2. Ye [22] has previously reported that sometimes the deposited film may have a surface normal slightly off from that of the substrate, although the film is highly textured to have only one desired diffraction peak. This could also be detected by the HRXRD scan because the high-resolution steps allow determination of the tilt angle difference between the substrate and the film.

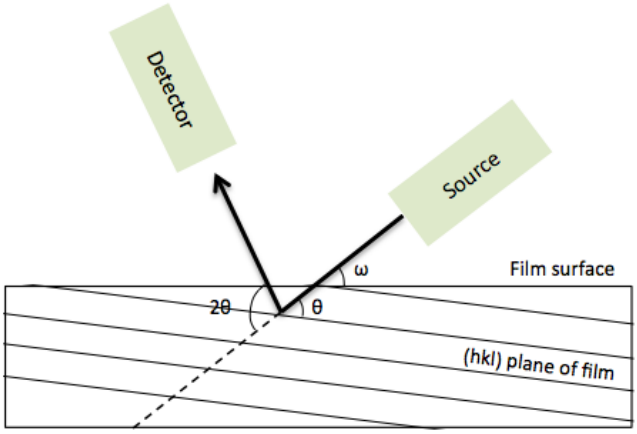

Figure 2-2. Schematic illustration of HRXRD scan settings. Each parameter was carefully adjusted to maximize signal from the epitaxial film.

In-plane orientation alignment of the film with the substrate was studied by using a Bruker D8 Discover system equipped with a 2D area detector. In this scan, 2θ can be properly centered to allow a simultaneous scan of the peaks in both MgO and Ni. When properly set, the system scans the sample to collect x-ray signal data for a range of rotation angles. Resulting pole figures can be analyzed to see if the in-plane alignment is satisfactory. Because of the crystallographic symmetry of the film, only a 180° rotation scan was sufficient to analyze the in-plane alignment for Ni(100) and Ni(110).

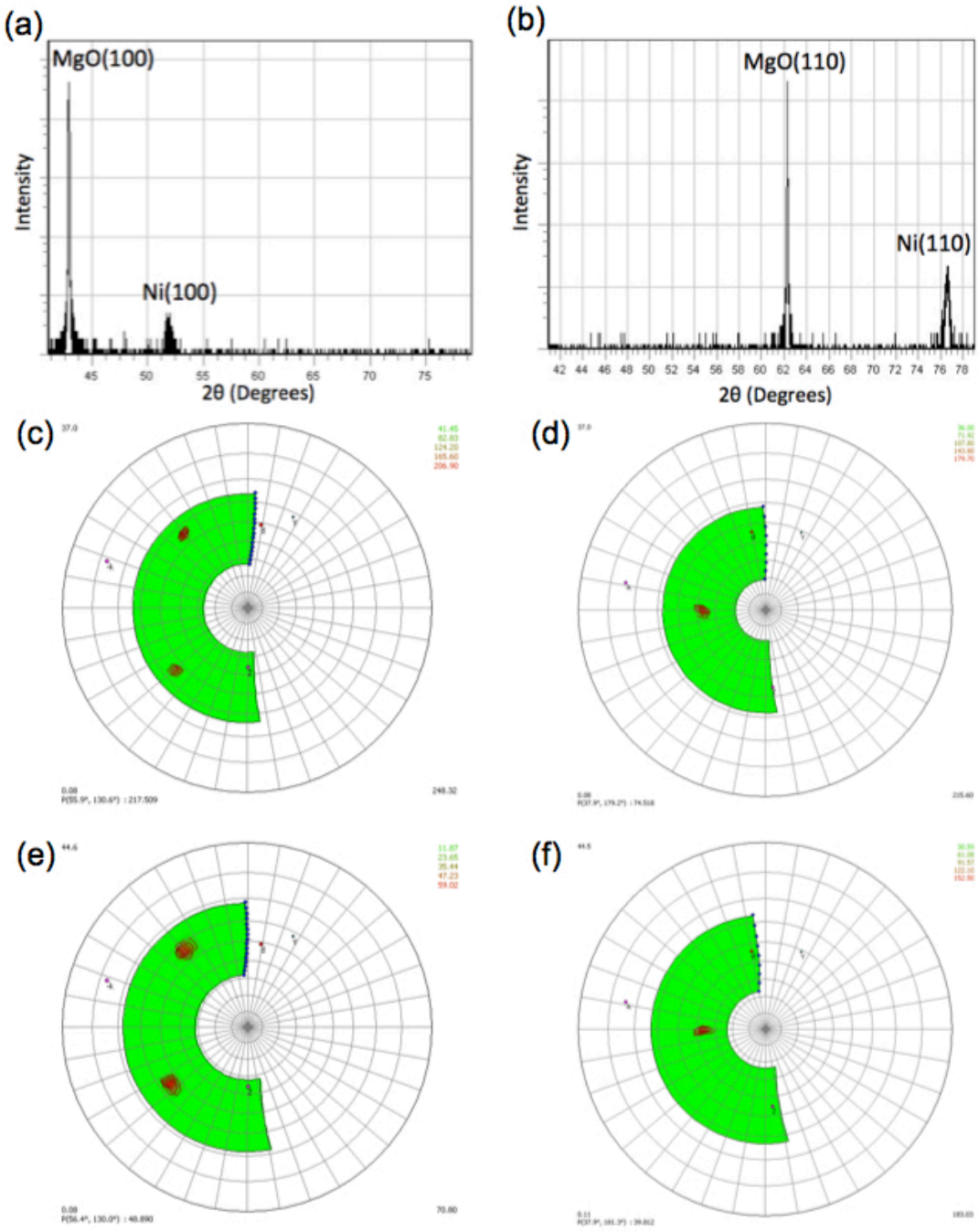

Figure 2-3. **(a)** 2θ-ω scan of Ni(100) film. **(b)** 2θ-ω scan of Ni(110) film. **(c)** (111) in-plane peak of MgO(100). **(d)** (111) in-plane peak of MgO(110). **(e)** (111) in-plane peak of Ni(100) deposited on MgO(100). **(f)** (111) in-plane peak of Ni(110) deposited on MgO(110).

Figure 2-3 illustrates the x-ray diffraction data for 130-nm thick Ni(100) and Ni(110) films, which were used in the study. Under the appropriate deposition conditions, the width of

the Ni peak was similar to the width of the MgO substrate peak, which is an indication that a satisfactory level of out-of-plane and in-plane alignments was achieved. Similar x-ray scans were also carried out for Ni(111) on sapphire, and a satisfactory level of out-of-plane and in-plane alignment was attained.

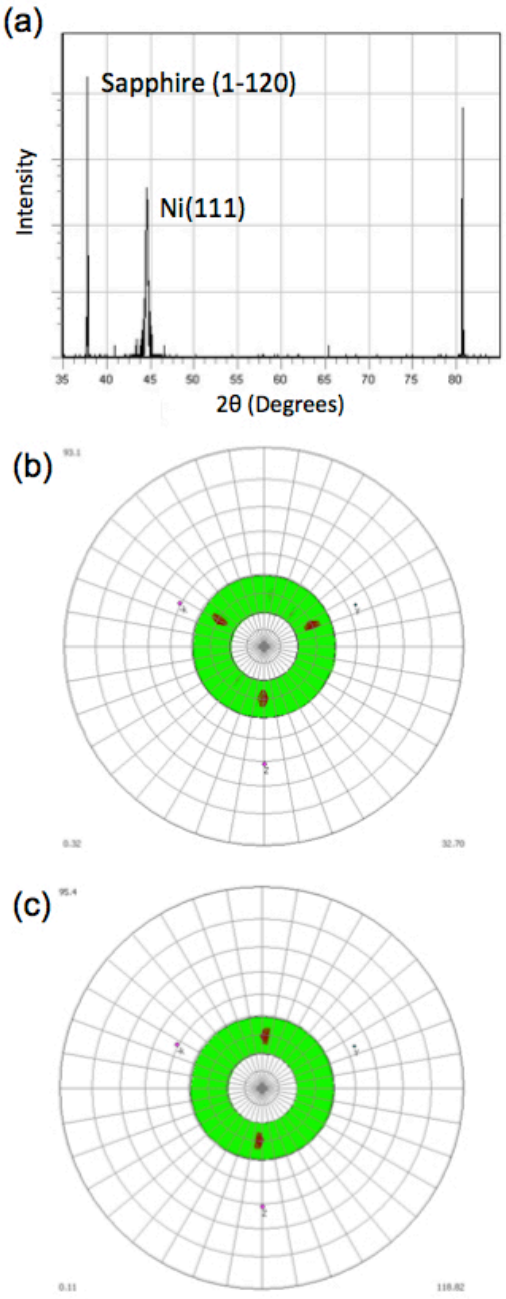

Figure 2-4. **(a)** 2θ-ω scan of Ni(111) film. **(b)** (2206) in-plane peak of sapphire ($1\bar{1}20$). **(c)** (113) in-plane peak of Ni(111) deposited on sapphire ($1\bar{1}20$).

2.3. Film Patterning

The as-deposited films were patterned by photolithography. After a dehydration step at 110°C for 5 minutes on a hot plate, the sample was coated with OCG 825 positive photoresist at a spin rate of 3000rpm for 30 seconds and baked again at 110°C for 5 minutes to evaporate solvent. Followed by an alignment step and exposure to UV light, the photoresist was developed in OCG 934 1:1 developer and baked at 130°C for 5 minutes.

After OCG 825 became obsolete, SPR 700 was used as photoresist. The resist was spin coated at a spin rate of 2700rpm and baked at 115°C for 4 minutes. After alignment and exposure, the photoresist was developed in CD 26 and baked at 130°C for 5 minutes.

Following the wet etching of Ni in 69% HNO_3, H_2SO_4, CH_3COOH and H_2O with a volume ratio of 7.2 : 2 : 5 : 28, the remaining photoresist was first removed in acetone and then in ultrasonicated RR41 (dimethyl sulfoxide).

Additionally, e-beam lithography was used to pattern structures with length scales beyond the photolithographic limit. In this case, 6% hydrogen silsesquioxane (HSQ) was spin-coated at 500rpm for 60 seconds and baked at 90°C. The electron beam exposure was conducted in a Raith 150 e-beam writing system with an accelerating voltage of 30kV. The exposed resist was developed in CD 26 and the subsequent Ni etching was conducted in a Plasmatherm RIE system at 200W with Ar and Cl_2 flow rates of 20sccm.

2.4. Thermal Annealing

To induce an appreciable degree of dewetting, a high temperature was required and therefore it was necessary to prevent oxidation of Ni by flowing a reducing gas (5% H_2 and 95% N_2). NiO can be reduced by hydrogen because oxidation of hydrogen to form water has a more negative energy of formation than that of Ni unless the temperature is far below 0°C [80]. A

Lindberg/Blue quartz tube furnace with stainless steel flow tubes was used, in which the flow rate of reducing gas is monitored and controlled by a rotameter installed between the gas inlet of the furnace tube and the gas cylinder. An Accucarb Carbon Probe purchased from United Process Control is inserted into the furnace tube to measure the accurate oxygen partial pressure during annealing. The diameter of the tube in the tube furnace is 3cm and the diameter of the oxygen measurement probe is 1in. A careful alignment is thus necessary to make the probe fit smoothly inside the tube furnace. Through the oxygen partial pressure measurement, it was determined that the major source of oxygen inside the furnace is the oxide substrate (MgO), which will be studied in detail in Chapter 3.

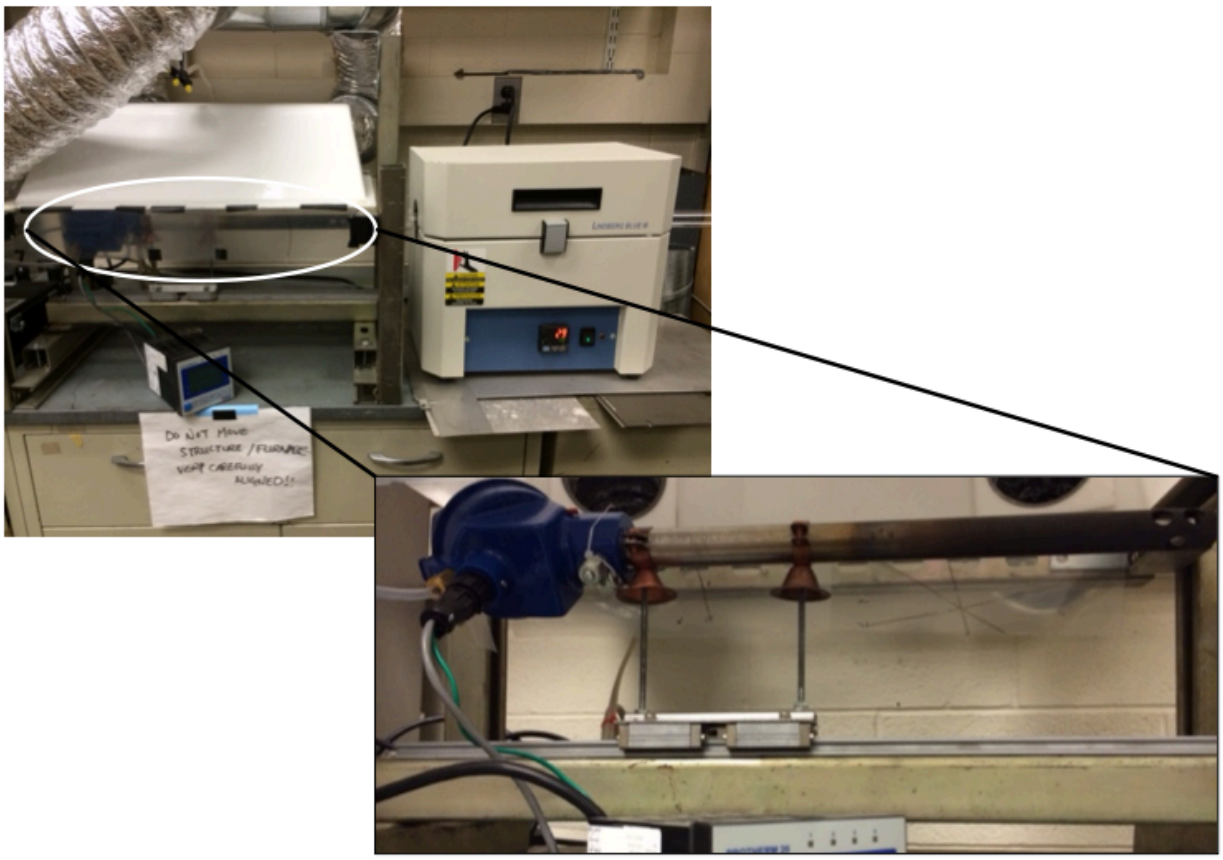

Figure 2-5. The tube furnace used for thermal annealing with an oxygen measurement tube installed. The probe is installed on a rail carefully aligned with the tube furnace so that the probe can be inserted smoothly in the tube.

2.5. Scanning Electron Microscopy

The morphology of dewetted films was usually observed by scanning electron microscopy. The imaging was carried out using an FEI/Phillips XL30 FEG ESEM. When Ni films are patterned and observed under a typical SEM, the exposed MgO surface is electrically insulating and thus accumulates excess electrons to cause a charging effect in the image. This could be prevented by a low-vacuum mode in an environmental scanning electron microscope, in which water vapor is introduced in the chamber and the positively ionized water molecules neutralize the MgO surface. Although the image resolution was somewhat degraded due to a high pressure, the quality of the image generally was reasonably good for the purpose of the research.

2.6. Atomic Force Microscopy

When a more accurate surface profile was needed, atomic force microscopy was used. AFM imaging was done in tapping mode with a Veeco Nanoscope IV AFM. A standard tapping mode silicon probe was used. A high resolution imaging with a scan rate of approximately 0.2 Hz was conducted after a desired feature was located with high rate scans. It was important to decrease the actual scan rate during imaging because the probe generally did not retain a good contact with the surface at a high scan rate due to the large height of the dewetted features.

2.7. Focused Ion Beam Cross-Sections

A focused ion beam was used to make cross-sections of dewetted Ni in a Helios Dual Beam Workstation. Because MgO substrates are electrical insulators, significant charging develops with use of electron and ion beams. Therefore, the samples were preliminarily coated with 40 nm carbon. After cross-sectioning was complete, the samples were additionally coated with 20 nm carbon to coat the exposed cross-section to minimize charging in the image. This

way, the charging effect in the image was minimized and reasonably good images could be obtained.

2.8. Low Energy Electron Diffraction (LEED)

To observe surface reconstructions of Ni surface under different annealing ambient, LEED measurements were made in collaboration with Wen Ma in the Yildiz Group at MIT Department of Nuclear Engineering. Once the sample is loaded in the chamber at a base pressure of low 10^{-9}torr, surface oxide was cleaned by Ar bombardment with an Ar pressure of $5x10^{-6}$torr at an accelerating voltage of 2kV for 1hr. After the cleaning and a vacuum annealing at 500°C for 1hr to heal the surface and desorb the Ar, pure H_2 or O_2 was introduced to the entire chamber to a pressure of $1x10^{-7}$torr for 10 seconds while the sample was annealed at 700°C and then the LEED measurements were conducted with a filament current of 2.7A and an emission current of 300μA.

2.9. Reflective High Energy Electron Diffraction (RHEED)

The LEED system mentioned above allows annealing of up to 700°C. To allow annealing at a higher temperature than 700°C, a RHEED system was constructed in a Perkin-Elmer ultrahigh vacuum e-beam evaporation system. Additionally, to accommodate a higher chamber pressure due to annealing and introduction of gases while the electron beam is on, a differential pumping system was added close to the electron gun. A turbomolecular pump purchased from Kurt Lesker was attached near the electron gun filament to decrease the pressure near the filament by one order of magnitude than the chamber pressure. This system also has a vacuum annealing capability of up to 900°C. The sample was loaded in the system at a base pressure of $1x10^{-8}$torr. The surface oxide was removed by heating the sample up to 800°C for 10 minutes. After the oxide removal, the 1x1 surface structure can be measured. Then, the desired

temperature was set, and gas is introduced via the flow tube located very close (<1mm) to the sample surface. The RHEED measurements were carried out with the following setup. The filament current was set to 3.3A, the emission current was set to 0.5mA, and the accelerating voltage was set to 10kV. The x- and y- deflection was adjusted until a RHEED pattern can be read.

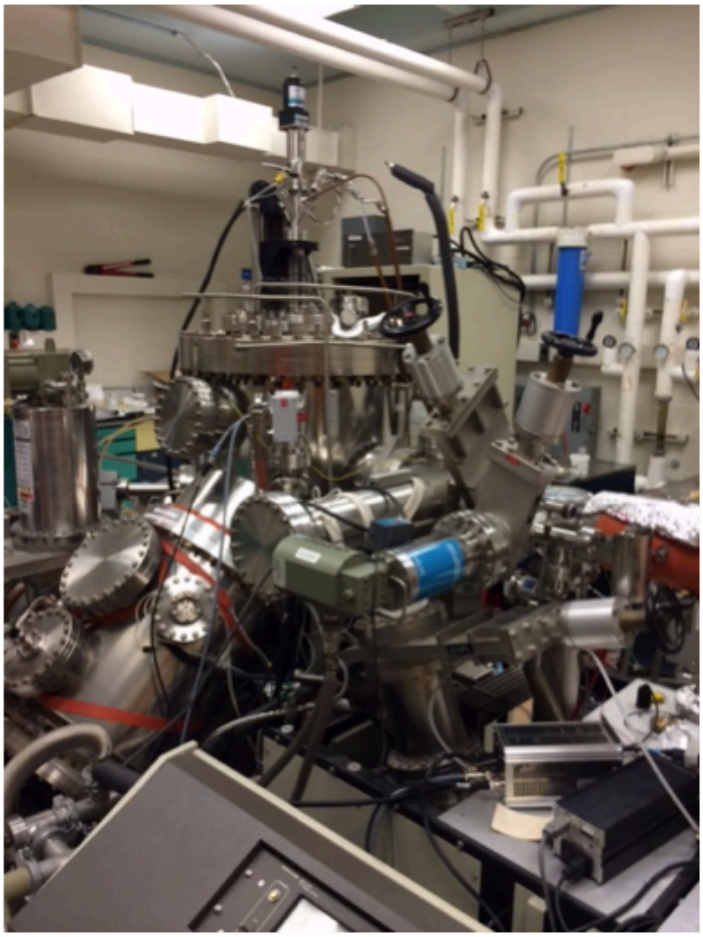

Figure 2-6. The Perkin-Elmer e-beam evaporation system. A RHEED system is also installed inside the main chamber. The system operates with a rotary pump and a cryopump.

Chapter 3. Effect of Annealing Ambient on Anisotropic Retraction of Edges

3.1. Introduction

Solid-state dewetting starts at three-phase boundaries of film, substrate, and ambient, resulting either from natural hole formation or patterned macroscopic edges [81]. Once three phase boundaries are present, dewetting proceeds by curvature-driven surface diffusion away from the three-phase boundaries into areas of small local curvature such as the surface of the flat film ahead of the boundaries. This results in the movement of the three phase boundaries or, edge retraction. At the edge, thickening rims form due to local differences in the diffusion flux.

Unlike polycrystalline films, single crystal films have anisotropy in surface energy and surface self-diffusivity, leading to more regular dewetting morphologies [81]. When the single crystal films are lithographically templated prior to dewetting, a very complex, regular patterns can be made via dewetting [66]. Also, analyses of experiments on templated dewetting of single crystal films can provide a basis for a better understanding of the effects of anisotropy in surface energy and surface diffusivity on capillarity-driven dewetting.

A more quantitative understanding of dewetting in single crystal films is needed to take advantage of templated dewetting for regular, sub-lithographic pattern formation. Ye and Thompson [22] previously studied solid state dewetting of Ni films patterned into large patches with initially straight macroscopic edges aligned with different in-plane orientations. In certain orientations the edges remained straight as they retracted, which are called kinetically stable edges. In other orientations, the edges developed an alternating series of in-plane facets whose in-plane normals are the same as those of kinetically stable edges. In Ni(100) films, edges aligned normal to the [010] and [011] in-plane directions are kinetically stable during retraction, and in Ni(110) films, edges normal to the [001], $[1\bar{1}1]$ and $[1\bar{1}0]$ orientations are kinetically stable. Kim et al.[23] further analyzed the retraction of the kinetically stable edges experimentally and with simulations.

Ye and Thompson [22] observed that the shape and in-plane orientation of the natural hole, defined by the kinetically stable edges with locally minimum retraction rates, can change under different annealing ambient. This is also illustrated in Figure 3-1. This indicates that the relative retraction rates in different crystallographic orientations change under different annealing ambient. Zucker et al.[26] conducted a more quantitative analysis by developing a computational model. In their work, the method of crystalline formulation was used to simulate the edge retraction of fully faceted 2-dimensional structures. By varying surface energy and diffusivity of individual facets, they found that surface diffusivity anisotropy has a greater impact than surface energy anisotropy. Furthermore, it was found that the surface diffusivity of the top facet of the retracting rim most strongly affects the dewetting kinetics. It is also known [70-72] that different annealing ambient can change the surface structure by the surface reconstruction induced by the adsorbed gases, resulting in the changes in relative surface diffusivities in different diffusion orientations. Thus, the change in the relative retraction rates under different annealing conditions can be attributed to the change in the surface structure.

In this chapter, more detailed analyses of the retraction kinetics during retraction of the kinetically stable edges in Ni(110) and Ni(100) are reported. Changes in relative retraction rates under different annealing ambient are related to the changes in the surface structure due to reconstruction of the Ni surface by different gases adsorbed to the Ni surface.

* This work was completed in collaboration with Wen Ma in the Yildiz Group at MIT Department of Nuclear Engineering. Part of this work is in preparation for submission to a journal article [82].

3.2. Experimental Procedures

130nm-thick single crystal Ni(110) and Ni(100) films were deposited on polished single crystal MgO substrates (purchased from MTI Corporation) using electron beam deposition. The as-deposited films were patterned using optical photolithography with SPR 700 positive photoresist and CD 26 developer followed by wet etching of Ni in 69% HNO_3, H_2SO_4, CH_3COOH and H_2O with a volume ratio of 7.2:2:5:28. More details of the film deposition and the patterning procedure are available in Chapter 2. Annealing of the patterned films was conducted in a tube furnace, with an oxygen concentration measurement probe installed, at 700°C with reducing gas (5% H_2 and 95% N_2) flowing at rates of 2310sccm and 95sccm and with another reducing gas (2% H_2 and 98% Ar) flowing at a rate of 390sccm to remove nickel oxide from the Ni surface and prevent oxidation during annealing. Under the condition of 390sccm of 2% H_2 and 98% Ar, the partial pressure of oxygen is the same as the condition with 5% H_2 and 95% N_2 flowing at 95sccm. The partial pressure of oxygen was measured using the abovementioned probe installed inside the tube furnace. Some samples were also annealed with Ar flowing at a rate of 2310sccm to measure the partial pressure of oxygen without presence of H_2. Scanning electron microscopy using an FEI/Philips XL30 FEG ESEM was used for measurements of retraction distances. AFM imaging was also conducted using the tapping mode in a Veeco Nanoscope IV AFM. A focused ion beam (Helios Dual Beam Workstation) was used to make cross-sections for SEM imaging of the rims that form during edge retraction. A low energy electron diffraction (LEED) was used to measure the surface structure of Ni(100) and Ni(110) annealed at 700°C under different annealing ambient. A reflective high energy electron diffraction (RHEED) was used to supplement the LEED measurements at 900°C. The details of the surface structure measurement experiments are provided in Chapter 2.

3.3. Results

Figure 3-1 shows retraction distance measurements for kinetically stable edges in Ni(110) and Ni(100) films versus annealing time where 5% H_2 + 95% N_2 was flowed at rates of 2310sccm and 95sccm to prevent oxidation. These retraction distance measurements are analogous to the edge retraction rates. It can be seen that there is a clear change in the relative retraction distances over time in different kinetically stable edges, except for the $[1\bar{1}1]$ retraction in Ni(110).

Figure 3-2 shows retraction distance measurements for kinetically stable edges in Ni(110) and Ni(100) film versus annealing time where 5% H_2 + 95% N_2 was flowed at a rate of 95sccm to prevent oxidation in one case and 2% H_2 + 98% Ar was flowed at a rate of 390sccm in another case. Both conditions were measured to have the same oxygen partial pressure. It can be seen that there is no significant difference in the retraction distances; thus, it can be concluded that H_2 and O_2 are the gases responsible for the changes in relative retraction rates, not N_2 or Ar.

Figure 3-3 shows oxygen partial pressure profiles along the tube furnace under different annealing conditions. It was found that the source of oxygen during annealing is the MgO substrate. Under the same flow rate of pure Ar, there was a partial pressure difference of about two orders of magnitude between when the samples are present in the furnace and when not. Furthermore, even though the measured oxygen partial pressure under Ar with samples was much lower than the oxidation threshold of Ni, which is known to be $3x10^{-9}$atm [73], the Ni film has slowly oxidized over several hours. Thus, it can be estimated that the oxygen partial pressure at the sample surface is much higher, close to the oxidation threshold, in the case of pure Ar flow.

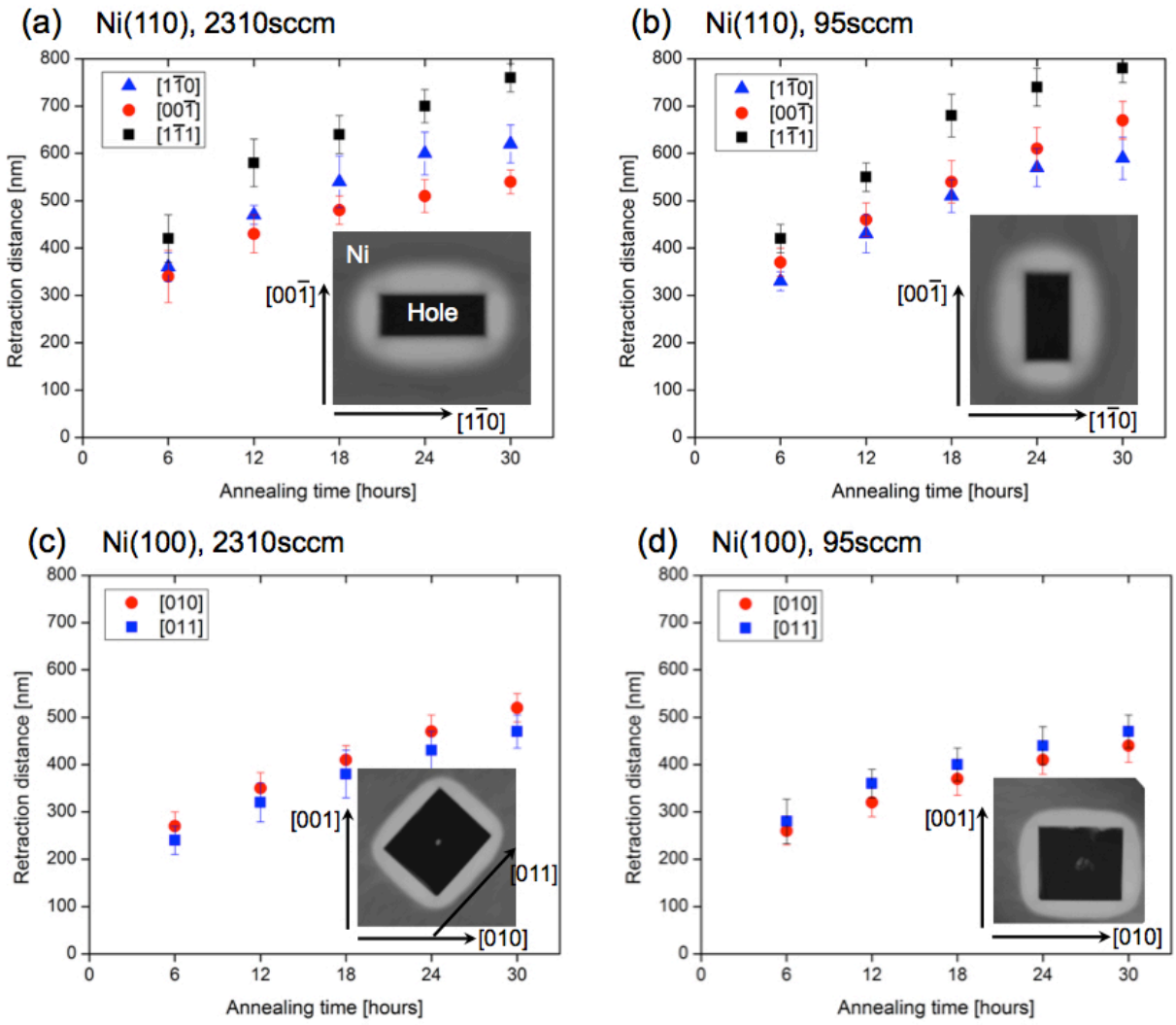

Figure 3-1. (a) and (c) Retraction distance versus annealing time with 5% H_2 + 95% N_2 flowing at a rate of 2310sccm. (b) and (d) Retraction distance versus annealing time with 5% H_2 + 95% N_2 flowing at a rate of 95sccm. The out-of-plane orientation of the Ni film and the in-plane retraction directions are indicated in each figure. The inset images are AFM images of the natural holes under each experimental condition. Corresponding in-plane directions are indicated with the images.

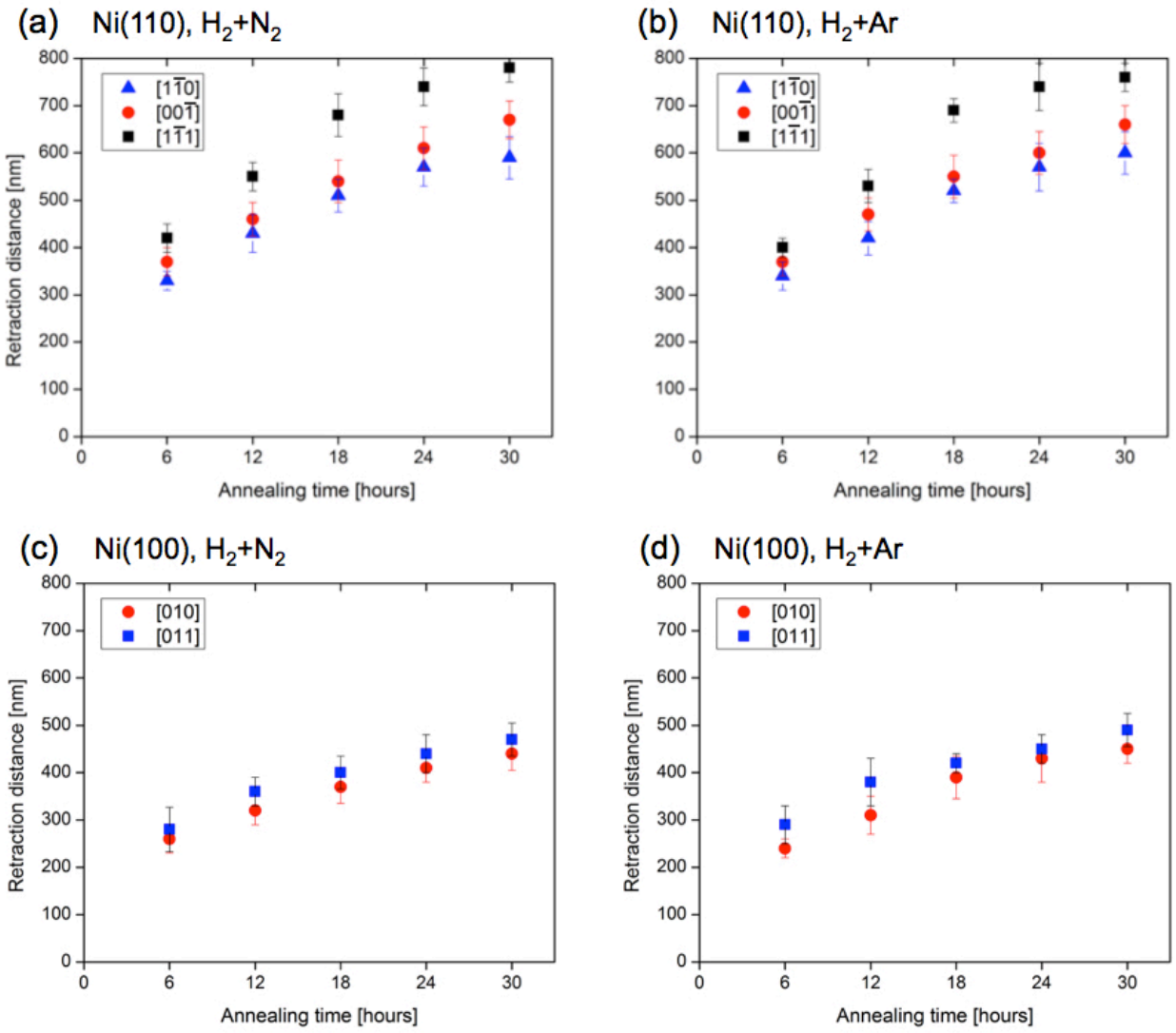

Figure 3-2. (a) and (c) Retraction distance versus annealing time with 5% H_2 + 95% N_2 flowing at a rate of 95sccm. (b) and (d) Retraction distance versus annealing time with 2% H_2 + 98% Ar flowing at a rate of 390sccm. Under these flow rates, the same partial pressure of oxygen was measured. The out-of-plane orientation of the Ni film and the in-plane retraction directions are indicated in each figure.

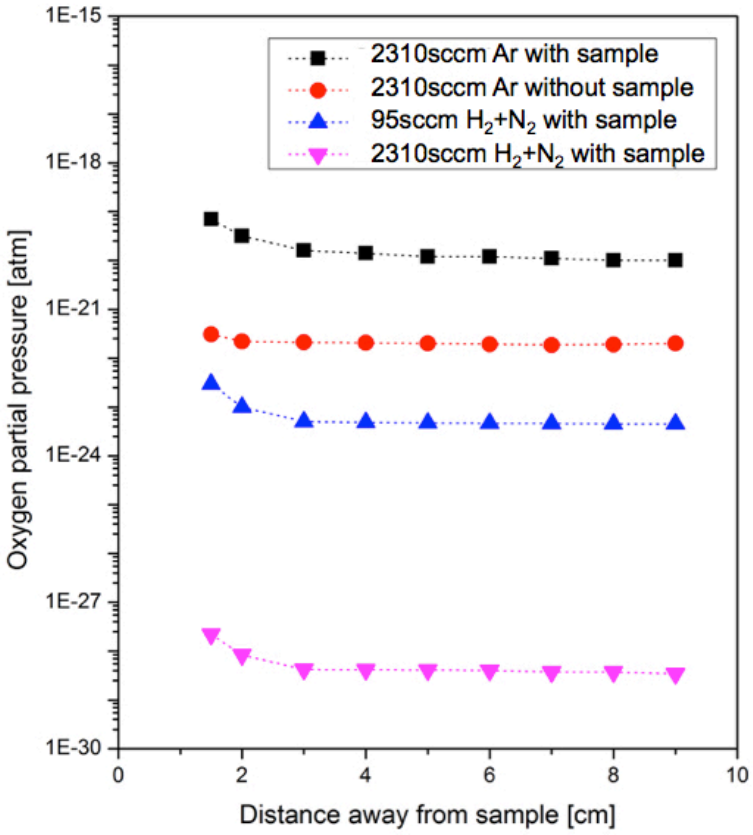

Figure 3-3. Oxygen partial pressure profiles along the tube furnace under different annealing ambient. A distance of zero indicates the sample surface. Due to the physical constraints of the oxygen probe, the closest distance away from the sample surface the probe could measure was 1.5cm.

To analyze the effect of H_2 and O_2 on the surface structure of Ni(110) and Ni(100), surface structure measurements were made and are illustrated in Figure 3-4. A summary of the results is also provided in Table 3-1. It can be clearly seen that H_2 and O_2 reconstruct the Ni surface in different ways. Also, these results are consistent with literature results [83-86].

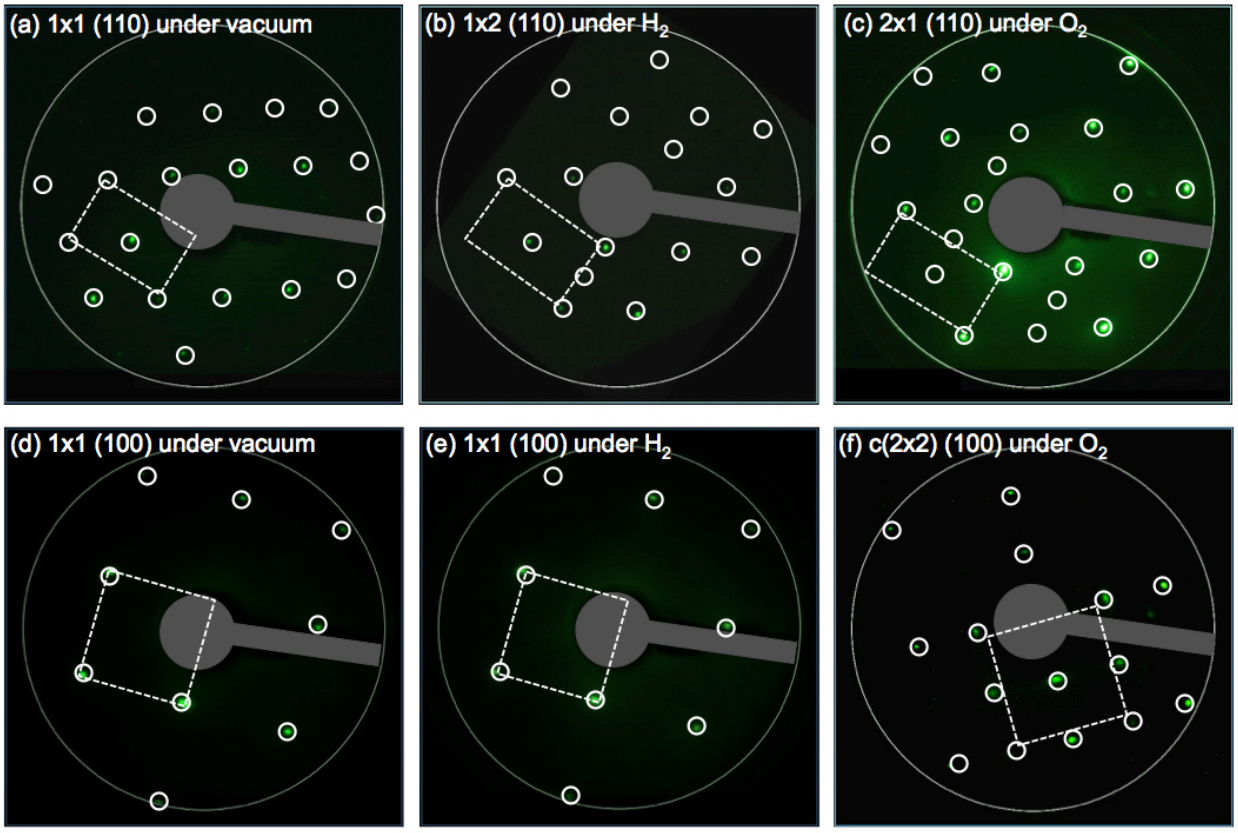

Figure 3-4. LEED patterns for Ni(110) and Ni(100) surfaces collected in vacuum or under low pressures of H_2 or O_2. Specific ambient conditions are indicated in Table 3-1. The patterns in the first row ((a)-(c)) are for (110) surfaces and those in the second row ((d)-(f)) are for (100) surfaces. White circles are drawn as visual aids to indicate the diffraction spots. White dashed lines indicate the unit cells of surface structures. Some diffraction spots are not visible because the electron source blocks the screen.

Table 3-1. Surface structure characteristics for Ni(110) and Ni(100) surfaces by LEED under different annealing ambient conditions.

Surface Condition	Vacuum	Hydrogen	Oxygen
Reconstructed (110)	1x1	1x2	2x1
Ambient Condition	Base P = low 10^{-9}torr	Surface coverage = 1L $P(H_2) = 1x10^{-7}$torr	Surface coverage = 1L $P(O_2) = 1x10^{-7}$torr
Reconstructed (100)	1x1	1x1	c(2x2)
Ambient Condition	Base P = low 10^{-9}torr	Surface coverage = 1L $P(H_2) = 1x10^{-7}$torr	Surface coverage = 1L $P(O_2) = 1x10^{-7}$torr

In addition, RHEED measurements were also made to supplement the LEED measurements. In the RHEED system, the samples can be heated up to 900°C, which has been the typical annealing temperature for the dewetting experiments in this thesis. In addition, gases were introduced via a flow tube very close to the sample surface, so the actual partial pressure of the gas can be made significantly higher than the base pressure in the chamber. The actual partial pressure at the sample surface can be estimated as follows [87]:

$$Surface\ P = (leak\ rate) \times \frac{\sqrt{2\pi MRT}}{N_A kT\pi d^2}, \tag{3-1}$$

where *leak rate* indicates the flow rate of the gas from the flow tube controlled by the leak valve, M is the molar mass of the gas molecule, R is the gas constant, T is the temperature, N_A is Avogadro's number, k is Boltzmann's constant, and d is the distance between the flow tube exit and the sample surface. Table 3-2 summarizes the results from the RHEED experiments, with the actual surface partial pressure estimation included. It should be noted that while the same results were observed at 700°C, no surface reconstruction was observed at 900°C, while retraction rate anisotropy still exists at 900°C. This is due to desorption of the adsorbed gases at high temperatures in vacuum. It was found that O_2 desorbs at approximately 800°C and H_2 desorbs at approximately 720°C, which can be determined by the loss of surface reconstruction. This is likely due to the fact that the surface pressure is significantly lower during the RHEED measurements. Under the typical tube furnace annealing, the overall pressure is on the order of 1atm, but during the RHEED experiments, the surface pressure could go only up to ~1torr. Even though this is a significantly higher pressure than the typical vacuum condition, this is still much lower than 1atm.

Table 3-2. Surface structure measurements of Ni(110) and Ni(100) by RHEED under different annealing ambient conditions at different temperatures. Details of the ambient conditions are also provided. The actual surface partial pressure was estimated using Equation (3-1).

Surface	Vacuum	Hydrogen	Oxygen
Reconstructed (110) Ambient Condition at 700°C	1x1 Base P = $5x10^{-8}$torr	1x2 Surface coverage = 1L $P(H_2) = 1x10^{-7}$torr	2x1 Surface coverage = 1L $P(O_2) = 1x10^{-7}$torr
Reconstructed (110) Ambient Condition at 900°C	1x1 Base P = $6x10^{-8}$torr	1x1 $P(H_2)$ up to 1torr	1x1 $P(O_2)$ up to 1torr
Reconstructed (100) Ambient Condition at 700°C	1x1 Base P = $5x10^{-8}$torr	1x1 Surface coverage = 1L $P(H_2) = 1x10^{-7}$torr	c(2x2) Surface coverage = 1L $P(O_2) = 1x10^{-7}$torr
Reconstructed (100) Ambient Condition at 900°C	1x1 Base P = $6x10^{-8}$torr	1x1 $P(H_2)$ up to 1torr	1x1 $P(O_2)$ up to 1torr

3.4. Discussion

As discussed previously and shown in Figure 3-3, the source of oxygen during annealing is found to be the MgO substrate. Additionally, there is a significant difference between the measured partial pressure under the 2310sccm 5% H_2 + 95% N_2 condition and the 95sccm 5% H_2 + 95% N_2 condition, as shown in Figure 3-3. The measured partial pressure of oxygen in atm is 5 orders of magnitude larger under the 95sccm of reducing gas than under the 2310sccm of reducing gas. This indicates that, at 95sccm, oxygen is more likely to adsorb to the sample surface, while, at 2310sccm, hydrogen is more likely to adsorb to the sample surface.

As previously mentioned, surface diffusivity on the top facet of the retracting rim most strongly affects the edge retraction kinetics. In both Ni(110) and Ni(100), the top facet of the retracting rim is parallel to the macroscopic plane of the as-deposited film. To aid further discussion, the reconstructed surface structures of Ni(110) and Ni(100) under different annealing conditions are provided in Figure 3-5.

In Ni(110), channels, that make diffusion along a certain orientation easier than the other orientations, form by surface reconstructions induced by O_2 and H_2. Under H_2, channels form along the $[1\bar{1}0]$ orientation, making diffusion along that orientation easier than the [001] diffusion. Under O_2, channels form along the [001] orientation, making diffusion along that orientation easier than the $[1\bar{1}0]$ diffusion. This is illustrated in Figure 3-5. As shown in Figure 3-1, this is consistent with the differences in the relative retraction distance under different annealing ambient. At 2310sccm of 5% H_2 + 95% N_2, where H_2 covers the sample surface, the $[1\bar{1}0]$ retraction is faster than the [001] retraction. At 95sccm of 5% H_2 + 95% N_2, where O_2 covers the sample surface, the [001] retraction is faster than the $[1\bar{1}0]$ retraction. In addition, as shown in Figure 3-1, the $[1\bar{1}1]$ retraction does not show much difference under the two flow rates. This is because neither of the surface channels resulting from surface reconstructions induced by H_2 or O_2 are parallel to the $[1\bar{1}1]$ retraction orientation.

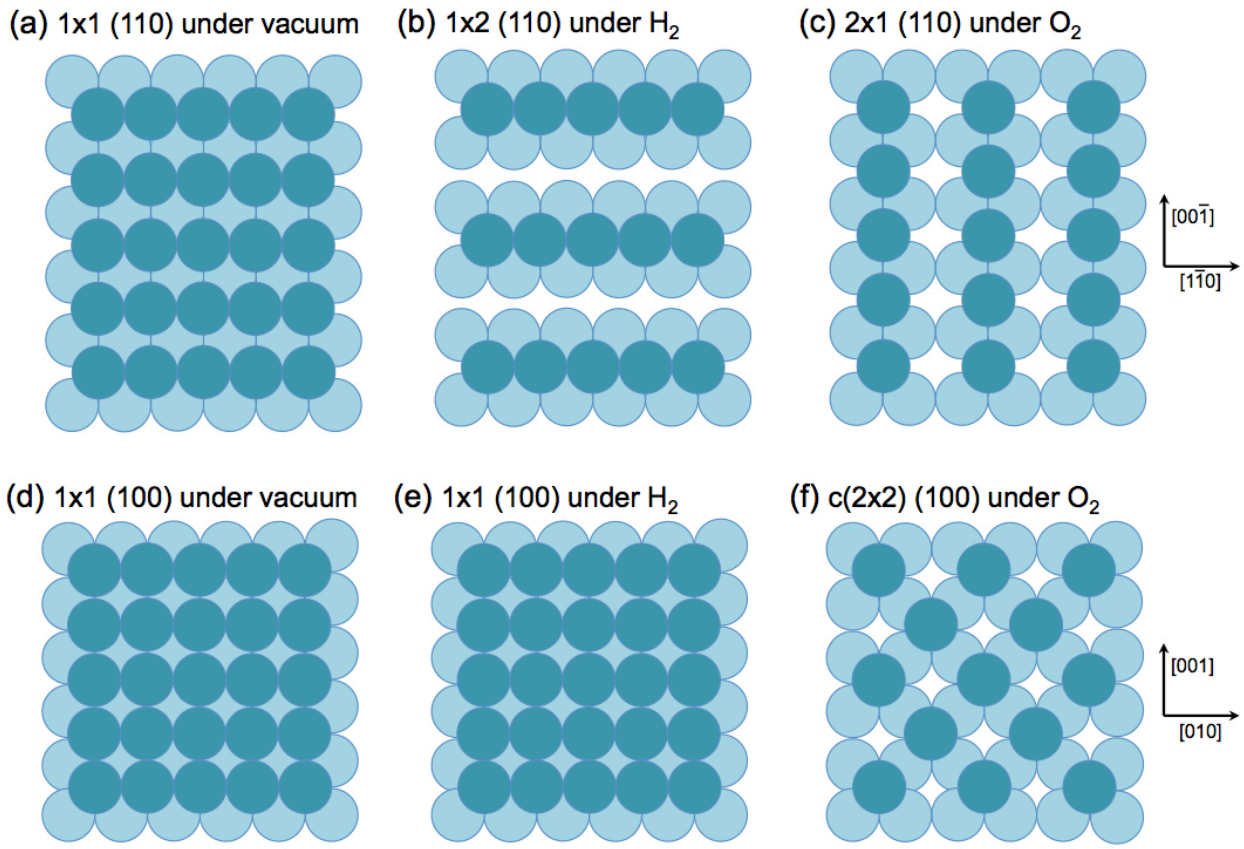

Figure 3-5. Surface structures of (a)-(c) Ni(110) and (d)-(f) Ni(100) under different annealing conditions. The darker spheres are the atoms on the top layer and the lighter spheres are the atoms underneath the top layer. Details of the annealing conditions are provided in Table 3-1.

O_2 causes a c(2x2) reconstruction of the Ni(100) surface, while H_2 does not cause a reconstruction. Interestingly the in-plane axes of the c(2x2) surface net are rotated by 45° compared to the surface net of the unreconstructed surface (Figures 3-5(e) and (f)). This correlates with the change in the relative retraction rates in the <110> and <100> directions (Figure 3-1) and changes in the in-plane orientation of growing square holes (insets in Figure 3-1). However, because the reconstruction remains 4-fold symmetric, the surface diffusivity should remain isotropic. Therefore, correlation of the changes in the orientations of the surface nets and changes in the retraction rate anisotropy cannot be explained simply in terms of relative changes in surface diffusivities.

Even though the observed change in the surface structure does not result in changes in the isotropy of the surface diffusivity, it can still contribute to changes in the relative edge retraction kinetics. As edges retract and rims form, the thickness of the rim increases in dewetting experiments with single crystal Ni [21-23] and silicon-on-insulator [25-27] films. It has been observed that during edge retraction in single crystal silicon films, growth of the rim height and advancing of the rim occurs through formation of ledges on the side of the top facet adjacent to the triple line and propagation of the ledges toward the leading edge of the rim. This has been observed in experiments [29, 31, 32, 88] and modeling simulations [28, 29, 32, 38, 89, 90]. It is reasonable to expect that this mechanism operates for Ni as well. This requires transport not only across the terrace but also over the edge of a terrace to the adjacent terrace.

Figure 3-6 illustrates possible differences in the paths for transport of adatoms over ledges with different in-plane orientations for terraces with the two different observed surface structures. The arrows in Figure 3-6 indicate the shortest diffusion paths. It can be seen that for a given reconstruction the nature of the shortest path is identical for the ledges with different in-plane orientations (compare Figures 3-6(a) and (c), and (b) and (d)). However, the nearest neighbor environment of the diffusing atoms changes for different ledge orientations. Therefore, it might be expected that the energy that drives diffusion over the ledge changes and that this changes the rate of ledge propagation.

In addition to changes in the energies that drive adatom motion over ledges, changes in the Schwoebel barrier [91] to diffusion over the edge may also occur. It has been found in other systems that the Schwoebel barrier for an atom diffusing on a (100) surface over ledges with different in-plane orientations can change due to surface reconstructions on Si(100) [92, 93] and GaAs(100) [94] surfaces. It seems likely that changes in the surface structure of Ni(100) can also lead to changes in the Schwoebel barrier for the ledges associated with kinetically stable edges with different orientations, leading to changes in the relative retraction rates.

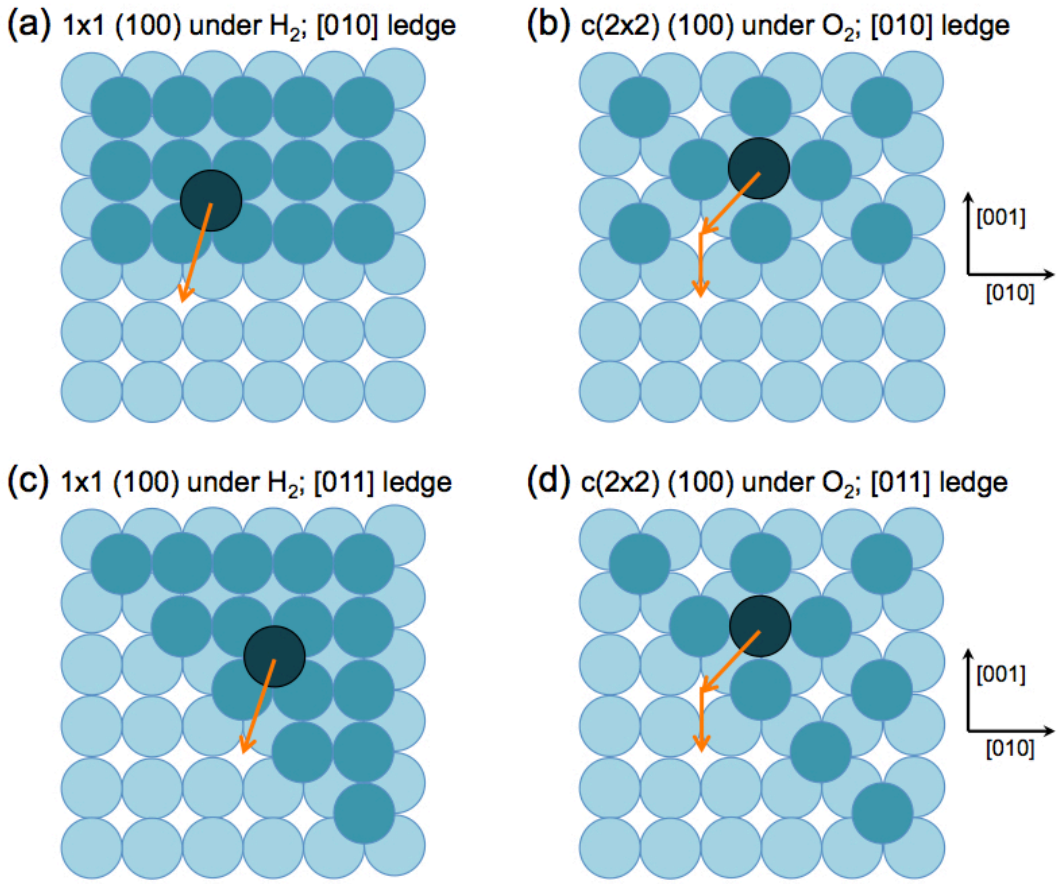

Figure 3-6. An illustration of ledges propagating in different directions for Ni(100) surfaces with different terrace/facet reconstructions. The single darkest sphere indicates an atom diffusing from the uppermost terrace to the adjacent terrace. The second darkest layer of spheres is the uppermost layer of atoms, and the lightest spheres form the layer underneath that layer, as well as the surface atoms of the adjacent terrace. Orange arrows indicate the shortest paths for diffusion of atoms over the ledges.

In addition, although the top facet diffusion affects the retraction kinetics most, other facets comprising the retracting rim are also responsible for the changes in the retraction kinetics. As shown in Figure 3-7, many of the facets comprising the rim are not 4-fold symmetric, allowing anisotropic diffusivity. For instance, both the [010] and [011] retractions in Ni(100) have {110} facets as part of the rim. It has been already discussed that, at 2310sccm of 5% H_2 + 95% N_2, channels form along the $[0\bar{1}1]$ direction on a $(0\bar{1}\bar{1})$ facet. This creates impediments to diffusion around the rim in the [011] retraction, while the channels make the diffusion around the

rim in the [010] retraction easier. On the other hand, at 95sccm, channels form along the [001] directions on the $(1\bar{1}0)$ facet. This creates impediments to diffusion around the rim in the [010] retraction, while the channels make the diffusion around the rim in the [011] retraction easier.

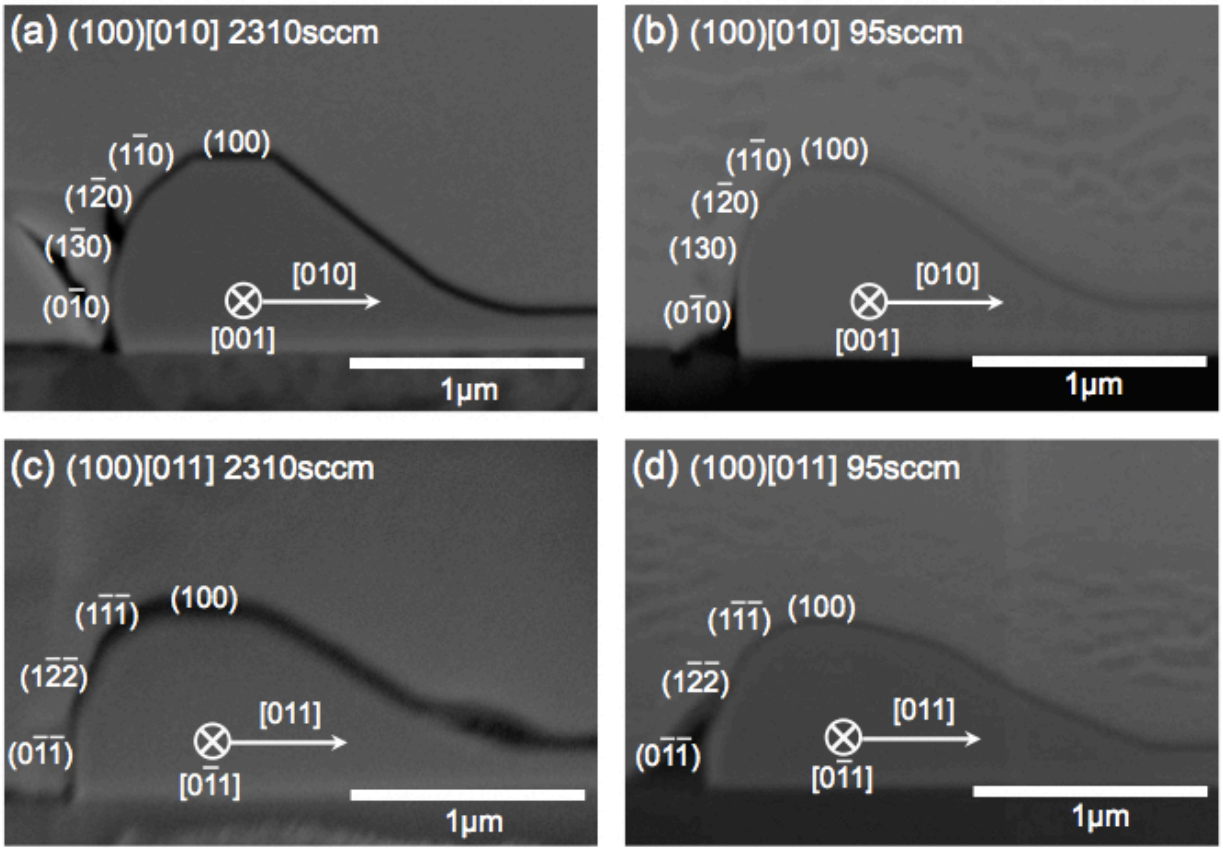

Figure 3-7. (a) and (c) Cross-sectional SEM images of retracting rims of kinetically stable edges for Ni(100) films annealed under reducing gas (5% H_2 + 95% N_2) flowing at 2310sccm. (b) and (d) Cross-sectional SEM images of retracting rims of kinetically stable edges for Ni(100) films annealed under reducing gas (5% H_2 + 95% N_2) flowing at 95sccm. The images were obtained after a 50-hour anneal. The macroscopic retraction direction of the kinetically stable edge and the direction normal to the cross-sectional plane (and parallel to the length of the edge) are also indicated in the individual figures.

3.5. Summary and Conclusion

Retraction distances versus annealing times, as a measure of the rate of edge retraction, were measured for kinetically stable edges in single crystal Ni(110) and Ni(100) films as a function of the composition and flow rate of gases in the annealing ambient. It was found that the edge retraction kinetics is strongly dependent on the flow rates of reducing gases, which change the relative partial pressures of oxygen and hydrogen in the furnace. The surface structures of Ni(110) and Ni(100) were characterized under ultrahigh vacuum conditions with and without the presence of low partial pressures of oxygen or hydrogen covering, and it was found that oxygen and hydrogen induce different reconstructions of the Ni surfaces. These changes in the surface structure were found to correlate with the observed changes in the relative retraction rates of the kinetically stable edges.

The surface reconstructions of Ni(110) films lead to channels that are rotated by 90^o in the presence of O_2 compared to in the presence of H_2, from a <001> to a <110>. It is expected that this will lead to corresponding changes in the direction for fastest surface diffusion, and that this causes the observed change in the relative rates of edge retraction in the [001] and $[1\bar{1}0]$ directions. This change in relative retraction rates, in turn, leads to the observed change of the in-plane orientations of growing rectangular holes under 5% H_2 + 95% N_2 reducing gas at high flow rates (for which O_2 is present at very low pressures and H_2 is present at high partial pressures) and under low flow rates (for which O_2 was found to be present at relatively high partial pressures).

The presence of O_2 was found to cause a c(2x2) reconstruction of Ni(100) surfaces, while no reconstruction was observed in the presence of H_2. The axes of the square surface nets were found to be rotated by 45^o in the two cases. This correlates with relative changes in the rate of edge retraction in <010> and <011> directions and the resulting 45^o in-plane rotation of growing square holes under different reducing gas flow rates. However, since four-fold symmetry is retained, so that surface diffusivity isotropy is retained, the observed correlation of the changes

in surface structure with changes in the relative rates of edge retraction cannot be explained by changes in the anisotropy of surface diffusion. It was argued that the surface reconstruction observed in the presence of O_2 leads to differences in the rate of ledge propagation on the top facets of rims on edges with different in-plane orientations, and that these differences cause changes in the relative edge retraction rates. Changes in the anisotropy of diffusion on other facets on the rims may also contribute to changes in relative retraction rates.

It was shown that changes in relative edge retraction rates observed under different annealing ambient conditions are correlated with changes in surface reconstructions. Changes in relative retraction rates significantly affect the course of the overall solid-state dewetting process, and affect the shapes and orientations of the complex patterns that result from partial dewetting. This chapter therefore provides an improved fundamental understanding of the ways in which changes in annealing ambient conditions can be used to control the patterns that are reproducibly formed through templated solid-state dewetting.

Chapter 4. Pinch-off and Mass Shedding

4.1. Introduction

As discussed in Chapter 1, when edges retract via capillarity-driven mass transport in single crystal films in the solid state, they expose the in-plane facets with locally minimum retraction rates. When the edges are originally aligned along such facets, they will remain straight, or stable, throughout retraction. These edges are called kinetically stable edges, and have been explored in Chapter 1 in detail. Natural holes in single crystal films are bound by the kinetically stable edges.

As discussed in Chapter 1, in dewetting simulations for films with isotropic surface energies and diffusivities or with anisotropic surface energies and isotropic diffusivities, it has been observed [15, 17, 18] that in the later stage of edge retraction, valleys form ahead of the retracting rims at the edge. When the depth of the valleys becomes large enough to reach the film-substrate interface, the retracting rim is separated from the remainder of the film and the newly developed edge again begins to retract, leaving a long wire behind. This phenomenon is referred to as mass shedding or pinch-off. To model edge retraction and pinch-off in films with anisotropic surface energies and surface diffusivities, the method of crystalline formulation has been used [13, 23-26], where the retracting rim is assumed to be only and completely bound by predetermined facets. However, even though pinch-off was observed in the simulation, no valley formation has been observed in such models unless faceted valleys are initially introduced. In this method, pinch-off occurred by the thinning of the bulk film due to mass transport from the bulk film towards the retracting rims.

Pinch-off of films by mass shedding during dewetting is difficult to observe experimentally, because random formation of natural holes often expose the substrate surface before pinch-off occurs. Dewetting in single crystal films significantly decreases such a problem, and the pinch-off phenomenon has recently been observed in solid-state dewetting of silicon-on-insulator films [18] and single crystal Ni films on single crystal MgO substrates [21].

Because single crystal films have anisotropic energies and diffusivities, it is expected that the pinch-off phenomenon will also be anisotropic and thus a more quantitative understanding of the phenomenon is crucial. Furthermore, a quantitative understanding of the pinch-off phenomenon by mass shedding can offer another controllable way to use solid-state dewetting to generate long ordered wires, as previously discussed in Chapter 1.

This chapter studies pinch-off of single crystal films during solid-state dewetting under different annealing ambient, using single crystal Ni films on single crystal MgO substrates as a model system. Ni(110) films were used in the experiments, as these films are known to show pinch-off via valley formation. A simple model was constructed to analyze valley formation and pinch-off. The critical pinch-off width, defined as the smallest patterned patch width that leads to pinch-off, was found to scale with the additional surface energy cost of microfaceted valley formation from the flat film.

4.2. Experimental Procedures

To more systematically study this phenomenon, arrays of 500μm-long single crystal Ni patches of varying widths aligned in the kinetically stable orientations were patterned, as illustrated in Figure 4-1. These kinetically stable orientations, which are $[1\bar{1}0]$ and [001] in Ni(110) films, can be analyzed with the 2-dimensional equilibrium shapes, as the rims at the edges retracting in these orientations are known to only have facets extending along the entire length of the edges [23].

130nm-thick single crystal Ni(110) films (The actual film thickness was measured by AFM imaging after deposition) were deposited on polished single crystal MgO(110) substrates (purchased from MTI Corporation) by electron beam deposition, after which the films were patterned by photolithography. Details of the film deposition and patterning can be found in Chapter 2. To prevent oxidation, annealing of the patterned films was conducted in a tube

furnace at 890°C in a reducing gas condition (5% H_2 and 95% N_2) with flow rates of 2310sccm, 590sccm, and 95sccm. Quantitative measurements were made using an FEI/Philips XL30 FEG ESEM with a water vapor pressure of 0.9torr to reduce charging of MgO substrates. AFM imaging of the patterned films was also conducted in between the annealing steps using the tapping mode in a Veeco Nanoscope IV AFM. To obtain cross-sections of equilibrated Ni particles, focused ion beam milling and scanning electron microscopy was carried out in a Helios Dual Beam Workstation. To prevent charging, samples were coated with 40nm-thick carbon films for use in the Helios Workstation.

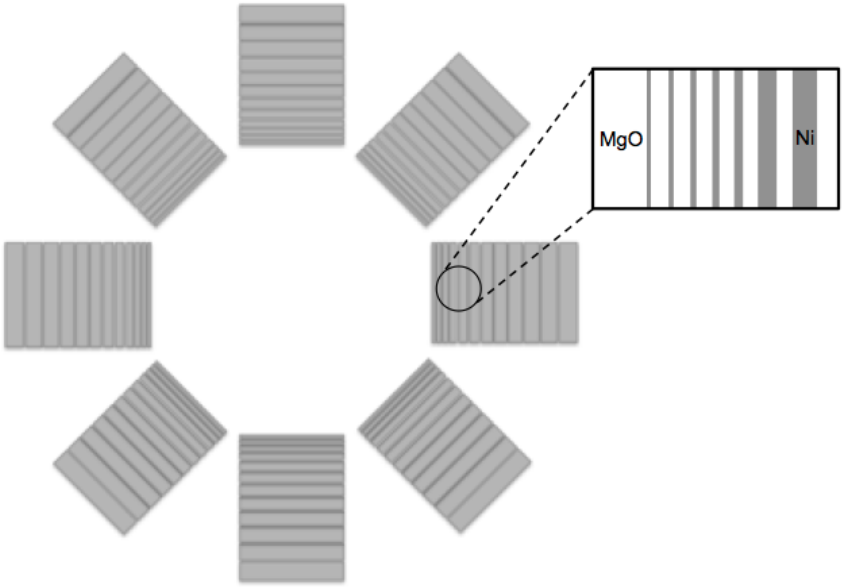

Figure 4-1. Schematic diagram of the experimental pattern. A row of long patches ranging 2-30μm in width (1μm increment) and 500μm in length is patterned in the [001] and [$1\bar{1}0$] directions in Ni(110) films.

4.3. Results

In the later stage of capillarity-driven edge retraction, formation of valleys ahead of the retracting rims is observed in Ni(110) films as shown in Figure 4-2. When the depth of such valleys becomes large enough to reach the film-substrate interface and pinch off the film, the

retracting rim is separated from the remainder of the film and the newly developed edge again begins to retract. Some terminologies for future discussion are also defined in Figure 4-2.

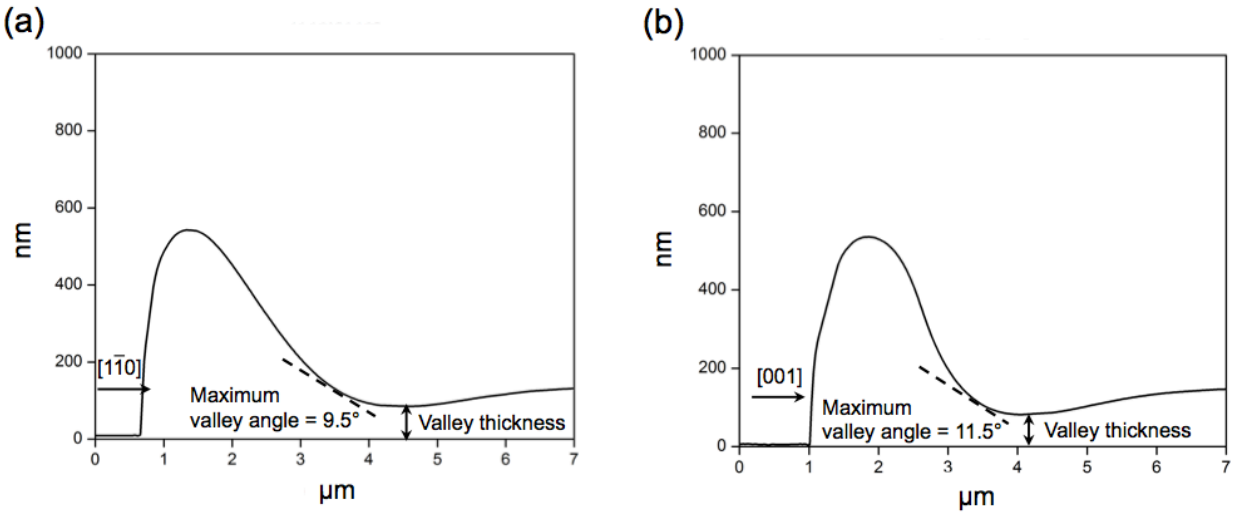

Figure 4-2. AFM images of retracting rims after a 10-hour anneal at 890°C under 2310sccm of reducing gas. All rims retract from the left to the right. (a) Rim retracting in the [1$\bar{1}$0] in Ni(110). (b) Rim retracting in the [001] in Ni(110).

Critical pinch-off widths, which were determined to be the smallest initial width of the patterns retracting in each kinetically stable orientation at which the entire 500μm-long patch pinched off to form two wires, were measured. Although some wider patches in Ni(110) resulted in the formation of 3 wires, as shown in Figure 4-3, the critical pinch-off widths for 3-wire formation were not measured for analysis as these wires were less well-defined and not all kinetically stable patches in different reducing gas flow rates resulted in the 3-wire formation. Experimentally measured critical pinch-off widths in different crystallographic orientations are summarized in Table 4-1. Significant differences in the critical pinch-off widths were measured for different patch orientations and for different annealing ambient conditions.

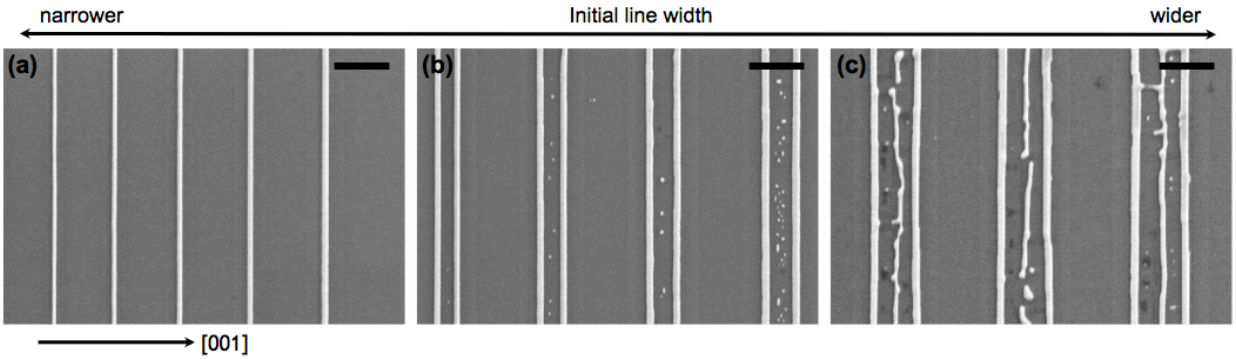

Figure 4-3. Retraction and pinch-off of patterned patches of varying widths in Ni(110) after a 28-hour anneal at 890°C under 2310sccm of reducing gas. Scale bars indicate 10μm. The crystallographic orientation of edge retraction is indicated in the figure.

Table 4-1. Critical pinch-off widths for 2-wire formation in the patterned Ni(110) films annealed at 890°C under different flow rates of reducing gas. All measurements are in units of μm. The actual thickness of the film was 130nm.

Film	Ni(110)	
Edge normal	$[1\bar{1}0]$	[001]
2310sccm	16.5	9.19
590sccm	21.3	11.9
95sccm	22.4	20.0

Also, the retraction distance over time and the smallest film thickness in the valley (valley thickness as defined in Figure 4-2) of the kinetically stable patches were measured and summarized in Figure 4-4. It can be seen that as edges retract, valleys form ahead of the retracting edges and these valleys deepen (decreasing valley thickness) over time until pinch-off. Wong et al.[15] used the finite-difference method to model pinch-off during edge retraction of a film with isotropic surface energy and diffusivity. They found that, in the isotropic system, the critical pinch-off width is the same regardless of the energy and diffusivity values, given the same initial film thickness. This means that there is a scaling relationship between the rates of

edge retraction and valley deepening in the isotropic system. However, as shown in Figure 4-4, patches retracting in the [$1\bar{1}0$] have a higher rate of edge retraction but a lower rate of valley deepening than patches retracting in the [001]. This indicates that no such scaling relationship exists between the rates of edge retraction and valley deepening in the Ni(110) system, in which surface energy and surface diffusivity are not isotropic.

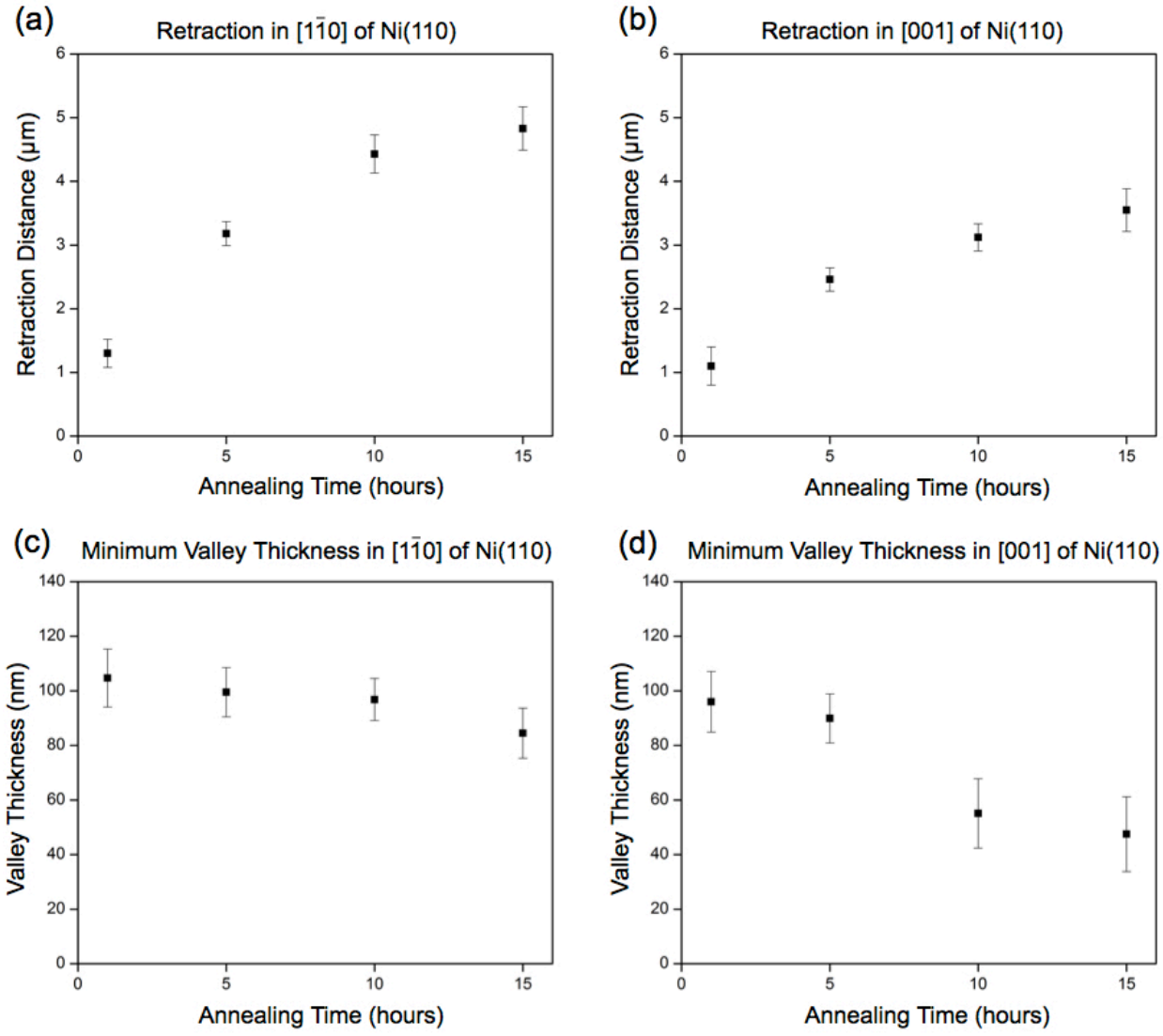

Figure 4-4. (a)-(b) Edge retraction distance over time in Ni(110) patches annealed at 890°C under 2310sccm of reducing gas. (c)-(d) Minimum Ni(110) film thickness at the valleys after annealing at 890°C under 2310sccm of reducing gas. The retraction orientations are provided in the plots. Measurements were made with the patches of 30μm in initial width and 500μm in initial length.

4.4. Discussion

As the edges of the patches in Ni(110) retract, two deepening valleys form ahead of the two retracting rims. If none of the valleys contact the film-substrate interface before the rims completely merge, no pinch-off occurs and only one wire is formed. If the valleys contact the film-substrate interface after the valleys merge to form only one valley, pinch-off leads to the formation of two wires (Figures 4-5(a) through 4-5(d)). If the patch is even wider and the individual valleys reach the film-substrate interface before the valleys merge, three wires are formed, as illustrated in Figures 4-5(e) through 4-5(h). If the inner patch, which is left for further retraction after two retracting rims pinched off, is wide enough to have another pinch-off, it is possible to form four wires, and this process can continue to form multiple wires.

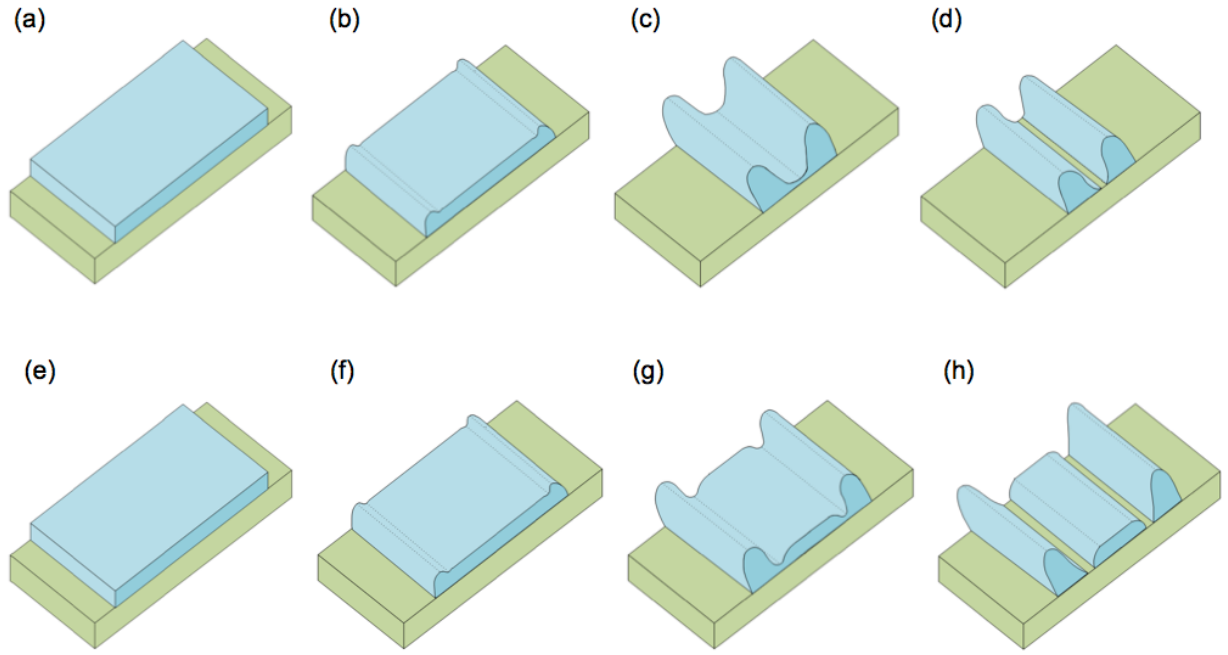

Figure 4-5. (a)-(d) Schematic representation of a 2-wire formation via pinch-off. Two deepening valleys ahead of the retracting rims merge before pinch-off. (e)-(h) Schematic representation of a 3-wire formation via pinch-off. Two deepening valleys separately pinch off the retracting rims.

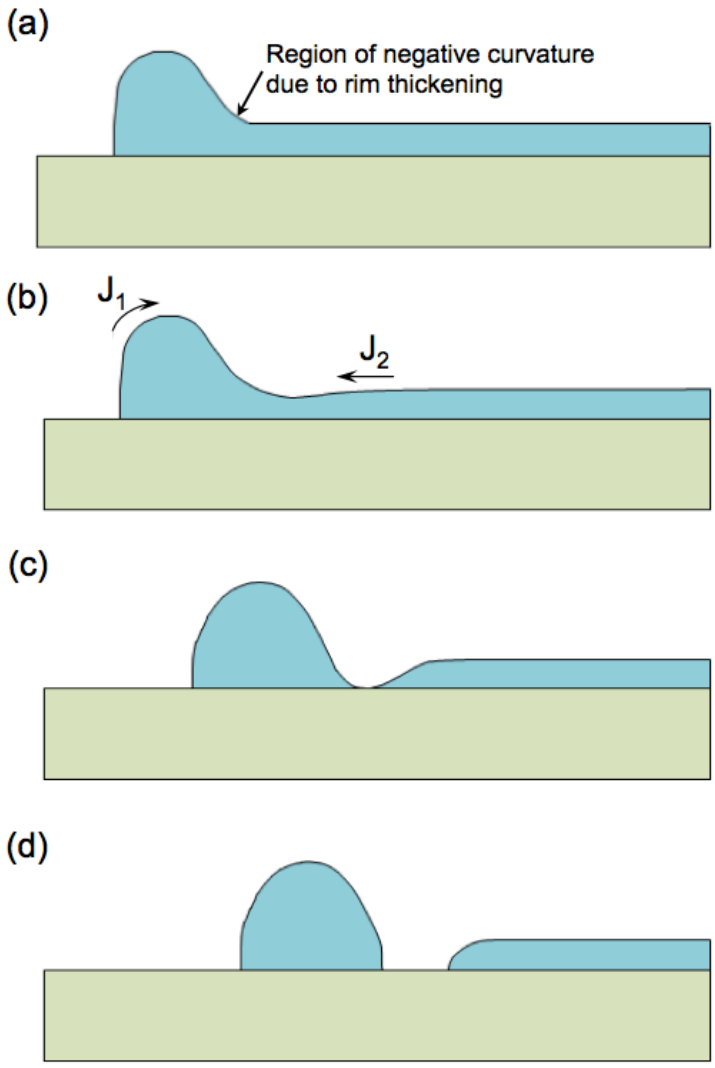

Figure 4-6. Schematic diagram of valley deepening and pinch-off.

Development of deepening valleys ahead of retracting edges may seem somewhat counterintuitive at first glance, because capillarity-driven material transport down the local curvature gradient should fill such valleys. This phenomenon can be understood by considering that the dominant mechanism of capillarity-driven mass transport is surface self-diffusion and that there are two different mass fluxes flowing into the valley. As illustrated in Figure 4-6, as the edge retracts and the rim thickens by the local accumulation of mass, a region of negative curvature locally develops ahead of the thickening rim. Along with the mass flux J_1 that is

responsible for the edge retraction, there is another mass flux J_2 due to the local curvature gradient from the flat film to the region of negative local curvature. The presence of this flux J_2 has also been identified elsewhere [26]. Because the dominant mechanism for mass transport is surface self-diffusion, only the material in the flat region close to the rim can be transported to the region of negative local curvature, due to a finite diffusion distance. Because the thickness of the film decreases away from the thickening rim, this material transport now generates another, but deeper, valley, and this will thus have a larger negative local curvature, which will subsequently increase the driving force for material flow from the flat film region close to the valley towards the valley. As this process continues, the depth of the valley will increase until some steady-state value is reached, and if the valley reaches the film-substrate interface during the process, pinch-off occurs.

It should be noted that the surface area of the system increases due to valley formation. Thus, unless the energy of the facets exposed during valley formation is significantly lower than the energy of the facet comprising the flat film, there is going to be a surface energy cost associated with the valley formation and subsequent pinch-off. In addition, comparing the critical pinch-off widths in Ni(110) films as shown in Table 4-1, there is clear anisotropy in the pinch-off behavior. To analyze this anisotropic pinch-off behavior, a simple model was developed that relates the surface energy cost associated with valley formation to critical pinch-off width.

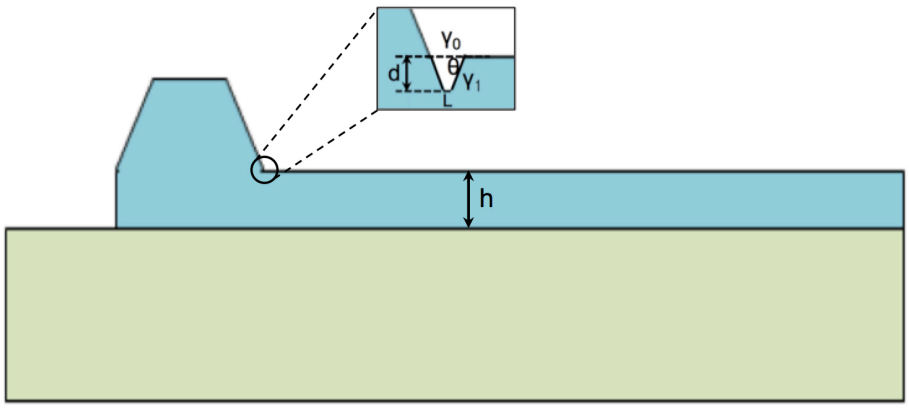

Figure 4-7. A schematic diagram of a simplified retracting rim and microfaceted valley formation for the purpose of modeling.

Zucker et al. [26] conducted a fully faceted crystalline formulation method simulation as discussed in detail in Chapter 1. In their simulation, they observed that valley formation and pinch-off occurs in a system of strong surface energy and surface diffusivity anisotropy only when microfaceted valleys are introduced in the system. As the single crystal Ni system also has strong surface energy and surface diffusivity anisotropy, it is reasonable to expect that valley formation initiates from microfaceted valleys, because the macroscopic plane of the as-deposited film is parallel to a stable equilibrium facet, as illustrated in Figure 4-8. Microfacets should still form in a way that minimizes the additional surface energy cost, and this can be done when such microfacets are composed of equilibrium facets. As illustrated in Figure 4-7, the geometry of the microfaceted valley is assumed to be completely faceted. More specifically, the valley is assumed to be bound only by the adjacent side facet in the equilibrium shape that is cross-sectioned in the direction parallel to the edge retraction direction. The adjacent side facet, which is defined as the equilibrium facet adjacent to the top facet in the equilibrium shape, is illustrated in Figure 4-8. As illustrated in Figure 4-2, the maximum valley angle, defined as the largest angle of the tangent drawn on the AFM profile of the valley, stays only at around 10° and this does not increase significantly until pinch-off. Therefore, the most important facet of interest is the side facet adjacent to the top facet, not the other facets with higher facet angles, as illustrated in Figure 4-8.

Using the simplified geometry, the additional surface energy cost associated with microfaceted valley formation can be calculated, by calculating the energy before and after valley formation:

$$Energy\ before\ valley\ formation = \frac{2\gamma_0 d}{\tan\theta} + \gamma_0 L \tag{4-1}$$

and

$$Energy\ after\ valley\ formation = \frac{2\gamma_1 d}{\sin\theta} + \gamma_0 L. \tag{4-2}$$

where d is the valley depth, γ_0 is the top facet surface energy, γ_1 is the side facet surface energy, and θ is the angle between the top facet and the side facet. L is the length of the finite facet connecting the two side facets for energetic consistency. The magnitude of L does not affect the calculation as the quantity of interest is the difference between Equations (4-1) and (4-2). Then, the additional energy cost associated with microfaceted valley formation is, after normalization by the valley depth (because the valley depth will be infinitesimally small) and the top facet surface energy (because the absolute value of the top facet surface energy cannot be obtained):

$$Normalized\ energy\ cost = \frac{1}{\gamma_0 d}\left(\frac{2\gamma_1 d}{\sin\theta} - \frac{2\gamma_0 d}{\tan\theta}\right) = \frac{2\frac{\gamma_1}{\gamma_0}}{\sin\theta} - \frac{2}{\tan\theta}. \quad (4\text{-}3)$$

Surface energies of the equilibrium facets relative to that of the top facet were measured from the cross-sections of the equilibrated Ni particles annealed at 890°C under different flow rates of reducing gas; the particles were cross-sectioned along the individual retraction orientations of the kinetically stable edges in Ni(110). A set of illustrative cross-sectional SEM images is provided in Figure 4-8. The same sets of equilibrium facets were observed in the cross-sections in the same orientation annealed under other flow rates of reducing gas. Relative surface energy measurements are also provided in Figure 4-9. As defined in Figure 4-8, facet angle refers to the angle between the top facet and the facet of interest.

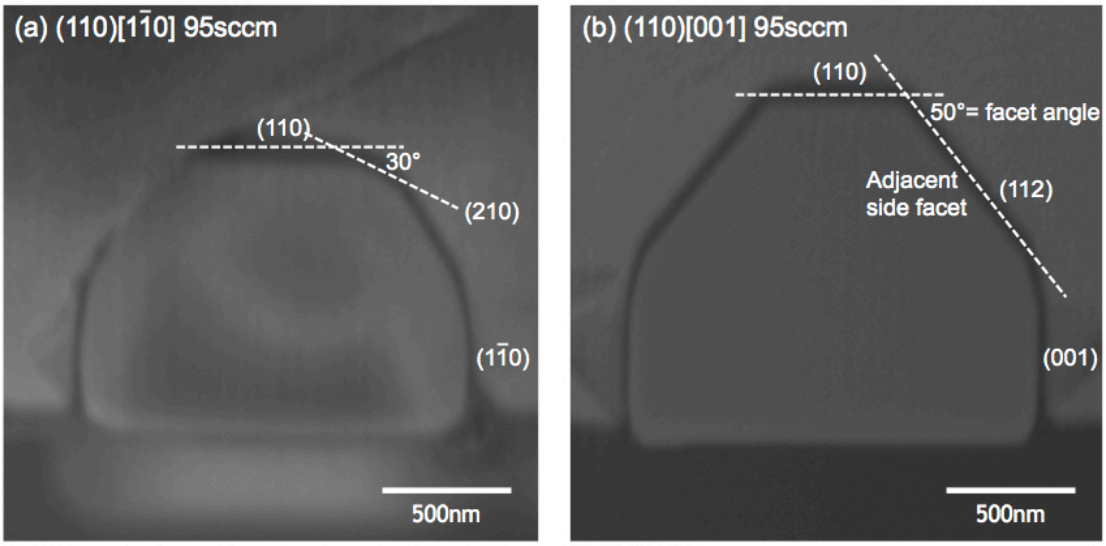

Figure 4-8. Cross-sectional SEM images of equilibrated Ni particles in Ni(110), annealed at 890°C under 95sccm of reducing gas.

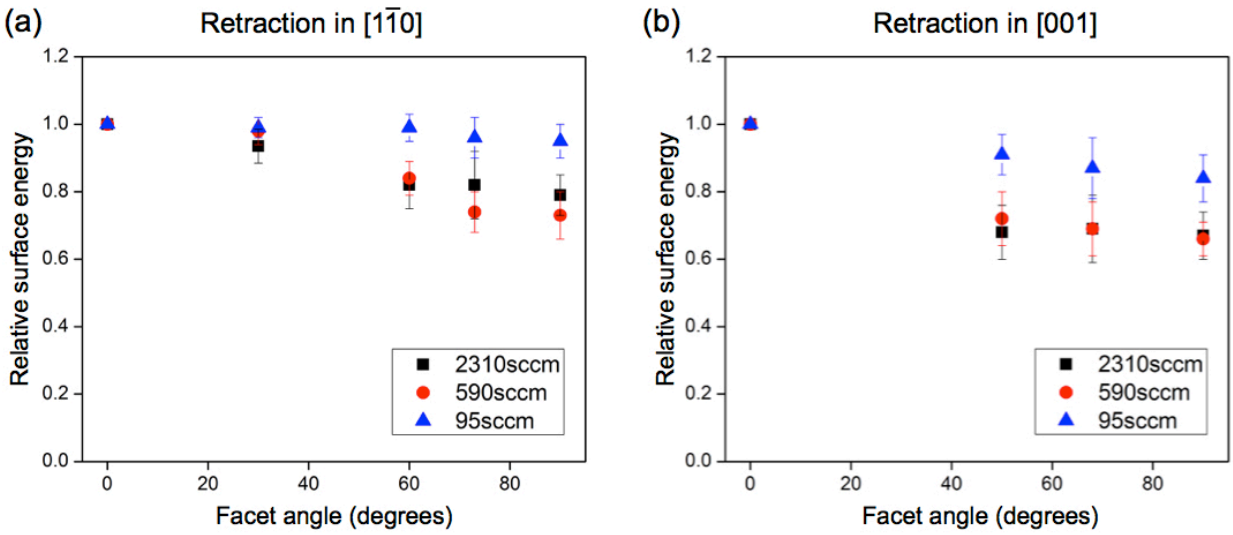

Figure 4-9. Surface energies of the equilibrium facets relative to the top facet surface energy in Ni(110). As defined in Figure 4-8, facet angle refers to the angle between the top facet and the facet of interest.

When the critical pinch-off width is plotted against the additional surface energy cost which was calculated using Equation (4-3), Figure 4-10 clearly shows a positive trend in the data.

As the additional surface energy cost associated with microfaceted valley formation increases, valley formation becomes more difficult and thus the critical pinch-off width increases. Some errors arise, however, which can be attributed to the simplified construction of the model. More specifically, the additional surface energy cost was normalized by the surface energy of the top facet, which is parallel to the macroscopic plane of the as-deposited film, because the absolute energy value could not be obtained and all measurements were made in Ni(110) films. However, this top facet surface energy may be different under different annealing ambient conditions, and this difference in the absolute value can cause errors among data points for different annealing conditions.

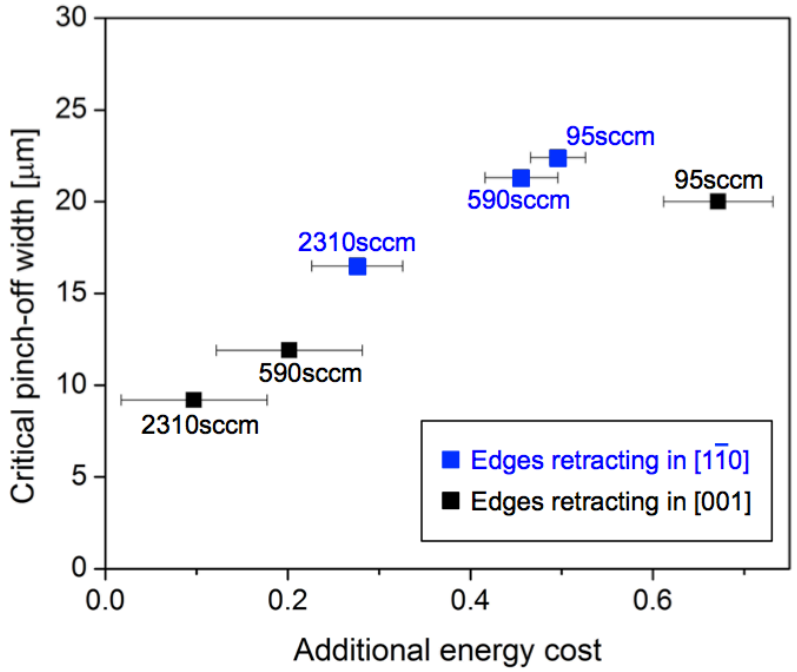

Figure 4-10. Critical pinch-off width vs. additional surface energy cost associated with microfaceted valley formation, in the kinetically stable patches in Ni(110) films. The additional surface energy cost is normalized by the valley depth and the top facet surface energy. The retraction orientation of the kinetically stable edges and the individual flow rates of the reducing gas are indicated in the figure.

4.5. Summary and Conclusion

During capillarity-driven edge retraction of pre-patterned single crystal Ni(110) patches, pinch-off of retracting rims occurs when the initial patch width is larger than the critical pinch-off width. Because single crystal Ni films have anisotropic surface diffusivities and surface energies, different critical pinch-off widths are measured in patches retracting in different crystallographic orientations. A strong dependency of the critical pinch-off width on the annealing ambient conditions was also observed.

In Ni(110) films, the formation of local valleys ahead of retracting rims is responsible for pinch-off. Because the formation of valleys involves exposure of other facets, a simple model was developed, assuming that valley formation initiates from microfaceted valleys, which are composed of the side facet adjacent to the top facet that appears in the equilibrium shape. The additional surface energy cost associated with microfaceted valley formation was calculated using the simplified geometry. A positive correlation was observed when the critical pinch-off width was plotted against the additional surface energy cost. As the additional surface energy cost associated with microfaceted valley formation becomes larger, valley formation becomes more difficult, and thus the critical pinch-off width increases.

Chapter 5. Fingering Instability

5.1. Introduction

As mentioned in Chapter 1, because of the large gradient in the local surface curvature near triple lines, or three-phase boundaries, atoms are driven to diffuse away from the triple lines toward the flat surfaces of the films. This capillary-driven atomic surface diffusion results in the retraction of triple lines and thickening of the film edges to form rims. The rims are often subsequently subject to instabilities that lead to more complex dewetting morphologies. One such instability is the fingering instability, in which portions of rims locally begin to retract faster than the adjacent regions, eventually leaving long fingers behind [14, 20, 28, 29, 31, 32, 95].

Figure 5-1 shows fingering during dewetting of rectangular patches that were lithographically patterned from a Ni(110) single crystal film grown epitaxially on a MgO(110) single crystal substrate. The patches have been annealed for 45 min. at 900^{o}C in vacuum (low 10^{-6} torr). The patches shown in Figure 5-1 are at an intermediate stage of dewetting. The originally straight edges of the patches formed rims as they retracted, and the rims and triple line developed fluctuations in their geometric characteristics, including the rim thickness. This initial instability leads to formation of strands or wires that are generally aligned along the retraction direction, and ultimately results in island formation due to a Rayleigh-like instability [14, 28, 29, 95]. Islands first form at the ends of the wires (as seen in the inset in Figure 5-1), and the spacing of these islands is related to the instability that leads to fingering. The retraction front then develops fingers with a different characteristic period. Similar phenomenology has been observed during dewetting of single crystal Si films in silicon-on-insulator (SOI) structures [20, 28, 29, 31, 32]. The origin of the initial rim instability has been discussed elsewhere [33]. Here focus will be granted on the characteristics of the fingers at the moving retraction front.

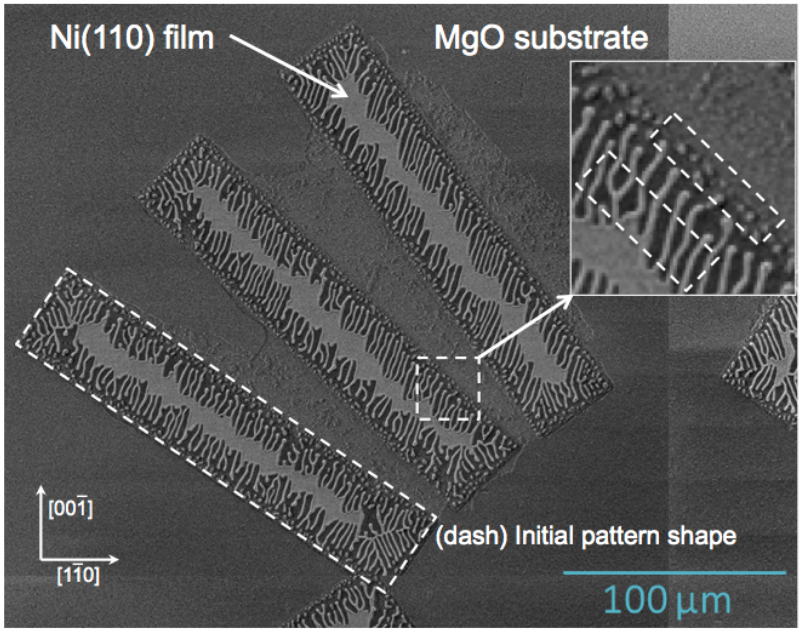

Figure 5-1. Fingering instability in a photolithographically patterned single-crystal Ni(110) film. Dashed lines in the large image indicate the initial shape of the pattern. It can be seen that the steady-state finger period is different from the wavelength of the initial edge instability (See inset). The Ni islands in the inset image are artifacts of the initial edge instability. The pattern was heated at 900°C under a vacuum level of low 10^{-6} torr.

A schematic illustration of the propagating fingers is provided in Figure 5-2, which will be used to define terminologies and quantities. The regions in which the substrate is exposed due to advancing of dewetting front will be called *fingers* and the rejected mass that separates the fingers will be referred to as a *wire*. The facetted end of a finger will be called the *tip*. The tips are characterized by *corners* at which the facetted *tip sides* meet, and the end of the tip side opposite to the corner, where the sides merge to form wires, will be called the *root*. Studies have been conducted on the fingering instability, but detailed modeling efforts have been made mostly on the early-stage edge instability. Formation of fingers during solid-state dewetting of thin films was first systematically studied by Jiran and Thompson [14, 95]. They observed that straight edges of patterned polycrystalline Au films underwent a fingering instability and that the dewetting front defined by the finger tips retracted at a constant rate. A simple analytic model for the dewetting kinetics of these dewetting fronts, based on the model of Brandon and Bradshaw [16],

was proposed based on this observation. Fingering instabilities of straight retracting edges have also been observed experimentally in silicon-on-insulator (SOI) films [20, 28, 29, 31, 32]. Due to crystallographic constraints, more regular finger morphologies are observed in single crystal films. It has been found that the average finger and wire widths reach constant values (as defined as *b* and *a* in Figure 5-2) and that the sides of the tip remain straight [20, 28, 29, 31, 32]. The sides form straight edges that have in-plane orientations for which retraction rates are locally minimum [22, 23].

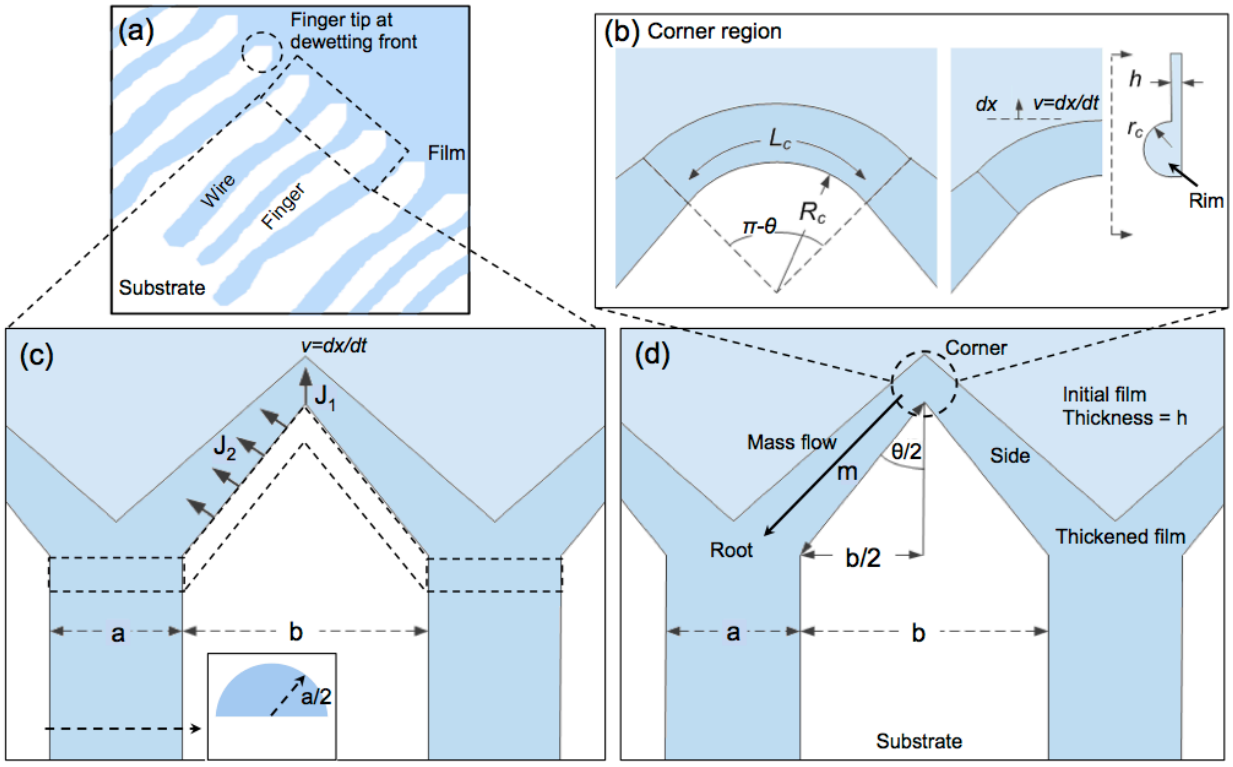

Figure 5-2. Schematic illustration of a fingering instability. Key terminologies used in the model are also defined.

Several analyses of the initial fingering instability and characteristics of the finger front have been presented. Kinetic Monte Carlo (KMC) simulations [28, 34] have been developed for dewetting of thin-film structures and finger morphologies that are similar to those observed in experiments were observed. In the simulations, as in experiments [1, 2, 4], the velocity of the finger

front was observed to evolve toward a constant value, implying a steady state constant shape of the tip corner. A numerical linear stability analysis was also developed and used to establish conditions under which rims are unstable and will develop fingered fronts [34, 35]. This analysis can also be used to estimate the initial period of islands resulting from the fingering instability. Müller and collaborators characterized the geometry of retracting finger fronts in SOI films, and developed a model relating the effective activation energy for front motion to these geometric characteristics [29]. They measured the steady-state finger period under different conditions and reported that the period was dependent on the steady-state tip retraction rate, initial film thickness, and annealing temperature.

Although models for the early-stage fingering instability exist as described above, no models exist for the steady-state finger morphology other than kinetic analyses of the fingering front (tip). In this chapter, an analytical model that describes the morphological characteristics of the steady-state fingering front in thin single crystal films as a function of film thickness and surface diffusivity is proposed. Expressions were developed for the period of the fingers and the tip retraction rate in the steady state. Furthermore, it was shown that the functional dependencies of the model on the key variables are consistent with experimental results reported elsewhere [29].

* This work was completed in collaboration with Solmaz Jahangir in the Valanoor Group at University of New South Wales Department of Materials Science and Engineering. Part of this work has been submitted to Acta Materialia [30].

5.2. Fingering Instability Model

Three important experimental observations are taken into account in the model: 1. There is a constant steady-state tip retraction rate [14, 95]; 2. The dewetting front (tip) has a constant shape in the steady state, with straight sides that correspond to kinetically stable facets [20, 28, 29, 31, 32]; 3.

The mass rejected during tip retraction diffuses along the side and accumulates at the root, making the existing fingers and wires longer [31]. In addition, the following geometric assumptions are made: 1. The corner of the tip is assumed to be round and characterized by a fixed in-plane radius of curvature; 2. The cross-sections of the rim at the corner and the wire are semicircular with substrate contact angles of 90^{o}; and 3. Surface diffusivities are isotropic along the circumference of the cross-sections of the rims in specific in-plane orientations. These assumptions are made to simplify the geometry and use the Brandon-Bradshaw model [16] to calculate the atomic flux at the corner. Note that this does not impose isotropic surface energy and surface diffusivity conditions for different in-plane orientations.

Because the mass rejected during the retraction of the dewetting front (tip) accumulates at the root to form wires [31], a volume conservation condition can be imposed. The rate at which the volume of the film that is consumed due to retraction of the tip must be to equal the rate at which volume is added to the wire at the root:

$$\dot{V} = ahv + bhv = \frac{\pi}{2}\left(\frac{a}{2}\right)^2 v \,, \tag{5-1}$$

where a is the wire width, b is the finger width, h is the initial film thickness, and v is the steady-state tip retraction rate. The first term on the left hand side accounts for volume of the preexisting film ahead of the wire; The second term is the rate of volume rejection from the tip; The right hand side is the rate at which volume that is added to the wire. This is illustrated in Figure 5-2(c). The length of the side m is related to b by

$$m = \frac{b}{2\sin\left(\frac{\theta}{2}\right)} \quad , \tag{5-2}$$

where θ is the angle at the corner, as defined by the kinetically stable side facets. Solving for a and taking the positive solution, gives:

$$a = \frac{4h}{\pi}\left(1 + \sqrt{1 + \frac{\pi m sin\left(\frac{\theta}{2}\right)}{h}}\right) \approx \frac{4h}{\pi}\left(\frac{\pi m sin\left(\frac{\theta}{2}\right)}{h}\right)^{\frac{1}{2}}$$

$$= \frac{4h}{\pi}\left(\frac{\pi \sin\left(\frac{\theta}{2}\right)}{h}\right)^{\frac{1}{2}} m^{1/2} = C_1 m^{1/2}\,, \qquad (5\text{-}3)$$

given that $m >> h$. All variables have been previously defined. Also, from Equation (5-2),

$$b = 2\sin\left(\frac{\theta}{2}\right) m = C_2 m\,. \qquad (5\text{-}4)$$

The radius of the rim at the tip is smaller than the radius at the root. As will be discussed later, the radius at the rim drives diffusion over the rim, so in principle, the tip side should retract faster at the tip than at the root. However, since the shape of the tip is crystallographically constrained and a steady state shape is retained, most mass removed from the tip must diffuse along the side to the root. The value of m is therefore set by the diffusion distance. This can be characterized by:

$$m = \frac{D_m}{v} \qquad (5\text{-}5)$$

where D_m is the surface diffusivity along the side. Using Equations (5-3), (5-4), and (5-5):

$$\lambda = a + b = \frac{C_1 {D_m}^{1/2}}{v^{1/2}} + \frac{C_2 D_m}{v} \qquad (5\text{-}6)$$

Under typical experimental conditions reported in the literature [4, 6-9], the first term dominates.

To derive an expression for the steady-state tip retraction rate v, another expression relating a and b is needed. As mentioned previously, the tip shape remains constant in the steady state [20, 28, 29, 31, 32]. It was also found that there is a constant steady-state tip retraction rate [14, 95],

which means that there is no rim thickening in the steady state. This means the atomic flux in the direction of tip retraction should be uniform:

$$J_2 = J_1/\sin\left(\frac{\theta}{2}\right), \tag{5-7}$$

where J_1 is the atomic flux at the corner and J_2 is the flux at the side, as shown in Figure 5-2(c). Assuming a round corner and a semicircular rim with an isotropic surface energy and diffusivity as illustrated in Figure 5-2(b), an expression for J_1 can be obtained from the Brandon-Bradshaw model [16]. Assuming that the in-plane radius of curvature at the corner R_c is much larger than the radius of the semicircular rim at the corner r_c:

$$J_1 = \frac{D_1\gamma\Omega^{1/3}}{kT}\nabla\kappa = \frac{D_1\gamma\Omega^{1/3}}{kT}\frac{1}{r_c}\frac{1}{\pi r_c}, \tag{5-8}$$

where D_1 is the surface diffusivity at the corner in the direction of tip retraction, γ is the isotropic surface energy, Ω is the atomic volume, kT is the thermal energy, and κ curvature of the rim ($1/r_c$). It should be noted that D_1 is different from D_m, the surface diffusivity along the side of the tip. The retraction at the corner is determined by the combination of the diffusivities on the facets around the perimeter of the rim, while D_m is the diffusivity along specific facets that define the sides of the tip.

The number of atoms per unit time being rejected along the rim from the corner is then,

$$\dot{N}_c = J_1 L_c = J_1 R_c(\pi - \theta), \tag{5-9}$$

where L_c is the length of the triple line in the corner region and R_c is the in-plane radius of curvature of the corner. Also, the number of atoms per unit time rejected along the rim due to the motion of the side is,

$$\dot{N}_m = J_2 m = J_1 m/\sin\left(\frac{\theta}{2}\right), \tag{5-10}$$

where m is the length of the side and other variables are as previously defined. The total number of atoms per unit time rejected into the root of the wire is then,

$$\dot{N}_{tot} = \dot{N}_c + \dot{N}_m = J_1 \left[R_c(\pi - \theta) + m/\sin\left(\frac{\theta}{2}\right) \right] \approx mJ_1/\sin\left(\frac{\theta}{2}\right), \tag{5-11}$$

as all of the rejected atoms diffuse along the rim of the side to be accumulated at the root [31]. These atoms are responsible for the incremental extension of the wire by a unit distance *dx* in unit time *dt*. At the root, the number of atoms accumulated per unit time to cause an incremental extension of the wire is

$$\dot{N}_f = \Omega^{-1} \frac{1}{2} \pi \left(\frac{a}{2}\right)^2 \frac{dx}{dt} - \Omega^{-1} ha \frac{dx}{dt} = \Omega^{-1} \left(\frac{\pi a^2}{8} - ha\right) v \approx \left(\frac{\pi}{\Omega 8}\right) a^2 v \,. \tag{5-12}$$

All variables are as previously defined. The second term on the left hand side of Equation (5-12) subtracts the initial number of atoms in the wire due to the preexisting film (divided by *dt*). As *a* >> *h*, the second term, however, is small relative to the first term, the rate at which atoms arrive from the tip. As volume must be conserved, $\dot{N}_f$ and $\dot{N}_{tot}$ must be equal. Solving for *a* by equating Equations (5-11) and (5-12) and substituting *m* using Equation (5-2) gives

$$a^2 = \frac{4J_1\Omega}{\pi \sin^2(\theta/2)} \frac{b}{v}, \tag{5-13}$$

where all variables have been defined previously. Using Equations (5-2) and (5-3),

$$a \approx \frac{4h}{\pi} \left(\frac{\pi \sin\left(\frac{\theta}{2}\right)}{h} \right)^{\frac{1}{2}} m^{\frac{1}{2}} = \frac{4h}{\pi} \left(\frac{\pi \sin\left(\frac{\theta}{2}\right)}{h} \right)^{\frac{1}{2}} \left(\frac{b}{2 \sin\left(\frac{\theta}{2}\right)} \right)^{\frac{1}{2}} = \left(\frac{8h}{\pi}\right)^{\frac{1}{2}} b^{\frac{1}{2}}, \tag{5-14}$$

where all variables are have been previously defined. Equations (5-13) and (5-14) have the same functional form in terms of *a* and *b*. Equating the constants in Equation (5-13) to the square of the constants in Equation (5-14) and solving for *v* using Equation (5-8) gives

$$v = \frac{D_1 \gamma \Omega^{4/3}}{kT} \frac{1}{2\pi r_c^2 h \sin^2(\theta/2)} \,. \tag{5-15}$$

5.3. Discussion

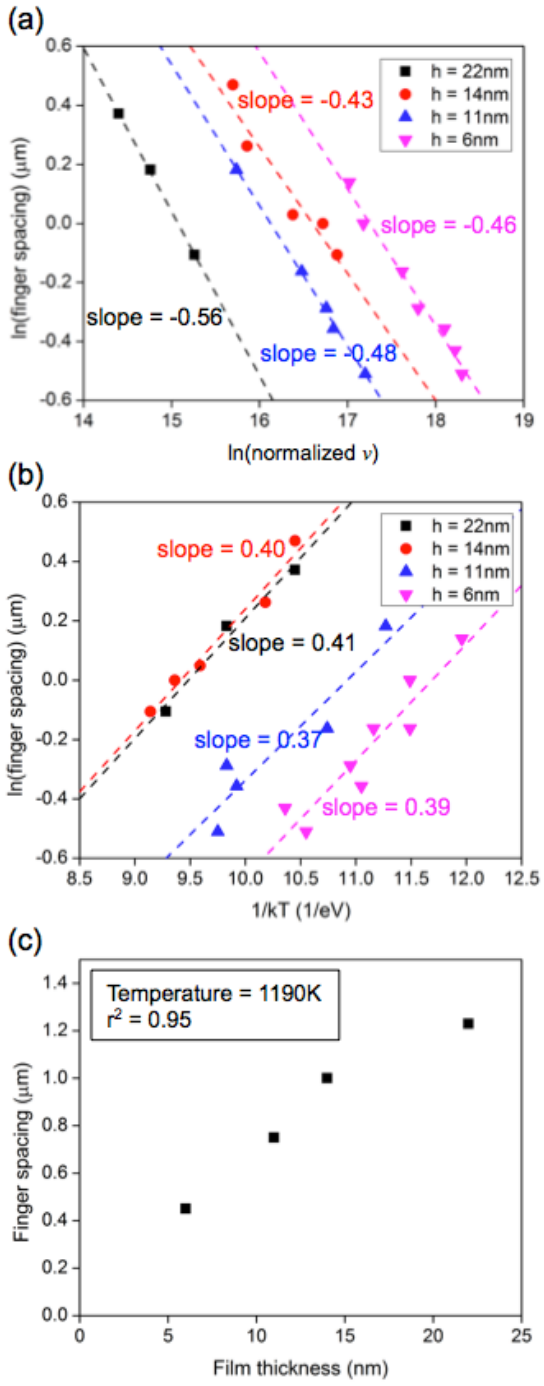

Figure 5-3. (a) Relationship between the finger period λ and the tip retraction rate v. v was normalized by the surface diffusivity along the side D_m to remove temperature effects. (b) Relationship between the finger period λ and the thermal energy (kT). (c) Relationship between the finger period λ and the initial film thickness h. All experimental data are reproduced from Cheynis et al.[29]

Cheynis et al.[29] reported values of a and b for SOI structures under different experimental conditions. Figure 5-3 is based on their experimental results, replotted in a way that allows testing of the model presented here. It was determined in Equation (5-6) that the steady-state finger period $\lambda \sim v^{-1/2}$, under the reported experimental conditions. Figure 5-3(a) corroborates this. To remove the effect of temperature on the finger period, the tip retraction rates were normalized by D_m, whose activation energy is estimated by Cheynis et al.[29] to be 2.0±0.2 eV. Also, from Equations (5-6) and (5-15), it can be seen that there are two variables strongly dependent on temperature (D_m and D_1). It is therefore expected that the relationship between $\ln(\lambda)$ and $1/kT$ is linear. Moreover, the sign of the proportionality constant will be determined by the relative magnitude of the activation energies (E) of D_m and D_1. It has been found that the kinetically stable edges that determine the tip shape are those with local minimum retraction rates [22] and the edge retraction kinetics is dominated by diffusivity [26]. Thus, it can be expected that $E_1 > E_m$, which will lead to a positive linear proportionality constant between $\ln(\lambda)$ and $1/kT$. Figure 5-3(b) corroborates this and shows, as expected, that the value of $E_1 - E_m$ is independent of h. Additionally, from Equations (5-3), (5-6), and (5-15), it can be seen that $\lambda \sim h$. The data reported by Cheynis et al.[29] were acquired at varying annealing temperatures. To remove the effect of temperature, the finger periods for different SOI film thicknesses were analyzed using the data at or near 1190K. This is the temperature for which the most finger period data was given for films of different thickness. Figure 5-3(c) shows that a linear relationship exists between λ and h. The statistical coefficient of determination, r^2, is 0.95.

5.4. Summary and Conclusion

In summary, an analytical model was developed for the steady state geometric characteristics of the fingers that arise from a fingering instability during solid-state dewetting of thin single crystal films. It was found that the finger period is dependent on the inverse square

root of the tip retraction rate, or $\lambda \sim v^{-1/2}$, under reported experimental conditions [4, 6-9]. An expression for the steady-state tip retraction rate *v* was also derived and it was determined that the finger period is linearly dependent on the initial film thickness, or $\lambda \sim h$. The key functional dependencies of the model have been tested with the experimental data reported by Cheynis et al. [29] and good agreement between the model and the experimental data was found.

Chapter 6. Corner Instability

6.1. Introduction

As mentioned in Chapter 1, unlike polycrystalline films, for which hole morphologies are complex [14, 16], single crystal films such as Ni [21, 22, 37] and Si [19, 28, 29] are known to initially form polygonal holes with morphologies defined by edges with locally minimum retraction rates. After the initial stages of growth, the corners on the polygonal holes are observed to retract faster than the centers of the straight edges. This is typically referred to as the "corner instability," and leads to dendritic or star-shaped holes [18, 20, 21, 27, 28, 61]. Kinetic Monte Carlo simulations of dewetting in single-crystal structures also exhibit corner instabilities [27, 38].

It has been observed that the retraction rate at corners reaches a constant value, while the retraction rate of the straight edges decreases over time [28]. This occurs because the rim at the tip of the retracting corners reaches a fixed height, while the rims along the straight edges thicken with time in a similar fashion to a retracting infinite, straight edge [28]. The corner instability is fundamentally related to the development of a time-independent shape of the tip of the retracting corner. However, it is not yet clear why the rim at the tip of the retracting corner reaches a constant value.

Previous work has suggested that the corner instability is associated with mass flow away from the tip of the retracting corner. Ye and Thompson [21] proposed that the corner instability arises due to mass flow away from the tip, onto the flat film. It was suggested that near the corner, there is a two-dimensional diffusion field, while along the edge, there is a one-dimensional diffusion field. The two-dimensional field implies transport to a larger area, and therefore enables faster retraction near corners. However, the film is not observed to thicken ahead of the retracting rim in experiments [61]. Also, isotropic models of dewetting show no net mass flow onto the flat film [15, 17], and anisotropic models show a small mass flow in the opposite direction, leading to thinning of the bulk film [26]. Rabkin *et al*. [61] suggested that mass rejected from corners flows along the thickening rim toward the centers of the straight edges, leading to a

constant rim size at the corner while the centers of the edges accumulate mass. However, no specific evidence of this mass flow has been presented.

In this chapter, an alternative mechanism for the corner instability is proposed based on a combination of modeling and experiments. A quantitative study of evolving hole morphologies in Ni thin films reveals specific characteristics of the time-dependent rim position, size and shape around the perimeter of the holes. A model is provided with geometric assumptions that are consistent with the observed morphology near the corners. The model and experiment are in quantitative agreement, showing that the mechanism found in the model is a plausible explanation for the corner instability.

* This work was completed in collaboration with Rachel V. Zucker in the Carter Group at MIT Department of Materials Science and Engineering. Part of this work has been submitted to Journal of Applied Physics [36].

6.2. Experimental Procedures

130nm-thick single crystal (100) Ni films were deposited on polished single crystal (100) MgO substrates (purchased from MTI Corporation) using electron beam deposition. When patterned holes were used (as in Figure 6-2(a)), the patterns were made using optical photolithography. Actual sizes (defined as the edge length) of the square hole patterns were measured after patterning. Details of the film deposition and patterning can be found in Chapter 2.

Annealing of the patterned film was carried out in a tube furnace at 890°C with reducing gas (5% H_2 and 95% N_2) flowing at a rate of 2310sccm to remove nickel oxide, and to prevent oxidation or adsorption of oxygen on the Ni surface during annealing. Scanning electron microscopy was carried out in an FEI/Philips XL30 FEG ESEM. Because MgO is electrically

insulating, a low vacuum mode with a water vapor pressure of 0.9torr was used in the ESEM to reduce substrate charging. AFM imaging was conducted using the tapping mode in a Veeco Nanoscope IV AFM.

For each experimental data point, 20 measurements were made from different holes of the same size. Error bars were constructed to be the 95% confidence interval, calculated by using the t-statistics and the standard statistical method.

6.3. Results

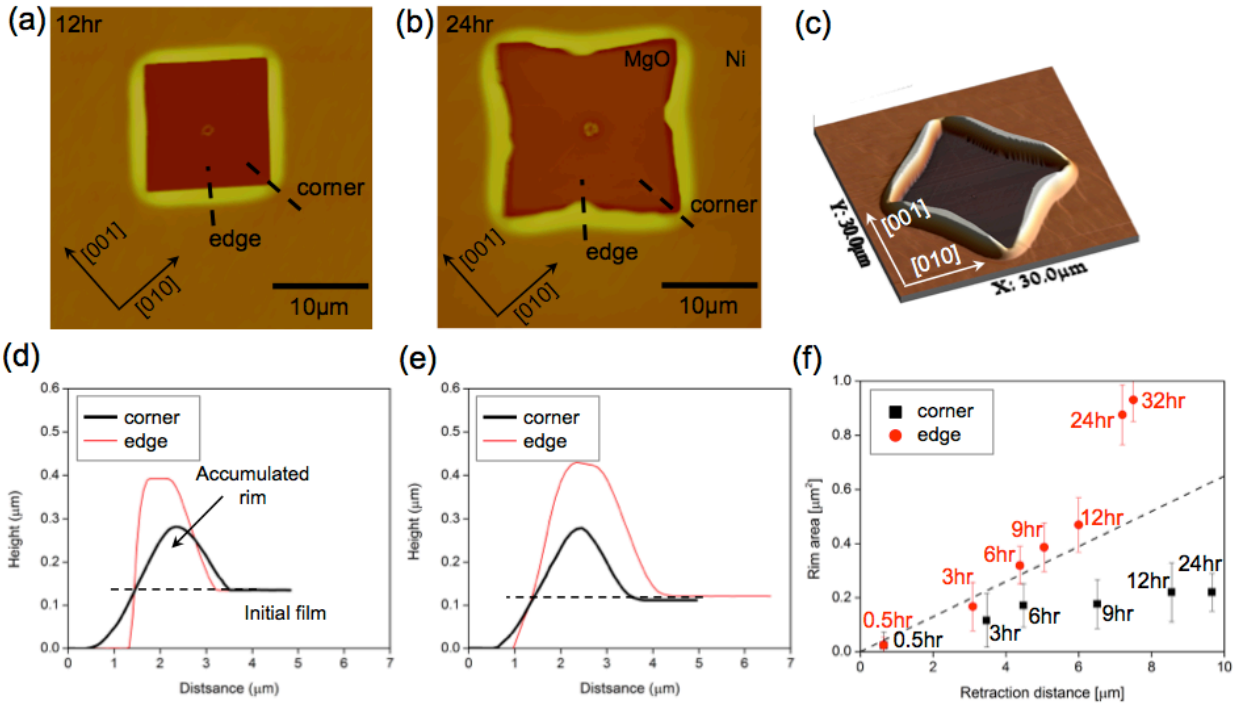

Figure 6-1. (a) A top-down AFM image of a natural hole after 12 hours of annealing. (b) A top-down AFM image of a natural hole after 24 hours of annealing. (c) A three-dimensional view of a natural hole after the corners became unstable. (d) A cross-sectional AFM profile of the edge and the tip at the corner of a natural hole after a 12-hour anneal. (e) A cross-sectional AFM profile of the edge and the tip at the corner of a natural hole after a 24-hour anneal. (f) The cross-sectional rim area at the edge and the tip of a natural hole at different retraction distances (distance is measured from the center of the hole). The dashed line is a linear fit for the first three data points for the edge, and is intended as a visual guide. The annealing time for each data point is indicated in the figure. Samples were annealed at 890°C under a reducing gas (5% H_2 + 95% N_2) flow of 2310sccm.

Figures 6-1(a) and 6-1(b) illustrate the development of a corner instability for a natural hole formed in a continuous, single-crystal film. As mentioned previously, polygonal holes are initially bounded by the in-plane edges with the slowest retraction rates. In Ni(100) films, the holes are initially bounded by edges with an in-plane normal of [011] under the reported experimental conditions. It can be seen that the hole's square shape is stable for some time before the corner instability occurs. After the corner instability occurs, another set of edges with locally minimum retraction rates (edges with [010] in-plane normals) form to accommodate the shape changes. In the three-dimensional view of a natural hole after the corner instability occurred (Figure 6-1(c)), the hole has a roughly uniform rim height along most of the edges. These regions are connected to the tip of the corner by straight sections with sloped rims. Henceforth, the term "tip" will be used to refer to the <1μm-sized region where the rim height is uniform and the triple line, or the three-phase boundary, has a large, negative curvature (using the convention that a solid sphere has positive curvature). The "transition region" refers to the sloped, straight section of rim on either side of the tip. The term "edge" refers to the central section of the rim which is roughly straight and has a uniform height. The triple line along the edge often develops a positive curvature after the corner instability develops. A similar structure around polygonal holes has been observed previously [28, 61].

To analyze the mass accumulation trend at the tip and the center of the edge, the cross-sectional area of the accumulated rim was quantified at the tip and the center of the edge using AFM scans. This is illustrated in Figures 6-1(d) and 6-1(e). The apparent contact angle, defined as the internal angle of the facet abutting the substrate surface, is not necessarily related to the equilibrium contact angle for isotropic materials, and AFM measurements underestimate its value. This is because of the finite width of the AFM tip; the AFM tip angle is 75^{o}. This is more significant at the tips, where the tip is confined on two sides.

Figure 6-1(f) shows the average cross-sectional rim areas at the edge and the tip for natural holes at different retraction distances. Increasing retraction distance corresponds to

increasing annealing time. The dashed line serves as a basis for comparison. If all of the material swept up due to retraction were incorporated into the rim, and no mass transfer occurred parallel to the rim, the rim cross-sectional area should grow linearly with retraction distance with a slope equal to the film thickness. The edge data follow this linear trend, to within experimental error, with the exception of the last two data points. However, the tip data follow a sublinear trend, and at late times, the cross-sectional area approaches a constant value. The late-stage data were collected well after the corners became unstable and the edges of the hole underwent significant bending. The "notch" visible at the midpoint of each edge in Figure 6-1(b) occurs through a combination of faceting along the triple line and interactions between the rim regions on either side of the midpoint. Therefore, the last two data points for the edge of the hole show effects that are not directly related to the onset of the corner instability.

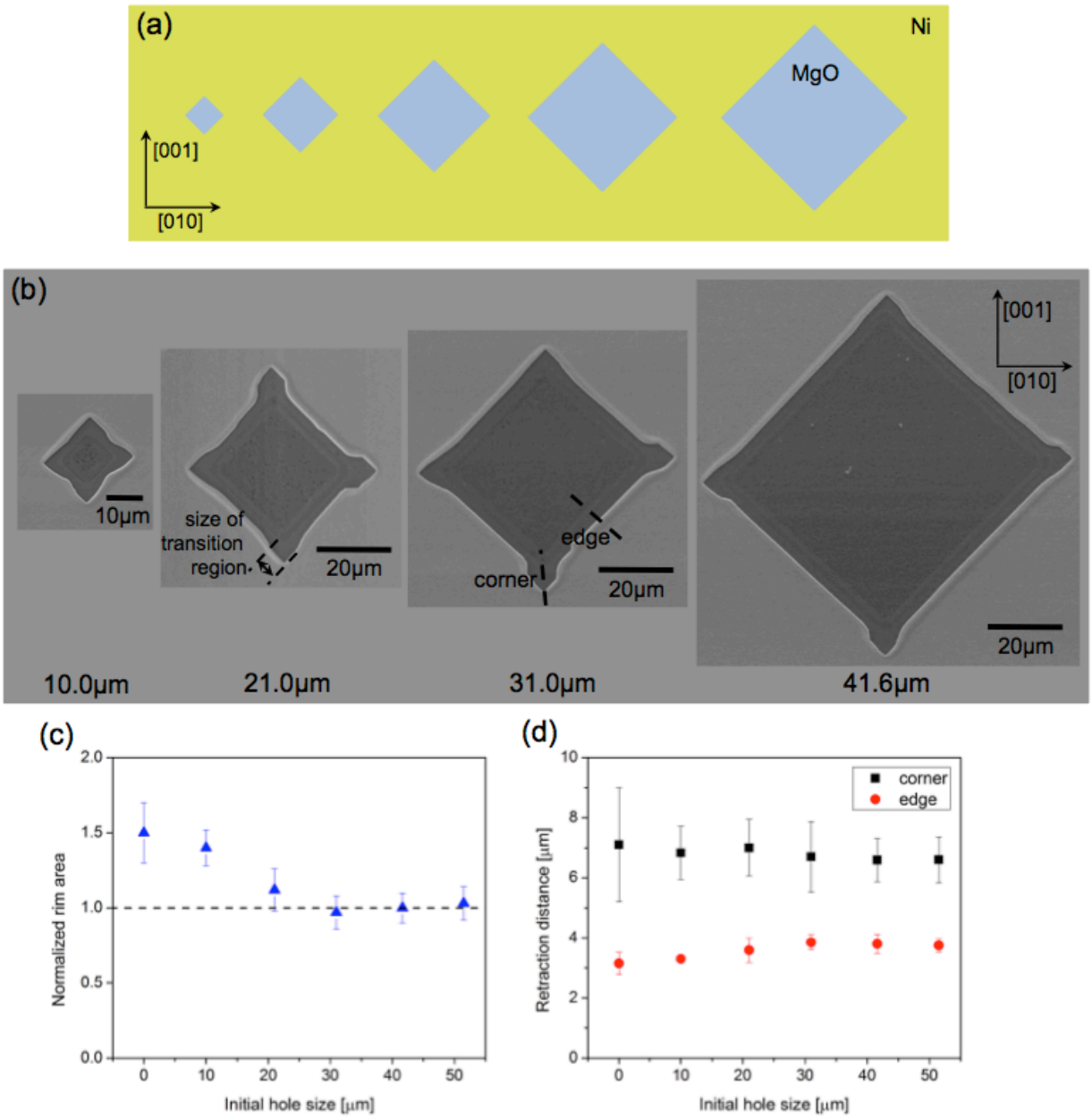

Figure 6-2. Experimental results for dewetting of holes that were lithographically pre-patterned in Ni(100) films. (a) Schematic illustration showing the relative sizes of the initial hole patterns. (b) SEM images of patterned holes after a 16-hour anneal show the corner instability. The initial hole sizes, defined as the length of the edge of the patterned square holes, are written below each hole. The images are scaled to have the same magnification. The spacing between the dashed black lines is the reported "transition" size. (c) The normalized rim cross-sectional areas at the center of the edges for different patterned hole sizes after a 16-hour anneal. The rim area is normalized by the retraction distance multiplied by the film thickness. (d) The retraction distances at the tip and the edge for different patterned hole sizes after a 16-hour anneal. An initial hole size of 0 indicates a natural hole. The samples were annealed at 890°C under a reducing gas (5% H_2 + 95% N_2) flow of 2310sccm.

The corner instability in patterned holes was also observed. Square holes of different sizes (defined as the edge length) were patterned and annealed under the same conditions described in the previous section. The pre-patterned holes are intentionally oriented so that they are bound by edges with local minimum retraction rates (the edges with [011] in-plane normals, identified in Ye and Thompson's work [21]). Figure 6-2(b) shows SEM images of the patterned holes after a 16-hour anneal. The length of the transition region (the straight, sloped portion of rim adjacent to the tip, as graphically defined in Figure 6-2(b)) is independent of the size of the patterned holes, and found to be 5.6μm±0.61μm. Figure 6-2(d) shows that only the holes with edge lengths less than two times the transition region length show a size effect. Therefore, retraction distances are at most weakly dependent of the initial hole size. These size-independent characteristics imply that the corner instability is a local phenomenon.

The rim area at the center of an edge shows some dependence on the initial hole size (Figure 6-2(c)). The measured rim area is normalized by the *retraction distance multiplied by the film thickness*. If only the mass locally accumulated due to retraction is incorporated into the rim, the normalized rim area is expected to have a time-independent value of 1. For 20μm-sized holes and larger, the edges behave as if the corner was not present and the edge was infinitely long. However, for natural and 10μm-sized holes, the rim is thicker than expected for an infinite, straight edge. This is consistent with the slightly lower retraction distance measurements in Figure 6-2(d) for these hole sizes as compared to the larger holes. The excess mass can be attributed to the "notch," mentioned previously. The notch occurs when the edges bend and distort as a consequence of the corner instability. The edges are so short on these holes that the notch formed within the 16-hour anneal time, whereas it occurs later for the larger holes. For large holes, it can be seen that the notching behavior and the corner instability phenomenon are not coupled.

6.4. Corner Instability Model

To determine the underlying mechanism for the corner instability, a simple model is presented. This modeling was conducted in collaboration with Rachel V. Zucker of the Carter Group at MIT Department of Materials Science and Engineering. A core assumption of this model is based on fundamental results from prior modeling efforts: the material contained in the rim is taken to be equal to the amount swept up during edge retraction. For isotropic materials (materials with both isotropic surface energies and diffusivities) rims develop an oscillatory cross-sectional profile, in which a set of valleys with rapidly decreasing depth forms ahead of the advancing rims [15, 17]. This implies that some mass from the first valley flows toward the rim, but this is a small fraction of the total mass incorporated due to retraction, and can be neglected. Similarly, for anisotropic films lacking a valley, an additional mass flow from the bulk film toward the rim is present. However, it is negligibly small over the experiments' time scales, comprising at most a few percent of the total rim mass [26].

Another assumption of the model is that the rim is semi-circular in cross-section and the surface tension is isotropic. The actual rim profile is in general more complicated, and varies with time, as shown in Figures 6-1(d) and 6-1(e). This complexity is difficult to capture in an analytical model, so a semi-circle is assumed to make calculations of volume within the rim straightforward. The model developed by Brandon and Bradshaw [15] shares the assumptions of mass conservation within the rim and a semi-circular rim profile. Despite its simplicity, the result that edges are expected to retract with time as $t^{2/5}$ has been shown to match experiments [23] and numerical simulations [14]. The success of their model indicates that the assumptions that volume is conserved and that rims have semi-circular cross-sectional shapes captures the essential physics.

6.4.1. Model Geometry

The geometry assumed for the model is informed by experimental results. The AFM profile shown in Figure 6-1(c) reveals three characteristic regions of the rim: 1) the corner "tip," which is <1μm in size, 2), the "edges," which are about 10μm in length and have uniform rim height, and 3) the "transition region," a straight section of rim with linearly-increasing height from the tip to the edge, which is about 5.6μm in length. These regions are shown in the schematic of the corner shown in Figure 6-3.

In the model, all lengths are normalized to the film thickness H, and the contact angle is 90°. This contact angle indicates that the surface energy of the substrate in contact with the vapor phase is equal to the interfacial energy of the substrate-film interface.

The tip of the corner is not perfectly sharp, but instead has uniform curvature along the triple line. The (negative) radius of curvature, b_{tip}, is on the order of a few times the film thickness. b_{tip} is fixed by the surface energy anisotropy of the Ni film, and its value is observed to be independent of time. The rim also has a uniform height in this region, r_{tip}. Therefore, this area will be modeled as a portion of a torus, as shown in Figure 6-3. The inner radius of the torus is b_{tip} and the cross-sectional radius is r_{tip}.

The rim on the edge of the hole has a uniform height. However, the observed rim width varies. For the purposes of the model, this variation in rim profile is neglected, and the rim height is taken as r_{edge}. This assumption is justified by the observation that the rim height does not vary significantly prior to the corner instability. The model is intended to capture the onset of the instability, rather than subsequent behavior, including notch formation. Therefore, it is also assumed that the edge is straight. Accounting for the rim's triple-line curvature does not significantly affect the model results.

Detailed AFM scans of the transition region of the rim reveal a linearly increasing rim-height from r_{tip} to r_{edge}. The triple line in this region is straight. Both of these observations are

incorporated into the model. The length of the sloped region is taken to be L, as shown in Figure 6-3. The angle between the transition regions on either side of the tip is α. For the (100) Ni-on-MgO system, $\alpha = 90°$. This value for α is set by the facets bounding the hole.

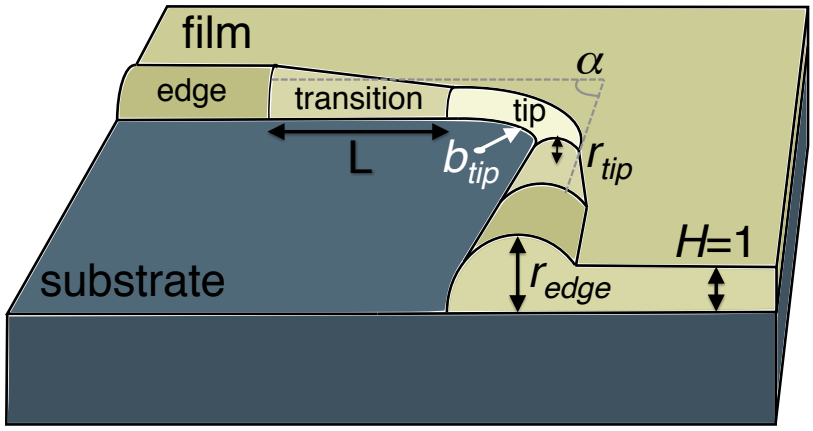

Figure 6-3. The assumed geometry of the corner of a hole. All distances are normalized to the film thickness H. The rim has height r_{tip} at the tip of the corner and height r_{edge} along the straight edge of the hole. The rim height gradually increases from r_{tip} to r_{edge} over a distance L. The anisotropy of the film material holds the apparent angle of the corner, α, and the radius of curvature of the triple line at the tip, b_{tip}, at constant values.

6.4.2. Retraction Velocity

The velocity of a surface along its normal, v, evolving due to capillary forces, was given by Mullins [11]. Extending his expression to two dimensions and non-dimensionalizing yields

$$v = \left(\frac{\partial^2 \kappa}{\partial s_{para}^2} + \frac{\partial^2 \kappa}{\partial s_{perp}^2}\right), \tag{6-1}$$

where κ is the dimensionless mean curvature (divide κ by the film thickness to obtain a velocity with units), s_{para} is the dimensionless arc-length coordinate parallel to the triple line, and s_{perp} is the dimensionless arc length coordinate perpendicular to the triple line. The dimensionless velocity is related to the real velocity u by $u = v\,B/H^3$, where $B = \frac{D\,\gamma\,\nu\,\Omega^2}{k\,T}$, and D is the surface self-diffusivity, γ is the surface energy density, Ω is the volume per atom, ν is the area density of

diffusing surface atoms, k is Boltzmann's constant, and T is temperature. For the case of a 90° contact angle, the normal velocity v at the triple line is also the dewetting retraction velocity, v_{retr}.

The curvature of the triple line at the corner tip is $\kappa_{tip} = \frac{1}{r_{tip}} - \frac{1}{b_{tip}}$, with r_{tip} and b_{tip} defined in Figure 6-3. The curvature of the triple line at the edge is $\kappa_{edge} = \frac{1}{r_{edge}}$ (assuming that the edge is straight, or that the radius of curvature for the triple line is much greater than r_{edge}, which is the case in all experimental results presented in Section 6.3).

To find the retraction velocity, it was assumed that the chemical potential is parabolic near the triple line, i.e., a second-order accurate approximation of the curvature along each direction is used. This allows us to estimate the second derivatives of curvature. In general, the second derivative of a parabola, $y(x)$, of best fit to three distinct points, (x_i, y_i), is

$$\frac{\partial^2 y}{\partial x^2} \approx \frac{2\,(x_1y_2+x_2y_3+x_3y_1-x_1y_3-x_2y_1-x_3y_2)}{(x_1-x_2)(x_2-x_3)(x_3-x_1)}. \tag{6-2}$$

The value of s_{para} at the tip of the corner is defined as zero, and the value of s_{perp} is defined as zero at the triple line, as shown in Figure 6-4. The curvature of the film surface is known everywhere along the s_{para} coordinate due to the assumed geometry. Three points are (arbitrarily) selected along the triple line $(s_{para}, s_{perp}, \kappa) = \left(0, 0, {}^{1}/_{r_{tip}} - {}^{1}/_{b_{tip}}\right), \left(b_{tip}\,{}^{\alpha}/_{2}, 0, {}^{1}/_{r_{tip}}\right)$, and $\left(b_{tip}\alpha, 0, {}^{1}/_{r_*}\right)$ for the parabolic fit, where α is the angle of the tip, $b_{tip}\,{}^{\alpha}/_{2}$ is the arc length from the midpoint of the tip to beginning of the transition region, and r_* is the rim radius of curvature a distance $b_{tip}\,\alpha$ away from the tip, as indicated in Figure 6-4. Taking into account the linear increase in rim height across the transition region, r_* is given by

$$r_* = r_{tip} + \frac{r_{edge} - r_{tip}}{L}\, b_{tip}\, \frac{\alpha}{2}. \tag{6-3}$$

Substitution into Equation 6-2 gives an estimate for $\frac{\partial^2 \kappa}{\partial s_{para}^2}$:

$$\frac{\partial^2 \kappa}{\partial s_{para}^2} \approx -\frac{4\,(b_{tip}(r_*-r_{tip})+r_* r_{tip})}{\alpha^2 b_{tip}^3 r_* r_{tip}}, \tag{6-4}$$

Equation 6-4 accounts for mass flow towards or away from the tip, parallel to the rim.

To compute $\frac{\partial^2 \kappa}{\partial s_{perp}^2}$, three points are selected along the s_{perp} coordinate, $(s_{para}, s_{perp}, \kappa) = \left(0, 0, {}^{1}/_{r_{tip}} - {}^{1}/_{b_{tip}}\right), \left(0, r_{tip}\left(\pi - \sin^{-1}\left(1/r_{tip}\right)\right), 0\right)$, and $\left(0, 2\, r_{tip}\left(\pi - \sin^{-1}\left(1/r_{tip}\right)\right), 0\right)$, where $r_{tip}\left(\pi - \sin^{-1}\left(1/r_{tip}\right)\right)$ is the arc length from the triple line to the flat film at the center of the tip, shown in Figure 6-4. These points are depicted in Figure 6-4. Using Equation 6-2, $\frac{\partial^2 \kappa}{\partial s_{perp}^2}$ can be estimated as

$$\frac{\partial^2 \kappa}{\partial s_{perp}^2} \approx \frac{b_{tip}-r_{tip}}{b_{tip} r_{tip}^3 \left(\pi - \sin^{-1}\left(1/r_{tip}\right)\right)^2}, \tag{6-5}$$

Equation 6-5 accounts for the driving force for the corner to retract.

Equations 6-1, 6-3, and 6-5 together provide the retraction velocity, $v_{retr,tip}$. With $\alpha = 90°$, for a given rim height and tip sharpness, b_{tip},

$$v_{retr,tip} = \frac{4\left(\frac{1}{r_{tip}} + \frac{1}{r_{edge}} - \frac{4}{r_{tip}+r_{edge}} - \frac{1}{b_{tip}}\right)}{L^2} + \frac{b_{tip}-r_{tip}}{r_{tip}^3\, b_{tip}\left(\pi - \sin^{-1}\frac{1}{r_{tip}}\right)^2}. \tag{6-6}$$

In Equation 6-6, the first term is negligible (less than 2% of the second term) when L > ~25. Experiments give L = 47 (in dimensionless units), so it can be expected that L has little to no effect on the retraction velocity.

The same method as above can be applied to arrive at an equation describing the retraction velocity on the edge of the hole. It is assumed that the edge is straight, so $\frac{\partial^2 \kappa}{\partial s_{para}^2} = 0$ for the edge. Therefore,

$$v_{retr,edge} = \frac{1}{r_{edge}^3 \left(\pi - \sin^{-1}\frac{1}{r_{edge}}\right)^2}. \tag{6-7}$$

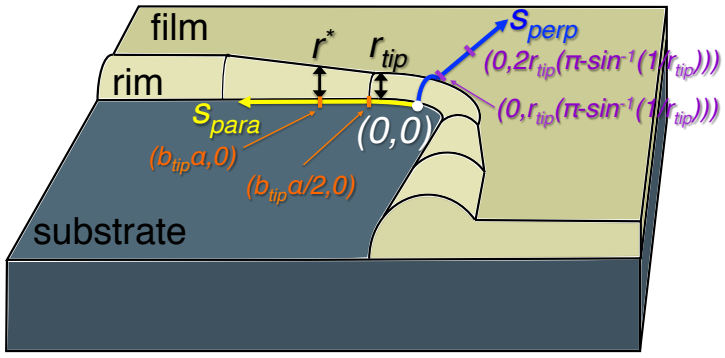

Figure 6-4. Schematic of the corner geometry. Definitions of the arc length coordinates s_{para} and s_{perp}. The origin is at the midpoint of the triple line at the corner tip, and the points used to calculate $\frac{\partial^2 \kappa}{\partial s_{para}^2}$ and $\frac{\partial^2 \kappa}{\partial s_{perp}^2}$ are marked.

6.4.3. Rim Height as a Function of Time

The change in the rim height as a function of time can be calculated by enforcing volume conservation within the rim. As the rim retracts at the corner tip, the arc length must increase, and a portion of the flat film will be incorporated into the rim. Figure 6-5 shows a schematic of the tip at time t and at time $t+dt$. The volume contained in the rim at time $t+dt$ must equal the volume contained in the rim at time t, plus the volume of flat film swept up due to retraction.

Given $r_{tip}(t)$ and b_{tip}, the volume in the rim at the tip can be found; this is equivalent to finding the volume of a portion of a torus. With these parameters, the retraction velocity is also known. Thus, the distance the film retracts in time dt is equal to $v_{retr,tip}\,dt$.

The portion of flat film swept up during retraction has width w, as shown in Figure 6-5. w can be found in terms of $r_{tip}(t+dt)$. Setting the total change in volume to zero provides an equation for $r_{tip}(t+dt)$. However, this equation is transcendental. To arrive at an analytical answer,

a first-order approximation is made: $r_{tip}(t+dt) = r_{tip}(t) + \varepsilon_{tip}\, v_{retr,tip}\, dt$, where ε_{tip} is an unknown, dimensionless parameter. The equation for $r_{tip}(t+dt)$ is expanded as a Taylor series in dt to first-order. The first-order expansion can be solved for ε_{tip}:

$$\varepsilon_{tip} = \left(-2 + 4\, r_{tip}\sqrt{r_{tip}^2-1} + r_{tip}^2\left(2 - \pi\sqrt{r_{tip}^2-1}\right) + 4\, b_{tip}\sqrt{r_{tip}^2-1} - 2\, r_{tip}^2\sqrt{r_{tip}^2-1}\,\tan^{-1}\left[\sqrt{r_{tip}^2-1}\right]\right) / \left(2 + r_{tip}^2\left(-2 + 3\,\pi\sqrt{r_{tip}^2-1}\right) - 4\, b_{tip}\sqrt{r_{tip}^2-1} + 2\, r_{tip}\sqrt{r_{tip}^2-1}\,(\pi\, b_{tip} - 4) + 2\, r_{tip}\sqrt{r_{tip}^2-1}\,(3\, r_{tip} + 2\, b_{tip})\tan^{-1}\left[\sqrt{r_{tip}^2-1}\right]\right). \quad (6\text{-}8)$$

A differential equation for $r_{tip}(t)$ is provided by computing $\frac{r_{tip}(t+dt)-r_{tip}(t)}{dt}$, which equals $\varepsilon_{tip}\, v_{retr,tip}$.

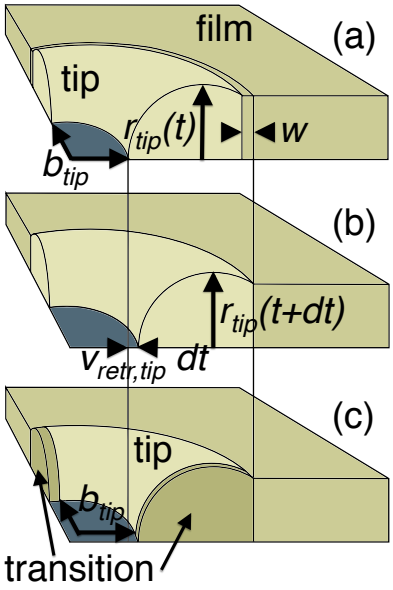

Figure 6-5. A detailed schematic of the tip geometry is shown. Part (a) shows the film at time t. Part (b) shows the film at time $t+dt$. The initial rim height, $r_{tip}(t)$, is known, and b_{tip} is constant. The new rim height, $r_{tip}(t+dt)$, is found by volume conservation: the volume in the rim at time t plus the volume swept up in the time dt must equal the volume in the rim at time $t+dt$. The volume swept up during retraction is that contained in the region of radial thickness w, shown in (a). Part (c) also shows the film at time $t+dt$. The dark-shaded portions of the rim are now part of the transition region, and are no longer part of the corner tip. This is because b_{tip} is fixed by the anisotropy of the film material, preventing the arc length of the tip region from increasing with time.

The same method can be applied to find $r_{edge}(t)$. ε_{edge} is given by

$$\varepsilon_{edge} = \frac{1}{-1+\pi\, r_{edge} - r_{edge}\, \sin^{-1}\frac{1}{r_{edge}}}. \tag{6-9}$$

The differential equations for $r_{tip}(t)$ and $r_{edge}(t)$ are coupled because $\frac{dr_{tip}}{dt} = \varepsilon_{tip}\, v_{retr,tip}$, and $v_{retr,tip}$ depends on both $r_{tip}(t)$ and $r_{edge}(t)$.

The differential equations for $r_{tip}(t)$ and $r_{edge}(t)$ do not have closed-form solutions. However, they can be integrated numerically. No specialized numerical solvers are needed, and the built-in numerical integration function in Wolfram *Mathematica 10* can perform the integration in a fraction of a second. At $t = 0$, $r_{tip} = 1$ and $r_{edge} = 1$. Plots of $r_{tip}(t)$ and $r_{edge}(t)$ are shown in Figure 6-7.

With expressions for $r_{tip}(t)$ and $r_{edge}(t)$, the retraction distance at the tip and edge as a function of time can be obtained. The expressions for $r_{tip}(t)$ and $r_{edge}(t)$ are substituted into Equations 6-6 and 6-7, respectively, to obtain the retraction velocities as a function of time. These can be integrated numerically to obtain retraction distances as a function of time, shown in Section 6.5.

6.4.4. Steady-state Rim Height at the Tip

While the rim height at the edge of the hole always increases with time, the rim height at the tip may increase or decrease. This occurs because mass is added to the rim during retraction, but the arc length of the rim must increase due to high curvature of the triple line at the tip. This effect is analogous to a Poisson's ratio of 0.5: lengthening the rim parallel to the triple line requires the height to decrease. This can be seen in Figure 6-5.

When the volume of the flat film swept up due to retraction is exactly balanced by the volume lost due to lengthening of the rim, the rim height stays constant. This balance occurs when ε_{tip} is equal to zero. $\varepsilon_{tip} = 0$ when b_{tip} equals the critical value $b_{critical}$:

$$b_{critical} = \frac{1}{4}\left(-4\, r_{tip} + \frac{2}{\sqrt{{r_{tip}}^2-1}} + {r_{tip}}^2\left(\pi - \frac{2}{\sqrt{{r_{tip}}^2-1}}\right) + 2\,{r_{tip}}^2\,\tan^{-1}\sqrt{{r_{tip}}^2-1}\right) \qquad (6\text{-}10)$$

A contour plot of ε_{tip} is shown in Figure 6-6. The black line is the trace of Equation 6-10, and provides the steady-state value of r_{tip}, r^*_{tip}, for a given value of b_{tip}. The rim height r^*_{tip} is at a stable equilibrium because a rim height greater than r^*_{tip} will decrease with time, and vice-versa.

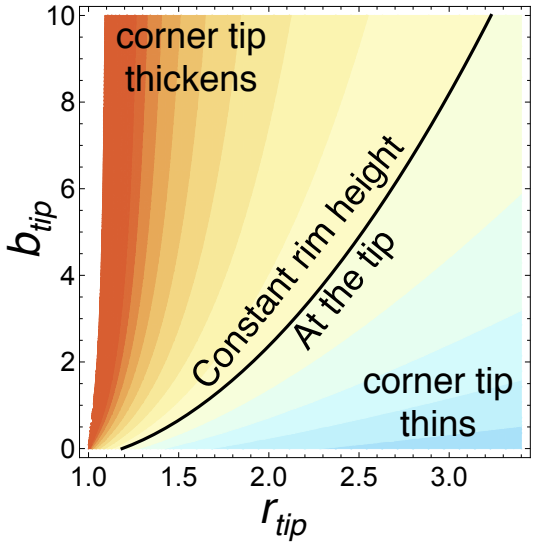

Figure 6-6. A contour plot of the rate of rim height change at the tip is shown. Warm colors indicate that the rim is thickening with time for a given r_{tip} and b_{tip}; cool colors indicate that the rim thins with time. The heavy black line is the steady-state rim height at the tip, r^*_{tip}.

6.5. Discussion

6.5.1. Mechanism of the Corner Instability

The main result from the model is that the corner instability arises from two competing effects: the mass swept up due to retraction tends to increase the rim height, while the increasing arc length of the hole tends to decrease the rim height. These two effects are shown in Figure 6-5. When these effects balance, the rim height at the tip remains constant.

Note that no long-range mass transport is necessary for a corner instability to develop. The effect is entirely local, and the only mass transport needed is contained within the rim at the corner tip. The only condition for the instability to occur is the pre-existence of a sharp negative-curvature corner in the film edge so that arc length increases are localized to the curved portion of the triple line. Therefore, the corner instability can occur in patterned isotropic films as well.

For a perfect circular hole, as modeled by Brandon and Bradshaw [15], the mass swept up dominates over the increasing arc length effect. Therefore, the rim height increases with time. However, a polygonal hole is fundamentally different. The edges remain straight, and so their arc length does not increase over time. All of the increase in arc length must therefore occur at the tip. Edge retraction is driven in the direction locally normal to the triple line, so the radius of curvature at the corner tip tends to increase, as shown in Figure 6-5(b). However, anisotropy forces the material at the edges of the tip to become straight, correcting the increase in radius of tip curvature. The material at the edges of the tip joins the transition region, as shown in Figure 6-5(c).

6.5.2. Evidence against Other Mechanisms for the Instability

A simple estimation shows that the mechanism proposed by Rabkin *et al.* [61] is unable to explain the corner instability for the geometry observed here. They suggest that the corner instability occurs by a mass flow, within the rim, from the tip region towards the edges. However,

the following calculation demonstrates that the driving force for mass flow points in the opposite direction, which should, if anything, inhibit the corner instability (this flow is accounted for in the model discussed previously).

The curvature at the tip is estimated to be $\kappa_{tip} = \frac{1}{r_{tip}} - \frac{1}{b_{tip}}$, with r_{tip} and b_{tip} as defined in Figure 6-3. The curvature at the edge is $\kappa_{edge} = \frac{1}{r_{edge}}$. The chemical potential, μ, for a system whose only contribution to the free energy is surface energy, is $\mu = \Omega\, \gamma\, \kappa$, where Ω is the atomic volume and γ is the surface energy density. The mass flux is $J = \frac{-D\, \nu}{k\, T} \frac{\partial \mu}{\partial s_{para}}$, where the s_{para} coordinate is taken to be parallel to the rim, and all other parameters have the same meaning as in Equation 6-1. The gradient in chemical potential, parallel to the rim, can be estimated as

$$\frac{\partial \mu}{\partial s} \approx \Omega\, \gamma\, \frac{\kappa_{tip} - \kappa_{edge}}{L} = \frac{\Omega\, \gamma}{L} \left(\frac{1}{r_{tip}} - \frac{r_{edge} + b_{tip}}{r_{edge}\, b_{tip}} \right), \tag{6-11}$$

with L equal to the arc length from the tip to the edge. Therefore, the mass flux becomes

$$J = \frac{\mathrm{D}\, \nu\, \Omega\, \gamma}{L\, k\, T} \left(\frac{r_{edge} + b_{tip}}{r_{edge}\, b_{tip}} - \frac{1}{r_{tip}} \right). \tag{6-12}$$

If the flux is positive, then the chemical potential is higher at the edge than at the tip, so mass flows from the edge towards the tip, and vice versa.

Using the experimentally-obtained value of b_{tip} = 3.89 and the model values for r_{tip} and r_{edge} shown in Figure 6-7, the mass flux is expected to initially be positive, indicating that material flows from the edge towards the tip. The flux decreases slowly with time, and will only reverse after the corner instability is already established, when r_{tip} = 2.32 and r_{edge} = 5.75, which corresponds to a dimensionless time of 29,000. Using the experimentally obtained values of r_{tip} and r_{edge}, the flux does not reverse during the experiment. If the triple line along the edge is bent as in Figure 6-1, it increases the flux towards the tip and further delays the sign change. Therefore, mass flow parallel to the triple line is not responsible for the corner instability for the observed geometry in this work.

6.5.3. Comparison of the Model and Experimental Results

The steady-state rim height at the tip predicted by the model matches experimental results to within experimental error. The experimental value of r^*_{tip} is 2.3±0.2, and b_{tip} is 3.89±0.2 (both quantities are normalized to the film thickness of 130nm). Using b_{tip} = 3.89 in Equation 6-10 gives r^*_{tip} = 2.32, which is in excellent agreement with the observed value. Furthermore, Equation 6-6 gives the relationship between r_{tip}, b_{tip}, L, and the retraction velocity of the tip. When L is large (> 25), the dependence on L is negligible, and the corner tip retraction velocity simplifies to

$$v_{retr,tip} = \frac{b_{tip} - r_{tip}}{r_{tip}^3 \, b_{tip} \left(\pi - \sin^{-1}\frac{1}{r_{tip}}\right)^2} \quad . \tag{6-13}$$

Using the experimental value for b_{tip}, the corner tip velocity should be $4.4 \times 10^{-3} \, B \, H^3$, which is 221nm/hr. Fitting the last 5 data points for the corner retraction distance vs. time (shown in Figure 6-7) with a line gives a corner tip velocity of 199nm/hr, which is within 11% of the model's prediction.

The rim height as a function of time from experiments and the model are shown in Figure 6-7. At the tip, the model and experiment agree to within experimental error. At the edge, the model overestimates the rim height, and therefore underestimates the retraction distance. However, the model qualitatively follows the trend of the data.

The discrepancies between the model and experiment at the hole edge may be due to the assumption that it is straight and that the rim has a uniform width. Figure 6-1 shows that the rim height is constant along the edge, but the width and retraction distance vary after the corner instability develops. In Figure 6-1(b), a notch is visible at the center of each edge of the hole. The notch is geometrically necessary to connect the slow-moving edge with the fast-moving corner tip. The rim is sufficiently wide at the notch that parts of the rim on either side of the

midpoint will interact, which is not accounted for in the model, but will slow the experimental edge retraction relative to the model prediction.

The overestimation of rim height on the hole edge could be also due to the anisotropy of the real system. The top of the rim on the hole edge is faceted, as shown in Figures 6-1(c) to 6-1(e). This facet may decrease the rim's weighted mean curvature relative to the assumed semi-circular rim, which would cause it to retract more slowly than the model rim.

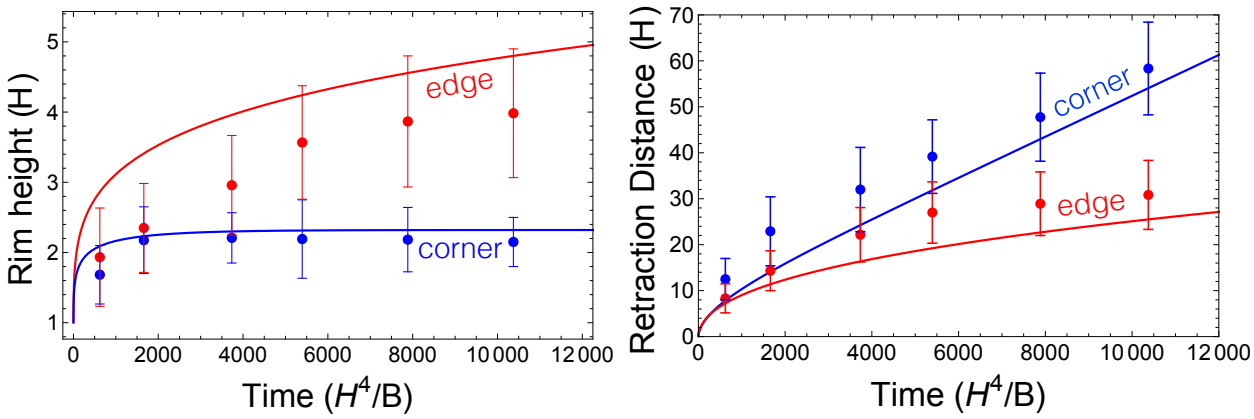

Figure 6-7. Experimental and model results for the rim height and retraction distance as a function of time. The red data and curves are for the edge of the hole, and the blue data and curves are for the tip. The model was run with experimentally obtained values for b_{tip} and L. The model overestimates the height of the rim at the edge, and therefore underestimates the retraction distance at the edge. However, the model correctly reproduces the retraction distance vs. time scaling, which goes as time to the 2/5 power.

6.6. Summary and Conclusion

The corners of a polygonal hole in a thin film become unstable during dewetting. The corners where facets meet rapidly evolve to and maintain a characteristic in-plane radius of curvature. For the Ni (100) films studied in this chapter, the radius of curvature was observed to be constant throughout the dewetting process. In addition, the rim at the tip itself is uniformly thin, and connects to the thicker rim along the edges of the hole via a straight, linearly-sloped

transition section of rim. These observations are sufficient to define the geometry of a model that reproduces the corner instability.

While the model does not include details of all physical processes which may affect dewetting at a corner, the model is sufficient to reproduce the dewetting behavior near a corner. In addition to the geometric constraints provided by the observed geometry, the model contains two assumptions: the rim cross-sectional profile is simplified to a circular arc, and mass does not leave the rim, and can only enter it as a consequence of being swept up due to retraction. The model indicates that if these assumptions are reasonable, then the corner instability arises due to a balance of mass flows. The addition of mass due to retraction tends to increase the rim height, but the need to increase the perimeter of the hole tends to thin the rim height as mass is spread over a longer length. The thinning effect only occurs at the tip because this is the only region with in-plane curvature of the triple line.

In the early stages of hole growth, the rim at the tip of the corner grows because it is still thin enough that additional mass can compensate for elongation of the rim adjacent to the tip. However, as the rim at the tip becomes thicker, an increasing fraction of the incoming mass is needed for elongation of the rim adjacent to the tip. Eventually, a steady state is reached, and the rim height stays constant. A constant rim height implies a constant retraction rate, which is observed experimentally. This is in contrast to what happens on the straight edges of the hole, where there is no arc length increase. There is only addition of mass to the rim due to retraction, so the rim always grows with time, and thus the retraction rate decreases with time.

The model and experiments are in good quantitative agreement, particularly in the value of the equilibrium rim height at the tip and the retraction velocity of the tip. Experiments on pre-patterned holes demonstrate that the onset of the corner instability and edge bending are not coupled. Experiments also show that the corner instability does not depend on the hole size, in agreement with the model result that no long-range mass transport is involved in the corner instability. Only mass flow within the corner tip region itself is necessary for the instability.

Chapter 7. Rayleigh-like Instability

7.1. Introduction

As discussed in Chapter 1, nanowires and narrow wires patterned from thin films are usually subject to a Rayleigh-like instability and, when heated, will undergo evolution to particles with a characteristic size and spacing. This process can occur while the wires remain in the solid state. For materials with isotropic surface energies, the characteristic sizes and spacings of the resulting particles or islands are expected to depend only on the initial cross-sectional area of the wires. However, crystalline solids rarely have isotropic surface energy.

Although observations of a Rayleigh-like instability of both patterned thin-film structures and free-standing nanowires have been made, as discussed in Chapter 1, no systematic experimental study has yet been conducted for single crystal wire-like structures. In this chapter, Rayleigh-like dewetting of long strips patterned from single crystal Ni films on single crystal MgO and sapphire was analyzed. Strips were patterned from films with different epitaxial orientations and were patterned with different in-plane crystallographic orientations. When these strips were annealed, they first dewet to form roughly equiaxed wire-like structures bound by facets. Subsequent Rayleigh-like dewetting led to particle spacings that were strongly dependent on the crystallographic orientations of the axes of the wires even for wires with the same cross-sectional areas. The rate of dewetting was also found to be strongly dependent on the crystallographic orientations of the wires even for wires with the same cross-sectional areas, and the slowest dewetting rate was associated with the largest final island spacing.

Wires patterned with in-plane orientations that evolve to be bound by equilibrium facets that extend along the wire axis are found to be highly resistant to dewetting. These wires very slowly dewet into widely spaced particles. These observations were correlated with the effects of surface energy anisotropy and with the relative orientations of equilibrium facets and the axes of the wires. While it was found that the particle spacing is proportional to the effective radius of the patterned structure as expected from the typical Rayleigh instability, it was also found that

for a given effective radius, the particle spacing depends on the total surface energy of the wire as well. The latter varies with the crystallographic orientation of the axis of the wire. These characteristics are also seen in Kinetic Monte Carlo simulations of Rayleigh-like dewetting.

* Part of this work has been published in Acta Materialia [39].

7.2. Experimental Procedures

130nm-thick single crystal (100), (110), and (111) Ni films were deposited on polished single crystal MgO substrates (purchased from MTI Corporation) using electron beam deposition. The out-of-plane orientations of the deposited Ni films match those of the MgO substrates. (111) Ni films were also deposited on polished $(1\bar{1}20)$ sapphire substrates (also purchased from MTI Corporation). For both substrates, the as-deposited films were patterned into strips with widths of 2, 3, and 4μm and lengths of 200, 300, and 400μm in 72 different in-plane orientations (5 degrees apart) using optical photolithography. Actual widths of the strips were measured after patterning. To measure retraction distance over time, large square patches that are 150μm wide were also patterned in Ni(111) on MgO and sapphire. Details of the film deposition and patterning can be found in Chapter 2. Additionally, e-beam lithography was used to pattern 130nm-wide strips with 1:1 width-to-thickness ratios. In this case, 6% hydrogen silsesquioxane (HSQ) was spin-coated at 500rpm for 60 seconds and baked at 90°C. The electron beam exposure was conducted in a Raith 150 e-beam writing system with an accelerating voltage of 30kV. The exposed resist was developed in CD 26 and the subsequent Ni etching was conducted in a Plasmatherm RIE system at 200W with Ar and Cl_2 flow rates of 20sccm.

Annealing of the patterned film was carried out in a tube furnace at 890°C with reducing gas (5% H_2 and 95% N_2) flowing at a rate of 2310sccm and 95sccm to remove nickel oxide, and to prevent oxidation or adsorption of oxygen on the Ni surface during annealing. Cross-sectional

samples were prepared and imaged using focused ion beam milling and scanning electron microscopy in a Helios Dual Beam Workstation and top-view scanning electron microscopy was carried out in an FEI/Philips XL30 FEG ESEM. Because MgO and sapphire are electrically insulating, a low vacuum mode with water vapor pressure of 0.9torr was used in the XL30 ESEM to reduce substrate charging. Samples were coated with 40nm-thick carbon films for use in the Helios Workstation.

7.3. Results

Figure 7-1 shows a schematic diagram of Rayleigh-like instability in patterned strips. It also defines some key terminology for subsequent discussions, such as *long edges* and *wire orientations*.

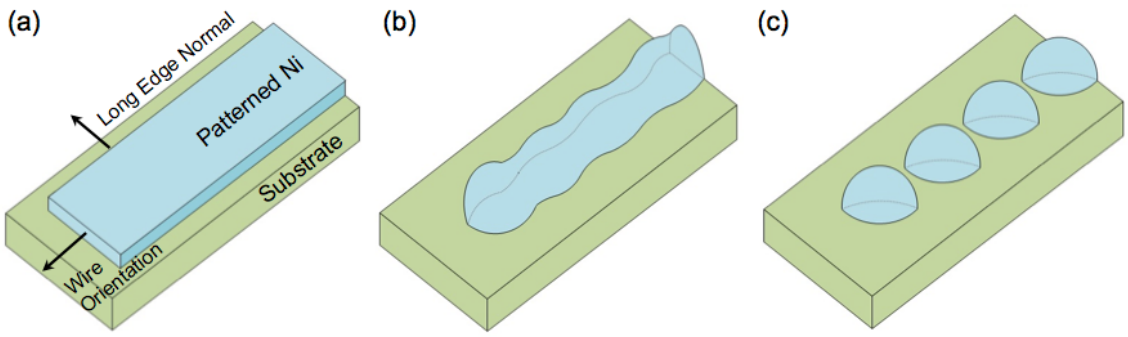

Figure 7-1. Schematic illustration of the formation of a wire-like structure from a film patterned into a strip, and the subsequent development of a Rayleigh-like decomposition of the wire into an array of particles.

As illustrated in Figure 7-2, patterned strips dewet to form wire-like structures, develop a Rayleigh-like instability, and break up into an array of regularly spaced particles. A clear orientation dependence of the particle spacing can be seen in this figure. Detailed measurements of particle spacings or perturbation wavelengths for wires patterned in Ni(111), Ni(100) and Ni(110) films are shown as polar plots in Figures 7-3, 7-4, and 7-5. It can be seen that wires

with specific in-plane orientations lead to especially large particle spacings or perturbation periods. These can be identified by the peaks in the polar plots. It was also observed that dewetting occurs more slowly for wires with these orientations. This can be seen in the images in Figure 7-2, which show wires that have been annealed for a fixed time. Wires with large island spacings or large perturbation periods are seen to be at an earlier stage of dewetting than wires that have fully dewetted into particles with smaller spacings. In addition, from Figures 7-4 and 7-5, it can be seen that the relative sizes of the stable peaks in the polar plots differ under different annealing ambients, demonstrating that the annealing ambient affects the Rayleigh-like instability behavior.

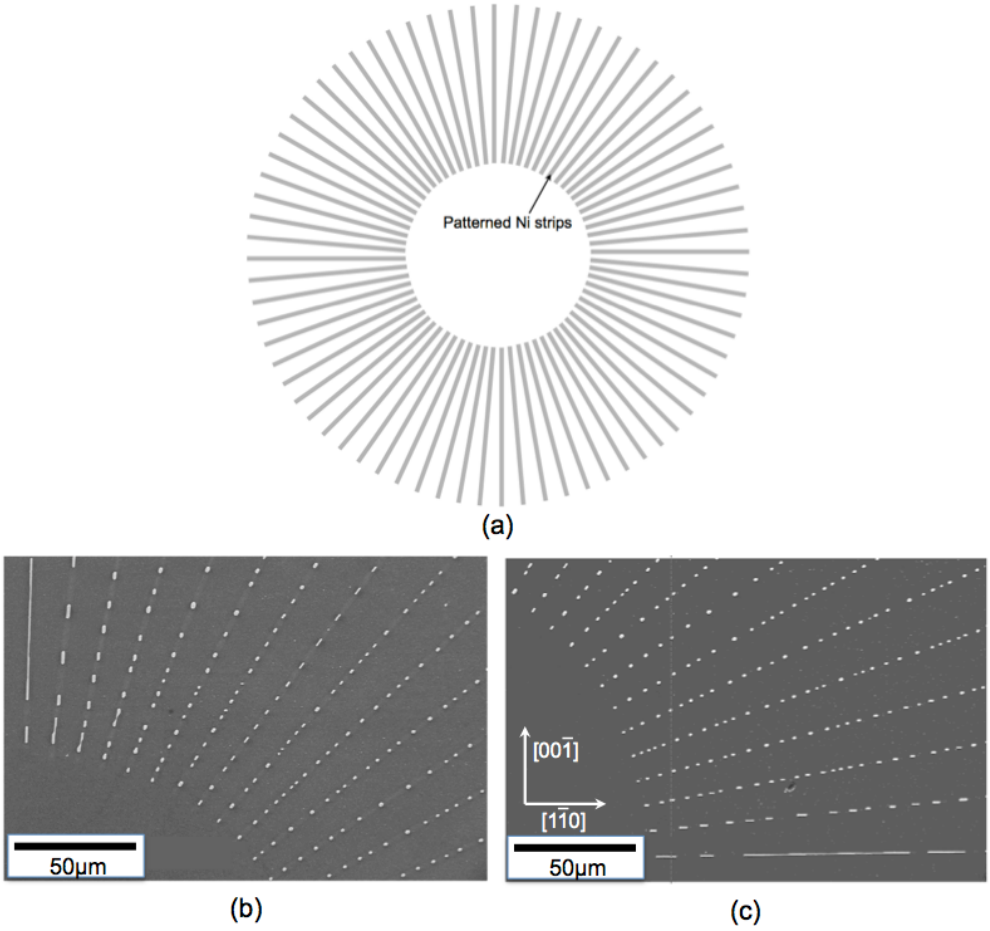

Figure 7-2. (a) Schematic diagram of patterned strips. (b)-(c) Development of a Rayleigh-like instability in Ni(110) strips with an initial width of 2.44μm and thickness of 130nm annealed at 890^0C under 2310sccm of reducing gas for 130 hours.

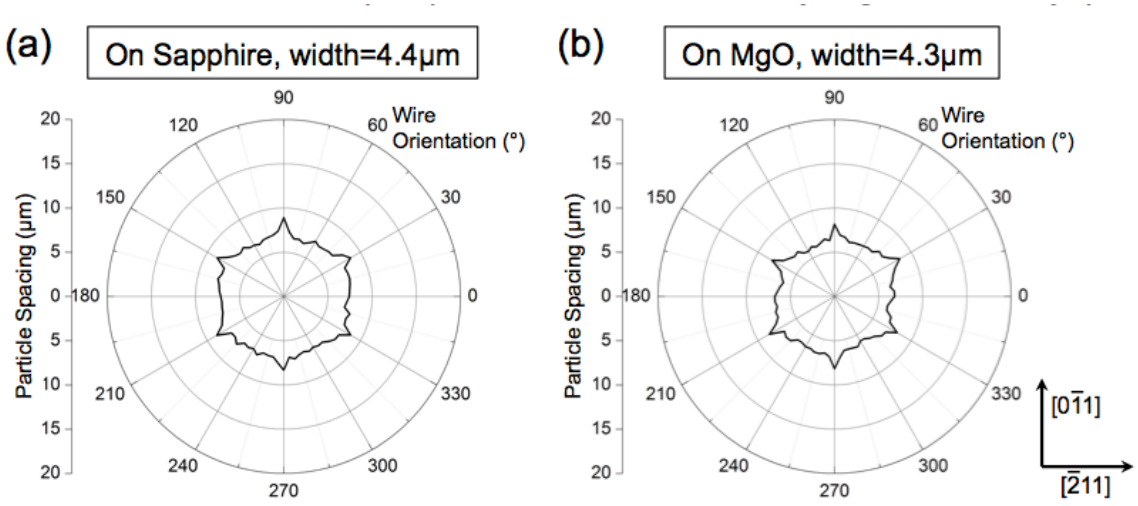

Figure 7-3. Particle spacing or perturbation wavelength as a function of the in-plane crystallographic direction of the axis of strips patterned from Ni(111) films on (a) sapphire($1\bar{1}20$) and (b) MgO(111), and annealed at 890^0C under 2310sccm of reducing gas for 300 hr. Initial strip widths are indicated in the plots. The strip thickness was 130nm in all cases. The angles are referenced to the [$\bar{2}$11] orientation.

SEM images of the cross sections and top-views of equilibrated fully-dewetted particles (Figures 7-6 and 7-7) and cross sections of fully-faceted wires (Figure 7-8) were obtained. It was found that the same sets of facets are present in the fully-faceted wires and the fully dewetted islands. The same sets of facets as in the condition of 2310sccm reducing gas are also present in the cross-sections of the wires and equilibrated particles annealed with 95sccm of reducing gas.

It was found that Ni reacts with MgO during annealing and that the dewetted Ni wires and particles sank into the MgO substrates. Because results for orientations other than Ni(111) could not be obtained on sapphire, it was first analyzed whether the reaction between Ni and MgO significantly affected the experimental results for the Ni-MgO system by comparing them to the results obtained for the Ni-sapphire system, for which no 'sinking' was observed and for which it is known that there is no reaction [73]. This was done by comparing results for (111) Ni films on both substrates. As shown in Figure 7-3, no significant difference in perturbation wavelengths was observed. Also, as shown in Figure 7-6, the same set of equilibrium facets was

found in fully dewetted particles, though the fully dewetted Ni particles on MgO were less equiaxed than those on sapphire. This is likely due to the physical constraint imposed on the dewetted particles by the trench made by the wires.

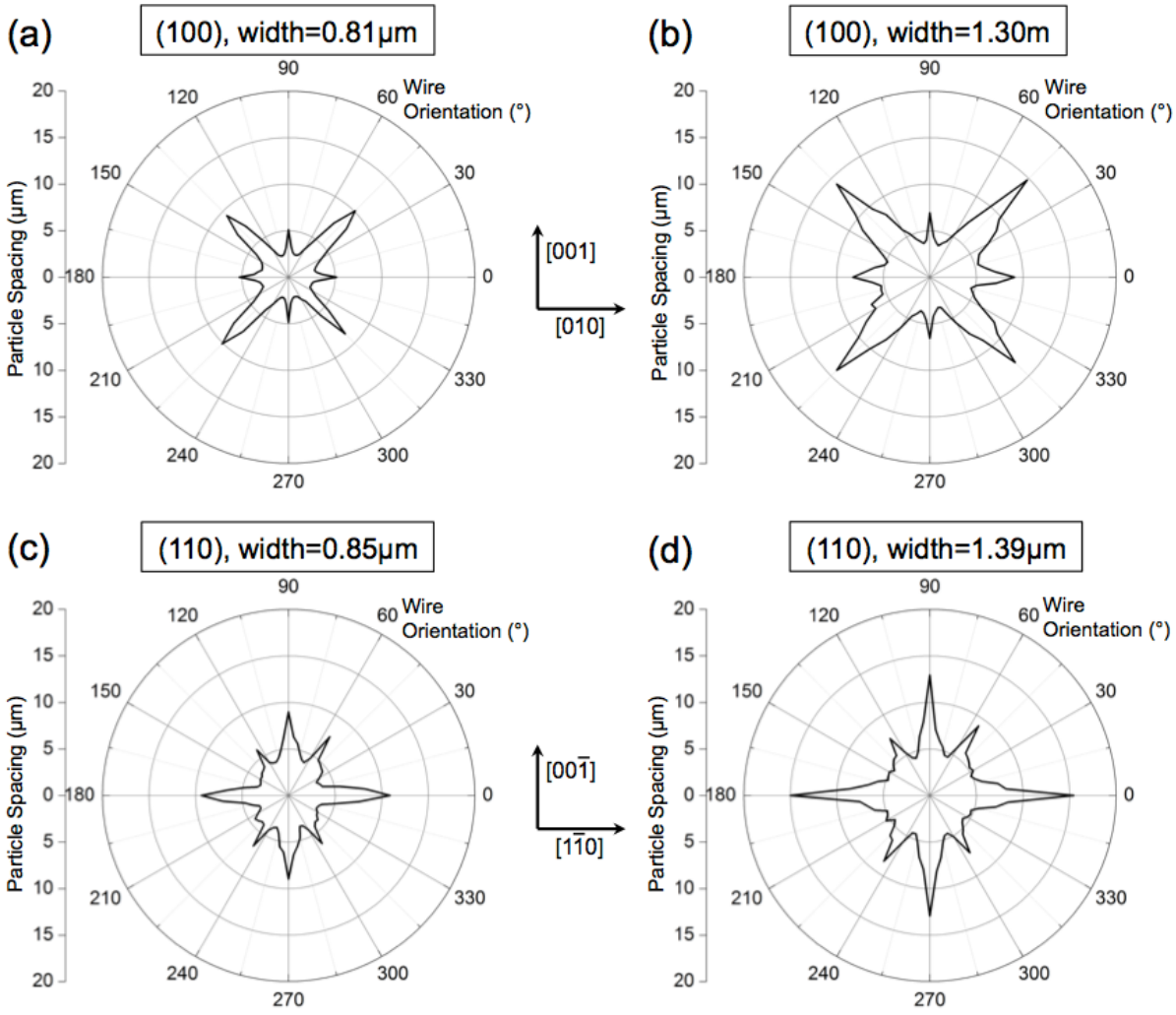

Figure 7-4. Particle spacing or perturbation wavelength as a function of the in-plane crystallographic direction of the axis of strips patterned from (a)-(b) Ni(100) and (c)-(d) Ni(110) films on MgO, after annealing at 890^0C under 2310sccm of reducing gas for 300 hr. Initial strip widths are indicated in the plots. The strip thickness was 130nm in all cases. The angles are relative to the [010] in-plane orientation for (100) films (in (a) and (b)) and the [1$\bar{1}$0] in-plane orientation for (110) films (in (c) and (d)).

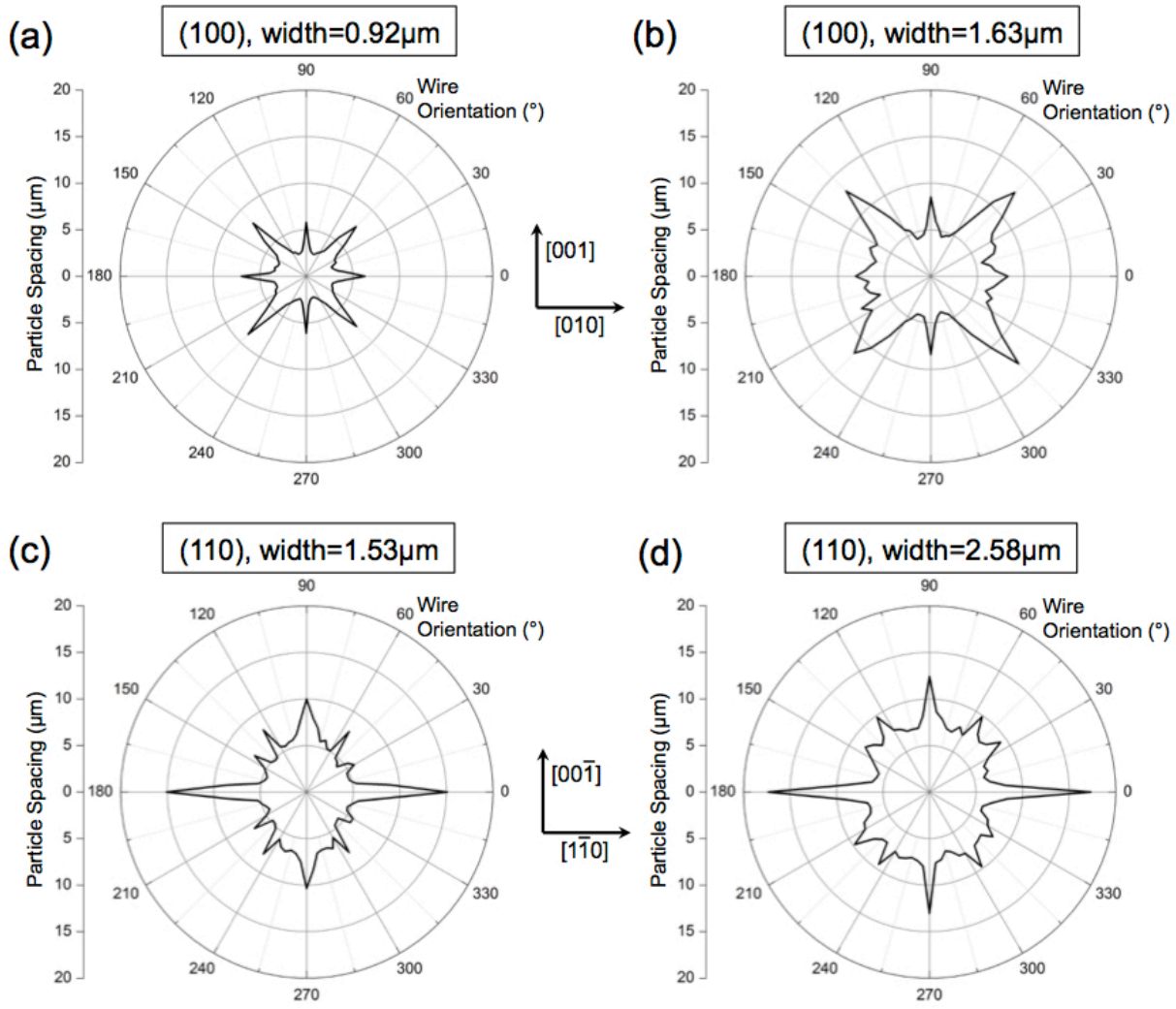

Figure 7-5. Particle spacing or perturbation wavelength as a function of the in-plane crystallographic direction of the axis of strips patterned from (a)-(b) Ni(100) and (c)-(d) Ni(110) films on MgO, after annealing at 890^0C under 95sccm of reducing gas for 300 hr. Initial strip widths are indicated in the plots. The strip thickness was 130nm in all cases. The angles are relative to the [010] in-plane orientation for (100) films (in (a) and (b)) and the [1$\bar{1}$0] in-plane orientation for (110) films (in (c) and (d)).

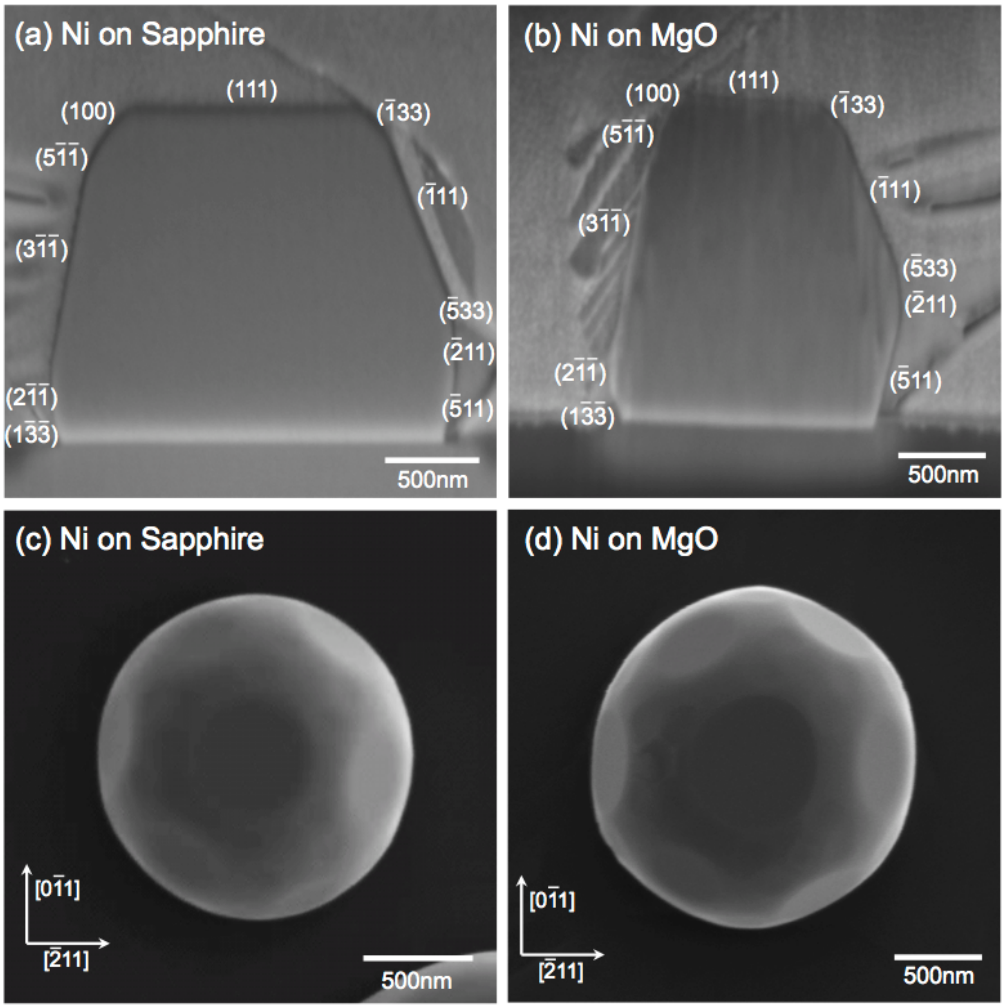

Figure 7-6. (a)-(b) Cross-sectional SEM images of equilibrated Ni particles on (a) sapphire($1\bar{1}20$) and (b) MgO(111). (c)-(d) Top-down views of Ni islands on (c) sapphire($1\bar{1}20$) and (d) MgO(111). The particles were annealed at 890^0C under 2310sccm of reducing gas.

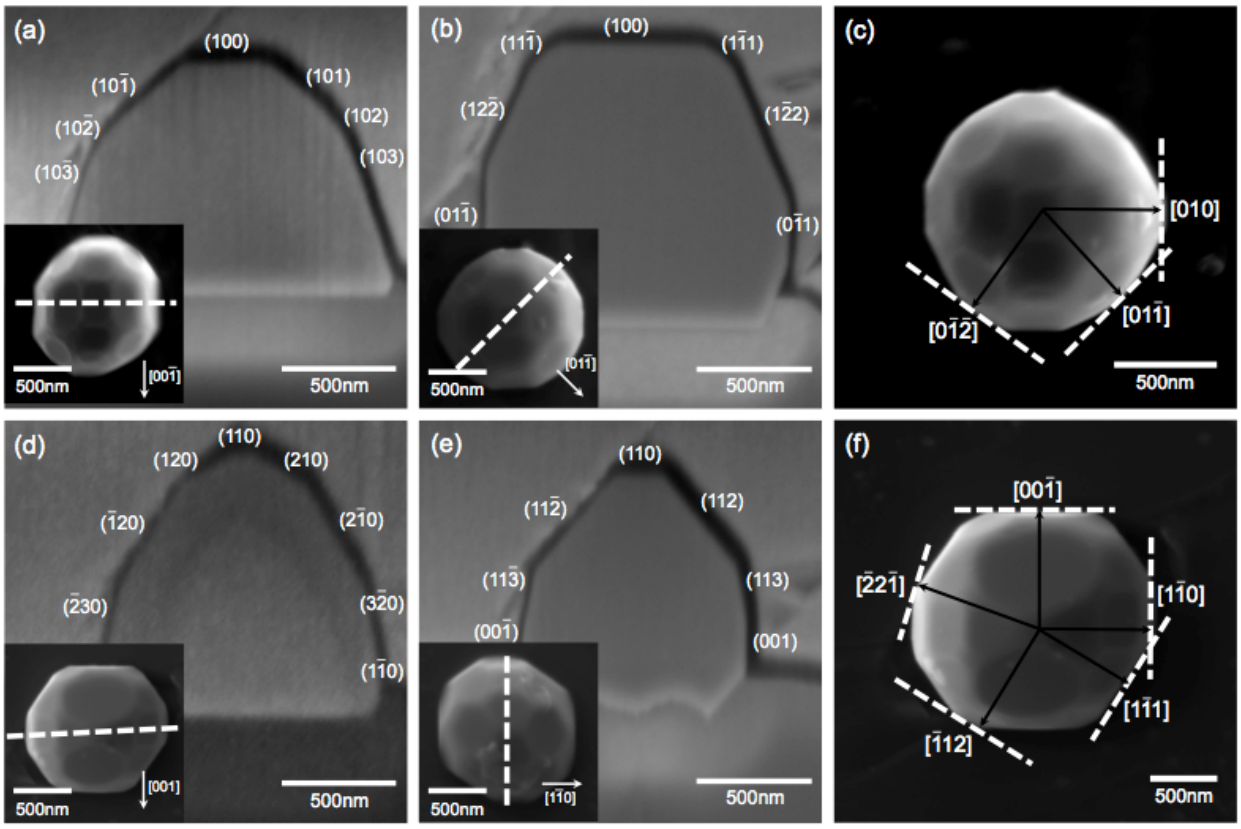

Figure 7-7. Cross-sectional and top-down SEM images of the equilibrated particles formed from (a)-(c) Ni(100) and (d)-(f) Ni(110) strips on MgO. Inset images show top views of the particles. Dashed lines indicate locations of cross sections. Arrows in the inset images indicate the orientation of the wire axis. The particles were annealed at 890^0C under 2310sccm of reducing gas.

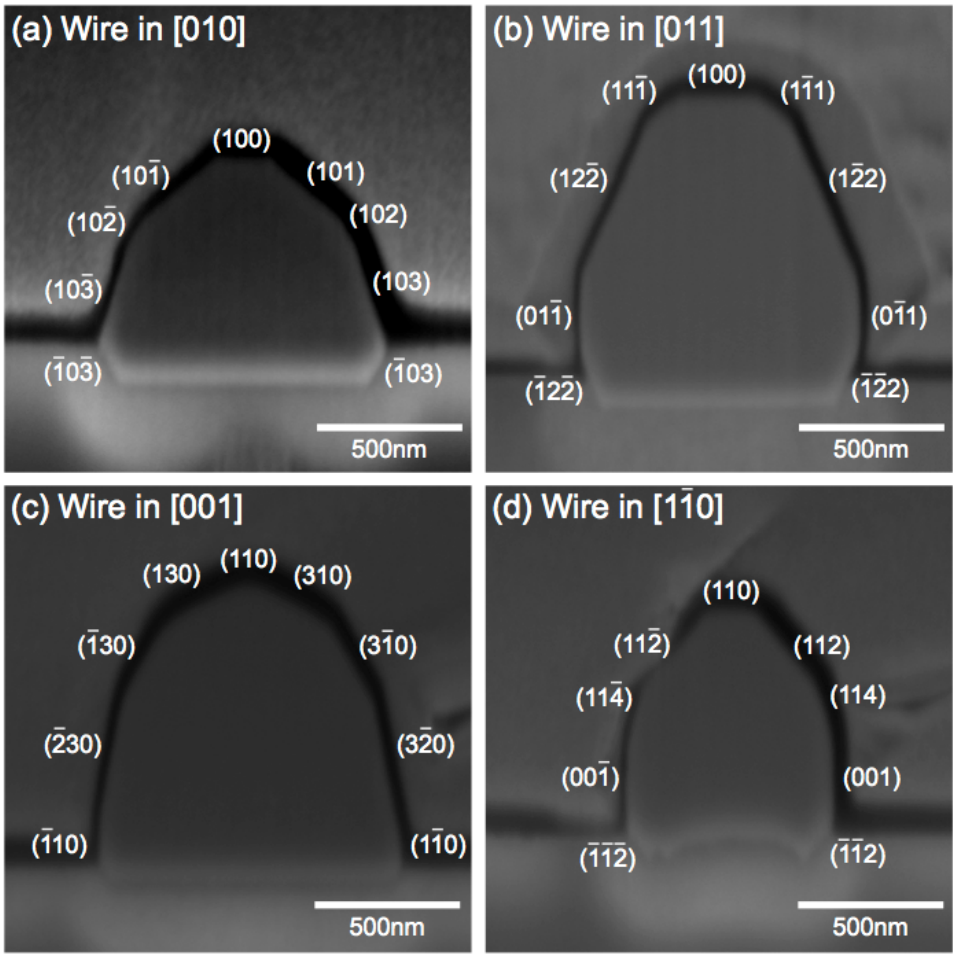

Figure 7-8. Cross-sectional SEM images of wires bound by facets with surface normals perpendicular to the wire axis of (a)-(b) Ni(100) and (c)-(d) Ni(110) wires on MgO. The same set of facets and shapes are observed for the equilibrated particle cross-sections. The particles were annealed at 890^0C under 2310sccm of reducing gas.

Furthermore, as shown in Figure 7-9, the kinds of facets observed in a retracting rim in Ni(111) on MgO and sapphire remain the same, although different contact angles expose a new facet below {211} in the Ni(111) film on sapphire. In addition, as demonstrated in Figure 7-10, there is no systematic difference in the retraction distance of patterned patches in the Ni(111) on MgO and sapphire. These further demonstrate that the reaction between Ni and MgO does not significantly affect the dewetting kinetics.

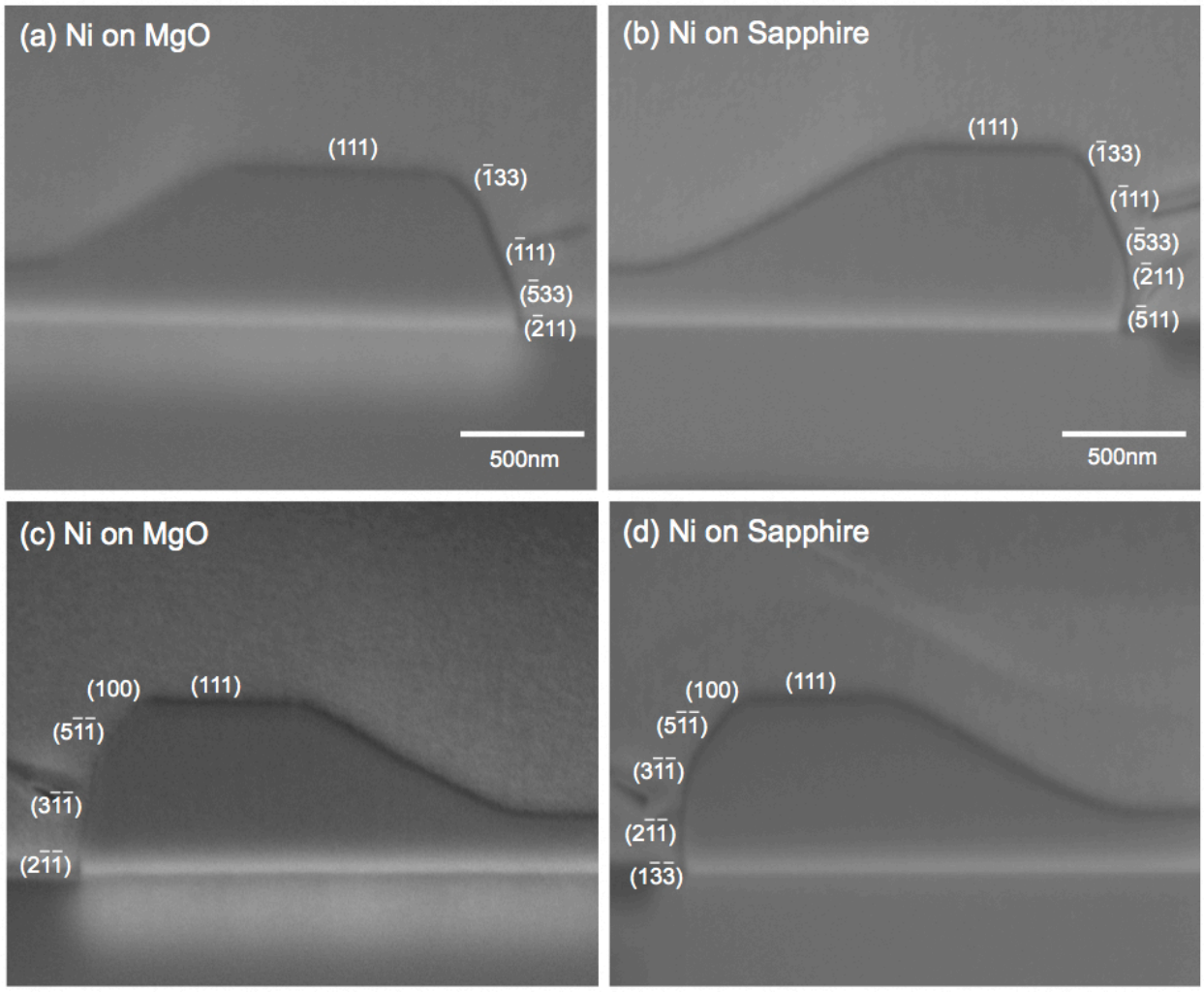

Figure 7-9. Cross-sectional SEM images of retracting rims on both sides of patterned square patches in the $[0\bar{1}1]$ orientation in Ni(111) on MgO and sapphire. Due to the hexagonal symmetry of Ni(111), the rims at the opposite edges of the same patch do not have the same set of facets. The patches were annealed at 890^0C for 10 hours under 2310sccm of reducing gas.

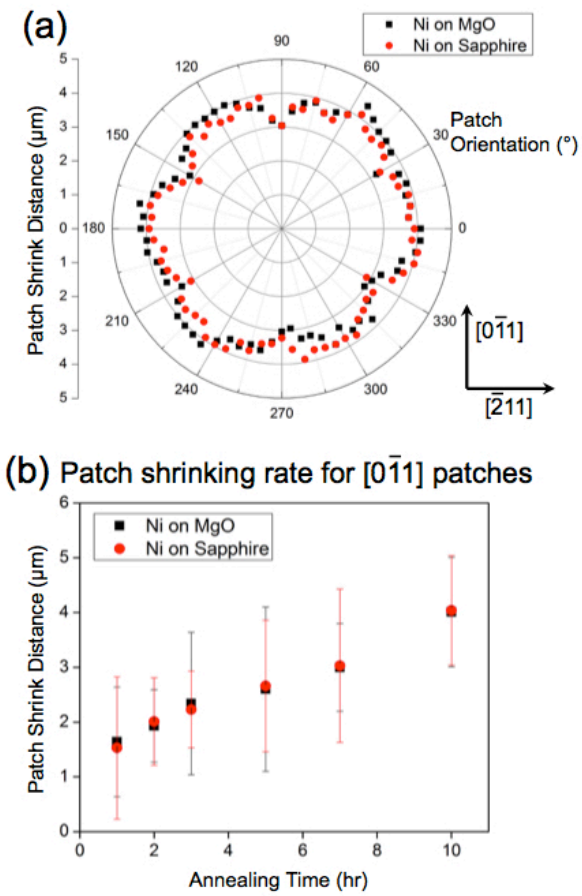

Figure 7-10. (a) Edge retraction distance of patterned square patches in Ni(111) on MgO and sapphire after 7 hours of annealing at 890^0C under 2310sccm of reducing gas. (b) Edge retraction distance of patterned square patches of Ni(111) on MgO and sapphire in the [0$\bar{1}$1] orientation.

Although the Ni-sapphire system avoids the issue of reaction between the wires and the substrate, the Ni-MgO system has more versatility as (100), (110), and (111) Ni films can be easily deposited. Furthermore, results for Ni(111) show only one set of relatively small peaks in the polar plots of Figure 7-3, limiting the extent to which the effects of crystalline anisotropy can be analyzed. Also, wires patterned from (111) films do not have the same equilibrium facets on their two sides, as illustrated in Figure 7-6. This further complicates analysis of the effects of crystalline anisotropy. Therefore the analysis was focused on the Ni(100) and Ni(110) films on MgO.

Ye and Thompson [22] studied single crystal Ni films patterned into large rectangular patches with edges aligned along different in-plane orientations, and characterized the retraction rate and morphology of the retracting edges. They found that edges with specific in-plane orientations remained straight (kinetically stable) during retraction, while the majority of the edges developed periodic in-plane facets as they retracted. The individual in-plane facets that formed on these edges had the same in-plane orientations as the kinetically stable retracting edges, and edges with kinetically stable orientations retracted more slowly than other edges.

To investigate a possible linkage between the development of in-plane facets on retracting edges and the particle spacing observed after complete dewetting of strips, the facet period was measured for strips with different widths (130nm, 2, 3, and 4μm) patterned from films of a fixed thickness (130nm). 130nm-wide strips did not significantly retract, but instead immediately developed perturbations that led to particle formation. Wider strips underwent significant retraction and developed in-plane edge facets before they formed wires that broke up into particles (Figure 7-11). Within experimental accuracy, the edges of these wider strips developed in-plane facets with periods, λ_f, that were independent of the initial strip width (Table 7-1). However, once the retracting edges coalesced to form wires, the wires subsequently decomposed into particles with a spacing λ_p that *did* depend on the initial strip width, and was always significantly larger than the facet period. If an effective wire radius is defined in terms of the initial strip width w and film thickness h such that

$$R_{eff} = \sqrt{wh}\,,$$

it was found that λ_p/R_{eff} is a constant (Table 7-1) for strips of all initial widths, as expected for decomposition due to a Rayleigh-like instability. It should also be noted that the trend in λ_p/R_{eff} applies to very narrow wires (130nm) patterned so as to have a width to thickness ratio of 1, and requiring no edge retraction. These results suggest that the instability that leads to faceting of retracting edges differs from the Rayleigh-like instability that develops once wires are formed.

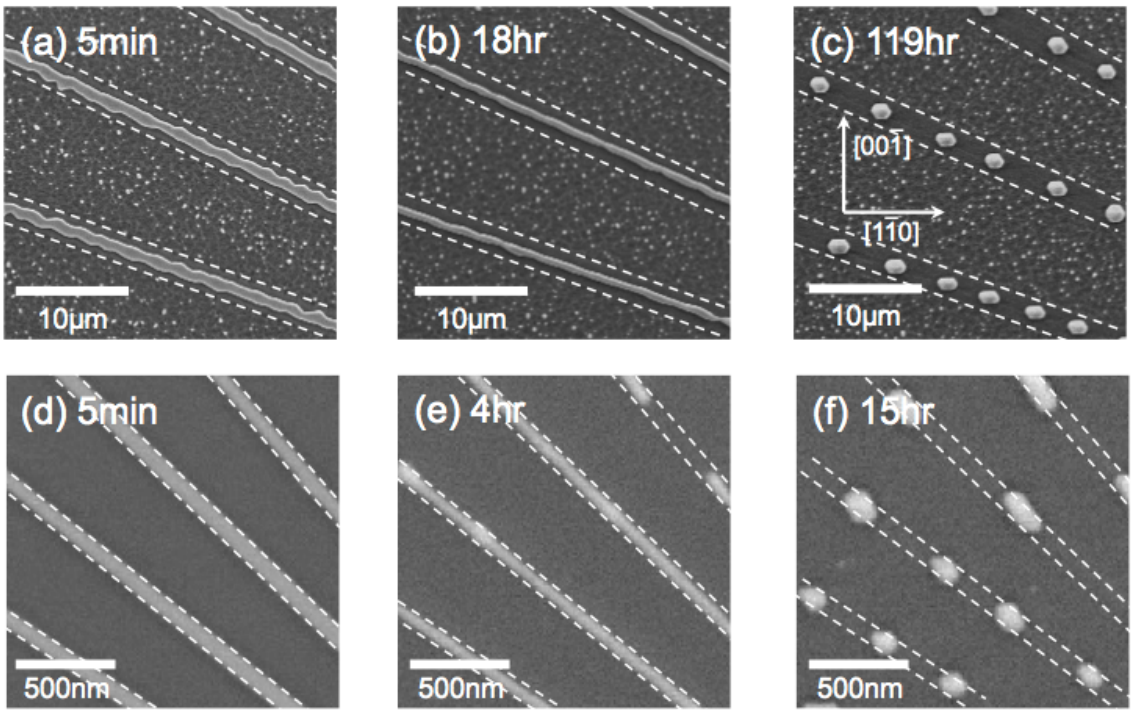

Figure 7-11. Development of a Rayleigh-like instability in strips patterned from (110) Ni films on MgO. (a)-(c) show strips with initial width-to-thickness ratios greater than 1 (w = 3.2μm and h = 130nm). (d)-(f) show strips with initial width-to-thickness ratios equal to 1 (w = 130nm and h = 130nm). Strips were annealed at 890^0C for the indicated times. Dashed lines indicate initial strip shapes. Note that the wide strip developed edge facets as its edges retracted, but that the period of these facets was much smaller than the final particle spacing. The narrow strips did not form edge facets before decomposing into particles.

Table 7-1. Facet period λ_f for in-plane facets formed on retracting edges of strips of width w patterned from 130nm-thick single crystal Ni films. λ_p is the final particle spacing for arrays of particles resulting from a Rayleigh-like instability. The effective radius R_{eff} is defined in the text, and scales with $\sqrt{w}$.

(100)-texture, strip axis 25^0 relative to the [001] in-plane direction

w (μm)	R_{eff} (μm)	λ_f (μm)	λ_p (μm)	λ_p/R_{eff}
0.13	0.13	None	2.0±1.5	15.4±11.5
1.8	0.49	2.83±0.78	10.7±4.2	21.8±8.57
2.8	0.60	2.8±0.6	11.7±3.3	19.5±5.5
3.7	0.69	2.87±0.6	13.3±5.1	19.3±7.4

(110)-texture, strip axis 35^0 relative to the $[1\bar{1}0]$ in-plane direction

w (μm)	R_{eff} (μm)	λ_f (μm)	λ_p (μm)	λ_p/R_{eff}
0.13	0.13	None	1.78±0.42	13.7±3.3
1.3	0.41	3.2±1.5	4.18±0.75	10.2±1.8
2.2	0.54	3.25±1.8	6.23±1.4	11.5±2.6
3.2	0.64	3.21±1.2	7.04±1.5	11.0±2.3

Particle spacings at the end and in the middle of the wires were compared in order to determine if the finite length of our patterned strips might affect the overall measured particle spacing. The kinetic solution derived by Nichols and Mullins [96] for the Rayleigh-like instability in isotropic solid structures predicted that for a cylindrical rod of finite length, ovulation occurs at the end of the rod and proceeds toward the body of the rod. In the current experiment it was found that while the ends of the wires *did* begin evolving earlier than other parts of the wires, the break-up of wires also occurred along their length. Particle spacings at the wire ends and along the length of the wires were found to be the same, within experimental error, and the spacings at the ends were neither consistently larger nor smaller than the spacings in the middle of the wires. This is illustrated in Figure 7-12.

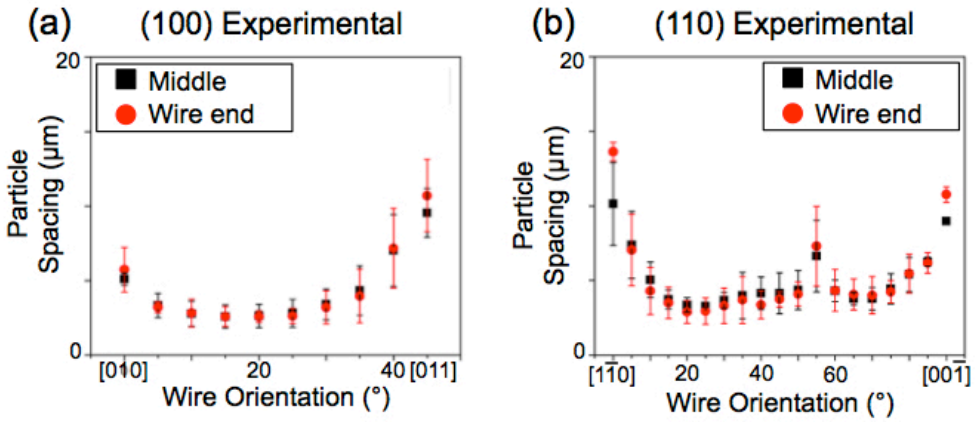

Figure 7-12. Comparison of perturbation wavelengths measured at the wire end and the body of the wire formed from (a) 0.809µm-wide strips in Ni(100) under 2310sccm of reducing gas, (b) 0.850µm-wide strips in Ni(110) under 2310sccm of reducing gas.

As discussed in Chapter 1, the minimum stable perturbation wavelength for a cylindrical free-standing or partially wetting wires with isotropic surface energy is proportional to R_o, the initial radius of the wire

$$\lambda_{crit} \propto R_0, \tag{7-1}$$

and the wavelength of the fastest growing perturbation is

$$\lambda_{max} = \sqrt{2}\,\lambda_{crit}. \tag{7-2}$$

It is this fastest growing perturbation that typically sets the final characteristic particle spacing, λ_p. Figures 7-13 and 7-14 show the particle spacing or perturbation period plotted as a function of R_{eff}, and demonstrates that a scaling relationship holds for λ_p and R_{eff} for wires formed from dewetting strips. However, the constant of proportionality for λ_p and R_{eff} is seen to depend on the crystallographic alignment of the wire and the out-of-plane orientation of the film as well. Also, the proportionality constant is found to depend on the annealing ambient.

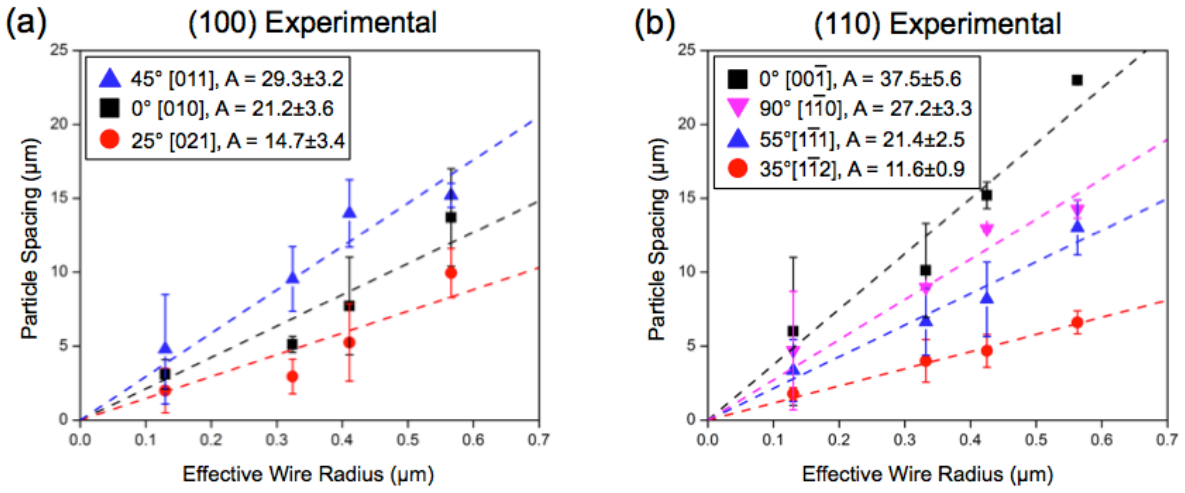

Figure 7-13. Linear relationship between particle spacing or perturbation wavelength and the effective radii of wires from (a) Ni(100) and (b) Ni(110) films on MgO annealed under 2310sccm of reducing gas. Angles in the legend indicate orientations of the axes of the wires and indices in brackets indicate the directions normal to the edges of the strips, as defined in Figure 7-1. For (a), 0 degrees corresponds to a wire with an edge normal in the [010] orientation; for (b), 0 degrees corresponds to a wire with edge normal [00$\bar{1}$]. *A* indicates the proportionality constant from a linear fit.

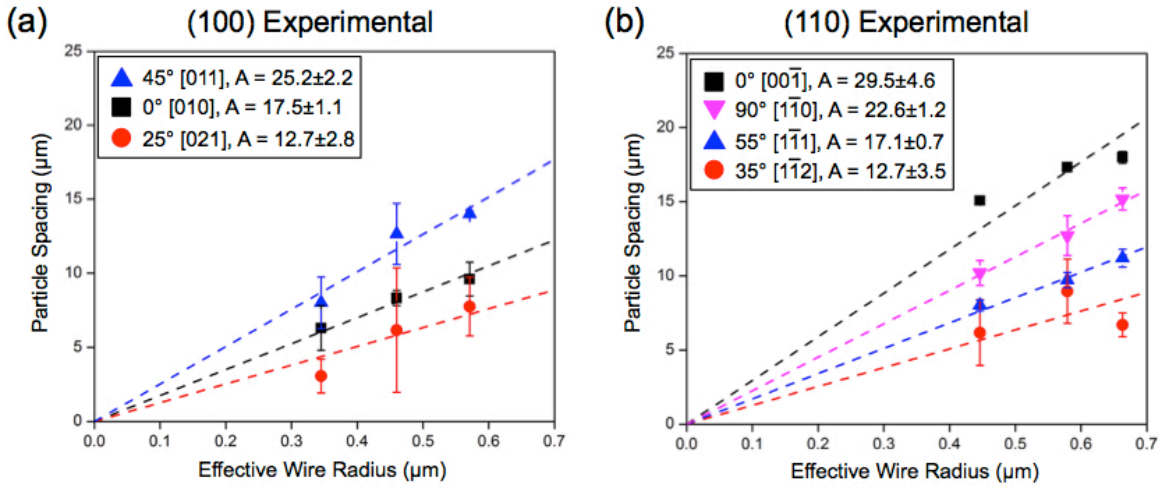

Figure 7-14. Linear relationship between particle spacing or perturbation wavelength and the effective radii of wires from (a) Ni(100) and (b) Ni(110) films on MgO annealed under 95sccm of reducing gas. Angles in the legend indicate orientations of the axes of the wires and indices in brackets indicate the directions normal to the edges of the strips, as defined in Figure 7-1. For (a), 0 degrees corresponds to a wire with an edge normal in the [010] orientation; for (b), 0 degrees corresponds to a wire with edge normal [00$\bar{1}$]. *A* indicates the proportionality constant from a linear fit.

7.4. Kinetic Monte Carlo Model

A Kinetic Monte Carlo (KMC) simulation was conducted using an algorithm similar to that used by Pierre-Louis et al.[97] in models of dewetting. Because crystalline Ni has a face-centered cubic (FCC) structure, the simulation was run for an FCC lattice. Two inputs in the simulation, the bond energy of Ni (J) and the Ni-MgO interfacial energy (E_s), were required. The bond energy was estimated using Ni surface energies experimentally determined for different facets in the presence of H_2 [74] and dividing the values by the number of first-order bonds in a unit surface, giving $J = 0.2$eV. The Ni-MgO interface energy (E_s) was taken to be 1.12J/m^2 [98] and the MgO surface energy was taken to be 1.15J/m^2 [99] for (100) surfaces, which gives $E_s = 0.5$eV. The KMC results were not very sensitive to changes in these values; a 50% change in J or E_s resulted in at most a 7% change in the observed particle spacings.

Results for two 6ML (monolayer) wide, 3ML thick, and 100ML long (110) strips with different in plane orientations are shown in Figure 7-15. As also seen in experiments, the dewetting rate depends on the in-plane crystallographic orientation of the strip. Examples of (110) and (100) particles are shown in top-view and side-view in Figure 7-16. These reveal the more limited number of equilibrium facets observed in the KMC simulations than in the experiments on Ni. The particle spacing as a function of in-plane orientation for (100) and (110) strips is shown in Figure 7-17. As in the experiments, the particle spacing at the end of wires was found to be indistinguishable from the spacing in the middle of the wires, within the observed variation of the simulation results from run to run. Also as observed in experiments, the wires that broke up into particles most slowly and broke up into particles with the largest spacings, were wires that were bound by equilibrium facets whose normals were perpendicular to the wire axis.

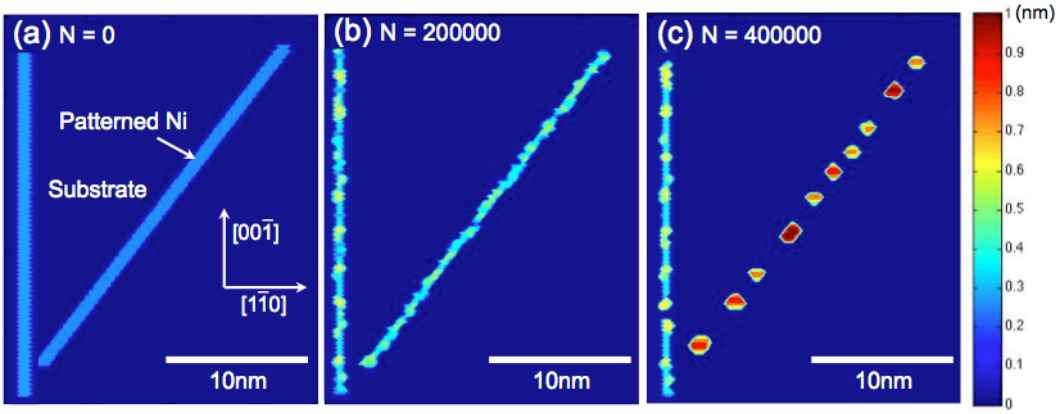

Figure 7-15. Break-up of Ni(110) wires in a Kinetic Monte Carlo simulation. *N* indicates the number of iteration steps.

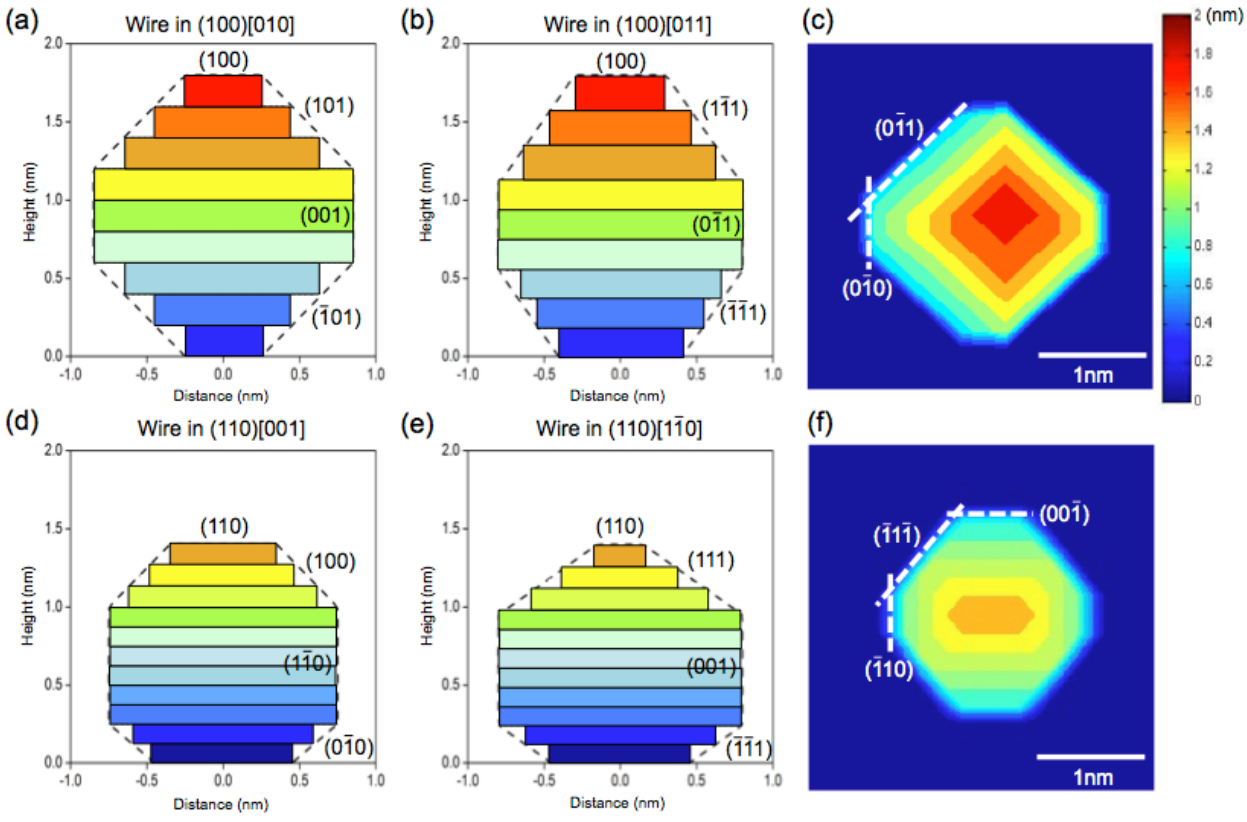

Figure 7-16. Cross-sections and top-down views of equilibrated Ni particles formed from (a)-(c) Ni(100) and (d)-(f) Ni(110) films in Kinetic Monte Carlo simulations. Dashed lines indicate monolayers.

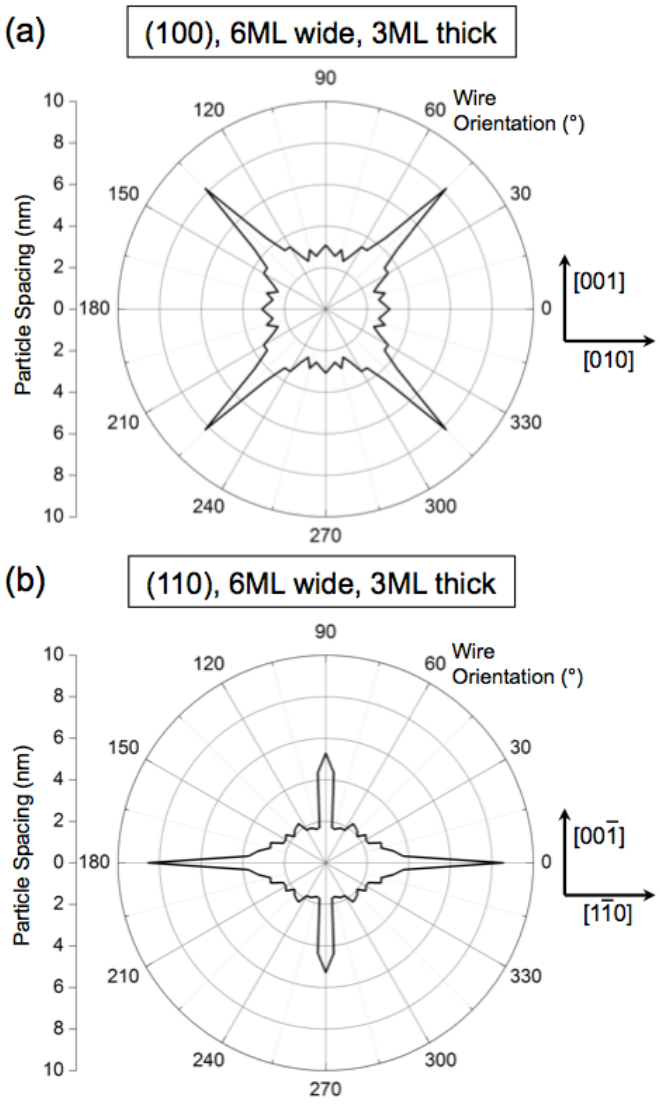

Figure 7-17. Particle spacing or perturbation wavelength from Kinetic Monte Carlo simulations for (a) (100) and (b) (110) FCC strips. The angles are relative to the [010] in-plane orientation for (100) films (in (a)) and the [1$\bar{1}$0] in-plane orientation for (110) films (in (b)).

To compare the simulation results with the experimental results, effective radii are normalized with respect to the values for 6ML wide lines. As in the case of the experiments, the facet period λ_f of the retracting edges of wide lines was found to be independent of the initial strip width, but the particle spacing λ_p was found to scale with the normalized effective radius R_{eff} (Table 7-2). Figure 7-18 shows the particle spacing as a function of the normalized R_{eff} for

lines with different in-plane crystallographic orientations. Again, λ_p scales with R_{eff}, but with a constant of proportionality that depends on the in-plane crystallographic orientations of the wires. Furthermore, no systematic difference between the λ_p at the end of the wire and in the middle of the wire was observed, as in the case of the experiments (Figure 7-19).

The general agreement between the behavior observed in the experiments and the KMC simulations suggests that the observed phenomenology is fundamental in origin, and not an artifact of the experiments.

Table 7-2. Facet period λ_f for in-plane facets formed on retracting edges of strips of width w in Kinetic Monte Carlo simulations. The value of w is normalized with respect to 6ML-wide strips. λ_p is the final particle spacing for arrays of particles resulting from a Rayleigh-like instability. The effective radius R_{eff} is defined in the text, and scales with $\sqrt{w}$. Here, the effective radius is normalized by the effective radius of a 6ML-wide, 3ML-thick strip.

(100)-texture, strip axis 25^0 relative to the [001] in-plane direction

R_{eff}	λ_f(nm)	λ_p (nm)	λ_p/R_{eff}
0.58	1.9±0.7	2.16±0.9	4.32±1.8
1	2.0±0.8	3.3±1.0	3.3±1.0
1.29	1.8±0.8	4.3±1.2	3.6±1.0

(110)-texture, strip axis 35^0 relative to the $[1\bar{1}0]$ in-plane direction

R_{eff}	λ_f(nm)	λ_p (nm)	λ_p/R_{eff}
0.58	1.25±0.74	1.25±0.74	2.50±1.48
1	1.18±0.6	2.29±1.0	2.29±1.0
1.29	1.3±0.75	3.0±0.9	2.5±0.75

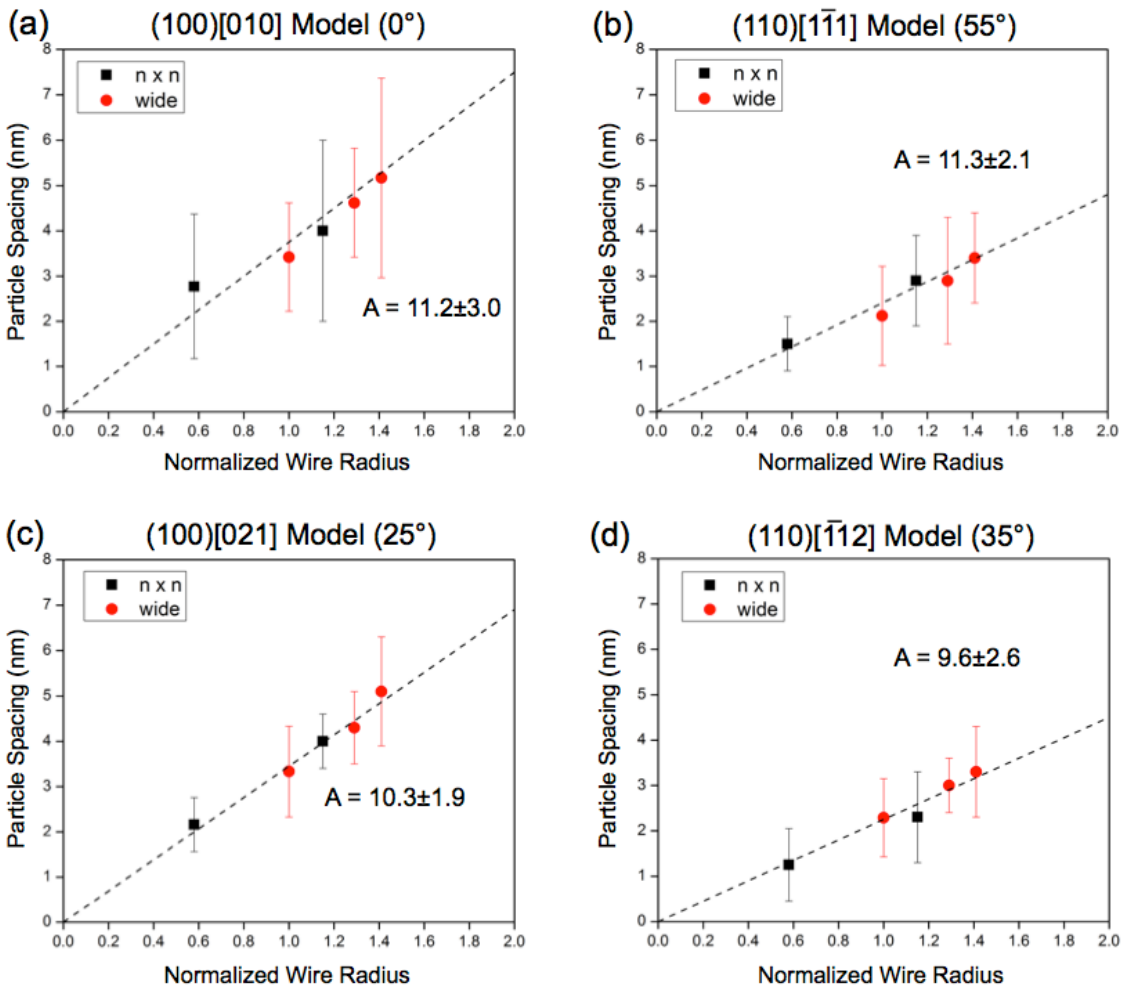

Figure 7-18. Particle spacing as a function of normalized effective radii from the Kinetic Monte Carlo simulations. “n x n” indicates strips with an aspect ratio of 1 and “wide” indicates strips with widths larger than their thickness. The indexes in square brackets are the in-plane directions normal to the edge of the strip and the angles are relative to the [010] in-plane orientation for (100) films ((a) and (c)) and the [1$\bar{1}$0] in-plane orientation for (110) films ((b) and (d)).

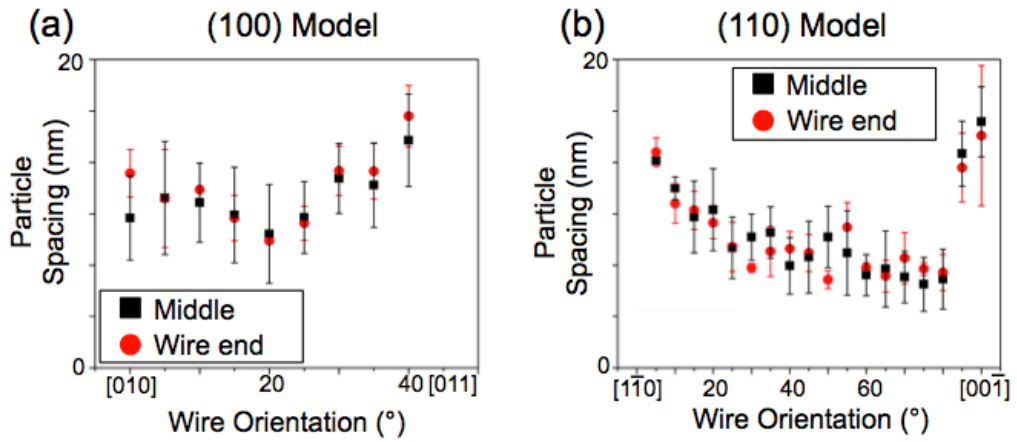

Figure 7-19. Comparison of perturbation wavelengths measured at the wire end and the body of the wire for (a) 6ML-wide, 3ML-thick, 100ML-long wires of Ni(100) in the KMC simulation, (b) 6ML-wide, 3ML-thick, 100ML-long wires of Ni(110) in the KMC simulation.

7.5. Discussion

As was discussed in Chapter 1, Cahn [61] was the first to develop a model that accounted for the effects of surface energy anisotropy on the Rayleigh instability of wires. He treated the simple case in which the surface energy was radially isotropic for rotations about the wire axis, but varied with the orientation of the surface normal relative to the wire axis ψ. Under these conditions he found

$$\lambda_{crit} = 2\pi R_0 \sqrt{1 + \frac{\gamma''}{\gamma_0}}, \tag{7-3}$$

where γ_0 is the surface energy for $\psi = 0$ and $\gamma'' = \partial^2\gamma/\partial\psi^2$ is the curvature of the gamma plot (γ vs. ψ) near $\psi = 0$. In the limit that $\gamma'' = 0$, this reduces to the result for isotropic surface energy. For positive γ'', surface energy anisotropy leads to an increased λ_{crit} for a given R and is stabilizing. Cahn [61], and later Du and Wong [100], noted that for perfectly flat singular facets, γ'' diverges and becomes ill defined. However, at non-zero temperatures, entropy leads to defects (e.g. individual and small clusters of adatoms and surface vacancies) that lead to a range of stable local orientations, causing $\gamma''$to be finite. γ'' will go to zero at the roughening temperature, and

will increase to become ill-defined only in the limit of a perfectly flat defect-free interface; however, the second derivative's behavior is well-defined in the limit of singularity. Also, in experiments there are other sources of defects, such as ledges resulting from imperfect lithographic alignments, that will lead to finite values γ''.

Stolken and Glaeser [101] subsequently showed that for Cahn's assumptions and for capillary driven surface diffusion

$$\lambda_{max} = \sqrt{2}\,\lambda_{crit}, \tag{7-4}$$

as in the case for isotropic surface energy and partially wetting cylinders. The higher the curvature of the gamma plot at the cusp at γ_0, the greater the effect of surface energy anisotropy, and the higher the value of λ_{max} and the interparticle spacing. The interparticle spacing also increases with decreasing γ_o.

In the present case wires that are bound by facets along their length will be focused on. An initial surface energy of the wire can be defined as

$$\gamma_{f,o} = \frac{\sum_i L_i \gamma_i}{\sum_i L_i}, \tag{7-5}$$

where L_i and γ_i are the length and surface energy of the i^{th} facet along the perimeter of the wire (including the wire-substrate interface). As in Cahn's model, the formation of a radial perturbation for which ψ departs from zero will have an associated energetic cost that will be a function of the magnitudes of γ_i''. A simple analogy to Cahn's analysis would then be to take

$$\gamma_f'' = \frac{\sum_i L_i \gamma_i''}{\sum_i L_i}, \tag{7-6}$$

so that

$$\lambda_{max} = \sqrt{2}\,2\pi R_{eff}\sqrt{1 + \frac{\gamma_f''}{\gamma_{f,o}}}. \tag{7-7}$$

Unfortunately, the values of γ_i'' are not known. Moreover, they are likely to be strongly affected by experimental conditions, especially near singular orientations. However, if it is assumed that the values for γ_i'' are finite and similar for all facets, it would be expected that log (λ_{max}) would scale inversely with log ($\gamma_{f,0}$). Figure 7-20 shows a plot of log (λ_{max}) vs. log ($\gamma_{f,0}$) for the wires bound by equilibrium facets in both experiments and the KMC simulations. The results are qualitatively consistent with the simple model outlined above. In the figure, particle spacings or wavelengths were normalized by effective radii to eliminate the size effect of the wires.

The scenario is significantly more complex for wire orientations that cannot be bound along their lengths by equilibrium facets. In this case, energies of edge facets can be lowered by decomposition into facets that are not parallel to the wire axis. This might lower λ_{crit} compared to the isotropic case. However, the effects of a perturbation in R_{eff} is governed by the collective effects of deviations from $\psi = 0$ for all of the facets. A detailed and general understanding of the effects of surface energy anisotropy on the stability of wires and the rate and characteristic length scale at which they decompose due to a Rayleigh-like instability will require significant advances in modeling and simulations.

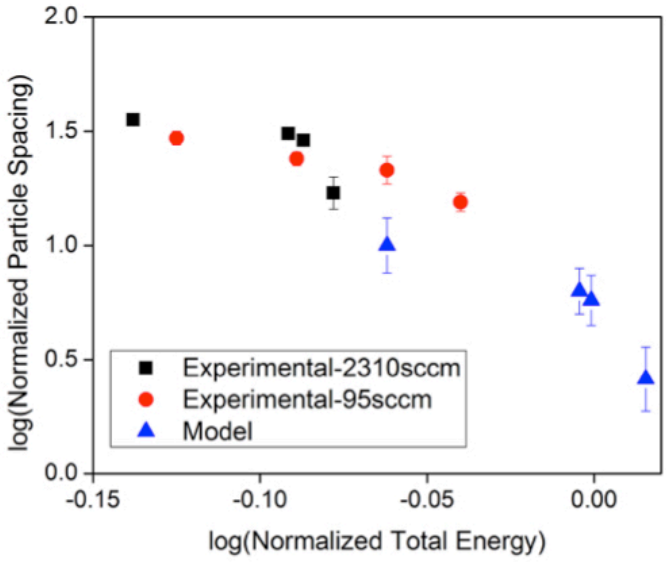

Figure 7-20. Relationship between the normalized particle spacing or perturbation wavelength as a function of the normalized surface energy of the wire perimeter, $\gamma_{f,0}$, as defined in the text. Data are shown only for wires bound by equilibrium facets with surface normals perpendicular to the wire axis.

7.6. Summary and Conclusion

The effects of surface energy anisotropy on Rayleigh-like instabilities of solid wires were investigated through dewetting of strips of single crystal Ni films on MgO and sapphire. Strips were patterned from films with different epitaxial orientations and were patterned such that their edges aligned along different in-plane crystallographic directions. When heated, the edges of the strips retracted and merged to form wires, which subsequently decomposed to form arrays of particles with characteristic spacings. The rate and characteristic length scale of this decomposition process depended strongly on the crystallographic orientation of the wires. Wires with orientations that are bound by equilibrium facets with surface normals perpendicular to the wire axis decomposed most slowly, and decomposed into particles or perturbations with the largest spacing. Strips with these orientations were also stable with respect to in-plane faceting during retraction of their edges. Wide strips with other crystallographic orientations developed periodic in-plane facets during edge retraction, with facet periods that were independent of the

initial strip width. After the edges of these strips coalesced to form wires, and those wires decomposed to form arrays of particles, the spacing of those particles significantly exceeded the in-plane edge facet period, and scaled with the initial strip width for a given strip thickness. This demonstrates that the instability that leads to in-plane faceting of retracting edges differs from the Rayleigh like instability that leads to formation of arrays of particles. Similar phenomenology was observed in Kinetic Monte Carlo models of Rayleigh-like decomposition of solid wires on substrates.

As in the case of systems with isotropic surface energies, the interparticle spacing was found to scale with the effective radius of the wires. However, unlike the case of wires with isotropic surface energies, the crystallographic orientation of single crystal wires also affected the scaling of the particle spacing with R_{eff}. This can be qualitatively explained in terms of the energetic cost of creating non-planar surfaces from equilibrium singular surfaces. It was found that the particle spacing for wires bound along their length by equilibrium facets increased for wires with low weighted surface energies around their perimeters.

The phenomenology observed here is similar to the phenomenology observed for cylindrical pores formed in single crystal sapphire. The experimental methodology developed here can be readily extended to other wire materials and different annealing ambients. Experiments of this type provide a rich basis for development of detailed models of the effects of surface energy anisotropy on Rayleigh-like instabilities, and for capillary-driven morphological evolution in the presence of strong surface energy anisotropy in general. An improved understanding of the decomposition of patterned thin film strips can also provide insight into strategies for producing patterned micro- and nanostructures with improved stability for applications in microsystems, as well as provide insights into ways in which dewetting of patterned films can be used to produce arrays of particles for use as catalysts or in photonic, sensing, and other devices.

Chapter 8. Summary and Future Work

8.1. Summary

During solid-state dewetting of thin single crystal films, regular dewetting morphologies are observed due to anisotropy in surface energy and surface diffusivity. When the continuous single crystal film is templated prior to dewetting, complex structures of sub-lithographic length scales can be reproducibly made, posing a potential for many applications. During solid-state dewetting, many dewetting phenomenologies occur, and understanding and modeling the characteristic length scales of the individual dewetting phenemenologies in a quantitative manner is crucial for the predictable use of templated solid-state dewetting in patterning applications. This thesis studied and modeled the individual dewetting phenomenologies in more detail.

In Chapter 3, anisotropic retraction of pre-patterned edges was discussed. It was found that edges retracting in certain in-plane orientations have locally minimum retraction rates and these are called kinetically stable edges. Among the kinetically stable edges, it was found that the relative retraction rates are different and the edges with smallest retraction rates define the shape of natural holes forming in continuous films. Furthermore, it was found that the relative retraction rates change under different annealing ambient conditions. Surface structure analysis revealed that there are different reconstructed surface structures under different ambient conditions and it was found that these surface structure changes are closely linked to the changes in the retraction rates.

In Chapter 4, pinch-off of retracting rims via valley formation was discussed. Critical pinch-off width, defined as the smallest width of the pre-patterned strip that pinched off, was measured for the rims retracting in different in-plane orientations. Different critical pinch-off width was measured for different in-plane retraction orientations and under different ambient conditions. It was found that surface energies of equilibrium facets change under different ambient conditions, and this leads to the changes in the additional surface energy cost associated

with the initiation of valley formation. This additional surface energy cost is found to be directly related to the critical pinch-off width.

In Chapter 5, fingering instability was discussed in detail. It was found that mass is rejected from the finger tip, so that the rim at the tip maintains a constant height and the fingered front moves at a constant rate. A steady-state model for the motion of a fingered front was developed and found to be in agreement with experiments. This model accounts for the lateral rejection of mass to form wire-like structures between the fingers, and shows that the finger spacing is determined by the velocity of the finger tips relative the diffusivity governing mass rejection.

In Chapter 6, corner instability during the propagation of polygonal natural holes in single crystal films was discussed. It was found that there is a steady-state rim shape at the corner that leads to a steady-state retraction rate, while the retraction rate at the straight edge decreases over time due to mass accumulation and rim thickening. A computational model was also developed. It was found from the model that corner instability occurs when a balance between two competing local effects was attained: Thinning of the rim height at the corner due to corner tip lengthening during tip retraction, and thickening of the rim height at the corner due to mass accumulation at the tip during tip retraction.

In Chapter 7, Rayleigh-like instability of wire-like structures in single crystal films was discussed. Similar to the traditional Rayleigh-Plateau instability, a linear dependence of the dewetted particle spacing on the effective radius of the wire-like structures was observed. However, due to anisotropy in surface energy and surface diffusivity, the final particle spacing and the time to fully dewet into particles were different for the wires patterned in different in-plane orientations. The wires in certain orientations were much more stable against the Rayleigh-like instability, and these wires had a locally maximum particle spacing. In addition, it was found that, for a fixed cross-sectional area, the total surface energy of the fully faceted wires determines the dewetted particle spacing.

8.2. Future Work

Once the individual phenomenologies observed during solid-state dewetting of thin single crystal films are analyzed quantitatively and sufficient predictive models are developed, many potential applications can be explored.

As introduced in Chapter 1, templated solid-state dewetting of thin single crystal films can be used to produce reproducible structures in the sub-lithographic length scale. Due to anisotropy in surface diffusivity and surface energy, anisotropic dewetting morphologies are observed in single crystal films. The possibility of the intentional use of templated dewetting in patterning applications has been explored by Ye and Thompson [66], and the formation of complex, ordered structures from pre-patterned single crystal Ni films was also observed alongside with this thesis research. These dewetting structures are illustrated in Figures 8-1 and 8-2. Once such structures are made in single crystal films on single crystal substrates, these patterns can be easily transferred to other appropriate substrates or devices. It is known [102, 103] that metallic nanostructures can be transferred using polymer-based materials that can be easily removed after the transfer.

However, these structures have thus far been generated from a relatively thicker films (~100nm), and thus, although the length scale of the resulting structures are much smaller than the original patterns, the structures are still on the order of μm. To decrease the length scale of the dewetted patterns, the initial film thickness has to be decreased. However, as introduced in Chapter 1, natural holes can form more easily with decreasing film thickness, and this can hinder the formation of ordered structures via templated dewetting. Improving the quality of the deposited single crystal film and identifying the cause and the mechanism of natural hole formation should precede before templated dewetting can be successfully used as a method to generate sub-lithographic nanostructures.

Although the cause of natural hole formation is not yet completely known, there are some preliminary studies and results on the cause of natural hole formation. Danielson [104] studied the

cause of natural hole formation in silicon-on-insulator films by focusing on the defects that can be present. He determined that the density of natural holes was not correlated with the density of preexisting voids or the density of stacking faults or dislocations. Instead, he found that when natural holes form, process-induced surface particles were observed at the holes and he proposed that these particles are the heterogeneous cause of natural hole formation. In addition, he found that when impurities like Ge are present on the surface of the SOI film, the density of natural holes increased significantly.

In single crystal Ni films, some preliminary results were also obtained on the cause of natural hole formation. Through collaborative experiments with Fabien Cheynis, Stefano Curiotto, and Pierre Muller at Centre Interdisciplinaire de Nanosciences de Marseille of Aix Marseille Universite in France, natural hole formation was observed to occur at surface defects that pin the movement of step lines. However, not all such defects evolved into natural holes. In addition, when other extrinsic defects are introduced via unexpected arcing in the in-situ low energy electron microscope, the natural hole density was found to increase significantly. Also, through collaborative experiments with Yoon Ah Shin of the Thompson Group at MIT Department of Materials Science and Engineering and Solmaz Jahangir of the Valanoor Group at University of New South Wales Department of Materials Science and Engineering, some preliminary results were obtained, which imply that the photoresist residue due to imperfect surface cleaning after photolithography and etching may be linked to natural hole formation. All of these are potential areas that can be rigorously tested in the future to determine the cause of natural hole formation.

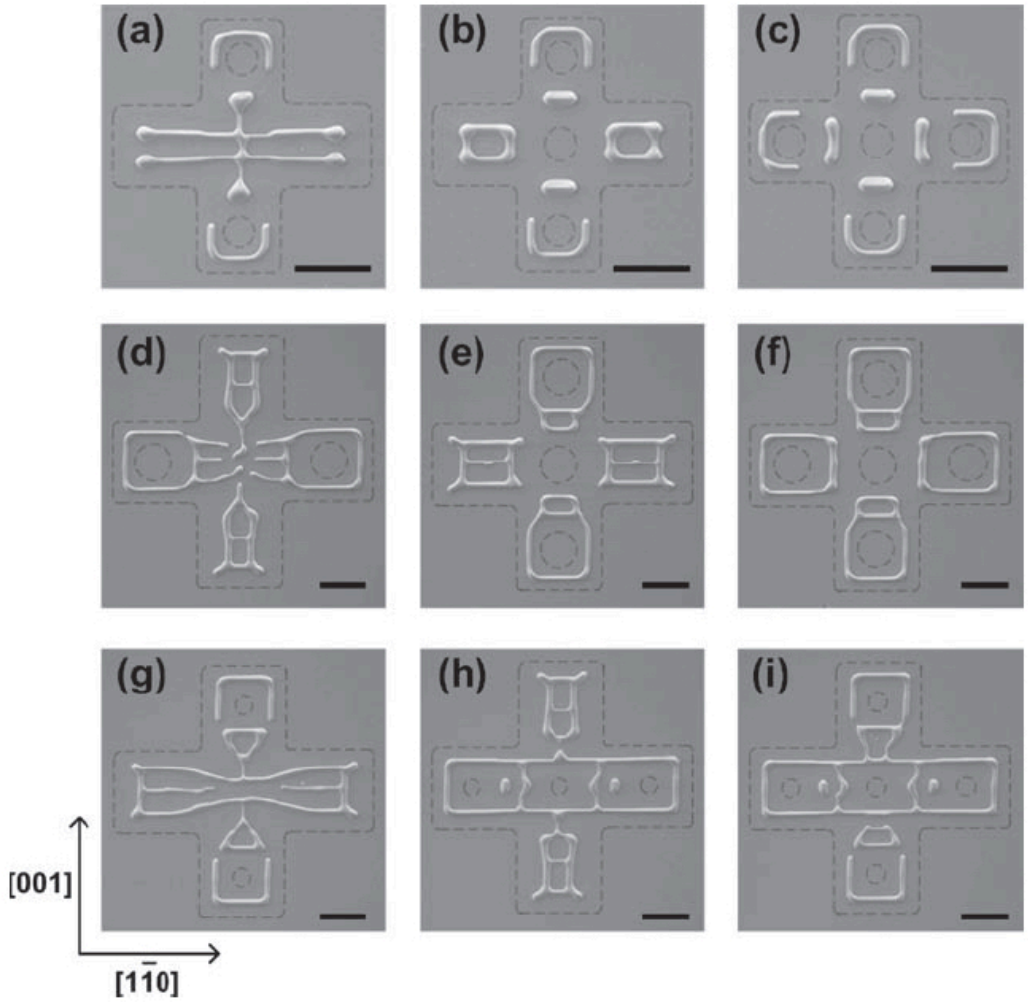

Figure 8-1. Dewetting of cross patches with pre-patterned internal circular holes patterned from a Ni(110) film [66]. (a)-(c) are SEM images of dewetted patterns with an initial edge length of 10.8μm. (d)-(i) are SEM images of dewetted patterns with an initial edge length of 18.4μm. The initial size of internal holes was bigger in the patches shown in (d) through (f) than in the patches shown in (g) through (i), as indicated by gray dashed lines. The gray dashed lines indicate the initial shapes of the patches. The annealing time was 1020 minutes and the thickness of the film was 120nm. Scale bars indicate 10μm.

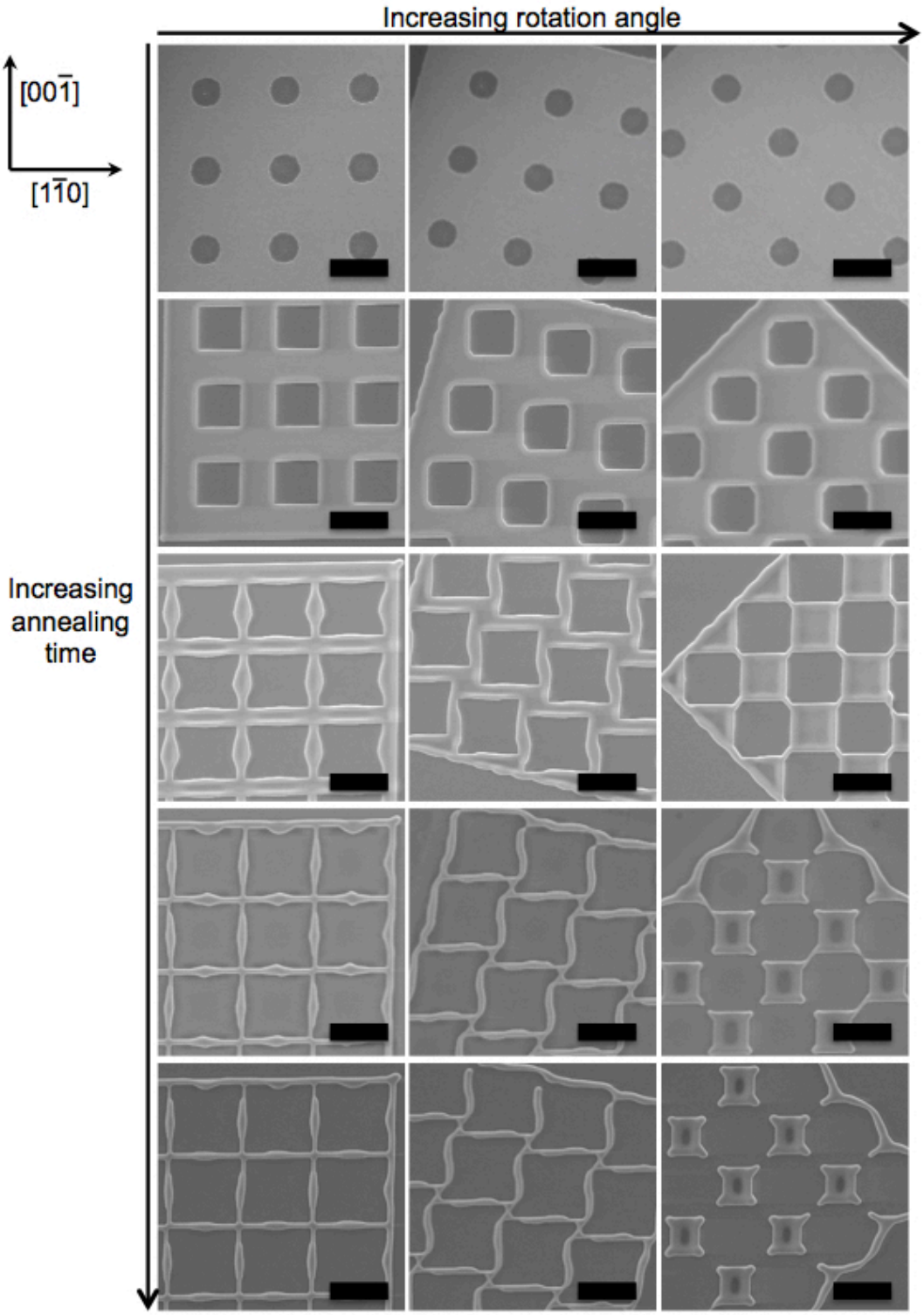

Figure 8-2. Propagation of pre-patterned holes on Ni(110) by dewetting. The square holes initially are 5μm in length and the initial spacing between the hole edges is 10μm. Bright regions in the micrographs are Ni. The angles of clockwise rotation are 0, 15, and 45 degrees, respectively, and the annealing times are 0, 1, 4, 9, and 12 hours, respectively. Scale bars, 10μm.

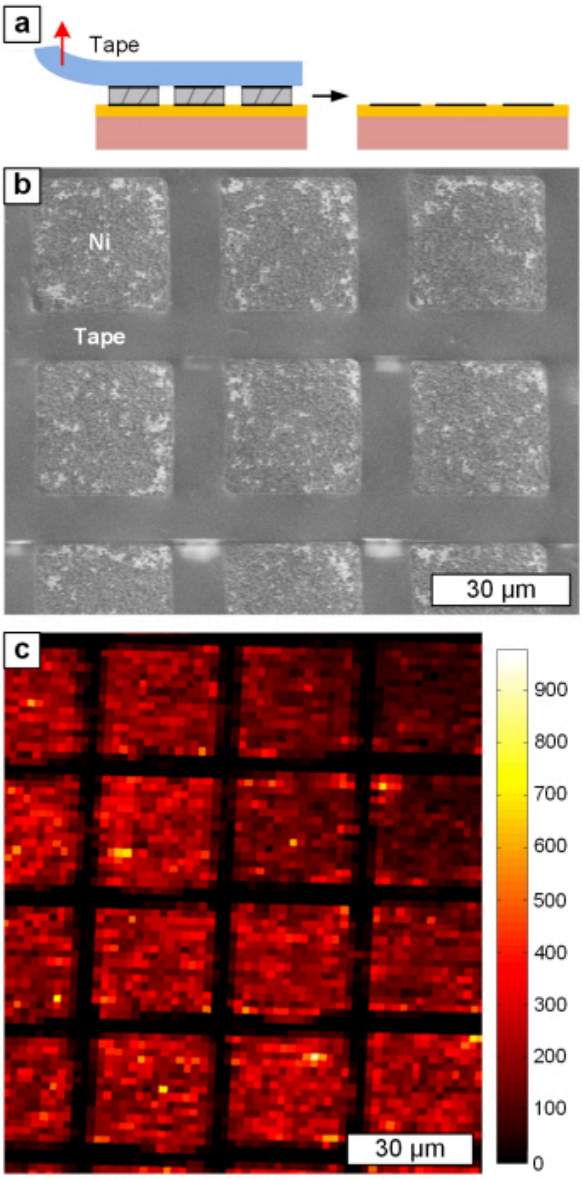

Figure 8-3. Fabrication of micro-scale graphene patterns by tape delamination of pre-patterned Ni, following interfacial graphene layer (IGL) growth [105]. The schematic in (a) shows the tape delamination of Ni leaving the patterned IGL on SiO_2. (b) SEM shows the delaminated Ni patterns on tape while the interfacial graphene on SiO_2 is confirmed by (c) 2-D Raman map.

McNerny et al.[105] have reported that graphene can be grown at the interface between a Ni film and the SiO_2 substrate. They have further shown that the graphene growth can be induced only at the interface between the patterned Ni film and the substrate, as shown in Figure 8-3. In their work, only simple square Ni patterns were tested for growth, but if graphene can be grown

at the film-substrate interface of complex Ni structures like those in Figures 8-1 and 8-2, patterned graphene could be easily generated for various potential applications.

Lastly, it is known [106] that, in fuel cells, maximizing the three-phase interface between the electrodes, the electrolyte, and the gas/liquid is important for efficiency. Furthermore, as electricity should be conducting, the electrodes should remain percolated. In annealing experiments of pre-patterned grid structures in single crystal Ni films as in Figure 8-2, it was found that the grids patterned to align with a certain set of crystallographic orientations are found to be highly stable against dewetting. These orientations generally correspond to the kinetically stable orientations (as introduced in Chapter 1), which are also found to be stable against the Rayleigh-like instability in the late stage of dewetting (Chapter 7). For example, the dewetted structure in the first column of Figure 8-2 remained stable and percolated even after 100 hours of annealing at 890°C. This poses a great potential for fuel cell applications, as such cells are often exposed to high temperatures but the structures of the electrodes designed to maximize the three-phase interface should remain percolated. In addition, as discussed in Chapter 4 and Chapter 7, straight wires with regular intervals can be easily made via pinch-off, and the wires in certain orientations are very stable at high temperatures. This can be an inexpensive method to control the triple line (three-phase boundary) density of the percolated structures of the electrode material in fuel cells and can be a useful tool to study the effect of the triple line density on the fuel cell efficiency.

Appendix A1. Templating of the Corner Instability

As discussed in Chapter 1 and Chapter 6, polygonal holes form in single crystal films due to crystallographic constraints and anisotropic surface diffusivity and surface energy. Therefore, well defined corners form in the polygonal natural holes, and these corners retract at a steady state velocity while the straight edges retract at a diminishing rate due to mass accumulation at the edge and rim thickening. This corner instability further complicates the natural hole morphology in the late stage of solid-state dewetting. Ye and Thompson [21] originally hypothesized that this corner instability is due to the larger diffusion field at the corners than at the straight edges, and the atoms diffuse from the sharp corners towards the flat film area. An illustration is reproduced from Figure 1-20.

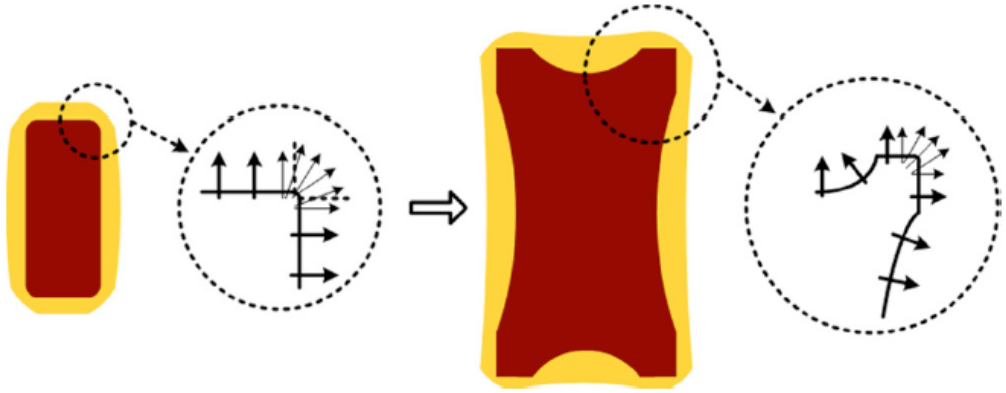

Figure A1-1. Schematic diagram of the diffusion field around a natural hole, after Ye and Thompson [21].

Based on the hypothesis, an additional series of experiments were designed to template the corner instability. If the difference between the size of the diffusion field at the corners and at the edges is critical for the initiation of the corner instability, it can be expected that if the

macroscopic in-plane angle of the corner is different, different corner instability behavior may be observed. Some key terminologies are graphically defined in Figure A1-2.

As illustrated in Figure A1-2, 130nm thick single crystal (100) and (110) Ni films were patterned via photolithography as discussed in Chapter 2. The films were patterned in a way that notches, or corners, of different angles exist in a given macroscopic orientation, and such corners were patterned in a multiple set of orientations with 15-degree intervals.

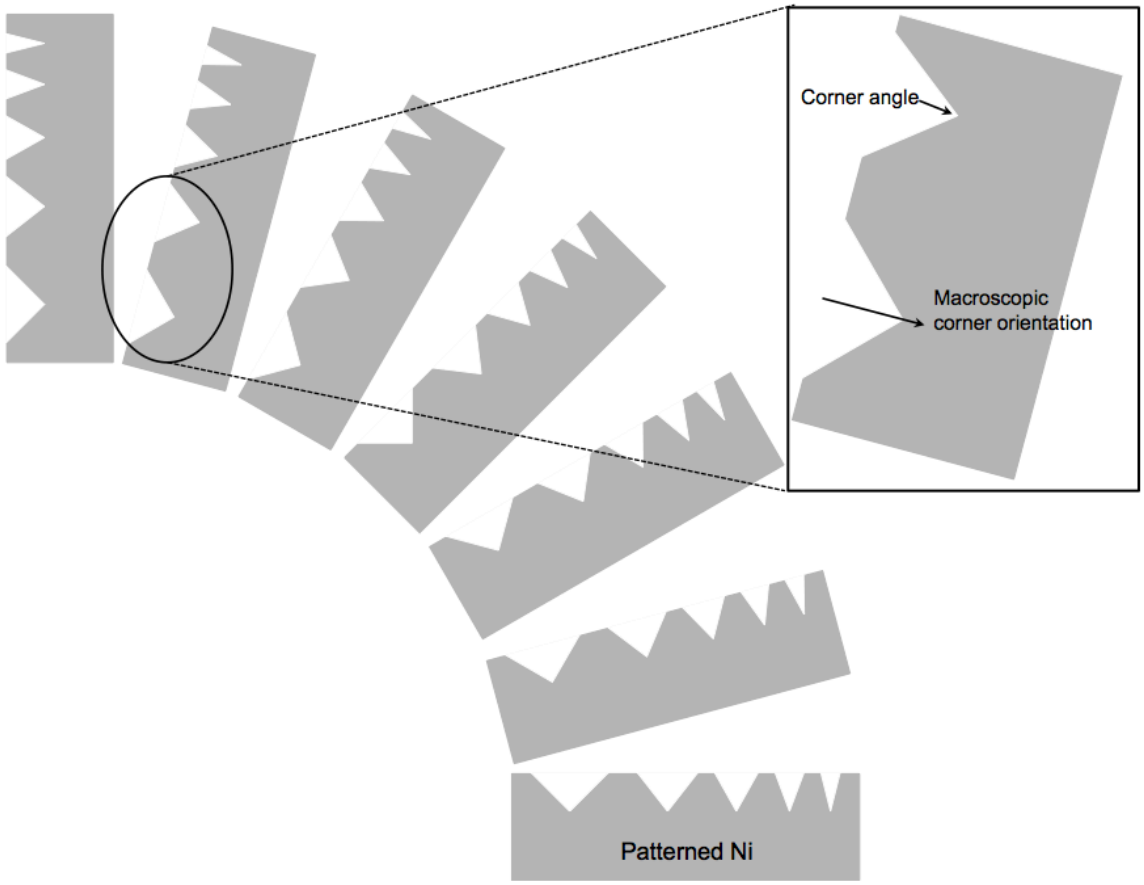

Figure A1-2. Schematic illustration of the pattern used to template the corner instability.

The patterned films were annealed for 12 hours at 890°C with a reducing gas (5% H_2 + 95% N_2) flowing at a rate of 2310sccm. Figures A1-3 and A1-4 show SEM images after the 12-hour anneal.

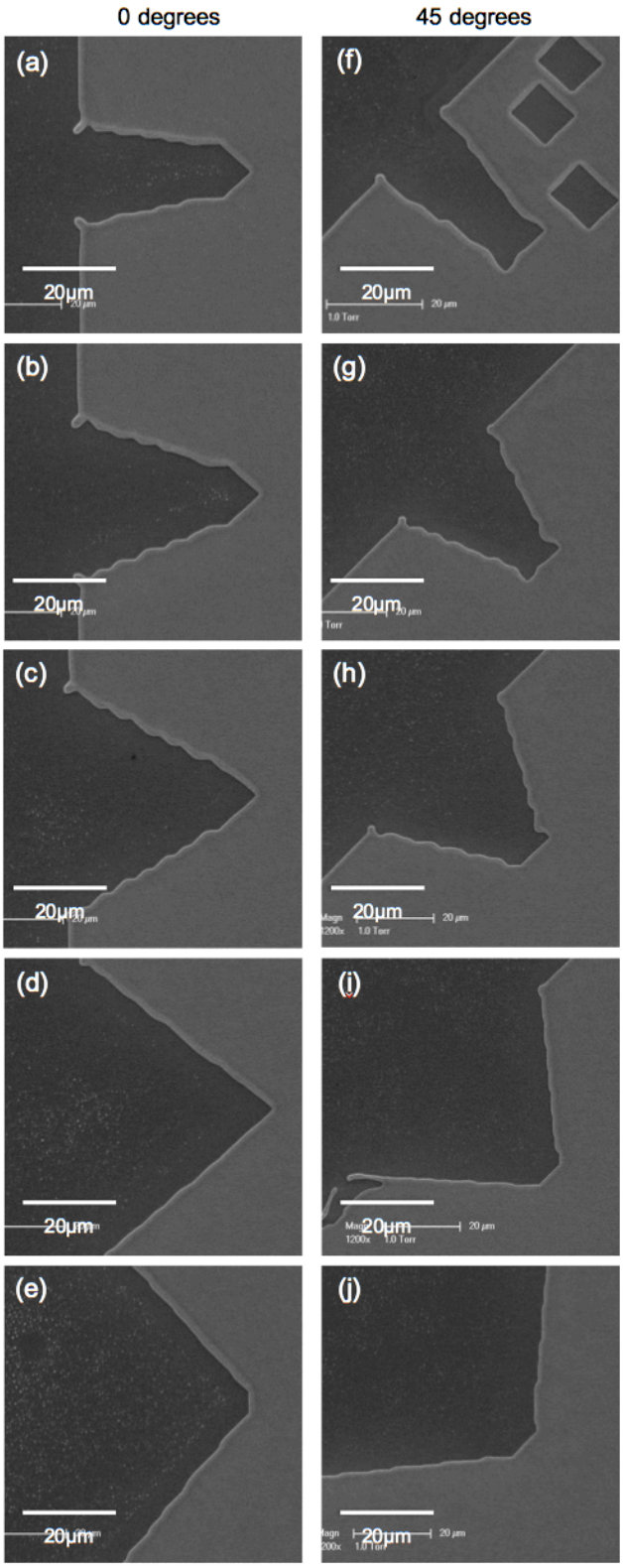

Figure A1-3. SEM images of the patterned corners in Ni(100) oriented along (a)-(e) 0 degrees from [010] and (f)-(j) 45 degrees from [010].

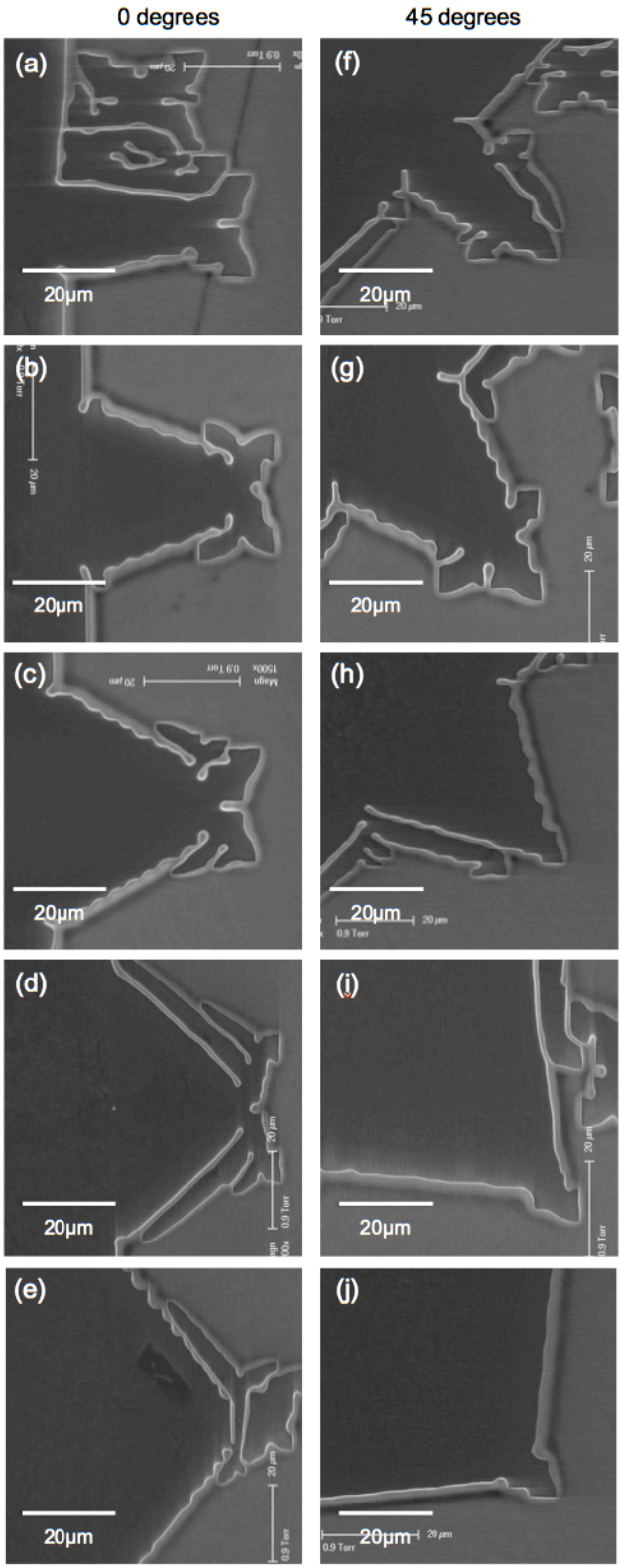

Figure A1-4. SEM images of the patterned corners in Ni(110) oriented along (a)-(e) 0 degrees from $[1\bar{1}0]$ and (f)-(j) 45 degrees from $[1\bar{1}0]$.

As expected from the fact that anisotropic diffusivity and surface energy exist in single crystal films, there is a clear difference in the dewetting morphology at the corner when the corners are patterned in different macroscopic orientations. After the anneal, quantitative measurements were also made to gauge the degree of corner instability for corners of different corner angles. The retraction distance was measured from where the patterned corner initially was to the farthest place the corner retracted along the macroscopic orientation that the corner was originally patterned in. Some key terminologies are graphically defined in Figure A1-2.

As shown in Figures A1-5 and A1-6, no significant differences exist in the retraction distance measurements for the corners with different corner angles for a given corner orientation. However, clear anisotropy exists in the retraction distance measurements for the corners in different corner orientations. As shown in Figures A1-3 and A1-4, the patterned corners do not remain the way they are patterned as they retract; rather, the morphology of the corner changes due to the formation of the kinetically stable edges that were discussed throughout this thesis. These kinetically stable edges define the shape of the natural holes that form in the film and thus define the shape of the corners in the natural holes. In certain corner orientations like those in 45 degrees from [010] in Ni(100) and 0 degrees from $[1\bar{1}0]$ in Ni(110), these kinetically stable edges make the patterned corner blunt and thus the retraction distance, now that the morphology at the corner resembles a straight edge, is smaller than the case where sharp corners retract. These blunt corners developed two "natural" corners and, in Ni(110), these corners propagated further and individually developed the corner instability, further complicating the dewetting morphology at the patterned corner. On the other hand, some other orientations like those in 0 degrees from [010] in Ni(100) and 45 degrees from $[1\bar{1}0]$ in Ni(110) are still parallel to the orientations where the corners in the natural holes align to, and these orientations show larger retraction distance than the other orientations.

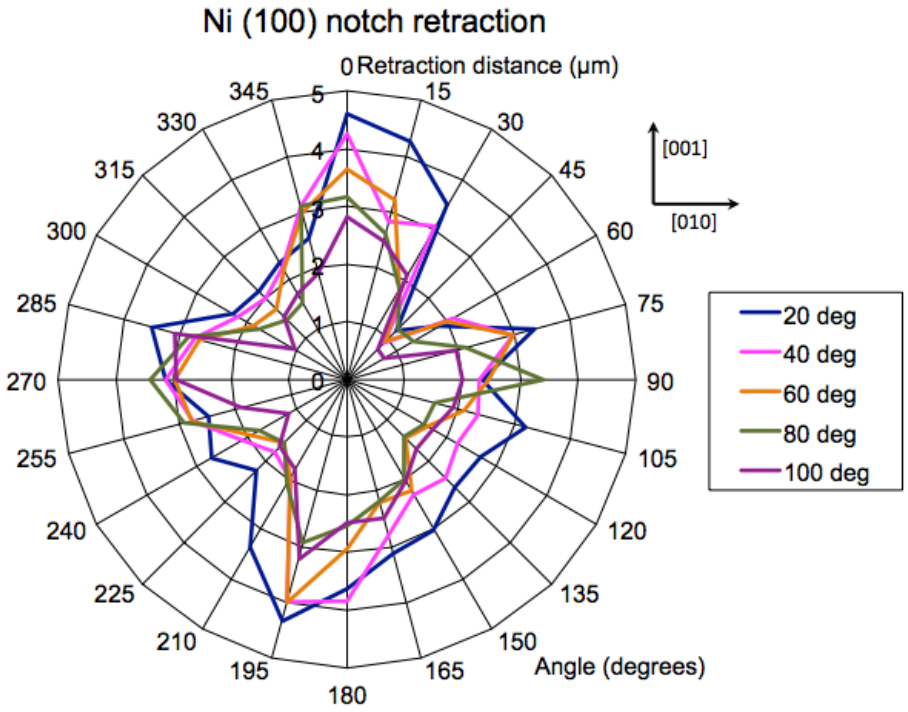

Figure A1-5. Retraction distance measurements for the corners patterned with different corner angles in different corner orientations in Ni(100) after a 12-hour anneal.

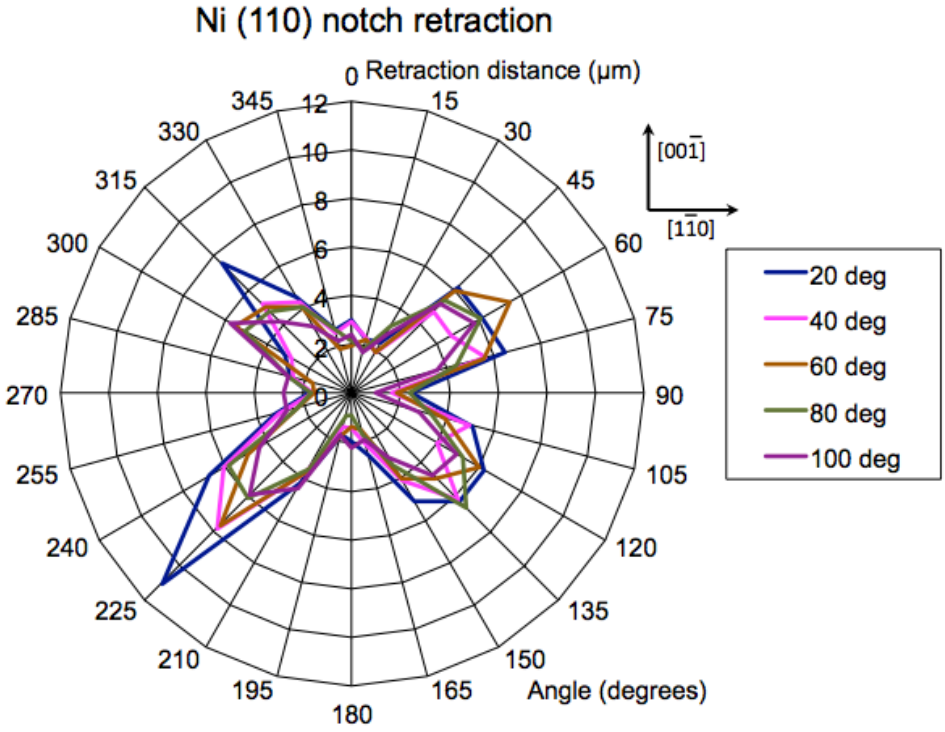

Figure A1-6. Retraction distance measurements for the corners patterned with different corner angles in different corner orientations in Ni(110) after a 12-hour anneal.

From the experiments, it was determined that corner instability initiates from the corners that naturally form due to the formation of the kinetically stable edges, rather than from the corners that were made from an arbitrarily defined set of edges. Furthermore, a more quantitative study of the corner instability showed that the diffusion field mechanism that was previously mentioned in Chapter 1 is not the right mechanism for the corner instability. This was discussed in detail in Chapter 6.

Appendix A2. Templating of the Fingering Instability

In Chapter 5, an analytical model was developed for the steady-state fingering instability and it was found that a good agreement exists between the model and the experimental data obtained elsewhere. In the single crystal Ni system, which was the model experimental system used throughout this thesis, no fingering instability has been observed in the past. More recently, however, fingering instability has been observed in some of the vacuum annealing experiments. This work is in progress via collaboration with Solmaz Jahangir in the Valanoor Group at University of New South Wales and Yoon Ah Shin in the Thompson Group at MIT Department of Materials Science and Engineering.

The first set of experiments was carried out with 130nm-thick patterned single crystal (110) Ni films, which was patterned via photolithography discussed in Chapter 2. These samples were annealed in the vacuum chamber with a base pressure of $1x10^{-6}$torr at different temperatures. A schematic of the initial pattern was illustrated in Figure A2-1.

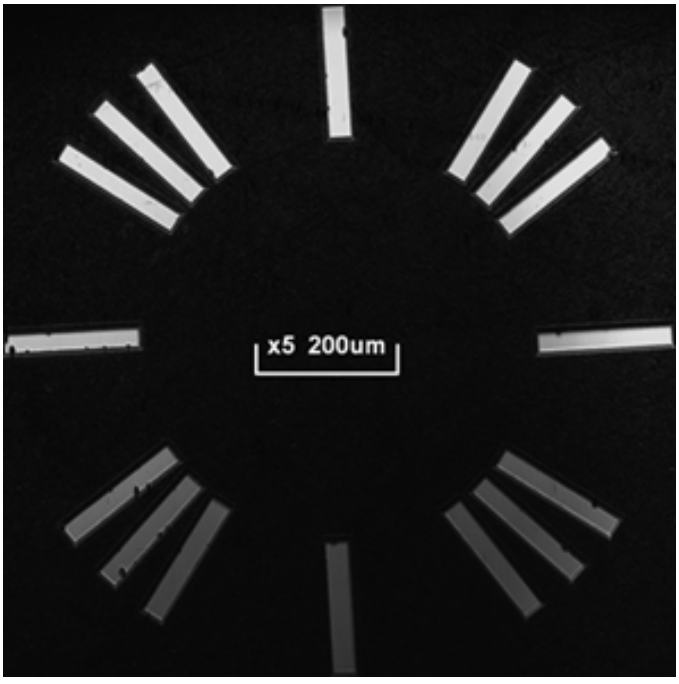

Figure A2-1. A schematic illustration of the initial pattern used for the experiments. Straight edges were patterned in different in-plane orientations in single crystal Ni(110) films.

After a 3-hour anneal, fingering instability was observed. Due to anisotropy in surface diffusivity and energy, the fingers propagated in a specific set of orientations, which were the $[1\bar{1}3]$ orientations. An SEM image of the fingers is presented in Figure A2-2.

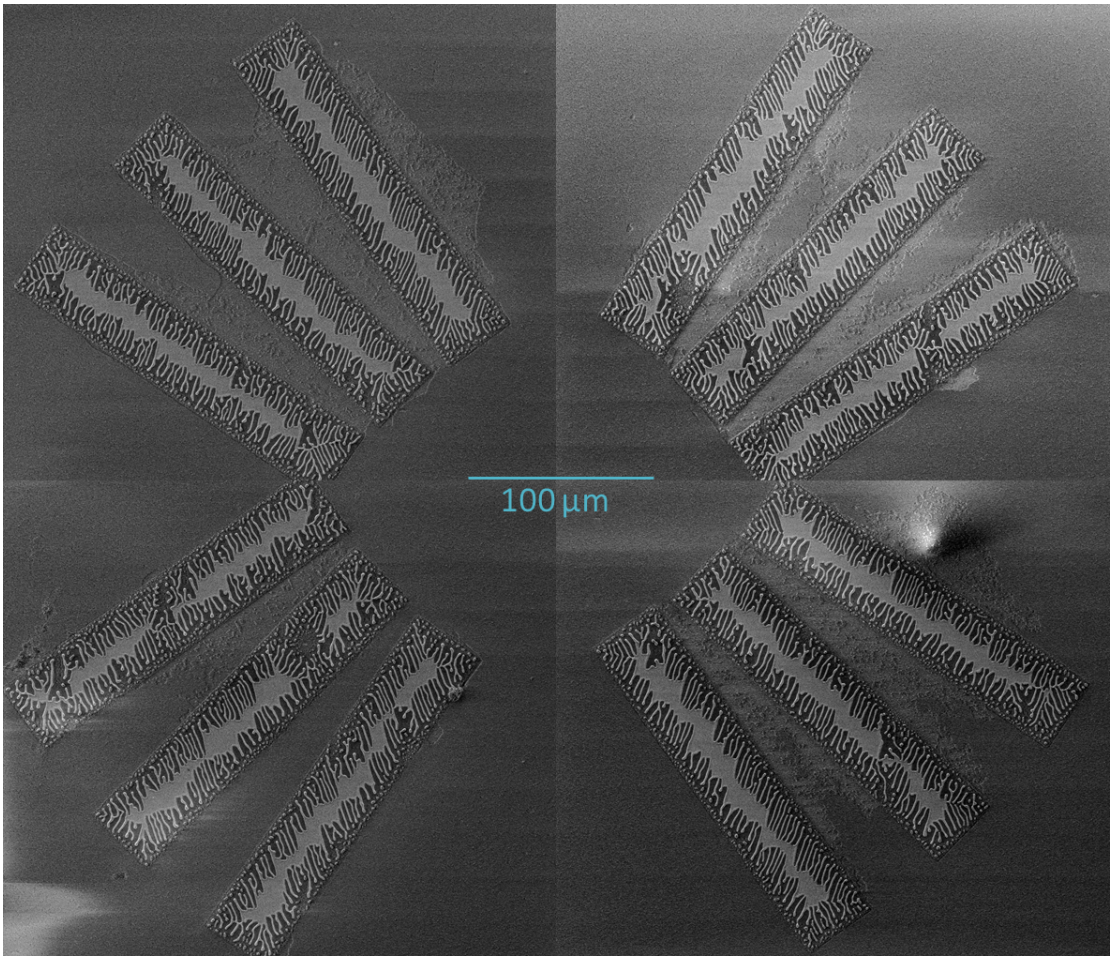

Figure A2-2. SEM micrograph of the Ni patches after a 3-hour anneal at 900°C. Fingering instability was observed, and the fingers propagated along the $[1\bar{1}3]$ orientations.

As shown in Figure A2-3, the steady-state finger wavelength was also measured for the samples annealed at different temperatures. We call this wavelength as the natural finger spacing as this developed without intentional templating. As predicted by the model developed in Chapter 5, a good linear relationship was observed between *ln(finger spacing)* and *1/kT*.

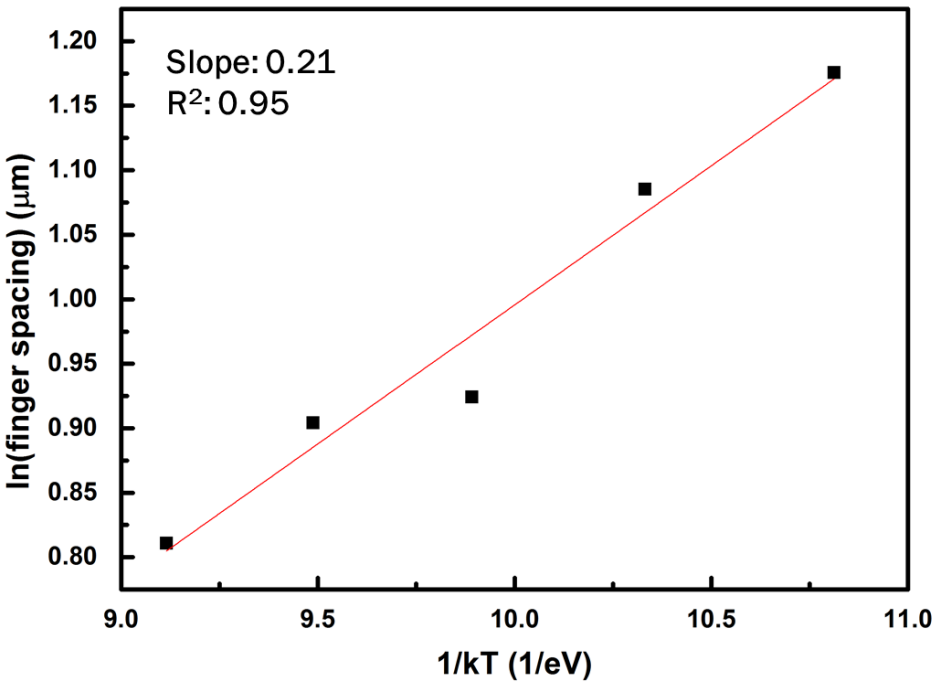

Figure A2-3. Relationship between steady-state finger spacing and annealing temperature.

Originally, it was postulated that the different annealing condition was the cause for the initiation of fingering instability. Our typical annealing experiments in the past have been carried out in the tube furnace operating under atmospheric pressure conditions, and this experiment was carried out under vacuum. However, fingering instability has also been observed in our tube furnace more recently and the actual cause for the instability needed to be identified.

After careful analysis, it was determined that there is a strong correlation between the roughness of the patterned edge and the degree of fingering instability. Multiple Ni(110) samples were patterned and annealed under different ambient conditions. After annealing for 6.5 hours at 900°C the degree of fingering instability was measured by measuring the percentage of the edge out of the total edge length in which fingering instability was observed. This was plotted against the RMS roughness of the as patterned edge. It was determined that when the patterned edge

roughness is above a certain value, fingering instability began to be observed. This is shown in Figures A2-4 and A2-5. It was further identified that the cause of this roughness is due to poor adhesion of the photoresist used for the patterning. Due to poor adhesion, small gaps exist between the photoresist and the film, and this causes rough edges during the wet etching step. The process parameters were optimized to a photoresist spin rate of 2700rpm and a soft bake temperature of 115°C for 4 minutes, and the poor adhesion issue has been resolved.

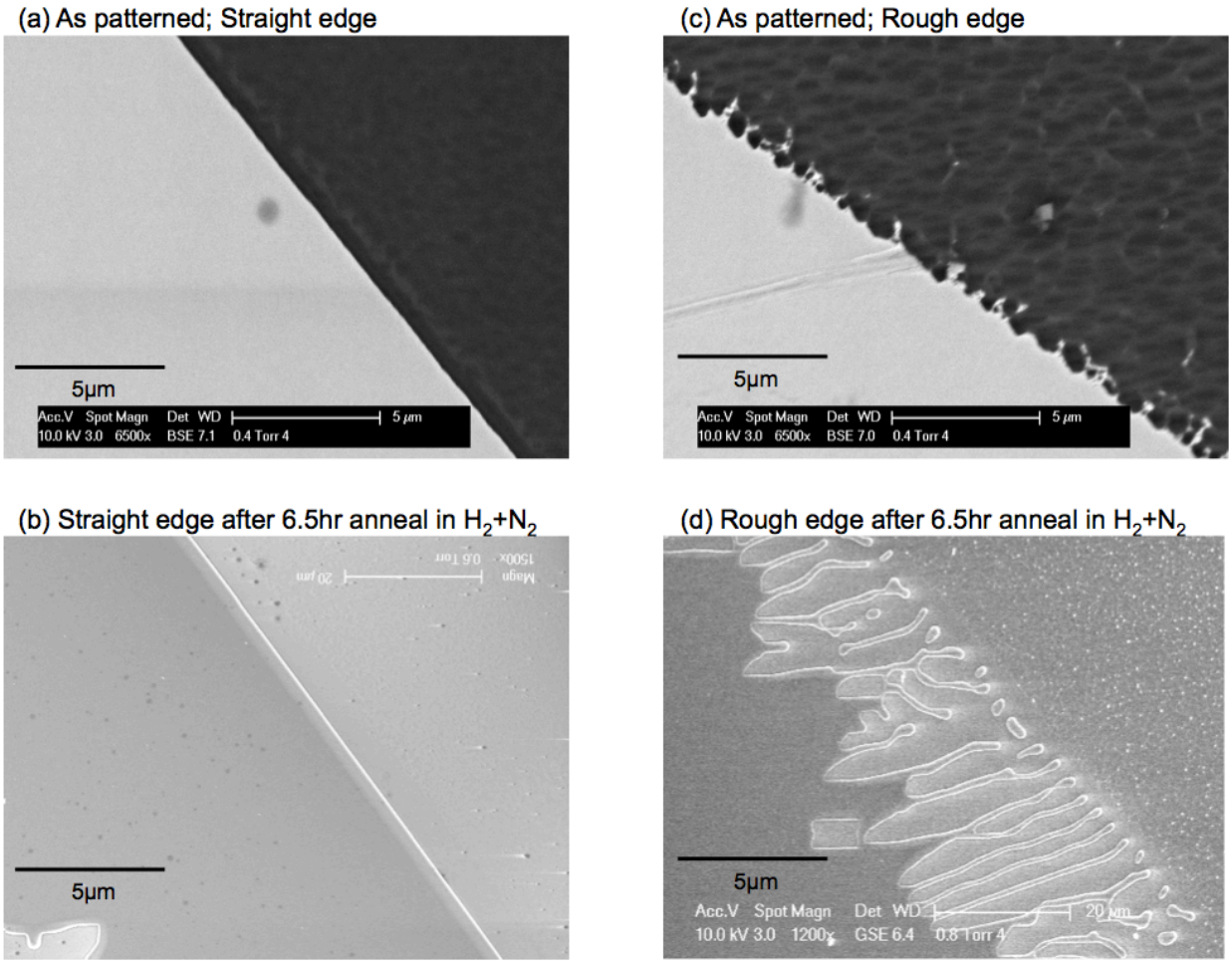

Figure A2-4. (a) SEM micrograph of the as patterned straight edge. (b) SEM micrograph of the straight edge after 6.5 hours of annealing under a reducing gas (5% H_2 and 95% N_2) flowing at 95sccm. (c) SEM micrograph of the as patterned rough edge, whose roughness was caused by poor adhesion of the photoresist. (d) SEM micrograph of the rough edge after 6.5 hours of annealing under a reducing gas (5% H_2 and 95% N_2) flowing at 95sccm.

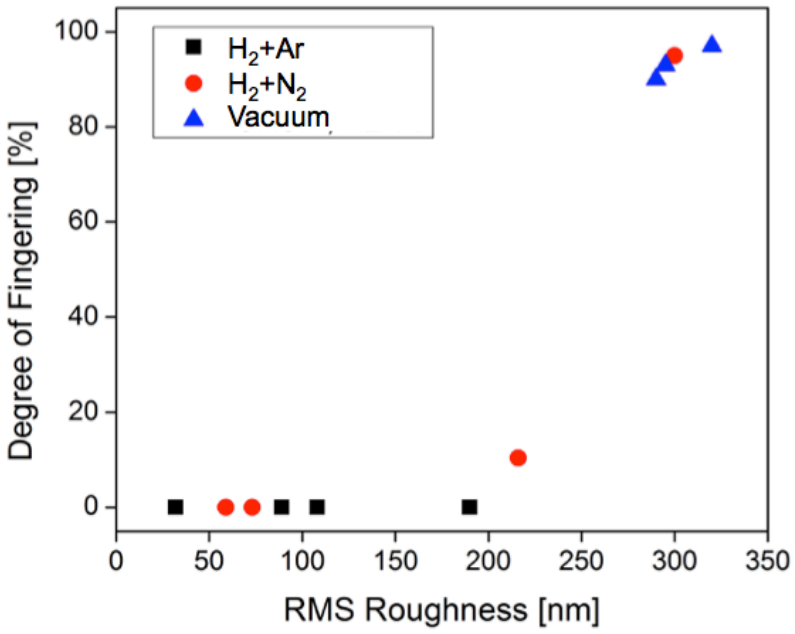

Figure A2-5. Degree of fingering instability versus RMS roughness of the as patterned edge. Different samples were annealed under different annealing conditions, but no ambient dependence was observed. Rather, above a certain RMS roughness value, fingering instability began to be observed. 2% H_2 + 98% Ar was flown at a rate of 390sccm and 5% H_2 + 95% N_2 was flown at a rate of 95sccm. These are the flow rates where the same oxygen partial pressure was measured. The base pressure for the vacuum annealing was $1x10^{-6}$torr. The annealing temperature was 900°C in all cases.

Noticing the fact that the roughness of the as patterned edge caused fingering instability, another set of experiments was designed to template the fingering instability. A set of rough edges with varying wavelengths and with the same amplitude (1.79μm) was intentionally patterned in 130nm-thick Ni(110) films. SEM micrographs of the as patterned edges are shown in Figure A2-6. The patterns were designed in a way that the macroscopic edges are vertical to the finger propagation orientation ($[1\bar{1}3]$) that was previously observed in the vacuum annealing experiments. Thus, the macroscopic edges were aligned to the $[\bar{2}21]$ orientations. It turned out that due to the photolithographic limitation and isotropic wet etching, the smallest wavelength (1.79μm) was not resolved. Then the samples were annealed in vacuum (base P = $1x10^{-6}$torr) at 800°C and 900°C. Representative SEM micrographs are provided in Figures A2-7 and A2-8.

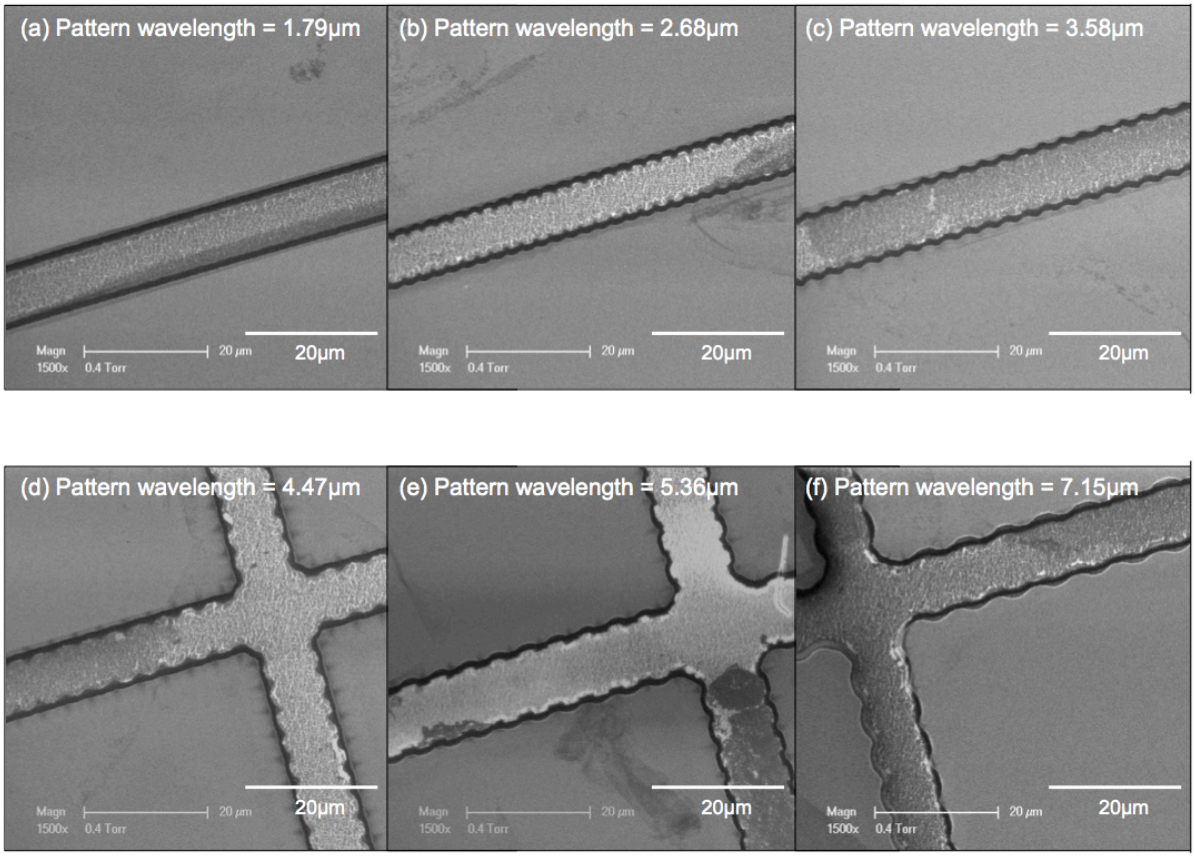

Figure A2-6. SEM micrograph of the as patterned edge with intentionally made perturbations. The smallest wavelength (a) was not resolved due to lithographic limits and isotropic etching.

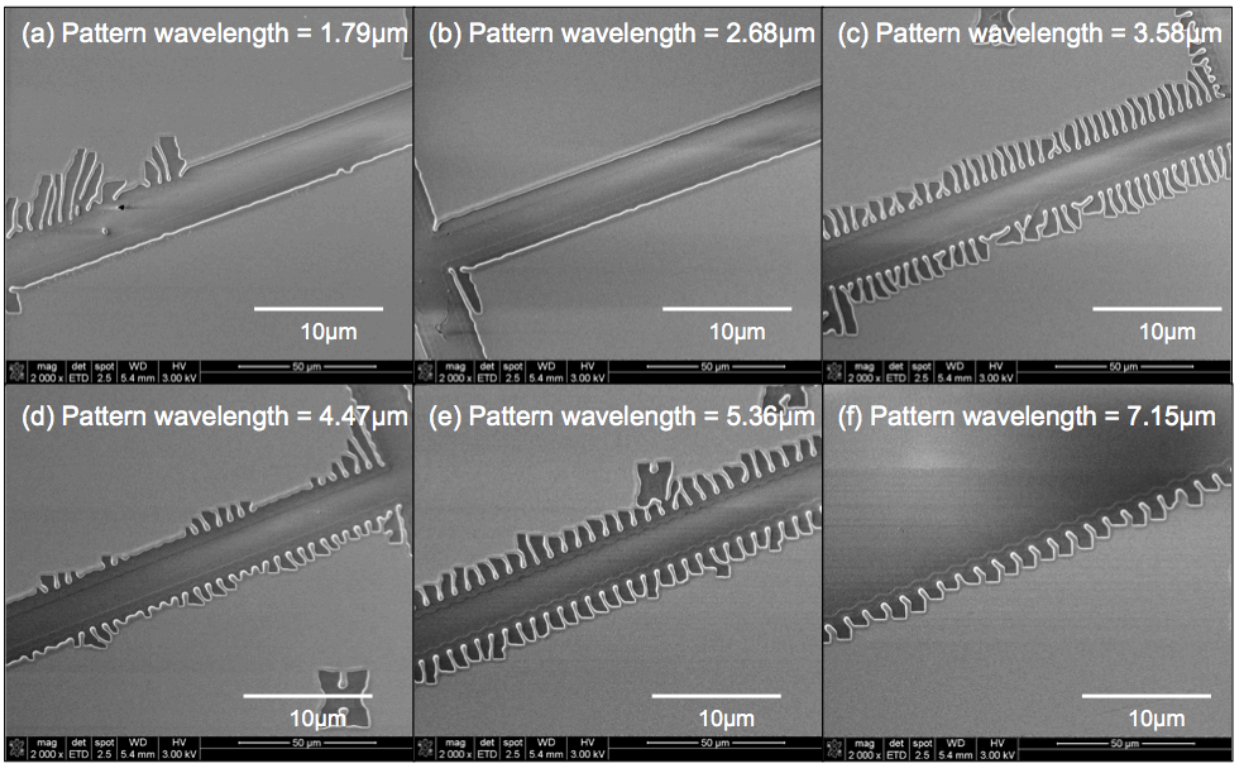

Figure A2-7. SEM micrograph of the patterned edges after a 240-min anneal at 800°C in vacuum.

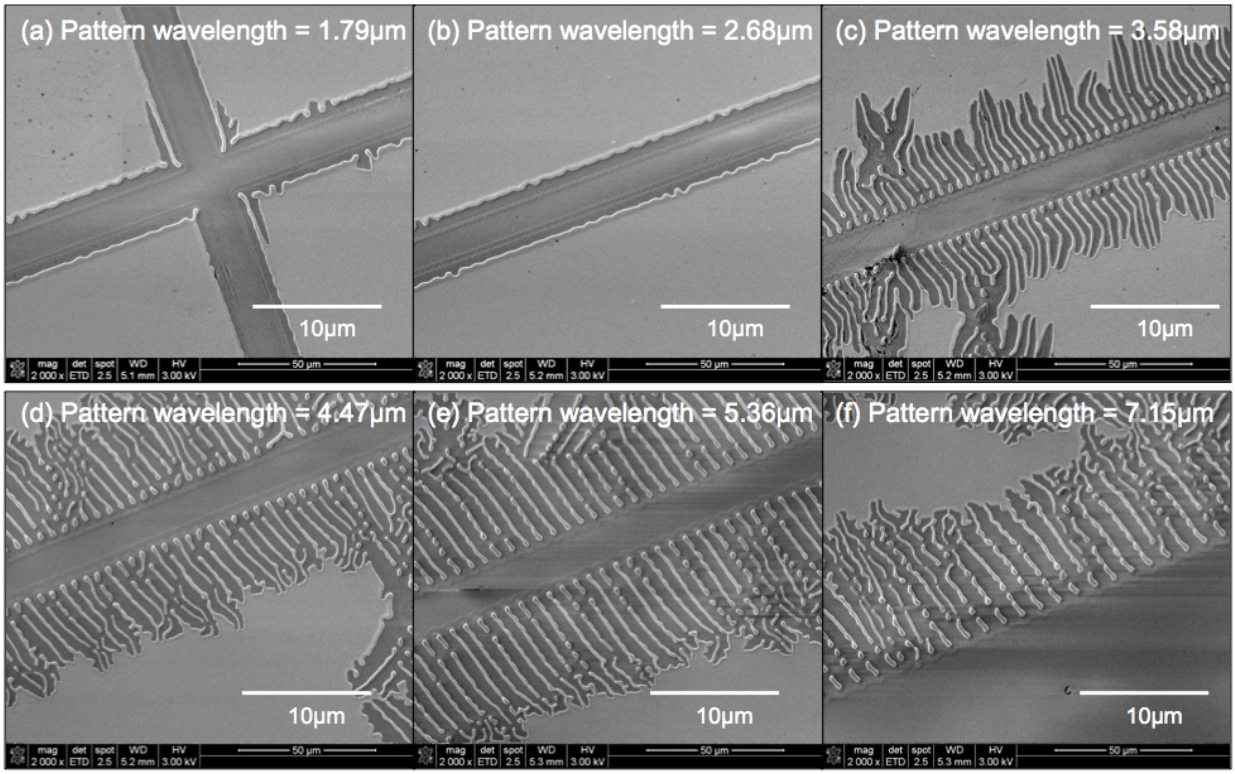

Figure A2-8. SEM micrograph of the patterned edges after a 180-min anneal at 900°C in vacuum.

No fingering instability was observed in the edges with the smallest intended perturbation wavelength because the perturbation was not resolved. This further corroborates the previous finding that the fingering instability is caused by the roughness in the edge. However, even though the perturbation was resolved for the second smallest wavelength, no fingering was observed in these edges, either. The third pattern with a wavelength of 3.58μm has the same perturbation wavelength as the natural finger spacing measured in the previous experiments without any intended edge roughness. It can be postulated that below the natural finger spacing, it is more difficult to develop fingers, which is a potential topic for future work.

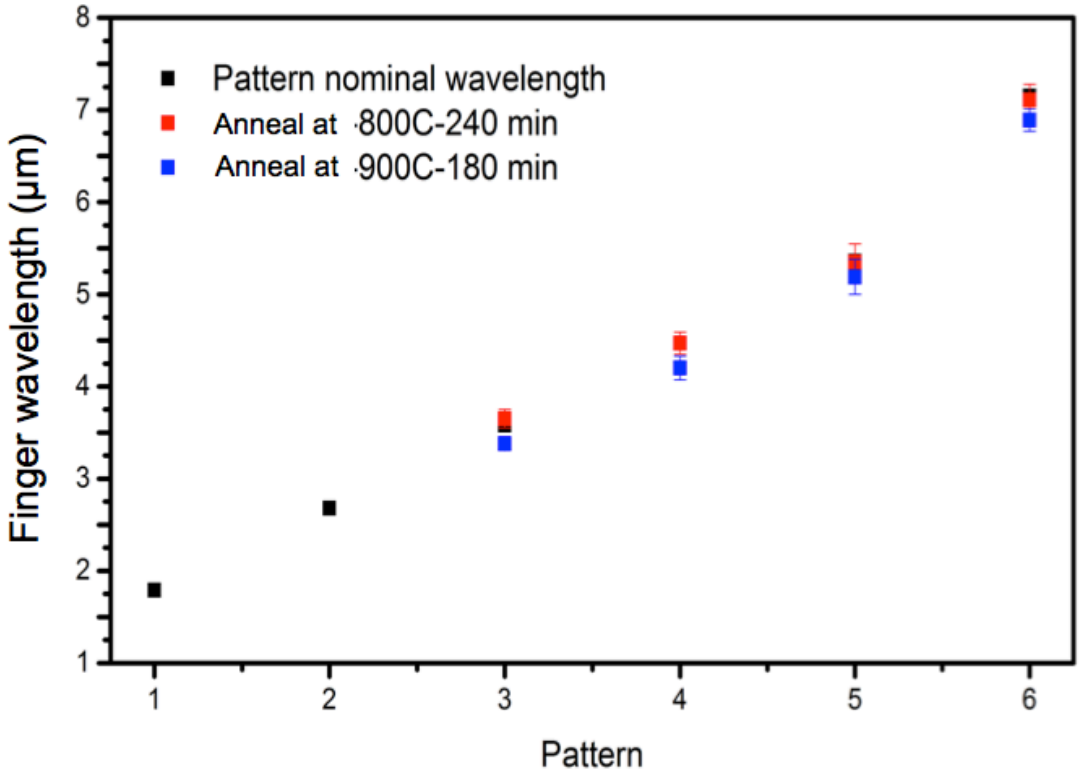

Figure A2-9. Steady-state finger wavelength measurement for patterns with different intended perturbation wavelengths at different annealing temperatures in vacuum. The intended wavelengths are: Pattern 1 = 1.79μm; Pattern 2 = 2.68μm; Pattern 3 = 3.58μm; Pattern 4 = 4.47μm; Pattern 5 = 5.36μm; Pattern 6 = 7.15μm. Note that no measurements exist for Patterns 1 and 2 as no fingering was observed.

As shown in Figure A2-9, steady-state finger spacing was measured for different patterns annealed at different temperatures. It was found that the resulting finger spacing follows the intended perturbation wavelengths patterned on the edge. Additionally, unlike the case in which fingers formed naturally from randomly distributed edge roughness (no intended edge perturbation), at most very weak temperature dependence was observed when perturbations with specific wavelengths were patterned.

The work presented here is part of an ongoing project. Some of the future work to be completed includes: 1. Resolving smaller perturbation wavelengths to ensure whether a lower limit exists below the natural finger spacing for the fingering instability; 2. Checking whether

there also is an upper limit for the fingering instability; 3. Identifying the cause of natural hole formation to minimize interruption during finger propagation, which is also necessary for the study of other dewetting phenomenologies and thus was discussed in Chapter 8 in more detail; 4. Observing the annealing ambient dependence of the fingering instability by conducting similar experiments under different annealing conditions.

Appendix A3. Solid-state Dewetting of Templated Hole Arrays

Throughout this thesis, the individual dewetting phenomenologies were discussed in detail and it was found that the dewetting behavior in single crystal films is highly anisotropic. The resulting dewetting morphology varies significantly depending on multiple factors. To identify some of the factors that affect the dewetting morphology, arrays of patterned holes were made in 130nm-thick single crystal (100) and (110) Ni films, and these patterns were annealed at 890°C with a reducing gas (5% H_2 + 95% N_2) flowing at a rate of 2310sccm. The patterns were made by photolithography that was discussed in Chapter 2.

As it can be seen from the following figures, the dewettng morphology is very different depending on many factors accounted for in the patterned hole arrays. First of all, a strong dependence on the macroscopic orientation of the patterns and the out-of-plane orientation of the film was observed. In addition, comparing Figures A3-1 and A3-2, and Figures A3-3 and A3-4, it can be seen that the resulting dewetting morphology is strongly dependent on the size of the patterned holes. Also, comparing Figures A3-3 and A3-5, it can be seen that the dewetting morphology is strongly dependent on the distance between the patterned holes. Furthermore, comparing Figures A3-1 and A3-7, A3-3 and A3-8, and A3-5 and A3-9, it can be seen that the dewetting morphology is strongly dependent on the shape of the patterned holes. Although strong dependence on many factors were observed, the individual dewetting morphology resulting from the same pattern is highly regular and reproducible. This can potentially be used in the sub-lithographic patterning applications, as highly regular and reproducible patterns can be easily made by simply making pre-patterns by lithography and letting the pre-patterns dewet at a high temperature. This potential applicability was discussed in Chapter 8.

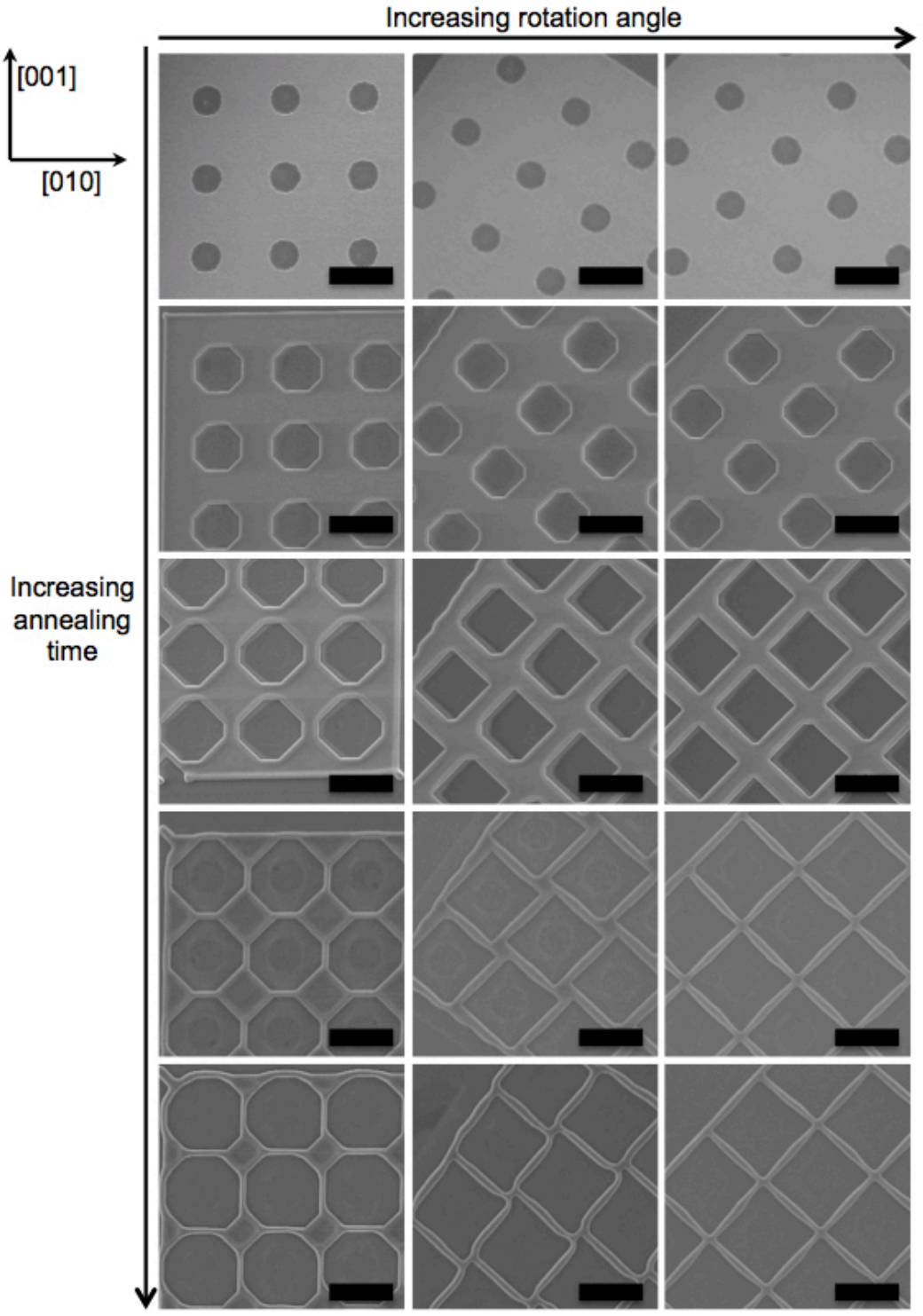

Figure A3-1. Propagation of pre-patterned holes on Ni(100) by dewetting. The square holes initially are 5μm in length and the initial spacing between the hole edges is 10μm. Bright regions in the micrographs are Ni. The angles of clockwise rotation are 0, 35, and 45 degrees, respectively, and the annealing times are 0, 1, 4, 9, and 12 hours, respectively. Scale bars, 10μm.

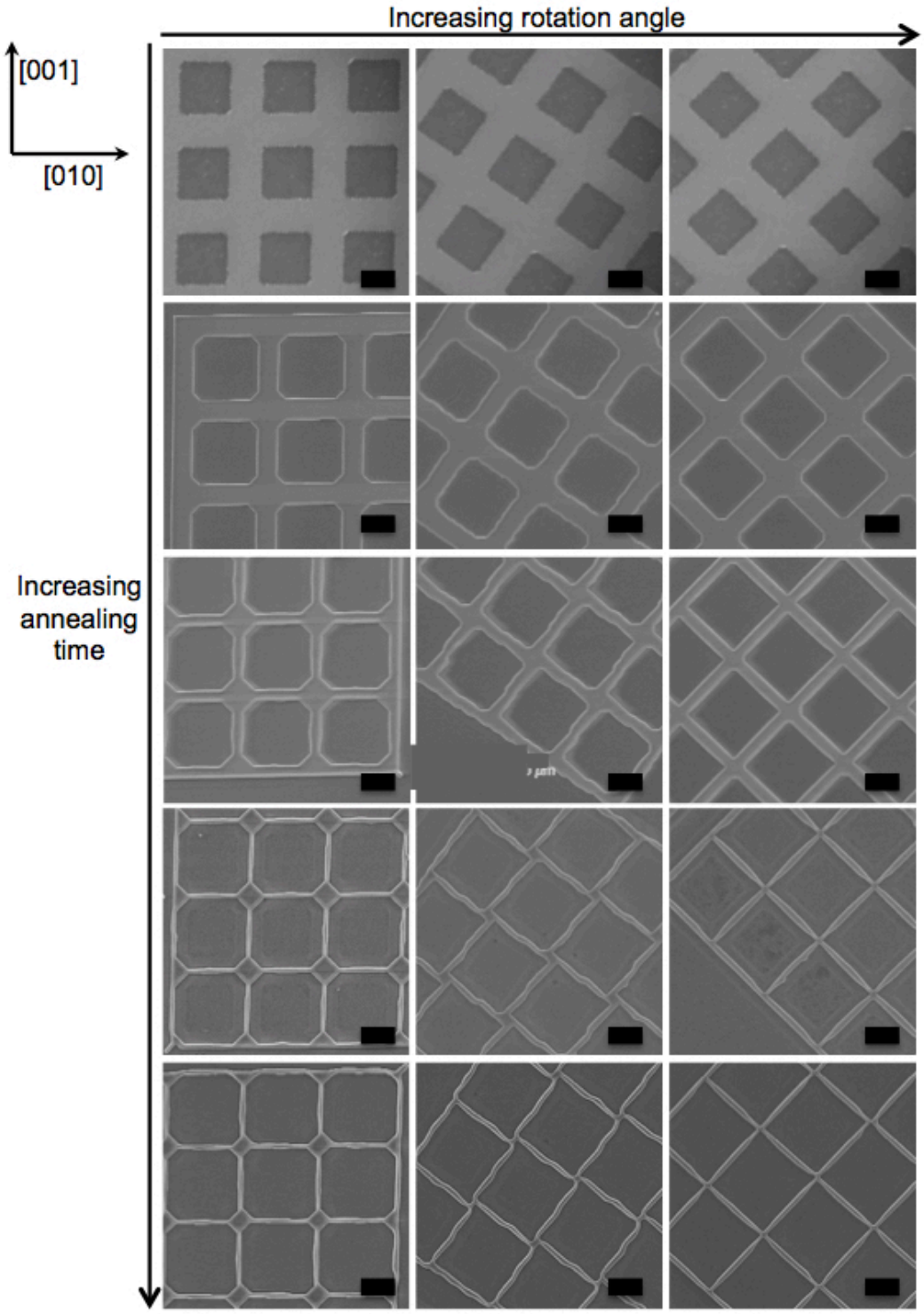

Figure A3-2. Propagation of pre-patterned holes on Ni(100) by dewetting. The square holes initially are 15μm in length and the initial spacing between the hole edges is 10μm. Bright regions in the micrographs are Ni. The angles of clockwise rotation are 0, 35, and 45 degrees, respectively, and the annealing times are 0, 1, 4, 9, and 12 hours, respectively. Scale bars, 10μm.

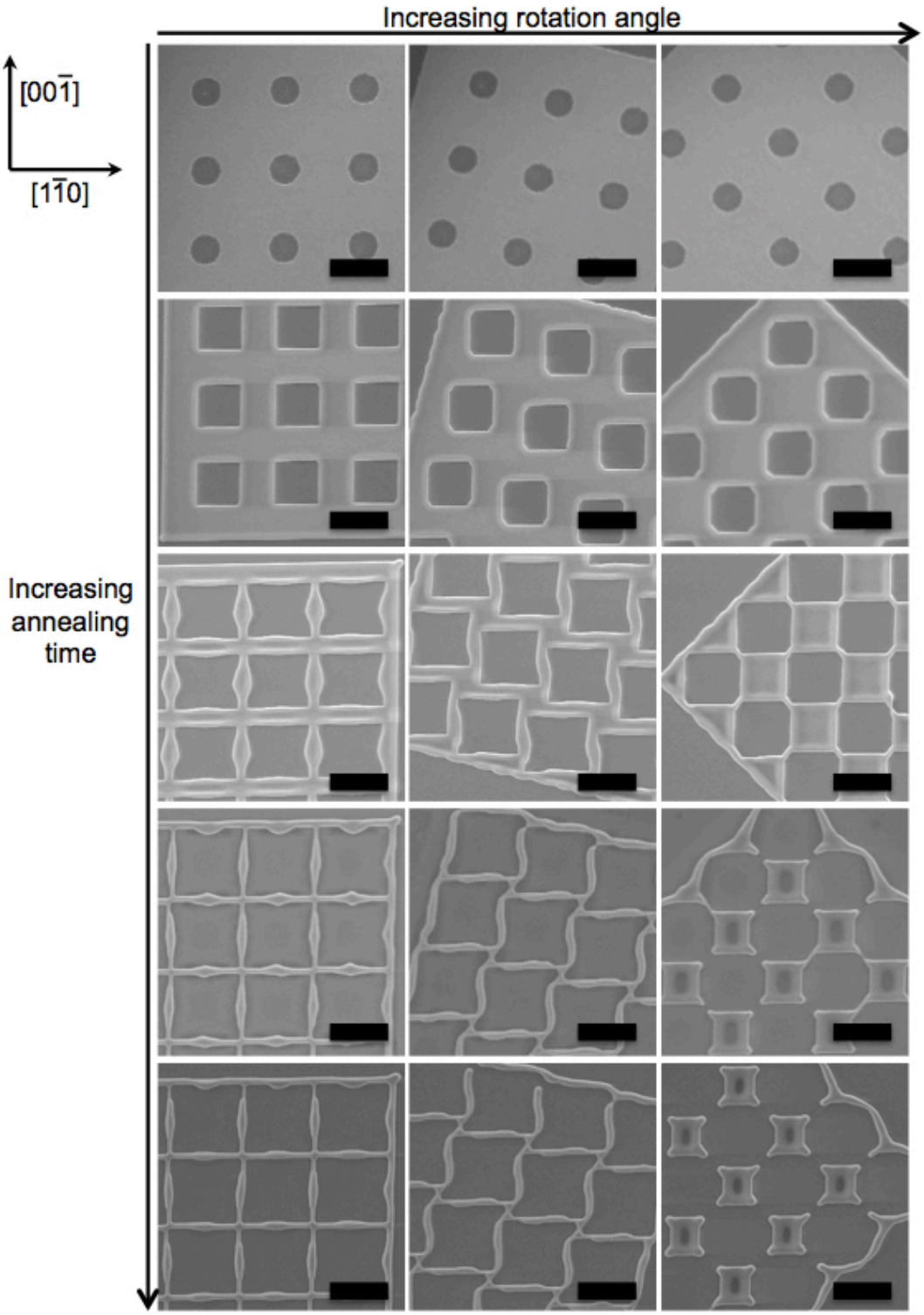

Figure A3-3. Propagation of pre-patterned holes on Ni(110) by dewetting. The square holes initially are 5μm in length and the initial spacing between the hole edges is 10μm. Bright regions in the micrographs are Ni. The angles of clockwise rotation are 0, 15, and 45 degrees, respectively, and the annealing times are 0, 1, 4, 9, and 12 hours, respectively. Scale bars, 10μm.

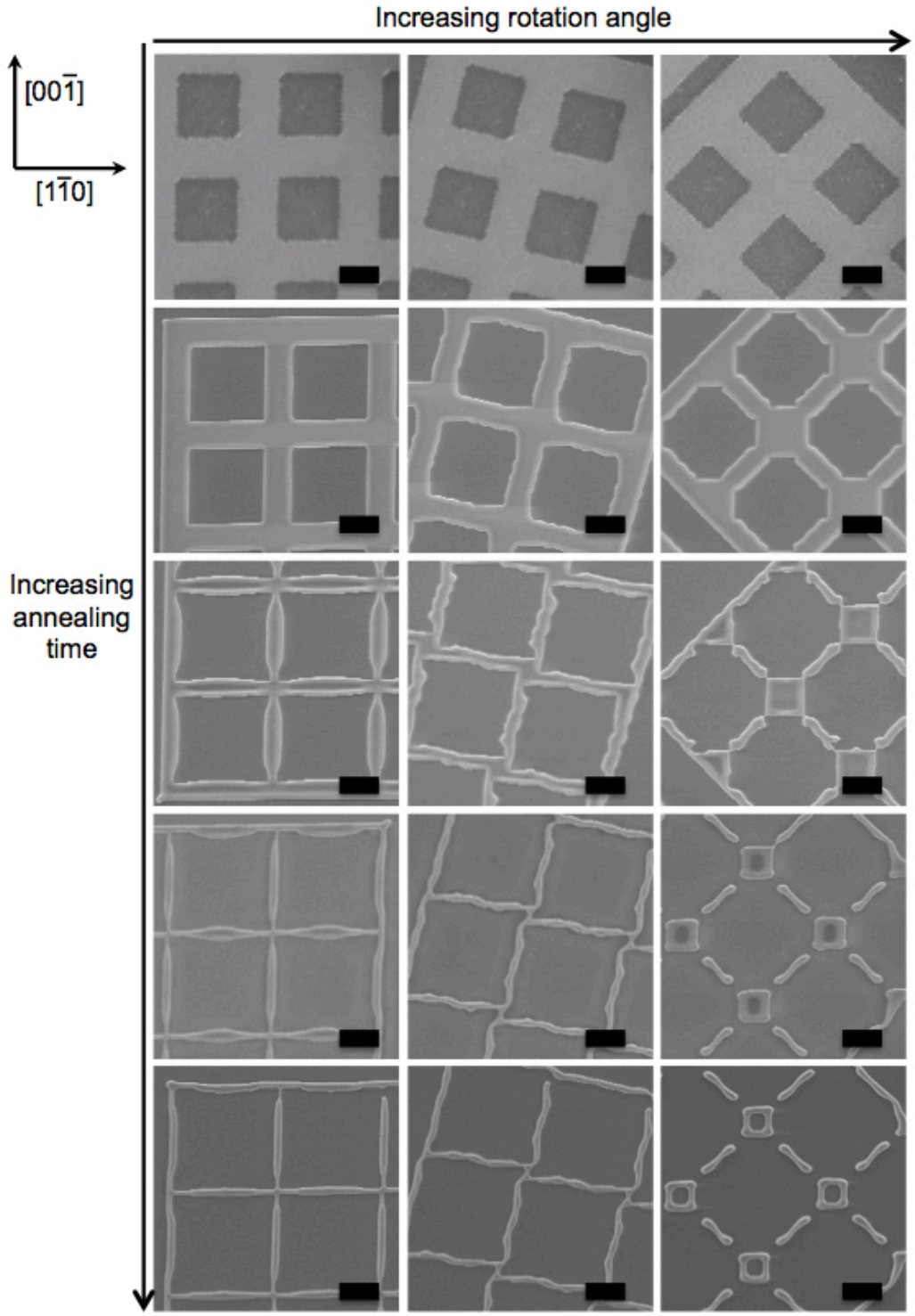

Figure A3-4. Propagation of pre-patterned holes on Ni(110) by dewetting. The square holes initially are 15μm in length and the initial spacing between the hole edges is 10μm. Bright regions in the micrographs are Ni. The angles of clockwise rotation are 0, 15, and 45 degrees, respectively, and the annealing times are 0, 1, 4, 9, and 12 hours, respectively. Scale bars, 10μm.

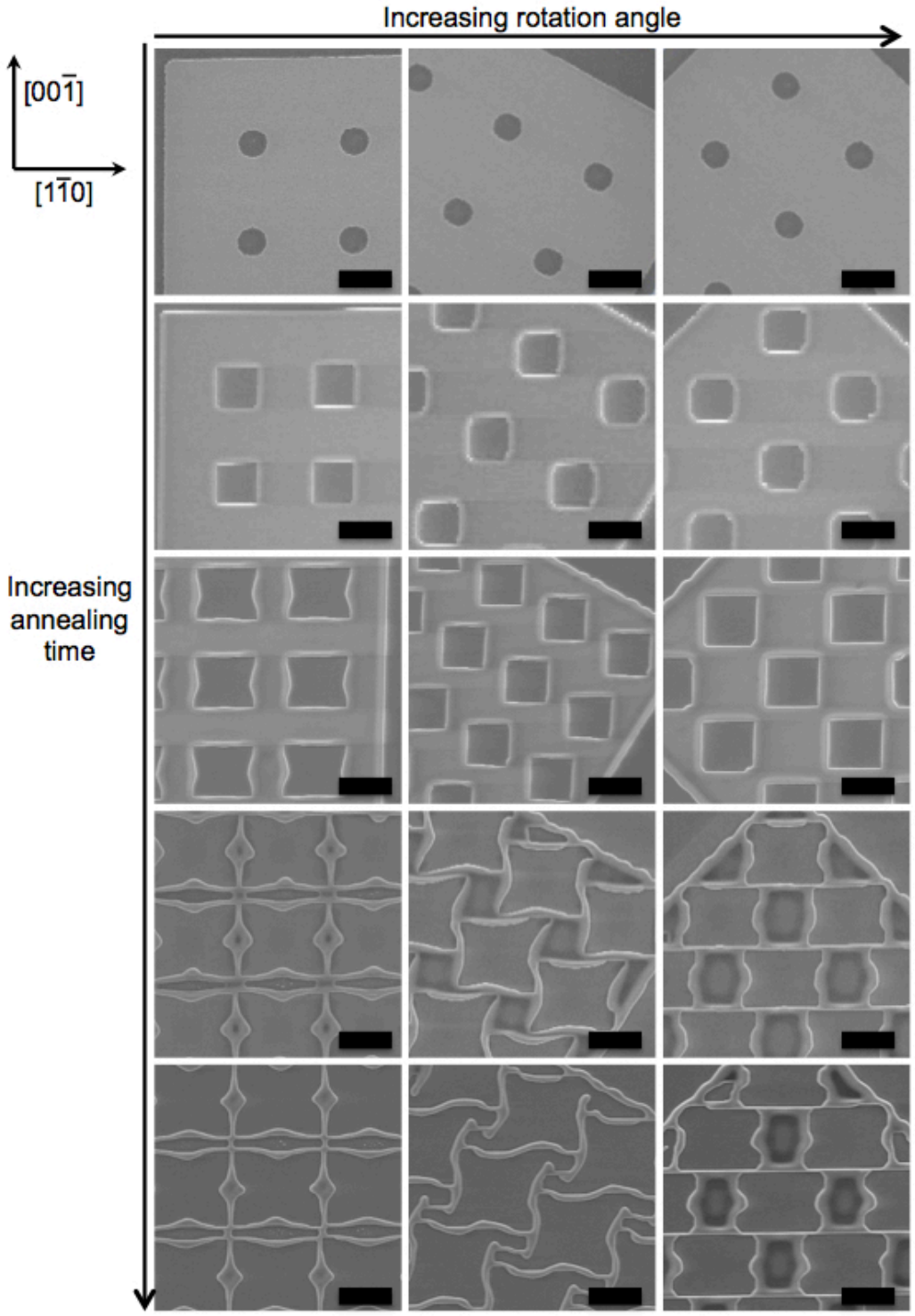

Figure A3-5. Propagation of pre-patterned holes on Ni(110) by dewetting. The square holes initially are 5μm in length and the initial spacing between the hole edges is 15μm. Bright regions in the micrographs are Ni. The angles of clockwise rotation are 0, 30, and 45 degrees, respectively, and the annealing times are 0, 1, 4, 9, and 12 hours, respectively. Scale bars, 10μm.

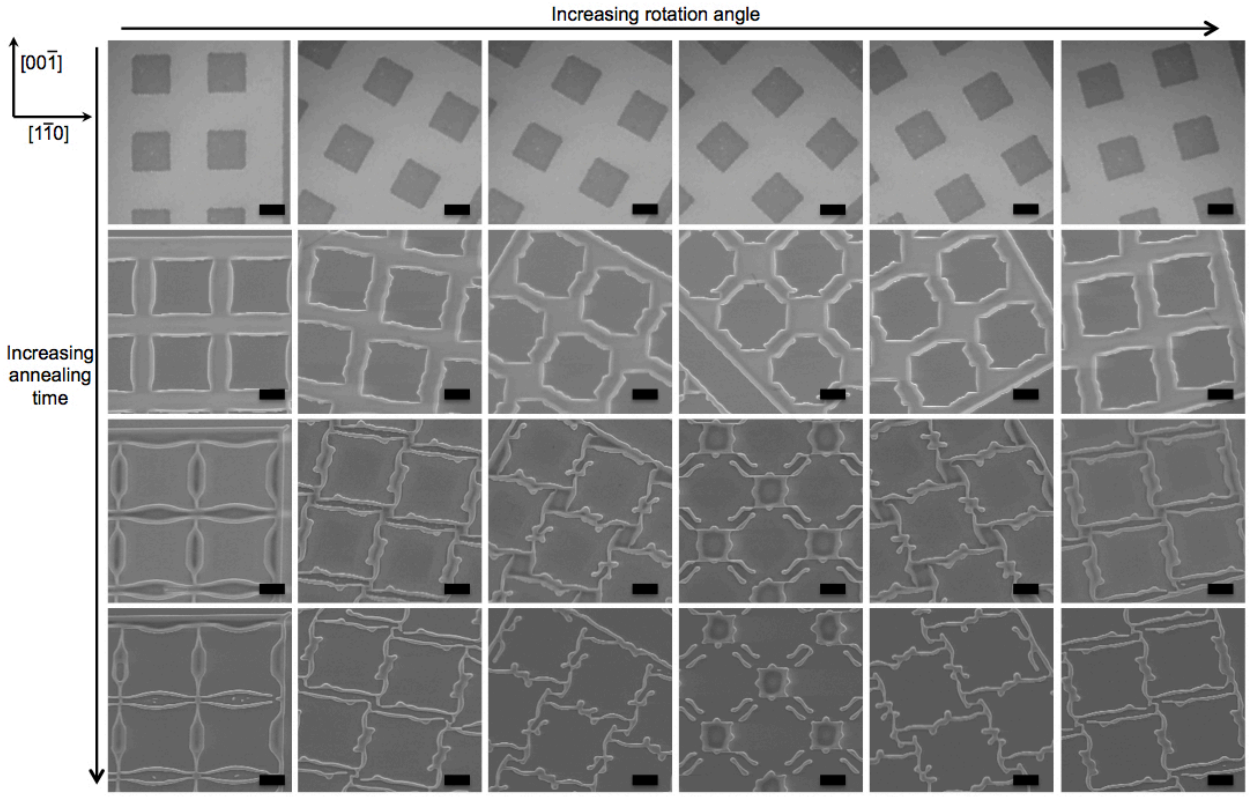

Figure A3-6. Propagation of pre-patterned holes on Ni(110) by dewetting. The square holes initially are 15μm in length and the initial spacing between the hole edges is 15μm. Bright regions in the micrographs are Ni. The angles of clockwise rotation are by a 15 degree interval, and the annealing times are 0, 4, 9, and 12 hours, respectively. Scale bars, 10μm.

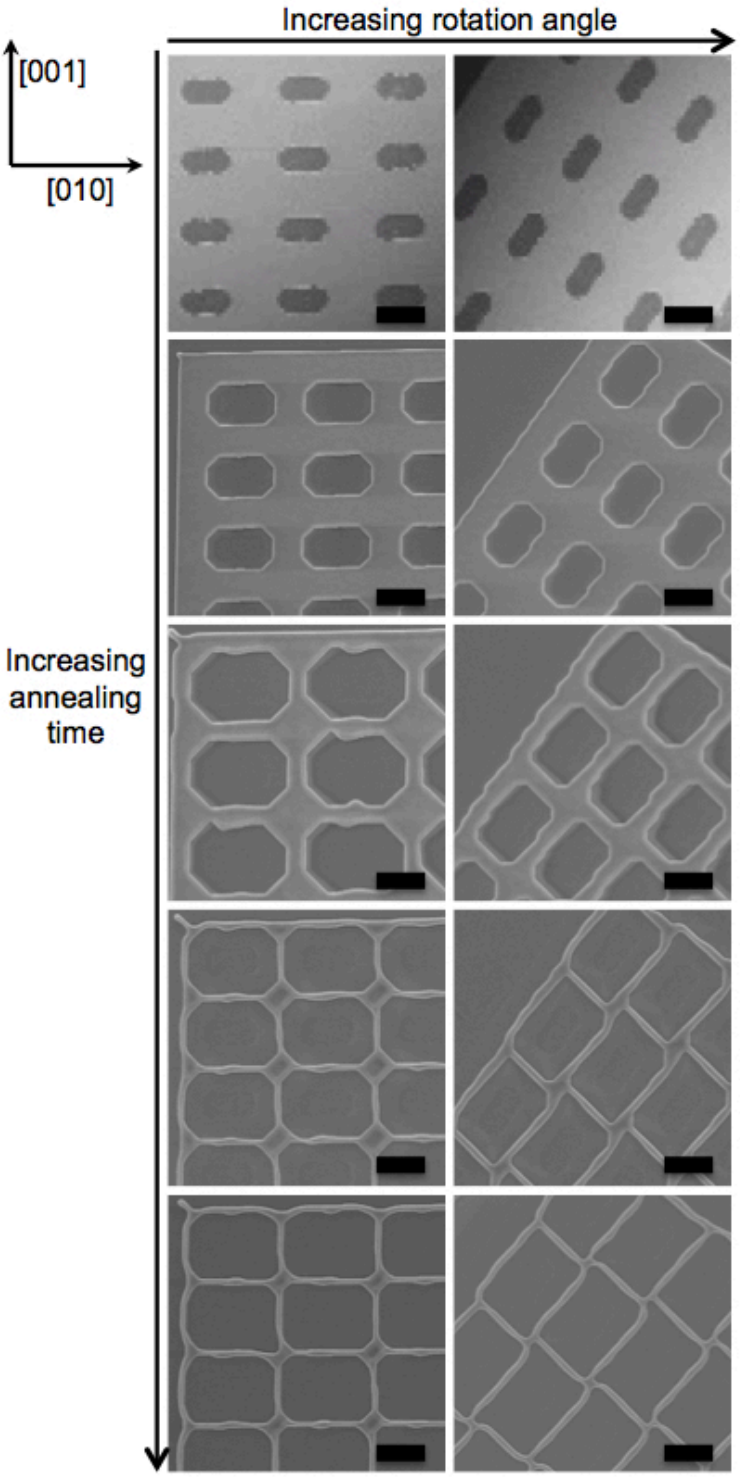

Figure A3-7. Propagation of pre-patterned holes on Ni(100) by dewetting. The rectangular holes initially are 5x10μm in size and the initial spacing between the hole edges is 10μm. Bright regions in the micrographs are Ni. The angles of clockwise rotation are 0 and 35 degrees, respectively, and the annealing times are 0, 1, 4, 9, and 12 hours, respectively. Scale bars, 10μm.

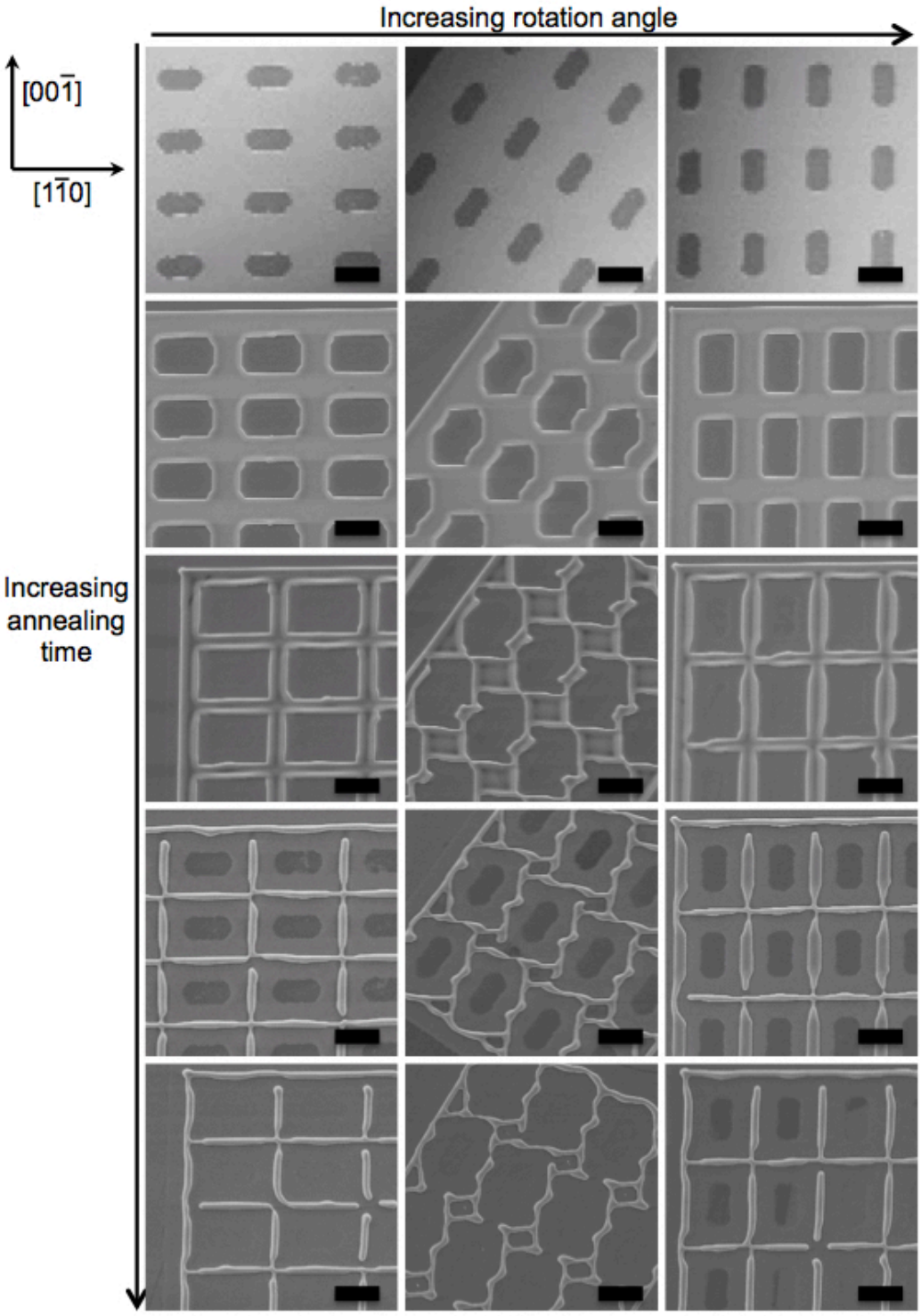

Figure A3-8. Propagation of pre-patterned holes on Ni(110) by dewetting. The rectangular holes initially are 5x10μm in size and the initial spacing between the hole edges is 10μm. Bright regions in the micrographs are Ni. The angles of clockwise rotation are 0, 35, and 90 degrees, respectively, and the annealing times are 0, 1, 4, 9, and 12 hours, respectively. Scale bars, 10μm.

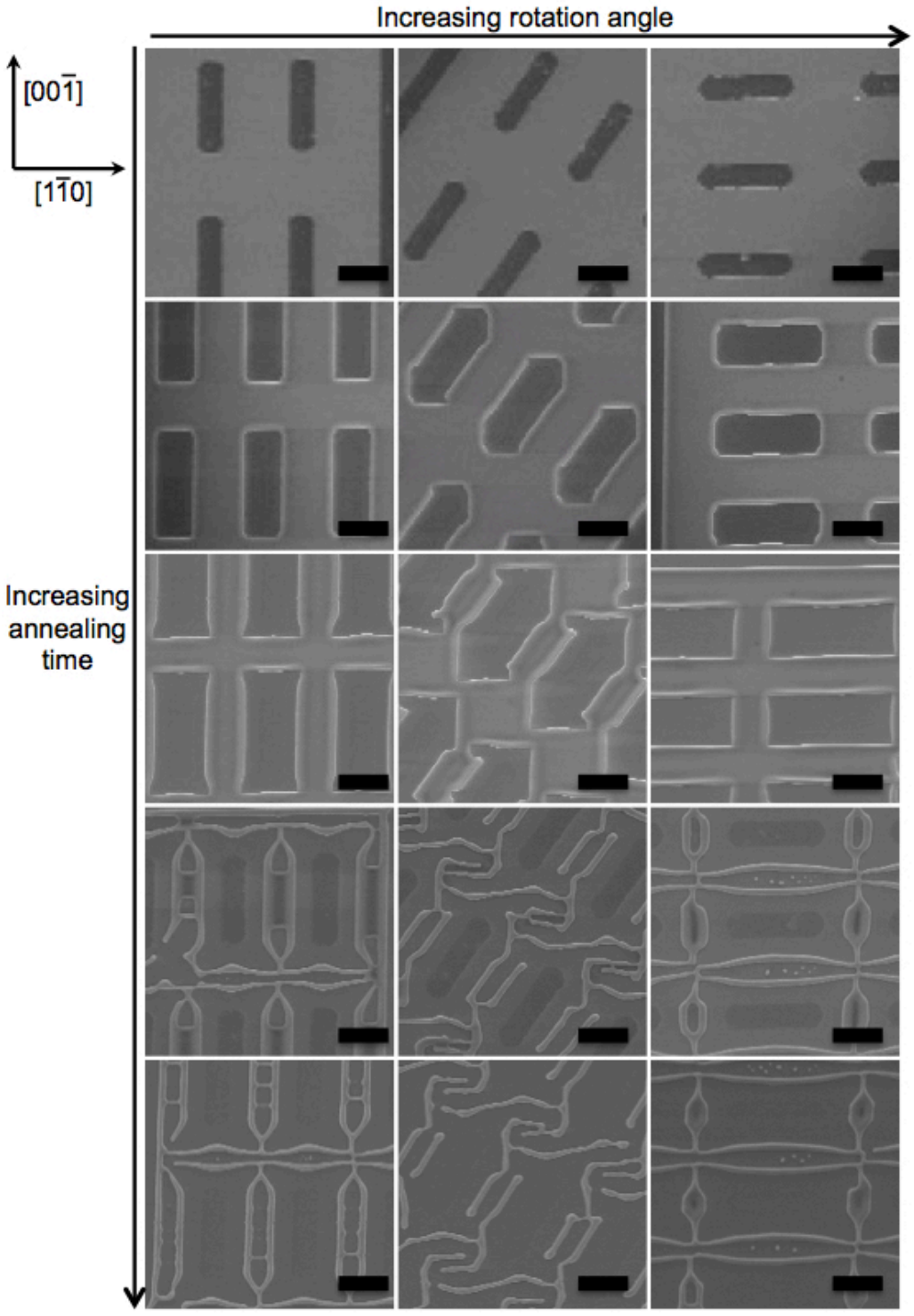

Figure A3-9. Propagation of pre-patterned holes on Ni(110) by dewetting. The rectangular holes initially are 5x20μm in size and the initial spacing between the hole edges is 15μm. Bright regions in the micrographs are Ni. The angles of clockwise rotation are 0, 35, and 90 degrees, respectively, and the annealing times are 0, 1, 4, 9, and 12 hours, respectively. Scale bars, 10μm.

In addition, there are certain stable orientations where the resulting dewetting morphology remains percolated for a very long annealing time. For instance, it was determined that the patterns aligned along the [010] and [011] orientations in Ni(100) and along the [001] and [$1\bar{1}0$] orientations in Ni(110) remained percolated up to a 100-hr anneal, while the percolated structure in the patterns in other orientations got disconnected earlier. These orientations correspond to the kinetically stable orientations that were discussed earlier. This can also be potentially useful for the applications where high temperature stability of the percolated structures is necessary, such as in fuel cell applications. This potential applicability is also discussed in Chapter 8.

Reference

1. G. H. Kim, M.S. Thesis, MIT, 2012.
2. K. N. Tu, Annual Review of Materials Science **15**, 147-176 (1985).
3. C. Jahan, O. Faynot, L. Tosti and J. M. Hartmann, J. of Cryst. Growth **280**, 530-538 (2005).
4. J. Mizsei, Sensors and Actuators B **16**, 328-333 (1993).
5. M. Chhowalla, K. B. K. Teo, C. Duati, N. L. Rupesinghe, G. A. J. Amaratunga, A. C. Ferrari, D. Roy, J. Robertson and W. I. Mine, Journal of Applied Physics **90** (10), 5308-5317 (2001).
6. V. Schmidt, J. V. Wittemann, S. Senz and U. Gosele, Advanced Materials **21** (25-26), 2681-2702 (2009).
7. R. W. Balluffi, S. M. Allen and W. C. Carter, *Kinetics of Materials*. (Wiley and Sons, Hoboken, NJ, 2005).
8. C. Herring, Physical Review **82** (1), 87-93 (1951).
9. G. Wulff and Z. Krist, Physical Review **34** (449) (1901).
10. W. L. Winterbottom, Acta Metallurgica **15** (2), 303-310 (1967).
11. W. W. Mullins, Journal of Applied Physics **30**, 77-83 (1959).
12. D. J. Srolovitz and S. A. Safran, Journal of Applied Physics **60** (1), 247-254 (1986).
13. J. Ye, Ph.D. Thesis, Massachusetts Institute of Technology, 2011.
14. E. Jiran and C. V. Thompson, Journal of Electronic Materials **19** (11), 1153-1160 (1990).
15. H. Wong, P. W. Voorhees, M. J. Miksis and S. H. Davis, Acta Materialia **48** (8), 1719-1728 (2000).
16. R. H. Brandon and F. J. Bradshaw, (R.A.E., Franborough, 1966).
17. D. J. Srolovitz and S. A. Safran, Journal of Applied Physics **60** (1), 255-260 (1986).
18. E. Dornel, J.-C. Barbe, F. d. Crecy, G. Lacolle and J. Eymery, Physical Review B **73** (11) (2006).
19. R. Nuryadi, Y. Ishikawa and M. Tabe, Applied Surface Science **159**, 121-126 (2000).
20. D. T. Danielson, D. K. Sparacin, J. Michel and L. C. Kimerling, Journal of Applied Physics **100** (8) (2006).
21. J. Ye and C. V. Thompson, Applied Physics Letters **97** (7) (2010).
22. J. Ye and C. V. Thompson, Acta Materialia **59** (2), 582-589 (2010).
23. G. H. Kim, R. Zucker, J. Ye, W. C. Carter and C. V. Thompson, Journal of Applied Physics **113** (043512) (2013).
24. W. C. Carter, A. R. Roosen, J. W. Cahn and J. E. Taylor, Acta Metallurgica Materialia **95** (12), 4309-4323 (1995).
25. L. Klinger, D. Amram and E. Rabkin, Scripta Materialia **64**, 962-965 (2011).
26. R. V. Zucker, G. H. Kim, W. C. Carter and C. V. Thompson, Comptes Rendus Physique **14** (7), 564-577 (2013).
27. R. Zucker, D. Chatain and W. C. Carter, Journal of Materials Science (2012).
28. E. Bussmann, F. Cheynis, F. Leroy, P. Muller and O. Pierre-Louis, New Journal of Physics **13** (2011).
29. F. Cheynis, E. Bussmann, F. Leroy, T. Passanante and P. Muller, Physical Review B **84** (245439) (2011).
30. G. H. Kim, S. Jahangir, N. Valanoor and C. V. Thompson, Acta Materialia (submitted) (2015).

31. F. Leroy, F. Cheynis, T. Passanante and P. Muller, Physical Review B **85** (195414) (2012).
32. F. Cheynis, F. Leroy and P. Muller, Comptes Rendus Physique **14**, 578-589 (2013).
33. R. V. Zucker, C. V. Thompson and W. C. Carter, In preparation (2015).
34. M. Dufay and O. Pierre-Louis, Physica Review Letters **106** (105506) (2011).
35. W. Kan and H. Wong, Journal of Applied Physics **97** (043515) (2005).
36. R. V. Zucker, G. H. Kim, J. Ye, W. C. Carter and C. V. Thompson, Journal of Applied Physics (submitted) (2015).
37. E. Rabkin, D. Amram and E. Alster, Acta Materialia **74** (30) (2014).
38. O. Pierre-Louis, A. Chame and Y. Saito, Physical Review Letters **103** (195501) (2009).
39. G. H. Kim and C. V. Thompson, Acta Materialia **84**, 190-201 (2015).
40. M. E. T. Molares, A. G. Balogh, T. W. Cornelius, R. Neumann and C. Trautmann, Applied Physics Letters **85** (22), 5337-5339 (2004).
41. S. Karim, M. E. Toimil-Molares, W. Ensinger, A. G. Balogh, T. W. Cornelius, E. U. Khan and R. Neumann, J. of Phys. D: Appl. Phys. **40**, 3767-3770 (2007).
42. X. H. Huang, Z. Y. Zhan, X. Wang, Z. Zhang, G. Z. Xing, D. L. Guo, D. P. Leusink, L. X. Zheng and T. Wu, Applied Physics Letters **97** (203112) (2010).
43. Z. F. Zhou, Y. Pan, Y. C. Zhou and L. Yang, Applied Surface Science **257**, 9991-9995 (2011).
44. M. Rauber, F. Muench, M. E. Toimil-Molares and W. Ensinger, Nanotechnology **23** (475710) (2012).
45. T. Barwicz, G. M. Cohen, K. B. Reuter, S. Bangsaruntip and J. W. Sleight, Appl. Phys. Lett. **100** (093109) (2012).
46. D. Raabe and J. Ge, Scripta Materialia **51**, 915-920 (2004).
47. H. S. Shin, J. Yu and J. Y. Song, Applied Physics Letters **91** (173106) (2007).
48. S. Karim, K. Maaz, G. Ali and W. Ensinger, Journal of Physics D: Applied Physics **42** (185403) (2009).
49. G. Rizza, F. Attouchi, P.-E. Coulon, S. Perruchas, T. Gacoin, I. Monnet and L. Largeau, Nanotechnology **22** (175305) (2011).
50. D. S. Deng, J.-C. Nave, X. Liang, S. G. Johnson and Y. Fink, Optics Express **19** (17), 16273-16290 (2011).
51. S. Tanaka, C. C. Umbach and J. Blakely, Surface Science **372**, 298-300 (1997).
52. K. Zhao, R. S. Averback and D. G. Cahill, Applied Physics Letters **89** (053103) (2006).
53. H. Li, J. M. Biser, J. T. Perkins, S. Dutta, R. P. Vinci and H. M. Chan, Journal of Applied Physics **103** (024315) (2008).
54. J. P. Naik, P. D. Prewett, K. Das and A. K. Raychaudhuri, Microelectronic Engineering **88**, 2840-2843 (2011).
55. J. P. Naik, K. Das, P. D. Prewett, A. K. Raychaudhuri and Y. Chen, Applied Physics Letters **101** (163108) (2012).
56. J. Plateau, *Experimental and Theoretical Statics of Liquids Subject to Molecular Forces Only*. (Gauthier-Villars, Paris, 1873).
57. L. Rayleigh, Proceedings of the London Mathematical Society **10** (4), 4-12 (1878).
58. F. A. Nichols and W. W. Mullins, Transactions of the Metallurgical Society of AIME **233** (1965).
59. W. C. Carter and G. A.M., Acta Metallurgica **35** (1), 237-245 (1987).

60. M. S. McCallum, P. W. Voorhees, M. J. Miksis, S. H. Davis and H. Wong, Journal of Applied Physics **79** (7604) (1966).
61. J. W. Cahn, Scripta Metallurgica **13**, 1069-1071 (1979).
62. D. E. Wolf and J. Villain, Physical Review B **41** (4), 2434-2444 (1990).
63. A.-G. Cheong and A. D. Rey, Journal of Chemical Physics **117** (10), 5062-5071 (2002).
64. K. F. Gurski and G. B. McFadden, Proceedings of the Royal Society A **459**, 2575-2598 (2003).
65. K. F. Gurski, G. B. McFadden and M. J. Miksis, SIAM Journal on Applied Mathematics **66** (4), 1163-1187 (2006).
66. J. Ye and C. V. Thompson, Advanced Materials **23** (13), 1567-1571 (2011).
67. J. D. Powers and A. M. Glaeser, Journal of American Ceramic Society **83** (9), 2297-2304 (2000).
68. M. K. Santala and A. M. Glaeser, Surface Science **600**, 782-792 (2006).
69. M. K. Santala and A. M. Glaeser, Acta Materialia **56**, 1967-1980 (2008).
70. J. M. Blakely and H. Mykura, Acta Metallurgica **9**, 595-599 (1961).
71. R. T. Tung and W. R. Graham, Surface Science **97**, 73-87 (1980).
72. C. M. Chang, C. M. Wei and J. Hafner, Journal of Physics: Condensed Matter **13** (2001).
73. H. Meltzman, D. Chatain, D. Avizemer, T. M. Besmann and W. D. Kaplan, Acta Materialia **59** (9), 3473-3483 (2011).
74. Y. Y. Huang, Y. C. Zhou and Y. Pan, Physica B **405**, 1335-1338 (2010).
75. A. L. Giermann and C. V. Thompson, Applied Physics Letters **86** (121903) (2005).
76. D. Kim, A. L. Giermann and C. V. Thompson, Applied Physics Letters **95** (251903) (2009).
77. S. Chikazumi, Journal of Applied Physics **32** (3), S81-S82 (1961).
78. H. Qiu, A. Kosuge, H. Maruyama, M. Adamik, G. Safran, P. B. Barna and M. Hashimoto, Thin Solid Films **241** (1), 9-11 (1994).
79. P. Sandstrom, E. B. Svedberg, J. Birch and J.-E. Sundgren, Journal of Crystal Growth **197** (4), 209-217 (1999).
80. D. R. Gaskell, *Introduction to the Thermodynamics of Materials*, 5th ed. (Taylor and Francis Group, New York, NY, 2008).
81. C. V. Thompson, Ann. Rev. of Materials Research **42** (42), 299-334 (2012).
82. G. H. Kim, W. Ma, B. Yildiz and C. V. Thompson, (unpublished, 2015).
83. K. Christmann, G. Ertl and O. Schober, Surface Science **40**, 61-70 (1973).
84. W. Oed, H. Lindner, U. Starke, K. Heinz and K. Muller, Surface Science **224**, 179-194 (1989).
85. L. H. Germer and A. U. MacRae, Journal of Chemical Physics **37**, 1382-1386 (1962).
86. K. Baberschke, U. Dobler, L. Wenzel and D. Arvanitis, Physical Review B **33** (8) (1986).
87. I. Utke, P. Hoffmann and J. Melngailis, Journal of Vacuum Science & Technology **26** (4), 1197-1276 (2008).
88. F. Leroy, F. Cheynis, T. Passanante and P. Muller, Physical Review B **88** (035306) (2013).
89. O. Pierre-Louis, A. Chame and M. Dufay, European Physics Journal B **77**, 57-63 (2010).
90. A. Chame and O. Pierre-Louis, Comptes Rendus Physique **14**, 553-563 (2013).
91. R. L. Schwoebel and E. J. Shipsey, Journal of Applied Physics **37**, 3682-3686 (1966).
92. W. Hong, Z. Zhang and Z. Suo, Physical Review B **74** (235318) (2006).

93. W. Hong, Z. Suo and Z. Zhang, Journal of the Mechanics and Physics of Solids **56**, 267-278 (2008).
94. Y. B. Zheng, S. J. Chua, C. H. A. Huan and Z. L. Miao, Journal of Crystal Growth **263**, 161-166 (2004).
95. E. Jiran and C. V. Thompson, Thin Solid Films **208**, 23-28 (1992).
96. F. A. Nichols and W. W. Mullins, Journal of Applied Physics **36** (6), 1826-1835 (1964).
97. O. Pierre-Louis, A. Chame and Y. Saito, Physical Review Letters **99** (13) (2007).
98. J. Chen and N. Chen, Journal of Physics: Condensed Matter **22** (21), 1-11 (2010).
99. A. R. C. Westwood and D. L. Goldheim, Journal of Applied Physics **34** (11), 3335-3339 (1963).
100. P. Du and H. Wong, Journal of Applied Physics **111** (113503) (2012).
101. J. S. Stolken and G. A.M., Scripta Metallurgica et Materialia **27**, 449-454 (1992).
102. C. D. Schaper, Nano Letters **3** (9), 1305-1309 (2003).
103. E. J. Smythe, M. D. Dickey, G. M. Whitesides and F. Capasso, ACS Nano **3** (1), 59-65 (2009).
104. D. T. Danielson, Ph.D. Thesis, MIT, 2008.
105. D. Q. McNerny, B. Viswanath, D. Copic, F. R. Laye, C. Prohoda, A. C. Brieland-Shoultz, E. S. Polsen, N. T. Dee, V. S. Veerasamy and A. J. Hart, Scientific Reports **4** (5049) (2014).
106. I. EG&G Services Parsons, Science Applications International Corporation, *Fuel Cell Handbook Fifth Edition*. (National Energy Technology Laboratory, October 2000).